Methods for Positioning Deeply-Towed Underwater Cables

by

Franz Stephen Hover

Submitted to the
Department of Mechanical Engineering, MIT
and the
Department of Applied Ocean Physics and Engineering, WHOI
in partial fulfillment of the requirements for the degree of

Doctor of Science

at the

MASSACHUSETTS INSTITUTE OF TECHNOLOGY
and the
WOODS HOLE OCEANOGRAPHIC INSTITUTION

January 1993

Author..
Department of Mechanical Engineering, MIT
Department of Applied Ocean Physics and Engineering, WHOI
January 14, 1993

Certified by..
Dana R. Yoerger
Associate Scientist, Woods Hole Oceanographic Institution
Thesis Supervisor

Accepted by..
Arthur Baggeroer
Chairman, Joint Committee on Oceanographic Engineering

Methods for Positioning Deeply-Towed Underwater Cables

by

Franz Stephen Hover

Submitted to the
Department of Mechanical Engineering, MIT
and the
Department of Applied Ocean Physics and Engineering, WHOI
on January 14, 1993, in partial fulfillment of the
requirements for the degree of
Doctor of Science

Abstract

This thesis considers the problem of positioning a very long, vertical tow cable in the ocean. Drill strings and tethers that support remotely-operated vehicles are examples of systems for which position control of the lower endpoint is important. Consistent with current practice, we assume that the cable can be manœuvered only by vessel motions at the top, and that it is tracked only at the endpoints.

A derivation of the equations of cable motion is given, followed by an analysis of the nonlinear frequency response of the plant, using the method of harmonic balances and a perturbation approach. The perturbation results are extended to give a closed-form estimate of the closed-loop limit-cycling behavior. The basic control approach is to consider input preshaping and regulation designs separately, merging them to form tracking controllers. The primary preshaping part is a frequency-domain dynamic inversion based on recent results in robotics; it requires the construction of a finite-dimensional model of the plant, and works for in-plane and coupled out-of-plane motions, as well as some other distributed-parameter physical systems. For regulator design, a number of observer-based approaches are considered, ranging from standard linear loopshaping to an approximately optimal nonlinear control law with nonlinear observation. Our solution to the nonlinear optimal control problem is novel in the sense that it can accommodate plant models of arbitrary order, a necessity for distributed plants.

The preshaping techniques are verified with full-scale results from experiments in the ocean with 2000 meters of cable, and the various closed-loop methods are compared based on scale-model laboratory tests.

Thesis Supervisor: Dana R. Yoerger
Title: Associate Scientist, Woods Hole Oceanographic Institution

Acknowledgments

Contents

List of Figures

8

List of Tables

Chapter 1

Introduction

1.1 Motivation

Towed underwater cables have been an important component of ocean systems for many decades. In early oceanographic work the cable was a simple steel wire for lowering sampling instruments, corers, dredging tools, and, less commonly, bathyspheres to specified depths. More recently, these cables have been constructed of state-of-the-art materials, and are often capable of supporting very high communication bandwidths through fiber optic technology. The cables have also grown in diameter to enable the transmission of substantial electrical and mechanical power. With these advances, cables remain an extremely effective way to reach the deep seafloor.

High-tension cables form an important subclass for towed systems. The tension is due to the weight of the mass at the bottom (referred to in the rest of the thesis as "the towfish"), and to the weight of the cable itself. High-tension cables are popular because the weight keeps them essentially vertical under the surface vessel. There is little danger of hitting the cable with the props, and approximate positioning of the towfish is accomplished merely by positioning the surface vessel. Currents acting in the water column cause the cable to billow only a small amount.

There are many situations in which the towfish must be positioned with an accuracy of ten meters or less. For a deep system, one solution is to put thrusters on the towfish, with the idea that the towfish can reach all points in a circle of given radius while the surface vessel is stationary. The size of this "footprint" is natu ally governed by the thrust capability of the towfish, and by the water weight of the system. Another approach to precise positioning,

13

the one which is developed in this thesis, is to incorporate our knowledge of the cable's dynamic response, and position the towfish solely by maneuvering the surface vessel. This eliminates the need to exert large forces at the towfish and frees the towfish from the power and space requirements of thrusters. For very heavy systems, the required thruster forces could be exceedingly large.

Figure 1-1 shows three high-tension ocean towing applications where accurate positioning is important and towfish thrusters are not used. In a) is drawn a deep-sea drilling deployment. The object is to position the drill bit assembly at the lower end accurately enough so that an existing hole can be reentered. As drawn, a cone of several meters' radius is often used to align the riser with the hole. The riser may be forty centimeters or more in diameter and weigh more than one thousand Newtons per meter submerged. The surface vessel is maneuvered with dynamic positioning, and the bit assembly is tracked using a short-baseline acoustic net.

In part b) of Figure 1-1, a two-vehicle ROV system for exploration, survey, or inspection is shown. The vertical cable is under high tension, while the tether connecting the towfish to the ROV is of very low tension. The presence of the heavy towfish and the low-tension cable isolates the ROV from heave motions of the surface vessel, making the ROV free to move within the tether radius using its own thrusters. In practice, it is the towfish that must be positioned within the tether radius of the ROV, since the ROV is interacting with the seafloor. The *ARGO/JASON* system, developed at the Deep Submergence Laboratory at the Woods Hole Oceanographic Institution, is similar to that drawn. The *ARGO/JASON* vertical cable is steel and 1.7 centimeters in diameter, and the towfish weighs approximately 4500 Newtons in water. The towfish is typically tracked using a long-baseline acoustic net.

An envisioned scenario for ocean mining is drawn in Figure 1-1c). Although ocean mining has not been pursued on a large scale yet, there is great interest, since large quantities of ferromanganese nodules have been located on the seafloor [3]. The proposed systems would be capable of recovering some 5000 tons of ore per day. One recent design calls for a large bottom-crawling collector which grinds the ore and separates it from the gangue; a pumping unit, drawn here as the towfish, provides the means to move the material along a full-depth vertical pipeline. This mining system is a cross between the systems of Figures 1-1a) and 1-1b) in that the main cable is extremely heavy and of a large diameter, and the motions of the pumping unit are slaved to those of the collector.

14
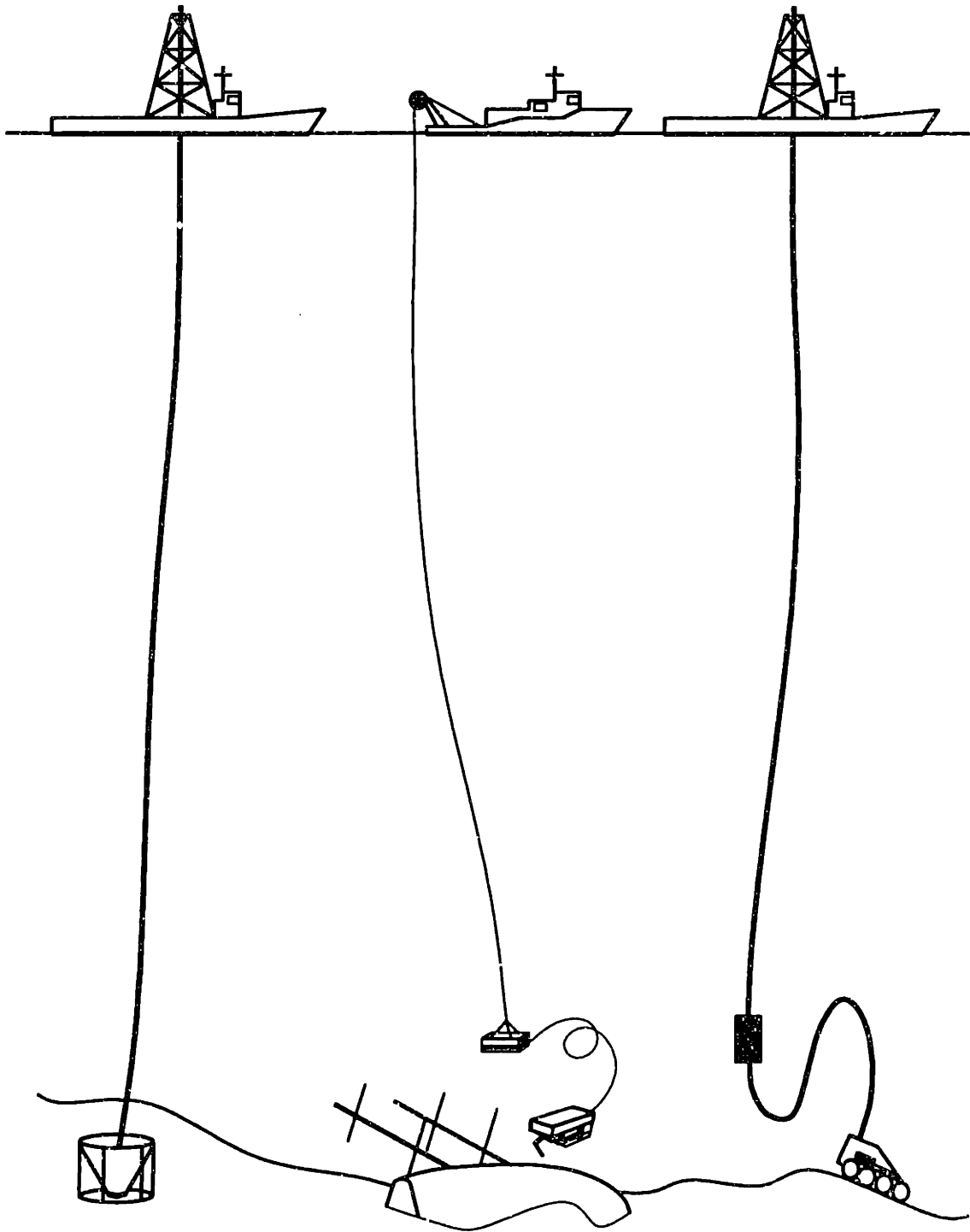
Figure 1-1: Three high-tension ocean towing applications: a) Borehole reentry with a drill string, b) ROV system, c) Ocean mining.

Accurate positioning of the towfish is required in all of these applications. This thesis develops appropriate techniques in open-loop and closed-loop senses, without requiring thrusters at the towfish.

1.2 Research Objectives

The plant under consideration is a difficult one to control, when tackled with the standard design procedures. The system is governed by partial differential equations, and can have significant geometric nonlinearities in addition to quadratic drag. Furthermore, we can only reasonably measure the position of a single or a few points along the member, and exert control on the system only at the top end.

It is the goal of this thesis to investigate a number of approaches, based on classical control theory, that can be applied to the positioning problem. We note at the outset that very few formal guarantees can be made, because an extreme simplification of the plant is used. Nonetheless, it it anticipated that designs based on the simple models will yield good properties from an operational viewpoint. The objectives of this research are as follows:

1. Provide an analytical approximation of the lateral frequency response of towed vehicle systems. Such an analysis will give some quantification of the expected behavior through simple calculations.

2. Develop a technique for improved dynamic response during standard point-to-point maneuvers, as would be required for an efficient change of position for *ARGO/JASON*. This procedure will improve upon the very slow settling times experienced during conventional maneuvers.

3. Develop a technique for computing vessel trajectories that lead to precision path-following for the lower endpoint of the member, as would be required for a sonar survey following a specific search pattern. Given the very long time-delay and the nonlinear nature of the cable, we hope to "sharpen up" the general response.

4. Develop feedback control algorithms for station-keeping and path-following in the presence of unmodeled dynamics, sensor noise, and physical disturbances such as currents. Feedback control is crucial in drill-hole reentry, for example, where a given watch circle of several meters must be maintained with the drill bit.

16

5. Verify the above procedures experimentally. Since no model is absolutely correct, experimental verification lends more credibility to the theoretical developments. In addition, experiments are likely to reveal the shortcomings of the design techniques, and to point to directions of further work.

1.3 Outline of the Thesis

Chapter 2 begins with a brief but complete derivation of the governing equations of motion for a cable-towfish system. The general nonlinear frequency response is approximated using harmonic balances and a perturbation technique; the effects of ambient current are included in the analysis. The perturbation formulation is extended to provide a closed-form estimate of the limit-cycling behavior of a cable system under linear closed-loop control. Comparisons with simulation data are presented for all the approximations, as verification.

The open-loop positioning problem is treated in Chapter 3. The rather ad hoc method of overshooting for point-to-point moves is briefly discussed, and then a full derivation of a dynamic inversion scheme is given. This scheme has a proof of convergence, and may be applied to a range of distributed-parameter problems. Full-scale experiments are described, which verify the point-to-point and trajectory-following techniques.

Chapter 4 discusses a number of important issues relating to regulator design, which is to be observer-based. The basic properties of the standard estimators and control laws are listed, and a new approach for approximating the solution to the optimal nonlinear feedback problem is derived. This approximate solution is novel and practical in the sense that it is nondynamical, does not require a look-up table, and can be applied to models of arbitrary order. Furthermore, the tools of its derivation may be useful in controller design for other plants with high order and nonlinearities with low-order polynomial approximations. At the close of the chapter, a set of proposed compensators is specified.

The application of closed-loop regulation and tracking is treated in Chapter 5. Some of the practical issues that arise in implementation of the theory are discussed, such as the explicit calculation of tolerable modeling errors in the different feedback strategies. This is a particularly interesting problem for nonlinear feedback because, as will be seen, the uncertainty must be expressed at the plant input. Two scale-model experiments are described and data are provided which demonstrate the relative merits of each control approach. These

17

data cover both regulation and tracking; the latter is accomplished by simply layering the regulators of Chapter 4 on top of the precalculated trajectories of Chapter 3.

Chapter 6 gives conclusions and recommendations, including an assessment of the practical advantages and disadvantages of the various estimation and control methods.

1.4 Related Literature

The dynamic responses of tethers and cables have been modeled accurately for a long time. References with relevance to ocean applications include Sanders [87], Ablow and Schecter [2], Triantafyllou [97], Bliek [19], Burgess [23], and Howell [56]. The dynamics of underwater vehicles are also well known; the seminal formulas have been given by Abkowitz [1], while the standard set of hydrodynamic terms has been provided by Feldman [42]. The response of towed underwater cable systems to vessel motions has been discussed by Mudie and Iverson [71], and Chapman [27]. These papers are primarily concerned with the transmission of vessel sway motions down the cable, and with the cable response during turns. An experimental study of half-turn maneuvers was carried out by Guerch [52], verifying the model developed in the paper by Iverson and Mudie [57].

The idea of preshaping actuator trajectories for complex motions of noncolocated systems has been used extensively in robotics applications. One of the originators was Smith [93], whose "posicast" approach utilized direct knowledge of the system's frequency response. The important papers of Bayo and his coworkers [9], [11], [12], [88] cover a range of approaches in robotics; the idea is to specify the desired trajectory of the endpoint and then explicitly compute the required motor torque to achieve it. Singer, Seering, and Singhose [89] [90] took a similar approach, with the goal of eliminating residual vibrations in a robotic arm at the end of a move. In contrast to Bayo's work, these papers use simpler plant models with only several natural modes.

Although experienced operators at sea have long been able to execute remarkably effective trajectories, the idea of actually precomputing vessel trajectories to effect specific towfish motions is only fifteen years old. An early work is Paul and Soler [80], where complete trajectories for fast point-to-point, in-plane maneuvers were generated, using iteration and finite-element modeling. In a different approach, predictive dynamic modeling was used in real time by Mudie and Kastens [72] to specify vessel trajectories that bring the towfish

18

closest (in the horizontal plane) to a specified target. These researchers conducted sea tests with 3300 meters of cable, and reported an average miss distance of 65 meters coming out of a turn of approximately two-kilometer radius. Cheng [29] has further investigated the use of predictive models; his approach provides a full display for the operator, who is to make the decisions on course changes. The technique was verified using simulations and human subjects.

As with the open-loop problem, feedback control of distributed parameter systems has been explored primarily in the area of robotics. There are a very large number of papers on this topic, so we list only a few of the most important works here. Modal control for generic systems was discussed by Balas [6], and Cannon and Schmitz [25] provided one of the first application papers, using the Linear Quadratic Gaussian/Loop Transfer Recovery (LQG/LTR) method on a finite-element model of a single-link arm. Sakawa et al. [86] addressed the flexible robot feedback problem with a modal approach, the sliding mode was used by Yeung and Chen [104], and an adaptive approach with prediction was developed by Cetinkunt and Wu [26].

Vincet et al. [101] recognized that to reposition noncolocated linear mass-spring systems, it often makes sense to decompose the control law into two parts. The first part is a saturated-input high-gain control law to execute the gross movement, followed by a passive control law to eliminate residual vibrations. In contrast to the previous references on feedback control, full-state measurement or estimation is not required here. Lyapunov arguments (e.g., [92]) indeed verify that any passive control law applied at the boundary of such a system (which could be nonlinear) leads to asymptotic stability. These observations are consistent with those of the paper by Liu et al. [62], who showed that a system of vibrating strings can be exponentially stabilized by placing linear dampers at each or both ends. This idea has been applied to vibration suppression in robots and structures by Paden et al. [78] (passive joint controllers), and Hagedorn [53] (active absorption of traveling waves).

In this thesis, the idea of splitting the control law into two parts will be used. The feedforward part is related to Bayo's work, and the feedback laws are model-based, in a robust control setting. For the linear single-input/single-output (SISO) feedback problem, one would typically use classical loopshaping ideas for this (e.g., [38]), while for multi-input/multi-ouput systems (MIMO), the LQG/LTR approach [39], [94] is popular. The synthesis of nonlinear estimators and nonlinear regulators was discussed by Grunberg and

Athans [50], [51], who provided a loop recovery procedure much LTR, called Loop Operator Recovery (LOR). This result will be used heavily in Chapter 4, and actually implemented in Chapter 5. [1]

The nonlinear estimation problem has been recently discussed in the survey paper by Misawa and Hedrick [68]. Among the most popular of techniques, the constant gain extended Kalman filter [84] and the full extended Kalman filter (e.g., [44]) have good properties that will be discussed in Chapter 4. On the control side, although the LQR has some intrinsic robustness when applied to nonlinear systems [82], a nonlinear optimal control approximation will be worked out as well. The statement of the optimal control problem for nonlinear systems can be found in the book by Athans and Falb [5], and the properties of optimal controllers with quadratic cost were discussed by Moylan and Anderson [70], Glad [46], and Tsitsiklis and Athans [99]. Actual solutions of the Hamilton-Jacobi-Bellman (HJB) equation have become possible with today's faster computers; methods of computation have been discussed by Beaman [13], Dwyer [40], O'Sullivan and Sain [77], Luus [66], [67], and Nagurka and Yen [73]. The analytical approach of this thesis is based on the work of Yoshida and Loparo [105], and is similar to that of Willemstein [103]. The latter approach has been applied to satellite control by Dwyer and Sen [41] and Dabbous and Ahmed [32].

The paper by Triantafyllou and Grosenbaugh [98] is one of the very few applications of feedback control to the towing problem. The authors adopted a linear second-order lumped mass model of the cable system, with a pure time delay, and applied the Smith regulator idea [93] to the LQG/LTR methodology. A high-order model developed by Burgess and Triantafyllou [24] was used for verification, in an in-plane example. The application of LQG control to ocean mining problems has been discussed by Okano [76], who reported that in large pipe deployments, the frequencies of vortex-induced vibration [64] are usually well-separated from the first five natural lateral modes of vibration for the pipe. Finally, the effect of atmospheric drag on slewing control of flexible space robots has been investigated by Juang and Horta [58]. Written from the viewpoint of extrapolating the response in a vacuum from experiments in air, these researchers found that the primary effect of the drag was to eliminate high-frequency vibrational modes. We expect a similar trend to be true in ocean cables, and this point will be investigated further in Section 2.6.2.

---

[1]It is expected that the more recent approaches such as H_∞ (e.g., [43], [47]) and the μ-synthesis approach (e.g., [37]) might lead to similar results, although as yet there are no tractable nonlinear extensions.

Chapter 2

Cable Dynamic Equations and Analysis

2.1 Introduction

In order to address our control aims in the context of underwater towed systems, it is impor-
tant to model the physical system as accurately as possible, while maintaining a formulation
that is reasonable for controller design purposes. This chapter provides a derivation of the
relevant equations of motion for cables, and discusses the approximations involved in mak-
ing a model of the plant for control. Because of quadratic drag, even the simplified models
have a complex dynamics, so we give two approximate analyses of the lateral frequency
response of a vertical underwater cable. The frequency-response results are then extended
to predict the limit-cycle behavior of a closed-loop system, with a linear control law and a
single measurement. Limit cycles are commonly observed in nonlinear control systems of
this type.

2.2 Cable Equations

We begin with the full three-dimensional coupled equations, and show how they may be
simplified. The equations without bending stiffness have been derived in the lagrangian
coordinate system by Bliek [19] for example, and bending stiffness was subsequently treated
in Howell [56]. The following development is based on these sources. An initial assumption
is that the cable is inextensible, consistent with the fact that axial vibrations usually have
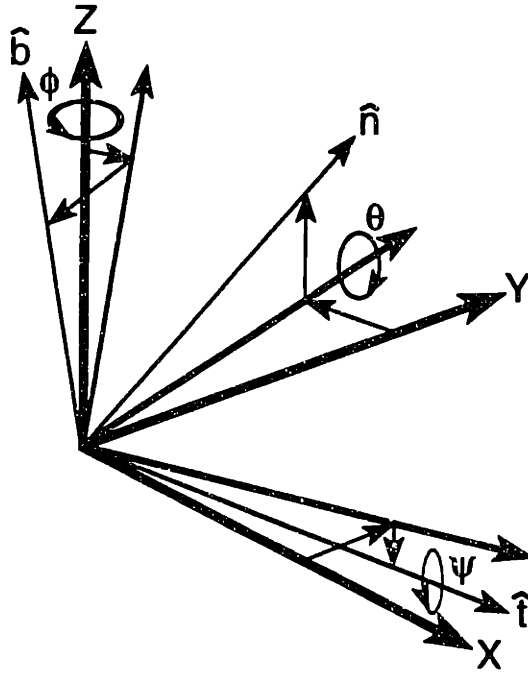
Figure 2-1: Euler angle convention.

a small effect on the lateral response of a vertical cable. In more general cases, where there is significant curvature in the cable, the geometric coupling can be important.

2.2.1 Reference Systems

The problem may be set in a lagrangian frame with the tangential, normal, and binormal unit vectors written as $[\hat{t}, \hat{n}, \hat{b}]$. The Euler angle convention provides a way to relate quantities in the inertial frame $[X, Y, Z]$ to those in the local frame. The ordering of angles is specified as shown in Figure 2-1;

1. Rotate by ϕ around Z; $X \rightarrow X'$ and $Y \rightarrow Y'$.

2. Rotate by θ around Y'; $X' \rightarrow X''$ and $Z \rightarrow Z'$. This brings X'' in line with $\hat{t}$.

3. Rotate by ψ around X'' to bring $Y' \rightarrow \hat{n}$ and $Z' \rightarrow \hat{b}$.

Substantial derivatives $(D(\cdot))$ in moving reference frames involve the Euler angles; let $\vec{\omega}$ be the rotation vector (the time rate of change of the cable element orientation), and $\vec{\Omega}$ be the Darboux vector (the spatial rate of change of the cable element orientation). Also, let t denote time, and s be the lagrangian cable coordinate. Then for an arbitrary vector $\vec{G} := G_1\hat{t} + G_2\hat{n} + G_3\hat{b}$ in the local frame, we have:

22

$$\frac{D\vec{G}}{Dt} = \frac{\partial \vec{G}}{\partial t} + \vec{\omega} \times \vec{G}, \tag{2.1}$$

$$\frac{D\vec{G}}{Ds} = \frac{\partial \vec{G}}{\partial s} + \vec{\Omega} \times \vec{G}, \tag{2.2}$$

where $\vec{\omega} = \omega_1 \hat{t} + \omega_2 \hat{n} + \omega_3 \hat{b}$, $\vec{\Omega} = \Omega_1 \hat{t} + \Omega_2 \hat{n} + \Omega_3 \hat{b}$, and

$$
\begin{aligned}
\omega_1 &= \frac{d\psi}{dt} - \frac{d\phi}{dt} sin\theta, \\
\omega_2 &= \frac{d\theta}{dt} cos\psi + \frac{d\phi}{dt} cos\theta sin\psi, \\
\omega_3 &= \frac{d\phi}{dt} cos\theta cos\psi - \frac{d\theta}{dt} sin\psi,
\end{aligned}
\tag{2.3}
$$

$$
\begin{aligned}
\Omega_1 &= \frac{d\psi}{ds} - \frac{d\phi}{ds} sin\theta, \\
\Omega_2 &= \frac{d\theta}{ds} cos\psi + \frac{d\phi}{ds} cos\theta sin\psi, \\
\Omega_3 &= \frac{d\phi}{ds} cos\theta cos\psi - \frac{d\theta}{ds} sin\psi.
\end{aligned}
\tag{2.4}
$$

2.2.2 Force and Moment Equations

From Figure 2-2, Newton's Law gives:

$$m\frac{\partial \vec{V}}{\partial t} + m\vec{\omega} \times \vec{V} = \frac{\partial \vec{F}}{\partial s} + \vec{\Omega} \times \vec{F} + \Sigma\vec{R}, \tag{2.5}$$

where m is the cable mass per unit length, $\vec{V}$ is the local velocity vector, $\vec{F}$ is the internal force vector, and $\Sigma\vec{R}$ is the the aggregate external force vector. Normally, $\Sigma\vec{R}$ consists of gravity, drag, and added mass terms.

To allow for bending stiffness terms, we must also write out the moment equations. Let $\vec{M}$ be the local internal moment vector; if the cross-section is circular, solid, and homogeneous, the moments can be written as follows:
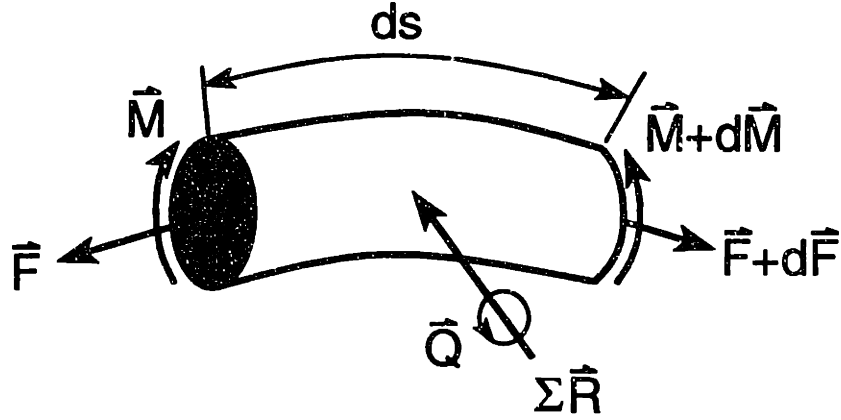
Figure 2-2: Forces acting on a cable element.

$$\vec{M} = \begin{bmatrix} GJ & 0 & 0 \\ 0 & EI & 0 \\ 0 & 0 & EI \end{bmatrix} \vec{\Omega}. \tag{2.6}$$

Here, G is the shear modulus, J is the polar moment of inertia, E is Young's modulus, and I is the bending moment of inertia. We define a matrix

$$H = \begin{bmatrix} J & 0 & 0 \\ 0 & I & 0 \\ 0 & 0 & I \end{bmatrix}$$

so that the moment equation is

$$H\frac{\partial \vec{\omega}}{\partial t} + \vec{\omega} \times (H\vec{\omega}) = \frac{\partial \vec{M}}{\partial s} + \vec{\Omega} \times \vec{M} + \vec{Q} + d\vec{r} \times \Sigma\vec{R} + \frac{d\vec{r}}{ds} \times \vec{T}. \tag{2.7}$$

Here, $\vec{r}$ is the position vector of the cable element, and $\vec{Q}$ is the applied moment to the element.

2.2.3 Simplifications

We neglect distributed external moments $\vec{Q}$, and note that in the limit as $d\vec{r}$ goes to zero, $d\vec{r} \times \Sigma\vec{R}$ goes to zero also, and $\frac{d\vec{r}}{ds}$ goes to $\hat{t}$. Thus, we have a simpler form for Equation 2.7:

$$H\frac{\partial\vec{\omega}}{\partial t} + \vec{\omega}\times(H\vec{\omega}) = \frac{\partial\vec{M}}{\partial s} + \vec{\Omega}\times\vec{M} + \hat{t}\times\vec{T}. \qquad (2.8)$$

Howell [56] carried out a nondimensional analysis which showed that certain terms of the force and moment vector equations can be neglected based on the physics of the cable system. These points will be taken into account here; they are outlined below.

1. The ratio of inertial moment to bending moment in rotation is on the order of $\frac{\rho_c g L}{E}$, or $10^{-6}L$ for steel cables, and lower for synthetic cables. Thus, we may usually neglect the rotational inertia terms. Here, ρ_c is the density of the cable, g is the acceleration due to gravity, and L is the length of the cable.

2. With no rotational inertia terms, the torsion on the length must be constant. If the cable is torque-balanced and there are no applied moments at the boundaries, then the torsion effects are zero. We may thus simplify matters by setting the Euler angle $\psi = 0$.

3. In nondimensionalized variables, the shear forces F_2 and F_3 are $O(\frac{EI}{(w_oL+W)L^2})$, where w_o is the weight in water per unit length of the cable, and W is the in-water weight of the towfish. The importance of bending stiffness terms can be judged on this quantity; high tension and large length generally make the bending moments small, and possibly negligible. For the current work, we expect that this ratio will be small, so the bending stiffness terms are included through the derivations only. An exception is that, in Section 5.2.2, which deals with model scaling of deep systems, this ratio is calculated to verify that the scaling is adequate with respect to bending stiffness.

2.2.4 Compatibility Relations

In addition to force (Equation 2.5) and moment relations (Equation 2.8), a cable is also subject to certain kinematic constraints, referred to as the compatibility relations. We have

$$\frac{D}{Dt}\frac{D\vec{r}}{Ds} = \frac{D}{Ds}\frac{D\vec{r}}{Dt}, \qquad (2.9)$$

and since $\frac{D\vec{r}}{Dt} = \vec{V}$ and $\frac{D\vec{r}}{Ds} = \hat{t}$, this is just

$$\vec{\omega}\times\hat{t} = \frac{\partial\vec{V}}{\partial s} + \vec{\Omega}\times\vec{V}. \qquad (2.10)$$

25

2.2.5 Governing Equations

The full set of governing equations consist of three force equations (2.5), two bending equations (2.8 with no torsional dynamics), and three compatibility relations (2.10). Let $[u, v, w]$ be velocities in the tangential, normal, and binormal directions, respectively. The bending equations are not prognostic, so the unknown variables are u, v, w, F_1, ϕ, and θ.

$$
\begin{aligned}
m(\frac{\partial u}{\partial t} + \omega_2 w - \omega_3 v) &= \frac{\partial F_1}{\partial s} + F_3 \Omega_2 - F_2 \Omega_3 + \Sigma R_1, \\
m(\frac{\partial v}{\partial t} + \omega_3 u - \omega_1 w) &= \frac{\partial F_2}{\partial s} + F_1 \Omega_3 - F_3 \Omega_1 + \Sigma R_2, \\
m(\frac{\partial w}{\partial t} + \omega_1 v - \omega_2 u) &= \frac{\partial F_3}{\partial s} + F_2 \Omega_1 - F_1 \Omega_2 + \Sigma R_3, \\
F_2 &= -EI\frac{\partial \Omega_3}{\partial s} - EI\Omega_1\Omega_2, \\
F_3 &= EI\frac{\partial \Omega_2}{\partial s} - EI\Omega_1\Omega_3, \\
\frac{\partial u}{\partial s} + \Omega_2 w - \Omega_3 v &= 0, \\
\frac{\partial v}{\partial s} + \Omega_3 u - \Omega_1 w &= \omega_3, \\
\frac{\partial w}{\partial s} + \Omega_1 v - \Omega_2 u &= -\omega_2.
\end{aligned}
\tag{2.11}
$$

In the above, we rely on our previous definitions of $\vec{\omega}$ and $\vec{\Omega}$ in terms of the Euler angles, with $\psi = 0$.

2.2.6 Applied Forces

We now consider the applied forces in the lagrangian coordinate system. They consist of gravity, drag, and added mass: $\Sigma \vec{R} = \Sigma \vec{R}(v, w, \phi, \theta) = \vec{R}_g + \vec{R}_d + \vec{R}_{am}$. The separate parts are as follows.

1. $\vec{R}_g = [-w_o sin\phi cos\theta, -w_o cos\phi, -w_o sin\phi sin\theta]$, where Y is taken to be upwards in the inertial frame.

2. $\vec{R}_d = [-\frac{1}{2}\rho d C_t u \mid u \mid, -\frac{1}{2}\rho d C_d v \sqrt{v^2 + w^2}, -\frac{1}{2}\rho d C_d w \sqrt{v^2 + w^2}]$, where ρ is the density of water, C_d and C_t are the normal and tangential drag coefficients of the cable, respectively, and d is the diameter of the cable. We assume that the same drag coefficient is valid in both the normal and binormal directions, using Morison's approach

26

[81].

3. $\vec{R}_{am} = [0, -m_a\frac{\partial v}{\partial t}, -m_a\frac{\partial w}{\partial t}]$, where m_a is the added mass per unit length. Added mass in the axial direction is neglected.

In situations with currents, the velocities in $\vec{R}_d$ above should be taken as the velocities relative to the ambient flow field. In addition, we have neglected hydrodynamic lift forces.

2.2.7 In-Plane Motions

The above equations collapse into a set of four equations if only in-plane motions are considered. There is only one Euler angle in this case; the unknowns are u, v, ϕ, and F_1. For convenience, from here on the tension is denoted by a T instead of F_1. We have

$$
\begin{aligned}
m\frac{\partial u}{\partial t} - mv\frac{\partial \phi}{\partial t} &= \frac{\partial T}{\partial s} + EI\frac{\partial \phi}{\partial s}\frac{\partial^2 \phi}{\partial s^2} - w_o sin\phi - \frac{1}{2}\rho dC_t u \mid u \mid, \\
(m + m_a)\frac{\partial v}{\partial t} + mu\frac{\partial \phi}{\partial t} &= T\frac{\partial \phi}{\partial s} - EI\frac{\partial^3 \phi}{\partial s^3} - w_o cos\phi - \frac{1}{2}\rho dC_d v \mid v \mid, \quad (2.12) \\
\frac{\partial v}{\partial s} &= \frac{\partial \phi}{\partial t} - u\frac{\partial \phi}{\partial s}, \\
\frac{\partial u}{\partial s} &= v\frac{\partial \phi}{\partial s}.
\end{aligned}
$$

Equations 2.12 represent the complete equations of motion for an inextensible in-plane cable. They are augmented by appropriate boundary conditions, three at each end. For our applications, the top end and the bottom end are pinned (no transmitted moment), and the top and bottom motions are given by the vessel forcing and the towfish dynamics, respectively.

2.3 General Behavior of Vertical Cables

Vertical cables in water are governed by a damped wave equation, which may or may not take into account bending stiffness. This fact indicates that a transfer function which takes motions of the top end to motions of the bottom end has a pure delay. If there is large bending stiffness, then the system can be non-minimum phase as well. These two properties are notorious for making controller design difficult. However, simulations show that the extreme forces of quadratic drag make it impossible to transmit any but the smallest of

27

motions all the way down an underwater cable. The cable thus serves as a very strong filter of motions, whose *gain increases as the amplitude of motion decreases.* This situation is illustrated in Figure 2-3, where simulation of Equation 2.38 (see Section 2.5.1) has been used to create an amplitude-dependent Bode plot. It is clear that when the excitation is very small, the gain and phase approach those of an undamped wave equation transfer function. As the excitation is increased, the gain peaks are reduced and shifted to lower frequencies, and the phase is smoothed and reduced (toward $-\infty$) on the frequency axis. These observations are consistent with the well-known behavior of linear systems when damping is increased. As the system is in fact nonlinear, the next two sections discuss how this dependence of dynamic response upon the amplitude of excitation may be characterized further. Understanding the nonlinear behavior of this system is important from a control point of view; for example, the attenuation which accompanies large excitations is stabilizing by virtue of the small-gain theorem [33], but the loss of phase that comes with these large motions can destabilize linear control systems.

Before treating the approximations, we note that Figure 2-3 above, and all of the other calculations for the chapter, are based on the nominal system described in Table 2.3.

2.4 Harmonic Balance

The first approximation technique we consider is a variation of the well-known *harmonic balance* or *equivalent linearization* procedure to find the in-plane dynamics of mooring systems [48]. This approach allows one to include the effects of static curvature (caused by currents perhaps), and elongation of the cable under dynamic loading. As such, and for completeness, the derivations which follow include these effects, even though Equations 2.12 do not.

2.4.1 Cable Equations

We consider the expansion $T \simeq \bar{T} + \tilde{T}$, where $\bar{T}$ is the static tension, and $\tilde{T}$ is the dynamic tension. Similarly, we let $\phi \simeq \bar{\phi} + \tilde{\phi}$. The static position of the cable is given uniquely by $\bar{\phi}$, so we let p and q denote the axial and lateral dynamic deflections, respectively. The cable coordinate system is oriented in the inertial frame as shown in Figure 2-4.

To compute the static configuration in the presence of a current U (positive in the X-
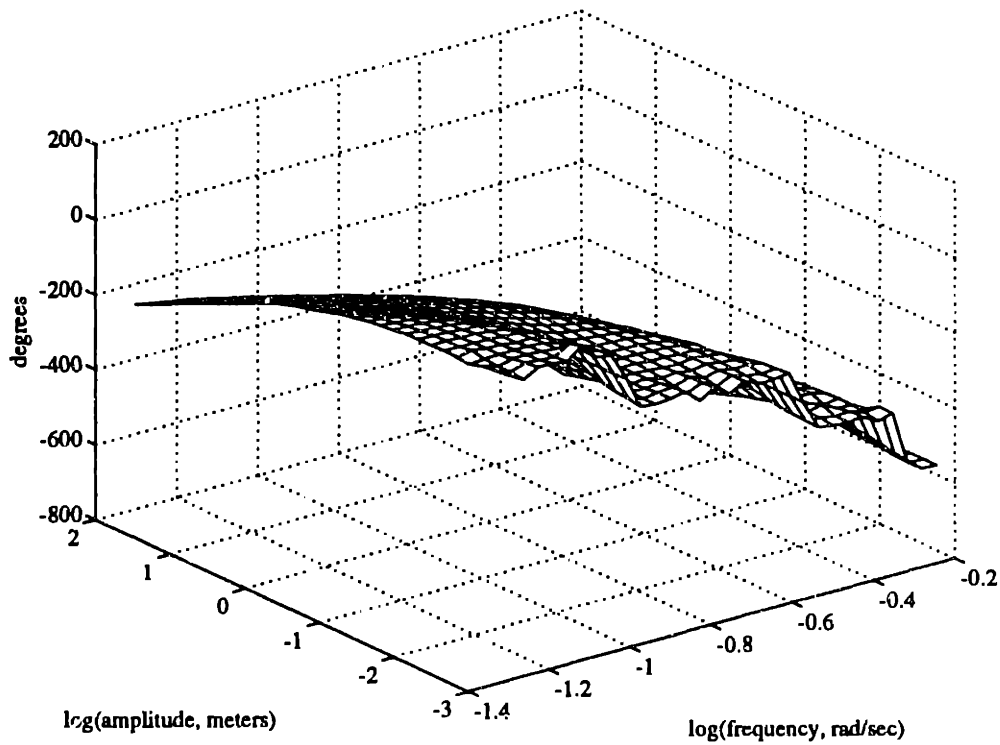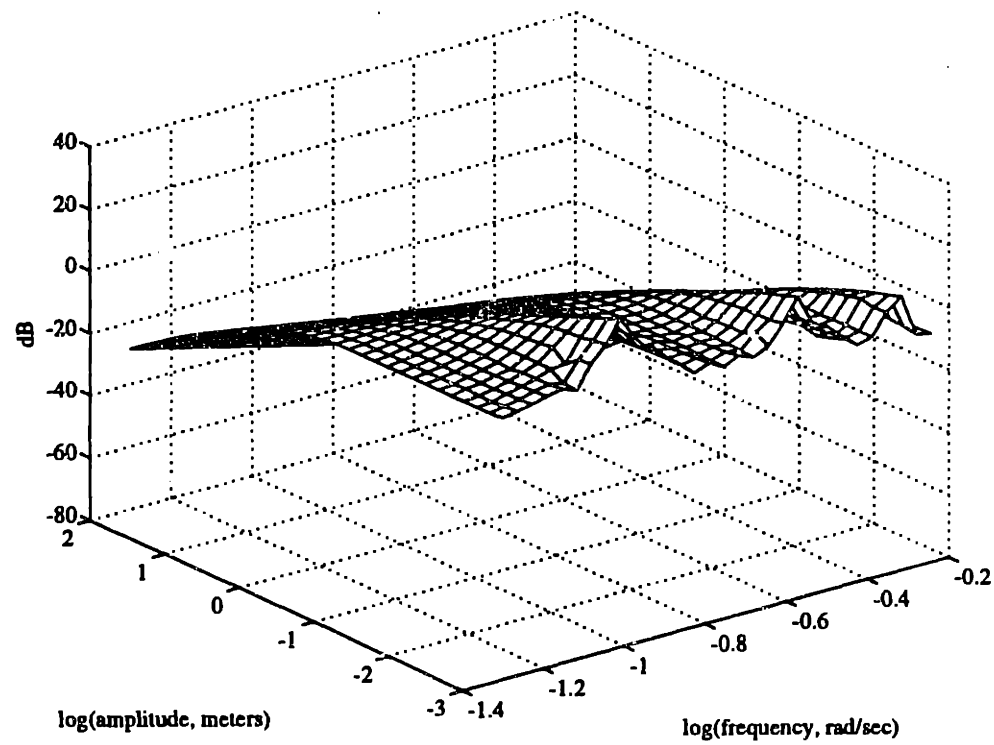
Figure 2-3: Nonlinear frequency response of the nominal system: gain (top) and phase (bottom).
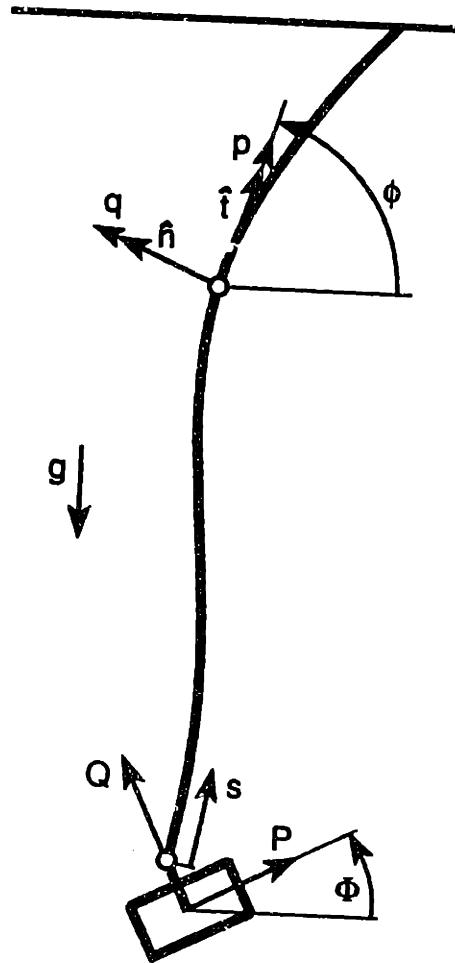
Figure 2-4: Cable configuration in the inertial frame.

cable length	L	$1000\ m$
cable diameter	d	$0.02\ meters$
cable water weight/length	w_o	$15\ N/m$
towfish water weight	W	$4000\ N$
cable mass/length	m	$1.6\ kg/m$
cable added mass (lateral)/length	m_a	$0.4\ kg/m$
effective horizontal mass of towfish	$M_P + M_{aP}$	$500\ kg$
effective vertical mass of towfish	$M_Q + M_{aQ}$	$500\ kg$
effective rotational inertia of towfish	J	$100\ kg \cdot m^4$
water density	ρ	$1025\ kg/m^3$
cable normal drag coefficient	C_d	2
cable tangential drag coefficient	C_t	0.01
drag coefficient of towfish	$C_{d,towfish}$	2
area of towfish vertical face	A_P	$1\ m^2$
area of towfish horizontal face	A_Q	$2\ m^2$
linear rotational damping of towfish	B_ϕ	$100\ N \cdot m/(m/s)$
distance between center of gravity and cable connection point	A_c	$1\ m$
cable elasticity	E	$200 \times 10^9\ N/m^2$

Table 2.1: Nominal system parameters.

direction), one can use a drag model of arbitrary complexity, as the static shape has to be computed only once. For example, a popular form that can induce lift is

$$R_{d,1} = \frac{1}{2}\rho d C_t U cos\bar{\phi} \mid U cos\bar{\phi} \mid \left(1 + \frac{\bar{T}}{EA}\right),$$ (2.13)

$$R_{d,2} = -\frac{1}{2}\rho d C_d U sin\bar{\phi} \mid U sin\bar{\phi} \mid \left(1 + \frac{\bar{T}}{2EA}\right).$$

This particular form can lead to decreased static tensions during towing because the lift forces carry some of the weight, while the drag forces become largely axial and therefore are controlled by C_t. As written, these static drag terms are influenced by elongation, in that stretching causes a decrease in diameter through Poisson's ratio. In addition, elongation will always show up in the representation of the static cable configuration in world coordinates.

In the dynamics, we assume that the quadratic drag acting upon the cable can be treated as a linear damping with spatial dependence. In particular, the describing function of $\zeta(s)sin(\omega t) \mid sin(\omega t) \mid$ is $\zeta(s)\frac{8}{3\pi}sin(\omega t)$; the cases of nonzero currents will be described

31

in Section 2.4.3. Under the assumptions of small dynamic angle and precomputed static configuration, the dynamic equations of Section 2.2.7 are:

$$\frac{\partial \bar{T}}{\partial s} = m\frac{\partial^2 p}{\partial t^2} + w_o \cos\bar{\phi}\,\tilde{\phi} + \frac{1}{2}\rho d C_t \frac{dp}{dt}\left|\frac{dp}{dt}\right|, \tag{2.14}$$

$$\bar{T}\frac{\partial \tilde{\phi}}{\partial s} = (m + m_a)\frac{\partial^2 q}{\partial t^2} + \frac{1}{2}\rho d C_d \left(\frac{\partial q}{\partial t} + U\right)\left|\frac{\partial q}{\partial t} + U\right| - \tag{2.15}$$

$$\frac{1}{2}\rho d C_d U \mid U \mid -w_o \sin\bar{\phi}\,\tilde{\phi} - \tilde{T}\frac{\partial \bar{\phi}}{\partial s},$$

$$\frac{\partial p}{\partial s} = \frac{\tilde{T}}{EA} + q\frac{\partial \bar{\phi}}{\partial s}, \tag{2.16}$$

$$\frac{\partial q}{\partial s} = \tilde{\phi}_1(1 + \frac{\tilde{T}}{EA}) - p\frac{\partial \bar{\phi}}{\partial s}, \tag{2.17}$$

where we have written the compatibility relations in terms of positions instead of velocities. Adopting linear damping coefficients $b_p(s)$, $b_q(s)$ which are to be found iteratively, one can write this in the frequency domain in matrix form:

$$\frac{d}{ds}\begin{bmatrix} \tilde{T} \\ \tilde{\phi} \\ p \\ q \end{bmatrix} = \begin{bmatrix} 0 & w_o\cos\bar{\phi} & -m\omega^2 + i\omega b_p(s) & 0 \\ -\frac{1}{\bar{T}}\frac{\partial\bar{\phi}}{\partial s} & -\frac{w_o\sin\bar{\phi}}{\bar{T}(s)} & 0 & \frac{1}{\bar{T}(s)}(-(m+m_a)\omega^2 + i\omega b_q(s)) \\ \frac{1}{EA} & 0 & 0 & \frac{\partial\bar{\phi}}{\partial s} \\ 0 & 1+\frac{\bar{T}(s)}{EA} & -\frac{\partial\bar{\phi}}{\partial s} & 0 \end{bmatrix}\begin{bmatrix} \tilde{T} \\ \tilde{\phi} \\ p \\ q \end{bmatrix}$$

or $\frac{d\vec{y}}{ds} = A(s)\vec{y}$. The constant term of Equation 2.15 transforms to a delta function, so it has no bearing on the frequency response. We let the cable be discretized into n nodes, numbered 1 at the towfish connection point, and n at the surface point, where there is an imposed motion. The unstretched distance between nodes is ds. Thus, we may approximate the evolution of $\vec{y}$ on the length as

$$\frac{\vec{y}_{i+1} - \vec{y}_i}{ds} \simeq \frac{A(s_{i+1})\vec{y}_{i+1} + A(s_i)\vec{y}_i}{2} \Longrightarrow \tag{2.18}$$

$$\vec{y}_{i+1} \simeq \left[I - \frac{ds}{2}A(s_{i+1})\right]^{-1}\left[I + \frac{ds}{2}A(s_i)\right]\vec{y}_i := B_i\vec{y}_i. \tag{2.19}$$

Then $\vec{y}_n$ is related to $\vec{y}_1$ as follows:

$$\vec{y}_n = B_{n-1}B_{n-2}\cdots B_1\vec{y}_1 := \beta\vec{y}_1. \qquad (2.20)$$

This represents four equations in six unknowns: $\bar{T}_1$, $\bar{T}_n$, $\bar{\phi}_1$, $\bar{\phi}_n$, and p_1 and q_1.

2.4.2 Towfish Dynamics

The required additional information is found by looking at the towfish dynamics; there is a relationship between the tension and angle at the connection point, and the motions of the towfish. With the variables P, Q, and Φ defined as shown in Figure 2-4, the basic equations for the towfish are as follows:

$$(M_P + M_{aP})\frac{\partial^2 P}{\partial t^2} = T_1 cos(\phi_1 - \Phi) - W sin\Phi - \frac{1}{2}\rho C_{d,towfish}A_P\frac{\partial P}{\partial t}\left|\frac{\partial P}{\partial t}\right|, \qquad (2.21)$$

$$(M_Q + M_{aQ})\frac{\partial^2 Q}{\partial t^2} = T_1 sin(\phi_1 - \Phi) - W cos\Phi - \frac{1}{2}\rho C_{d,towfish}A_Q\frac{\partial Q}{\partial t}\left|\frac{\partial Q}{\partial t}\right|, \qquad (2.22)$$

$$J\frac{\partial^2 \Phi}{\partial t^2} + B_\Phi\frac{\partial \Phi}{\partial t} = -T_1 A_c cos(\phi_1 - \Phi). \qquad (2.23)$$

The static solution requires that $\bar{\phi}_1 - \bar{\Phi} = \frac{\pi}{2}$, so that Equation 2.22 can be solved alone to obtain $\bar{\Phi}$. Again, one could use a sophisticated drag law for the vehicle in the steady state; for example, the static drag force in the X-direction can be approximated as

$$X \text{ drag:} \quad \frac{1}{2}\rho C_{d,towfish}(A_P \mid cos\bar{\Phi} \mid + A_Q \mid sin\bar{\Phi} \mid)U \mid U \mid cos\bar{\Phi}. \qquad (2.24)$$

Given $\bar{\Phi}$, then Equation 2.21 may be used to find $\bar{T}_1$, and the static cable equations can be integrated up to the water surface. This gives the total static configuration.

The towfish dynamics, under the assumption of small dynamic angles, is given by the frequency-domain equations

$$(-(M_P + M_{aP})\omega^2 + i\omega B_P)P = \bar{T}_1(\bar{\Phi} - \bar{\phi}_1) - W cos\bar{\Phi}\bar{\Phi}, \qquad (2.25)$$

$$(-(M_Q + M_{aQ})\omega^2 + i\omega B_Q)Q = \bar{T}_1 - W sin\bar{\Phi}\bar{\Phi}, \qquad (2.26)$$

$$(-J\omega^2 + i\omega B_\Phi + \bar{T}_1 A_c)\bar{\Phi} = \bar{T}_1 A\bar{\phi}_1. \qquad (2.27)$$

where, as for the cable, the damping is based on describing functions, and to be found iteratively. Thus, we can easily write

$$
H \begin{bmatrix} P \\ Q \\ \Phi \end{bmatrix} = G \begin{bmatrix} \tilde{T}_1 \\ \tilde{\phi}_1 \end{bmatrix},
\tag{2.28}
$$

where H is a 3×3 matrix. We also need a kinematic relationship between the motions of the towfish and the motions of the connection point:

$$
\begin{bmatrix} p_1 \\ q_1 \end{bmatrix} = \begin{bmatrix} 0 & 1 & 0 \\ -1 & 0 & A \end{bmatrix} \begin{bmatrix} P \\ Q \\ \Phi \end{bmatrix} := R \begin{bmatrix} P \\ Q \\ \Phi \end{bmatrix}.
\tag{2.29}
$$

Breaking the matrix β of Equation 2.20 into 2×2 blocks numbered β_{11}, β_{12}, β_{21}, and β_{22}, the relationship between the towfish motions and the motions of the top point is

$$
\begin{bmatrix} P \\ Q \\ \Phi \end{bmatrix} = H^{-1} G (\beta_{21} + \beta_{22} R H^{-1} G)^{-1} \begin{bmatrix} p_n \\ q_n \end{bmatrix}.
\tag{2.30}
$$

This calculation complete, one may then use Equations 2.28 and 2.29 to get $\vec{y}_1$. The local "state vectors" $\vec{y}_i$ may then be found all the way through the cable using Equation 2.18.

In order to carry out iteration for the drag nonlinearity, one may assume an initial spatially-varying damping $b_q(s)$, $b_p(s)$ as well as initial values for B_P and B_Q, and find all the vectors $\vec{y}_i$. The equivalent linearization is then found at each point; this leads to a different set of damping coefficients, which in the next iteration gives a new set of motions. The iterations are continued until the motions settle sufficiently.

This straight iterative loop has been found to be stable in general, although it may take a very long time to converge. To speed up the calculations, a Newton-Raphson or bisection approach may be helpful. For the present work, bisection of the successive motion estimates has been used, and acceptable results can be obtained in less than five iterations, for most cases.

2.4.3 The Effects of Current

Let $v(s,t) = \zeta(s)sin(\lambda t)$, and the current be U. In actuality, $v(s,t)$ has some phase angle associated with it, and U may be a function of depth, but we forego these dependencies (without loss of generality) to keep the following formulations simple. We investigate three cases of quadratic drag:

1. $U = 0$; see Figure 2-5(a). We can use $\frac{8}{3\pi}sin(\lambda t)$ as the describing function for $sin(\lambda t) \mid sin(\lambda t) \mid$, so that

$$v(s,t) \mid v(s,t) \mid \simeq \zeta(s) \mid \zeta(s) \mid \frac{8}{3\pi}sin(\lambda t). \qquad (2.31)$$

   The Fourier component associated with this force is therefore $b_1^1(s) := \frac{8}{3\pi}\zeta(s) \mid \zeta(s) \mid$.

2. $U > 0$, without loss of generality, and U is large enough that $U + \zeta(s) \geq 0$ everywhere on the length. See Figure 2-5(b). Then $(U + v) \mid U + v \mid$ is positive everywhere also. This signal can be decomposed into its Fourier components; the D.C. component is positive, and gives rise to an offset in the static shape. The first harmonic component of $(v + U) \mid v + U \mid$ is given by

$$b_1^2(s) = \frac{1}{T} \int_{-T}^{T} (U + \zeta(s)sin(\lambda t) \mid U + \zeta(s)sin(\lambda t) \mid sin(\lambda t)dt, \qquad (2.32)$$

   where $2T$ is the period of oscillation. Because $U + v$ is positive, we may as well integrate with the quadratic part replaced by a square. Applying some standard integral identities, it is found that $b_1^2(s) := 2U\zeta(s)$. This leads to the approximation

$$(v(s,t) + U) \mid v(s,t) + U \mid \simeq 2U\zeta(s)sin(\lambda t). \qquad (2.33)$$

   This term reflects that fact that $(v + U)(v + U) = v^2 + 2Uv + U^2$ is dominated by $2Uv$ when U is large. The U^2 term is canceled by the static solution.

3. $U > 0$, but there are regions in each cycle where $U + v(s,t)$ goes negative. See Figure 2-5(c). The crossover points $\beta_i(s)$ (there are two) can be found in the time range $(-T, T)$ by setting

35
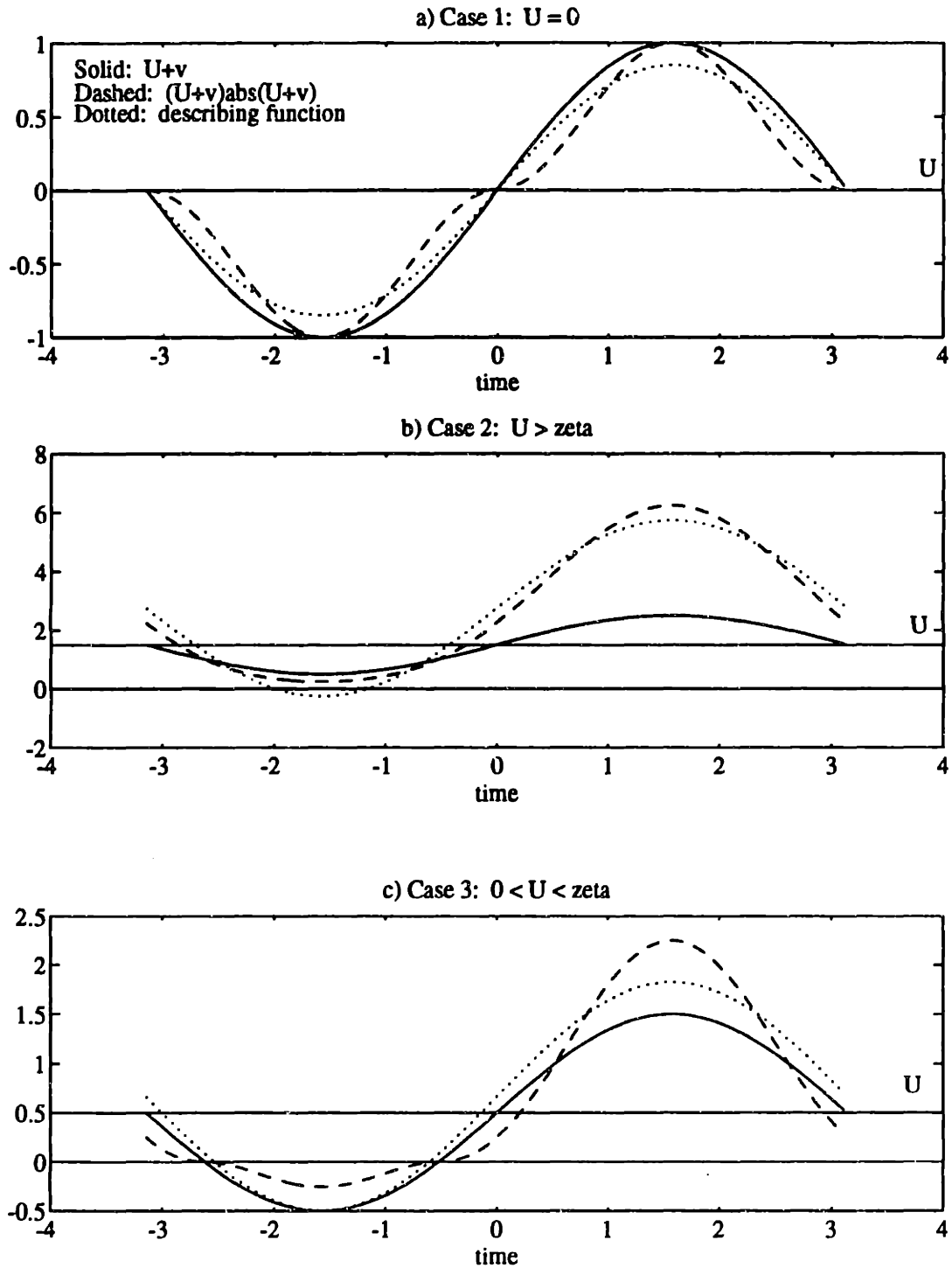
Figure 2-5: Describing functions for three drag regimes based on equalized first Fourier coefficients.

$$\zeta(s) sin\left(\frac{\pi \beta_i(s))}{T}\right) + U = 0 \text{ , or}$$

$$\beta_i(s) = \frac{T}{\pi} sin^{-1}\left(\frac{-U}{\zeta(s)}\right). \tag{2.34}$$

Through careful manipulation of integrals, one is able to deduce the first harmonic amplitude [97];

$$b_1^3(s) := sgn(\zeta(s))\frac{4}{\pi}\left[-U \mid \zeta(s) \mid sin^{-1}\left(\frac{-U}{\mid \zeta(s) \mid}\right) + \frac{1}{3}(U^2 + 2\zeta^2(s))\sqrt{1 - \frac{U^2}{\zeta^2(s)}}\right],$$
$$\tag{2.35}$$

where $sgn(\cdot)$ is the sign of the argument. It may be verified that in the limit as $\zeta(s) \to U$, b_1^3 approaches b_1^2. In addition, as $U \to 0$, b_1^3 approaches b_1^1.

In Figure 2-6 are plotted the contours of b_1^i for a range of values of $\zeta(s)$ and of U. The portion above the $U = \zeta(s)$ line is due to Case 2 above, the portion on the $\zeta(s)$-axis is from Case 1, and the area connecting the $U = \zeta(s)$ line to the $\zeta(s)$-axis is from Equation 2.35. It can be seen that b_1 depends quadratically upon $\zeta(s)$ when there is no current, but that when the current is large, this relationship is linear. Case 3 considerations provide a smooth contour between these two simpler regimes.

2.4.4 Harmonic Balance Results

The data of Figure 2-3 has been plotted against the predictions of the harmonic balance method, in Figure 2-7. Each curve here represents one frequency response curve for a particular amplitude, each of which is listed to the left of the curves. Overall, the matching between simulation results and the harmonic balance method is extremely good, although in the high-amplitude, high-frequency regime, one notes some discrepancy. This is due to an a priori tolerance specification in the harmonic balance algorithm. An important observation is that the simulation required fourteen hours to run while the harmonic balance data were generated in approximately fifteen minutes, all on a one megaflop workstation.
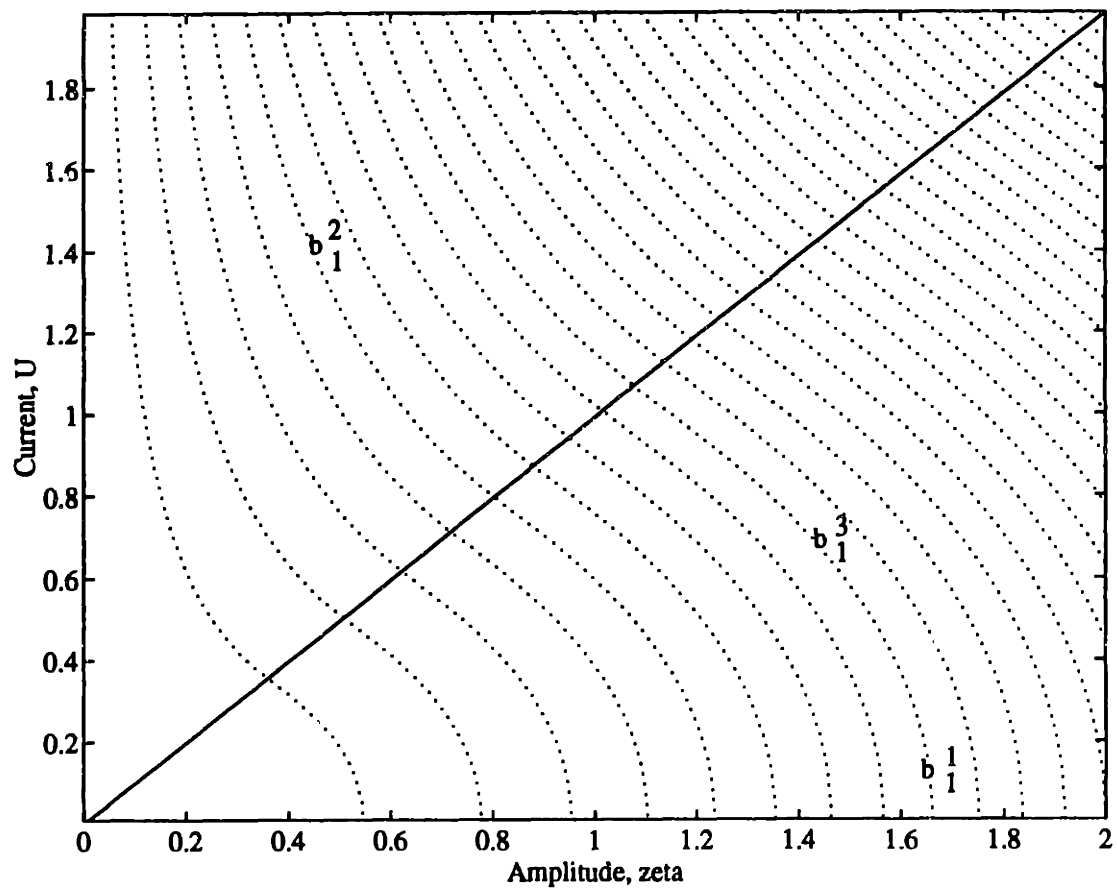
Figure 2-6: Contours of b_1 for various values of u and ζ.
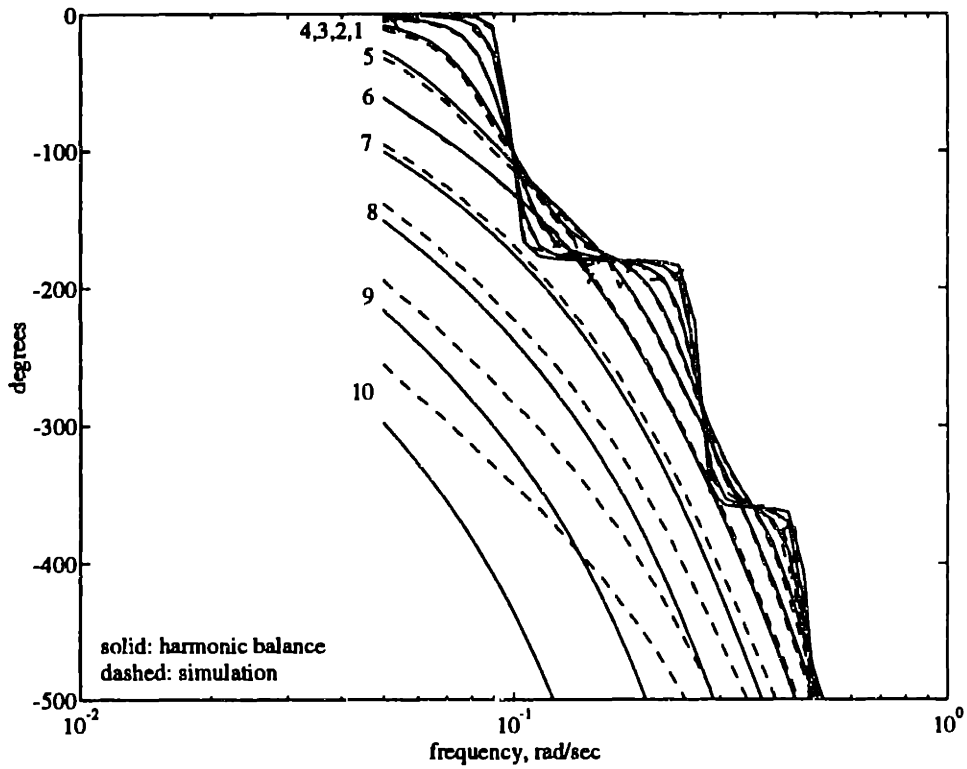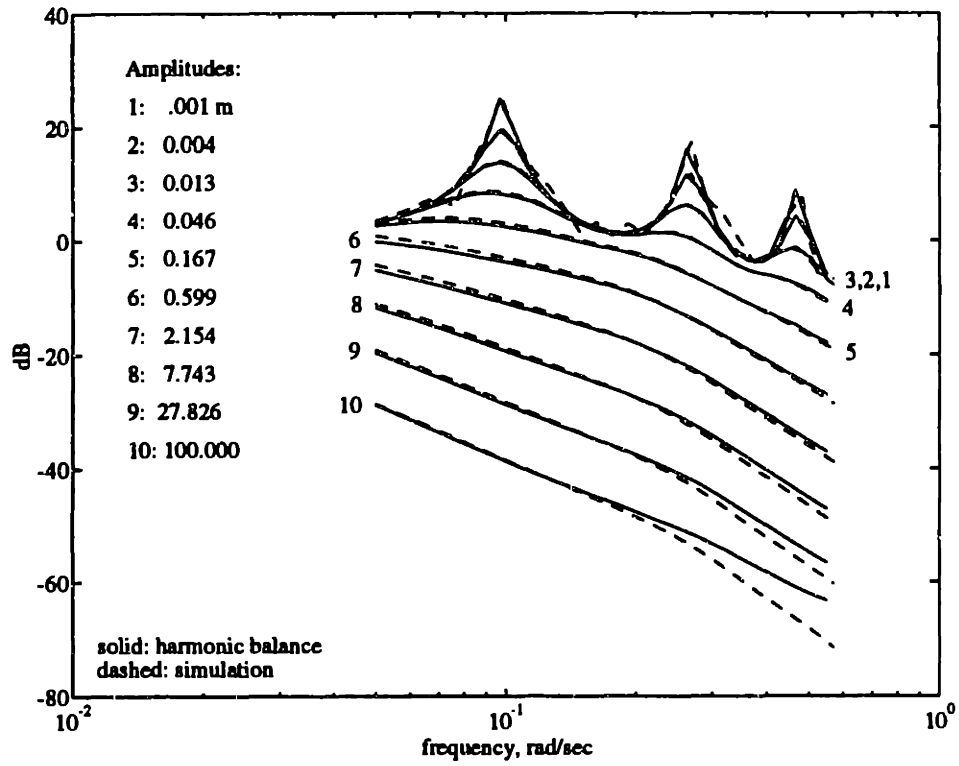
Figure 2-7: Comparison of simulation and harmonic balance frequency response estimates: gain (top) and phase (bottom).

In order to assess the impact of current on the lateral frequency response, the above calculations were repeated, with a current of two centimeters per second. As might be anticipated, the *current introduces significant attenuation and phase loss in the plant*; Figure 2-8 shows this trend clearly, when compared to Figure 2-7. We see that the curves associated with the four lowest excitation amplitudes are coincident because of the linear drag of Case 2. The remainder of the curves are in the regime of Case 3, which dictates that the current has a diminishing effect with growing amplitudes. In general, as the current becomes larger, one sees more and more of the response controlled by linear damping, and a smooth transition into amplitudes that are large enough that quadratic drag is still dominant.

Since the harmonic balance method incorporates axial dynamics with geometric coupling and elongation, calculations were also made for the nominal system's heave response and coupled dynamics. For the pure heave frequency response, wave periods between two and twenty seconds were considered, with towpoint motion amplitudes ranging from one to four meters. The results are shown in Figures 2-9 and 2-10; the first shows the dependence of towfish heave amplitude on frequencies, while the second indicates the dynamic tension amplitudes at the top and bottom ends of the cable. For this length of cable, there are no pronounced resonance effects, as is clear from the response amplitudes. However, when the excitation amplitude is large, the dynamic tensions at both cable ends can be large also. The two-meter excitation curve, for example, suggests that snap loading at the towfish may occur for frequencies above .8 radians per second, and snap loading at the surface may occur above 1.5 radians per second. The designer would be well-advised to modify the system parameters in this situation.

The harmonic balance method was developed primarily for studying the dynamics of mooring lines, in which significant curvature and geometric coupling may take place due to gravity alone. For a heavy, towed vehicle system, we have seen that the lateral response of the cable in the wave frequency range is confined to a segment near the surface. Thus, when both surge and heave motions are imposed at the surface, it is generally the heave alone which is observed at the towfish. This point is illustrated in in Figure 2-11, where the vertical and horizontal towfish responses are given, for a towpoint motion of two meters surge and heave, with the heave leading the surge by ninety degrees. The current for this run is one meter per second, which leads to a static towfish offset of 229 meters. The dynamic tension curves are indistinguishable from those in Figure 2-10, which, along with
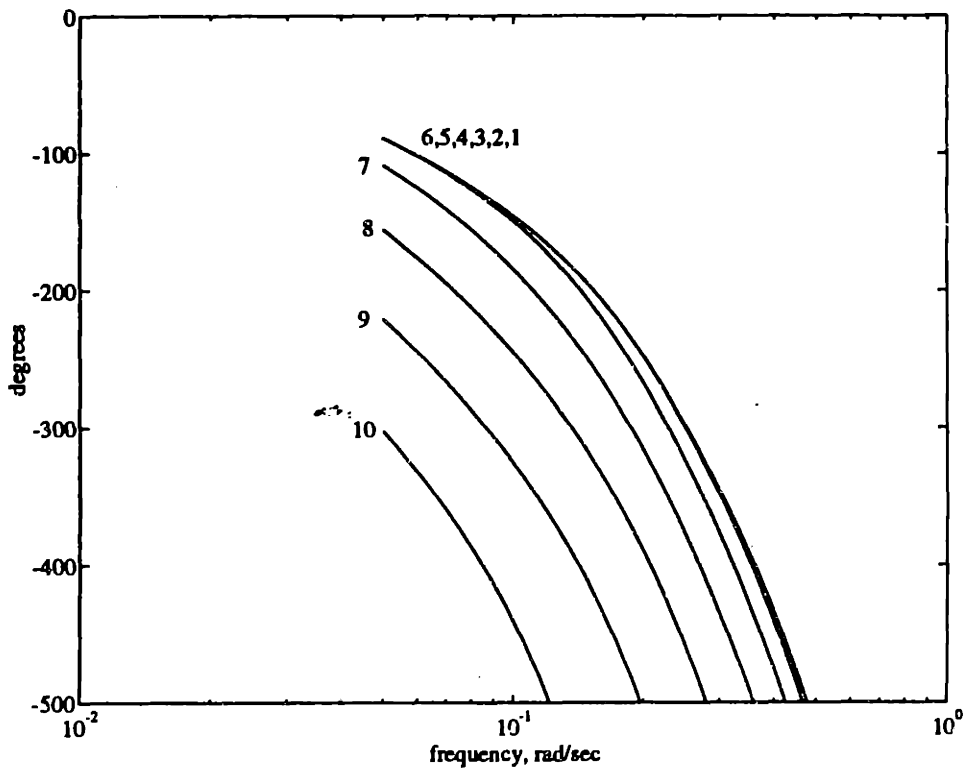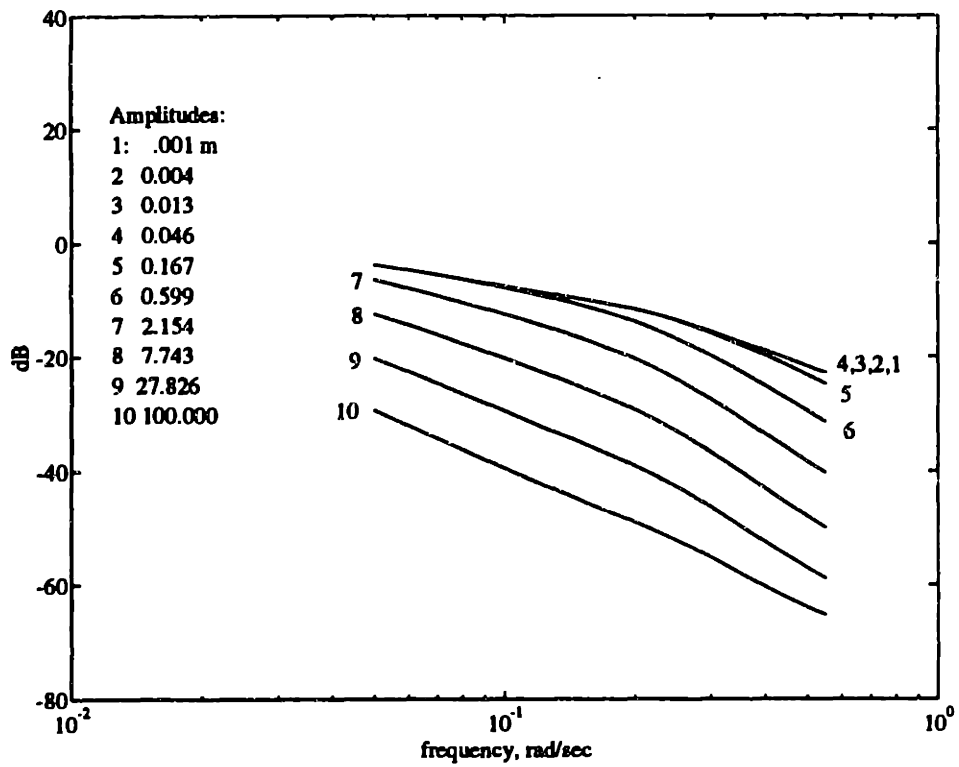
Figure 2-8: Harmonic balance frequency response estimates with a current of .02 meters/second: gain (top) and phase (bottom).
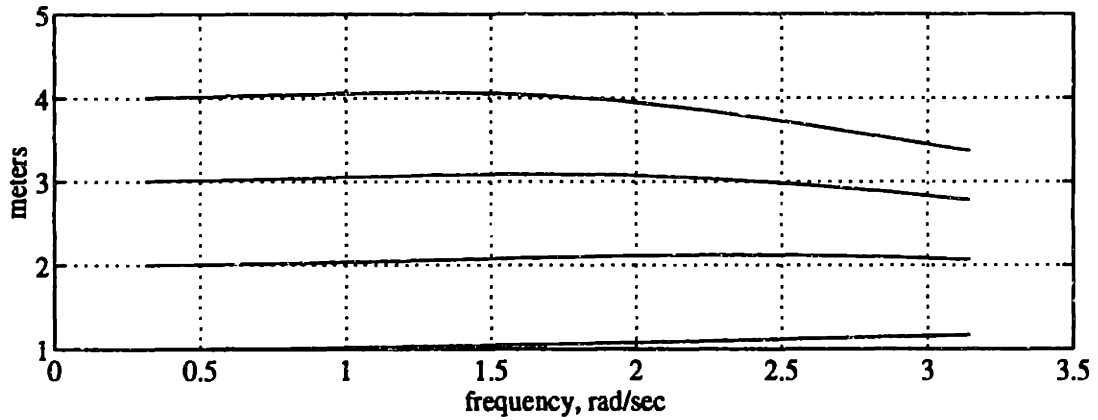
Figure 2-9: Amplitude of towfish heave frequency response.
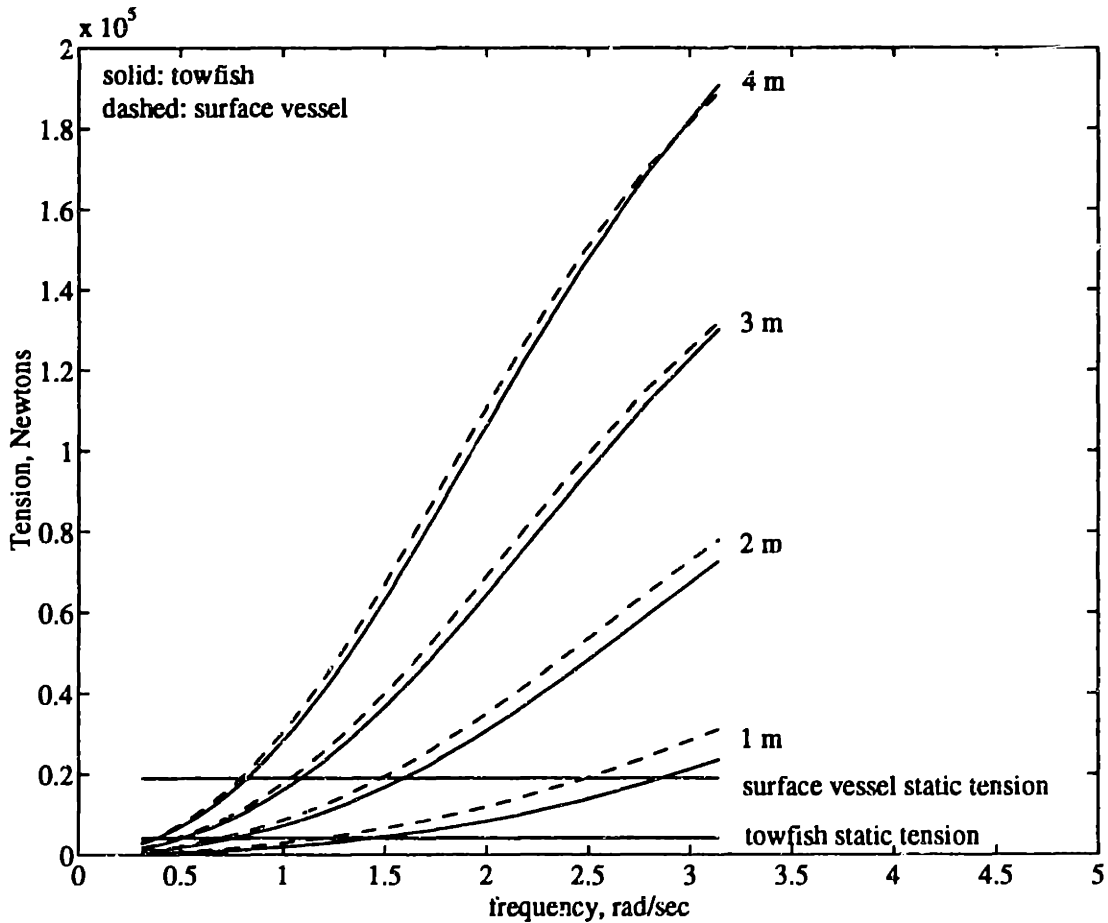
Figure 2-10: Cable tension frequency response during heaving.

42
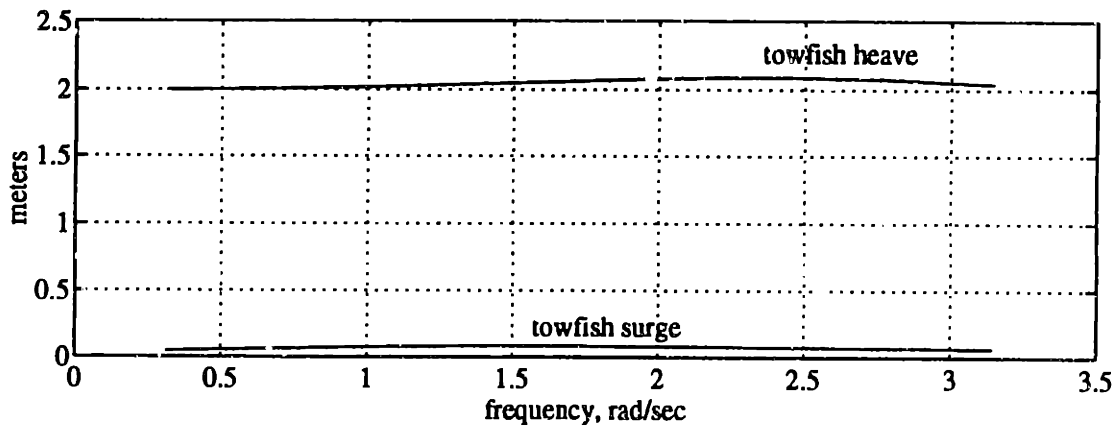
Figure 2-11: Surge and heave towfish response during coupled motions.

Figure 2-11, leads one to conclude that the effects of geometric coupling are small for heavy cable systems towed at low speeds. One must remember, however, that the static tension induced by towing may be significantly larger than that due to weight alone; hence, the total tension can be affected by towing.

2.5 Perturbation Analysis

Our second approximation of the lateral dynamics of a towed cable is a more classical *perturbation* study using the multiple-scale technique, with the first-order in-plane equations (to be detailed). As perturbation methods work best near natural modes, the generality of harmonic balances is lost. Nonetheless, the perturbation approach is worthwhile because it yields simple algebraic relationships that govern the response, and provides a closed-form solution for limit cycling behavior in the closed loop.

2.5.1 First-Order Three-Dimensional Equations for a Vertical Cable

When the cable is known to be nearly vertical, an expansion may be used which is more suitable than that for the equivalent linearization approach above. In particular, we now allow for higher-order terms, to be indexed by the small parameter ϵ which characterizes the excitation amplitude. It is known from physics that the tension T and axial velocity

43

u contain only even-powered terms in ϵ, and that v, w, ϕ, θ all contain only odd-powered terms in ϵ.[1] Thus,

$$T = T_0 + \epsilon^2 T_2 + O(\epsilon^4),$$

$$\phi = \epsilon\phi_1 + \epsilon^3\phi_3 + O(\epsilon^5),$$

$$\theta = \epsilon\theta_1 + \epsilon^3\theta_3 + O(\epsilon^5),$$

$$u = u_0 + \epsilon^2 u_2 + O(\epsilon^4),$$

$$v = \epsilon v_1 + \epsilon^3 v_3 + O(\epsilon^5), \text{ and}$$

$$w = \epsilon w_1 + \epsilon^3 w_3 + O(\epsilon^5).$$

Although we have dropped the arguments, it must be remembered that the tension, angles, and velocities are functions of t and s. In addition, since we will not be discretizing the cable, the subscripts of variables in this section refer to the associated order in the expansion, not the spatial coordinate as before. For our physical scenario, the static solution (denoted by an "0" subscript) is given by:

$$T_0 = W + w_o s, \tag{2.36}$$

$$u_0 = 0,$$

where the coordinate s is assumed zero at the bottom of the cable. We see that the zeroth-order solution is one in which there is no motion, and the tension is created only by the weight of the system.

We now write out the three-dimensional equations in the first-order approximation: they are

$$m\frac{\partial v_1}{\partial t} = -EI\frac{\partial^3\phi_1}{\partial s^3} + \frac{\partial\phi_1}{\partial s}T_0 + \Sigma R_2(\phi_1, \theta_1, v_1, w_1),$$

$$m\frac{\partial w_1}{\partial t} = EI\frac{\partial^3\theta_1}{\partial s^3} - T_0\frac{\partial\theta_1}{\partial s} + \Sigma R_3(\phi_1, \theta_1, v_1, w_1), \tag{2.37}$$

---

[1] If the top of the cable is excited with a lateral in-plane motion $\epsilon \sin(\lambda t)$, for example, T and u respond the same irrespective of the sign of ϵ. On the other hand, the lateral motions clearly depend on ϵ's sign.

$$\frac{\partial v_1}{\partial s} = \frac{\partial \phi_1}{\partial t},$$
$$\frac{\partial w_1}{\partial s} = -\frac{\partial \theta_1}{\partial t}.$$

It is important to note that, except for drag forces, these equations are *uncoupled*; that is, two of the equations describe purely in-plane motions, while the other two describe purely out-of-plane motions. If q and r are in-plane and out-of-plane deflections, respectively, then the relevant equations are:

$$(m + m_a)\frac{\partial^2 q}{\partial t^2} = T\frac{\partial^2 q}{\partial s^2} - EI\frac{\partial^4 q}{\partial s^4} - \frac{1}{2}\rho_w C_d d\frac{\partial q}{\partial t}\sqrt{\left(\frac{\partial q}{\partial t}\right)^2 + \left(\frac{\partial r}{\partial t}\right)^2} + w_o\frac{\partial q}{\partial s}, \quad (2.38)$$

$$(m + m_a)\frac{\partial^2 r}{\partial t^2} = T\frac{\partial^2 r}{\partial s^2} - EI\frac{\partial^4 r}{\partial s^4} - \frac{1}{2}\rho_w C_d d\frac{\partial r}{\partial t}\sqrt{\left(\frac{\partial q}{\partial t}\right)^2 + \left(\frac{\partial r}{\partial t}\right)^2} + w_o\frac{\partial r}{\partial s}.$$

In the presence of ambient current, the normal component should be added to $\frac{dq}{dt}$ above, and the binormal component to $\frac{dr}{dt}$.

We do not consider higher-order expansions of Equations 2.12, as they have been carried out by Howell [56] to investigate the geometric nonlinearities. More importantly, we do not anticipate that the coupling which comes with the higher-order approximations is necessary for our scenario. The motions are assumed to be very slow and overdamped, and the cable system is quite heavy, maintaining its nearly vertical orientation.

2.5.2 First-Order Two-Dimensional Equations for a Vertical Cable

When only the in-plane motions are considered, the zeroth-order solution is the same as in the three-dimensional case, and only two first-order equations need to be considered:

$$(m + m_a)\frac{\partial v_1}{\partial t} = T_0\frac{\partial \phi_1}{\partial s} - EI\frac{\partial^3 \phi_1}{\partial s^3} + \Sigma R_2(\phi_1, 0, v_1, 0), \quad (2.39)$$

$$\frac{\partial \phi_1}{\partial t} = \frac{\partial v_1}{\partial s}.$$

Equation 2.38 can be used for the evolution of the lateral displacement q.

2.5.3 Linear Analytical Solution for In-Plane Motions

There exists an exact analytical solution to the first-order problem in the two-dimensional case when there is no bending stiffness and the damping is linear. This linear solution is well known; however, working it out in this section helps to form a foundation for our later results.

From Equations 2.40 and 2.21, the first-order equations of motion for the cable, the towfish, and the compatibility relation are given respectively by:

$$
\begin{aligned}
(m + m_a)\frac{\partial v_1}{\partial t} &= (w_o s + W)\frac{\partial \phi_1}{\partial s} + w_o \phi_1 - b v_1, \\
(M_P + M_{aP})\frac{\partial \underline{v}_1}{\partial t} &= W\underline{\phi}_1 - B\underline{v}_1, \\
\frac{\partial v_1}{\partial s} &= \frac{\partial \phi_1}{\partial t},
\end{aligned}
\tag{2.40}
$$

where b and B are the linear damping coefficients of the cable and towfish, respectively. Note that an underlined quantity (e.g., $\underline{\nu}_1$) indicates it is to be evaluated at the lower end of the cable. Similarly, a quantity with an overbar (e.g., $\bar{\nu}_1$) indicates that it is to be taken at the top of the cable. We make use of a number of nondimensional variables:

$$
\begin{aligned}
\sigma &:= \frac{s}{L}, \\
\tau &:= t\sqrt{\frac{g}{L}}, \\
\theta &:= \phi\frac{L}{d}, \text{ and} \\
\nu &:= \frac{v}{d}\sqrt{\frac{L}{g}}.
\end{aligned}
$$

Then the Equations 2.40 can be written in nondimensional terms as follows:

$$
\begin{aligned}
\frac{\partial \nu_1}{\partial \tau} &= (k_1 \sigma + k_2)\frac{\partial \theta_1}{\partial \sigma} + k_1 \theta_1 - k_3 \nu_1, \\
\frac{\partial \underline{\nu}_1}{\partial \tau} &= k_4 \underline{\theta}_1 - k_5 \underline{\nu}_1, \text{ and} \\
\frac{\partial \nu_1}{\partial \sigma} &= \frac{\partial \theta_1}{\partial \tau},
\end{aligned}
\tag{2.41}
$$

46

where

$$k_1 := \frac{w}{(m + m_a)g},$$

$$k_2 := \frac{W}{L(m + m_a)g},$$

$$k_3 := \frac{b}{m + m_a}\sqrt{\frac{L}{g}},$$

$$k_4 := \frac{W}{(M_P + M_{aP})g},$$

$$k_5 := \frac{B}{M_P + M_{aP}}\sqrt{\frac{L}{g}}.$$

We define a new spatial variable $\psi := k_1\sigma + k_2$, so that taking the derivative of the cable equation of motion with respect to σ and using the compatibility relation, the following result is obtained:

$$\frac{\partial^2\theta_1}{\partial\tau^2} = \psi k_1^2\frac{\partial^2\theta_1}{\partial\psi^2} + 2k_1^2\frac{\partial\theta_1}{\partial\psi} - k_3\frac{\partial\theta_1}{\partial\tau}. \tag{2.42}$$

We now use separation of variables with

$$\theta_1(\psi, \tau) = R(\psi)N(\tau) = a(e^{i\lambda\tau} + cc)R(\psi), \tag{2.43}$$

where cc indicates the complex conjugate of the preceding term, a is a scalar amplitude, and λ is a nondimensional excitation frequency. With the definition

$$\alpha := -\frac{\lambda^2 - ik_3\lambda}{k_1^2},$$

a form of Bessel's equation is obtained for the first phasor component:

$$\psi^2\frac{d^2R}{d\psi^2} + 2\psi\frac{dR}{d\psi} + \psi\alpha R = 0. \tag{2.44}$$

Since α is complex, it is helpful to make a change of variables before giving the solution. Letting the complex spatial variable z be

$$z := 2\sqrt{\alpha\psi},$$

47

and performing some algebra gives the solution of Equation 2.44 as

$$R(\psi) = \frac{1}{z}(J_1(z) + cY_1(z)), \tag{2.45}$$

where J_k is the kth-order Bessel function of the first kind and Y_k is the kth-order Bessel function of the second kind. The scalar c is to be determined from the lower boundary condition, and the coefficient of $J_1(z)$ has been absorbed into a. This leads to an expression for the velocity in the cable:

$$\nu_1 = -\frac{1}{2\alpha k_1}\frac{dN}{d\tau}(J_o(z) + cY_o(z)). \tag{2.46}$$

The constant c may be found easily from the bottom boundary condition as

$$c = -\frac{k_4 J_1(\underline{z}) + \underline{z}\,\underline{\alpha}J_o(\underline{z})}{k_4 Y_1(\underline{z}) + \underline{z}\,\underline{\alpha}Y_o(\underline{z})}, \text{ where} \tag{2.47}$$

$$\underline{\alpha} := \frac{-\lambda^2 + ik_5\lambda}{2\alpha k_1}.$$

Finally, the amplitude a may be specified from the top boundary condition. We impose

$$\bar{\nu} = i\lambda e^{i\lambda\tau} + cc, \tag{2.48}$$

which leads to the final unknown for this problem:

$$a = \frac{-2\alpha k_1}{J_o(\bar{z}) + cY_o(\bar{z})}. \tag{2.49}$$

The amplitude and phase response of the system may be found from these relations, by taking the magnitude and the argument of a. When the mass and damping characteristics of the clump weight go to zero, one requires that $c = 0$, leading to the classical shape for a freely hanging cable [19]. For the case with nonzero towfish mass and weight, an example Bode plot is given in Figure 2-12. The response is typified by an infinite number of peaks, and the figure shows that, as for finite-dimensional systems, added damping shifts the peaks to lower frequencies with lower gain. The first three natural frequencies for the nominal system are 0.0982, 0.2678, and 0.4725 radians per second.

48
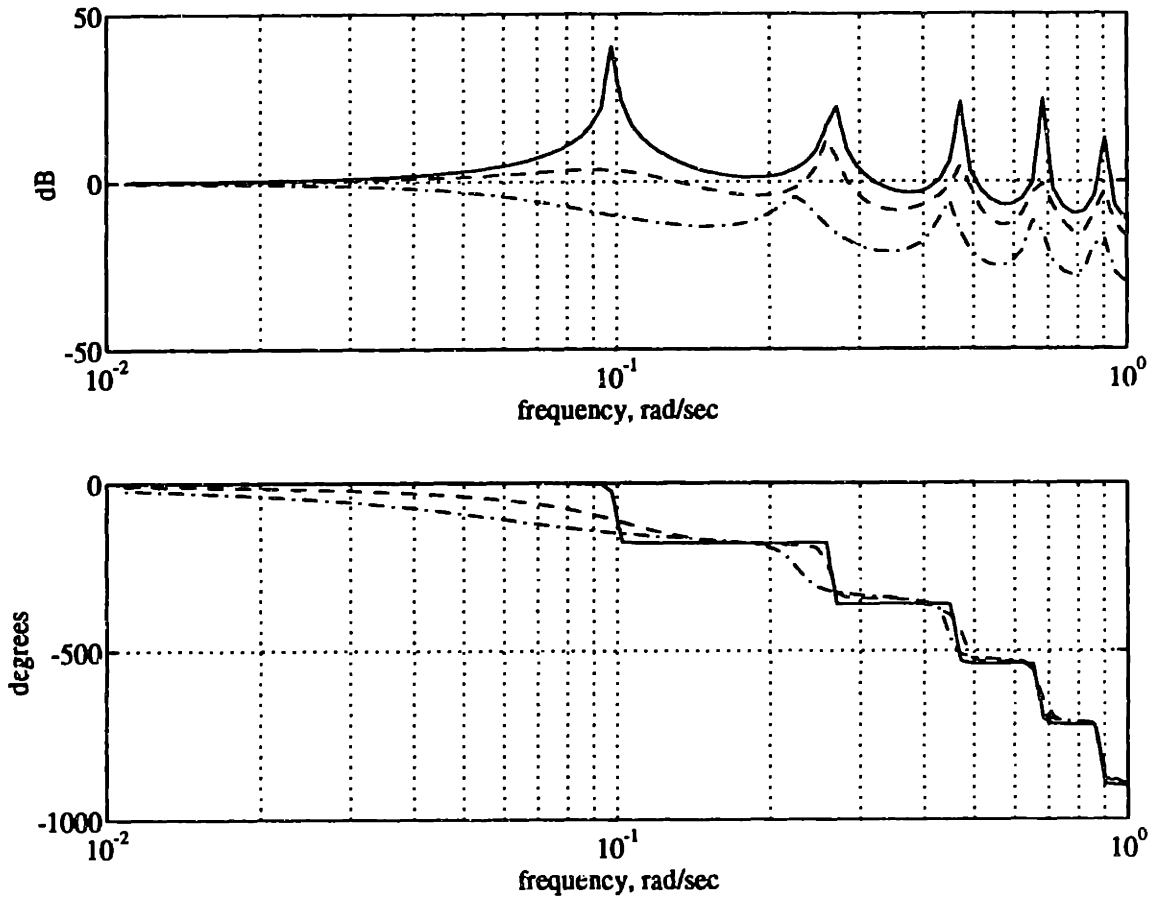
Figure 2-12: Bode plot for hanging cable with three values of linear damping.

The control system designer must be aware that in applications where the plant has minimal damping, the presence of multiple peaks above the primary cutoff frequency may impose restrictive performance conditions. Furthermore, the presence of currents in the fluid has no effect on the response with the linear drag law.

2.5.4 Nonlinear Frequency Response

In this section, we try to uncover more rigorously the mechanism that leads to the amplitude-varying frequency response in Figure 2-3. The goal of the analysis is to characterize the shape of the figure using a few algebraic relations, instead of through simulation or harmonic balance. An important simplification is that we will neglect nonlinear drag on the towfish itself. This condition is reasonable given the very large area of the cable compared to the towfish, and is necessary for the analysis to proceed smoothly.

We begin with the same notation as above. Here, however, the response is assumed to be a perturbation of one of the natural modes. As such, the undamped natural modes first must be identified by setting the motions at the upper boundary equal to zero. The variables k_3 and k_5, which quantify the effects of linear drag, are set to zero, and quadratic drag is incorporated in the cable equation as follows:

$$\frac{\partial \nu}{\partial \tau} = (k_1 \sigma + k_2)\frac{\partial \theta}{\partial \sigma} + k_1 \theta - \epsilon(\nu + u) \mid \nu + u \mid, \qquad (2.50)$$

where $\epsilon = \frac{\rho C_d d^2}{2(m+m_a)}$. It should be noted that this is a new expansion in that ν_1 and θ_1 of Equation 2.42 have been replaced by ν and θ. In other words, we have *adopted what was the first-order equation for the physical cable to describe the complete system for this analysis.* For applications, ϵ generally will be between .1 and .3, so a perturbation solution of Equation 2.50 can be expected to give reasonably good results. Also, the effects of a nondimensionalized ambient current u have been included in the cable equation.

To carry out multiple-scale analysis (e.g., [16]), we let $\underline{\tau}$ be a slow time scale such that $\underline{\tau} = \epsilon^2 \tau$. The expansion is only to be carried to third-order in ϵ, so only one slow time scale is necessary. The variables ν and θ thus become functions of z, τ, and $\underline{\tau}$, and they may be expanded in terms of ϵ as follows:

$$\nu \;=\; \epsilon\nu_1 + \epsilon^3(\nu_3 + \frac{\bar{\nu}}{\epsilon^3}\sigma) + O(\epsilon^5), \tag{2.51}$$

$$\theta \;=\; \epsilon\theta_1 + \epsilon^3(\theta_3 + \frac{\bar{\eta}}{\epsilon^3}) + O(\epsilon^5), \tag{2.52}$$

where η is the nondimensional cable displacement. The top excitation should be $O(\epsilon^3)$; it can be written as:

$$\bar{\eta} = \epsilon^3 h(e^{i\lambda\tau} + cc). \tag{2.53}$$

The scalar h dictates the nondimensional size of this excitation.

The third-order equation comes out as follows:

$$\frac{\partial \nu_3}{\partial \tau} - (k_1\sigma + k_2)\frac{\partial \theta_3}{\partial \sigma} - k_1\theta_3 = -\frac{\partial \nu_1}{\partial \underline{\tau}} + h(\sigma\lambda^2 + k_1)(e^{i\lambda\tau} + cc) - (\nu_1 + u)\mid \nu_1 + u \mid. \tag{2.54}$$

Secular terms indeed appear in the right-hand side, so we can pursue the perturbation solution by setting them equal to zero.

Toward this end, the first two terms on the right-hand side of Equation 2.54 are straight-forward, but the last must be treated with the same care as in the harmonic balance. We use precisely the same results here as given in Section 2.4.3, with the following link. Suppose first that the amplitude a is replaced by a slowly-time-varying equivalent:

$$A(\underline{\tau}) = G(\underline{\tau})e^{i\xi(\underline{\tau})}, \tag{2.55}$$

where $G(\underline{\tau})$ and $\xi(\underline{\tau})$ are real. Then defining

$$\zeta(\underline{\tau}, z) := \frac{\omega_n G(\underline{\tau})}{a k_1} J(z),$$

where $J(z) := J_o(z) + c Y_o(z)$ and ω_n is a natural frequency of the system, leads to

$$\nu_1(\tau, \underline{\tau}, z) = \zeta(\underline{\tau}, z) sin(\omega_n \tau + \xi(\underline{\tau})). \tag{2.56}$$

The complete right-hand side of Equation 2.54, for the three drag cases of Section 2.4.3,

is as follows:

$$\frac{\omega_n}{2\alpha k_1}(ie^{i\omega_n\tau}\frac{dA}{d\underline{\tau}}+cc)J(z)+h(\sigma\lambda^2+k_1)(ie^{i\lambda\tau}+cc)+\left\{\begin{array}{l} \text{Case 1: } \frac{4}{3\pi}\zeta\mid\zeta\mid(ie^{i\omega_n\tau}e^{i\xi(\underline{\tau})}+cc) \\ \text{Case 2: } U\zeta(ie^{i\omega_n\tau}e^{i\xi(\underline{\tau})}+cc) \\ \text{Case 3: } \frac{b_1^3(\underline{\tau},z)}{2}(ie^{i\omega_n\tau}e^{i\xi(\underline{\tau})}+cc) \end{array}\right\}.$$

(2.57)

Recalling that $\sigma = \frac{z^2}{4k_1\alpha} - \frac{k_2}{k_1}$, we make the following definitions so that the Galerkin procedure can be used to eliminate the spatial dependence:

$$\alpha_1 := \int_{\underline{z}}^{z} J^2(z)dz$$

$$\alpha_2 := \int_{\underline{z}}^{z} z^2 J(z)dz$$

$$\alpha_3 := \int_{\underline{z}}^{z} J(z)dz$$

$$\alpha_4 := \int_{\underline{z}}^{z} J^2(z)\mid J(z)\mid dz$$

$$\alpha_5(\underline{\tau}) := \int_{\underline{z}}^{z} b_1^3(\underline{\tau},z)J(z)dz^2$$

$$\gamma_1 := \frac{\omega_n\alpha_1}{2\alpha k_1}$$

$$\gamma_2 := \frac{h\lambda^2\alpha_2}{4\alpha k_1} - \frac{k_2}{k_1}h\lambda^2\alpha_3$$

$$\gamma_3 := k_1 h\alpha_3$$

$$\gamma_4 := \frac{4\omega_n^2\alpha_4}{3\pi\alpha^2 k_1^2}$$

$$\gamma_5 := \frac{U\omega_n\alpha_1}{\alpha k_1}$$

$$\gamma_6(\underline{\tau}) := \frac{\alpha_5(\underline{\tau})}{2}.$$

Making the substitutions into Equation 2.57 and dividing through by $e^{i\omega_n\tau}$, the following requirement is obtained:

$$\gamma_1 i\left(\frac{dG}{d\underline{\tau}} + Gi\frac{d\xi}{d\underline{\tau}}\right) + (\gamma_2 + \gamma_3)(cos(\delta\underline{\tau} - \xi) + isin(\delta\underline{\tau} - \xi)) + \left\{\begin{array}{c} \gamma_4 G \mid G \mid i \\ \gamma_5 Gi \\ \gamma_6 i \end{array}\right\} = 0, \quad (2.58)$$

where $\delta := \frac{\lambda - \varphi_n}{\underline{\tau}^2}$. Following Nayfeh and Mook [74] in expressing the steady-state amplitude as a function of the detuning parameter δ, we look at the three drag cases separately:

1.
$$\mid G \mid \simeq \sqrt{\frac{-\gamma_1^2\delta^2 + \sqrt{\gamma_1^4\delta^4 + 4\gamma_4^2(\gamma_2 + \gamma_3)^2}}{2\gamma_4^2}} \simeq \sqrt{\frac{\gamma_2 + \gamma_3}{\gamma_4}}, \text{ when } \delta \to 0. \quad (2.59)$$

2.
$$\mid G \mid \simeq \frac{\gamma_2 + \gamma_3}{\sqrt{\gamma_1^2\delta^2 + \gamma_5^2}} \simeq \frac{\gamma_2 + \gamma_3}{\gamma_5}, \text{ when } \delta \to 0. \quad (2.60)$$

3. The equation

$$\gamma_6^2 + \gamma_1^2\delta^2 G^2 - (\gamma_2 + \gamma_3)^2 = 0 \quad (2.61)$$

must be solved. Since the amplitude of this case is known to be less than that of Case 1, it suffices to decrement from the Case 1 result until Equation 2.61 is satisfied.

2.5.5 Trends of the Nonlinear Frequency Response

An investigation of the above equations indicates that there are several simple mechanisms at work. First, the analysis always predicts attenuation away from resonant frequencies through Equations 2.59 and 2.60. This trend is coincident with intuition and with simulation results, as shown in Figure 2-7. However, the perturbation technique is only valid near a natural frequency; Figure 2-13 shows how the analysis compares with simulation results, in complete analogue with Figure 2-7. The perturbation solution was computed with respect to the three natural modes in the frequency range, switching at the discontinuities in the figure. One finds that the matching is very good in the *immediate* neighborhood of the natural modes, but is quite poor at any distance from them. Presumably, the fact that the describing functions are always applied to the natural mode shapes, even away from the natural frequencies, is responsible for the poor fit.
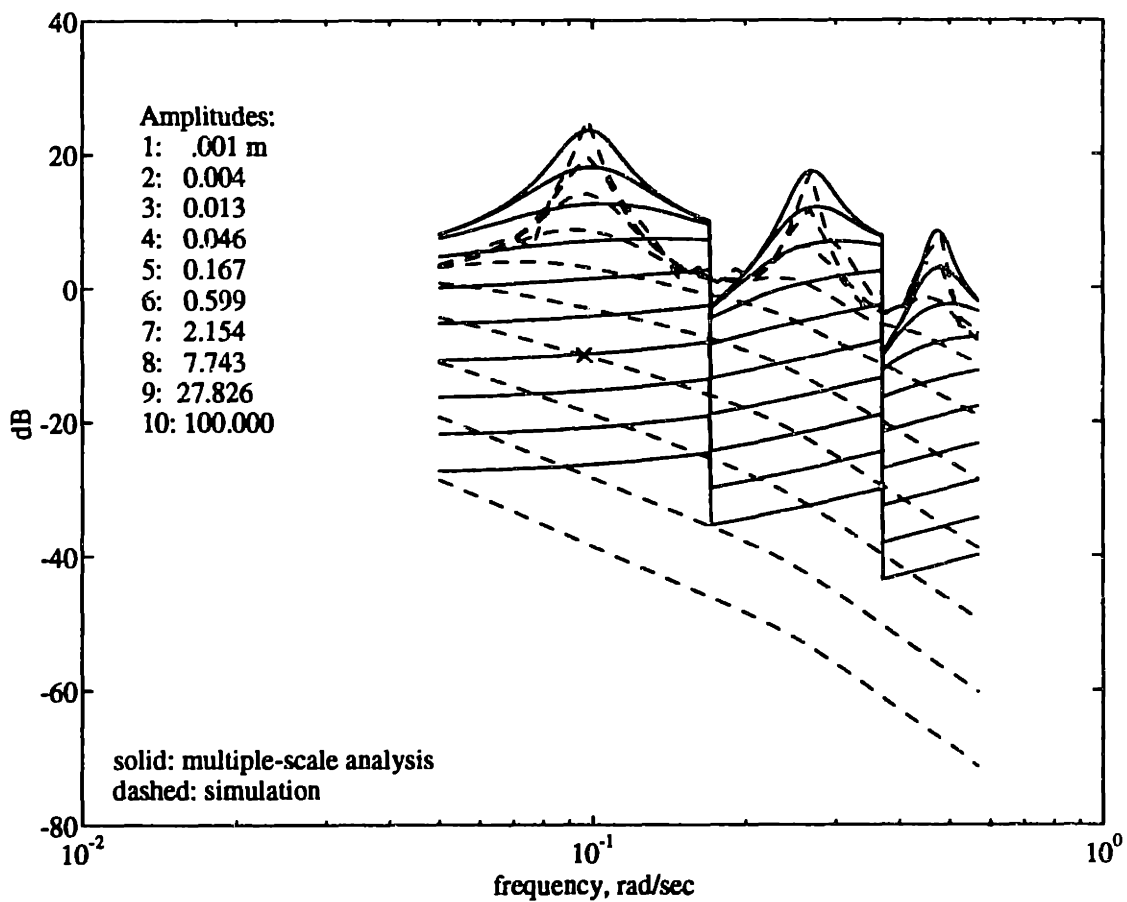
Figure 2-13: Comparison of nonlinear frequency response: simulation vs. perturbation approximation.

An important second characteristic of this perturbation analysis is that $|\,G\,| \propto \sqrt{h}$, so *the gain is inversely related to the square root of the amplitude.* Equation 2.59 indicates this effect, which is roughly consistent with the simulation results of Figure 2-13, especially near the natural modes. Thus, in one equation, we have characterized the mechanism that makes the filtering action of the cable stronger for large velocities.

With respect to current effects, it is clear from Figure 2-6 that the b_1-contours are forced leftward in significant currents. This fact shows explicitly that the frequency response is reduced in the presence of current, consistent with the harmonic balance predictions. In fact, increasing the currents makes the sustainable response ζ approach zero asymptotically, as b_1^2 for a given amplitude of oscillation may be arbitrarily large. It is also interesting to note that the maximum sensitivity of the b_1 contours to changes in current is along the $U = \zeta$ line; the sensitivity is very low for small currents.

Figure 2-14 shows a comparison of the frequency response in current found by simulation, harmonic balance, and the perturbation method. The excitation for which these calculations were made is denoted by the "x" in Figure 2-13 (.093 radians per second, 2.154 meters amplitude). The performance of the harmonic balance technique is good, except that the simulations indicate a "saturation current," beyond which there is *no* measured response. The towfish surge response predicted by harmonic balance smoothly approaches zero as the current is increased. The multiple-scale prediction is accurate when the current is small, but becomes increasingly poor as the current is increased, and again the complete loss of the response above the saturation is not evident.[3] The deterioration of accuracy in large currents is not unexpected, given the large amount of approximation involved and the fact that the cable motions may actually have very little similarity to any natural modes.

2.6 Control Considerations

2.6.1 Model Reduction

The models described so far have used a number of assumptions about the geometry (e.g., first-order equations only) and the physics (form of the drag law, etc.). The transfer function from top motions to bottom motions is, however, still infinite-dimensional, as the usual

---

[3]The steps in the analytical approximation are a result of the incremental procedure used to solve Equation 2.61.
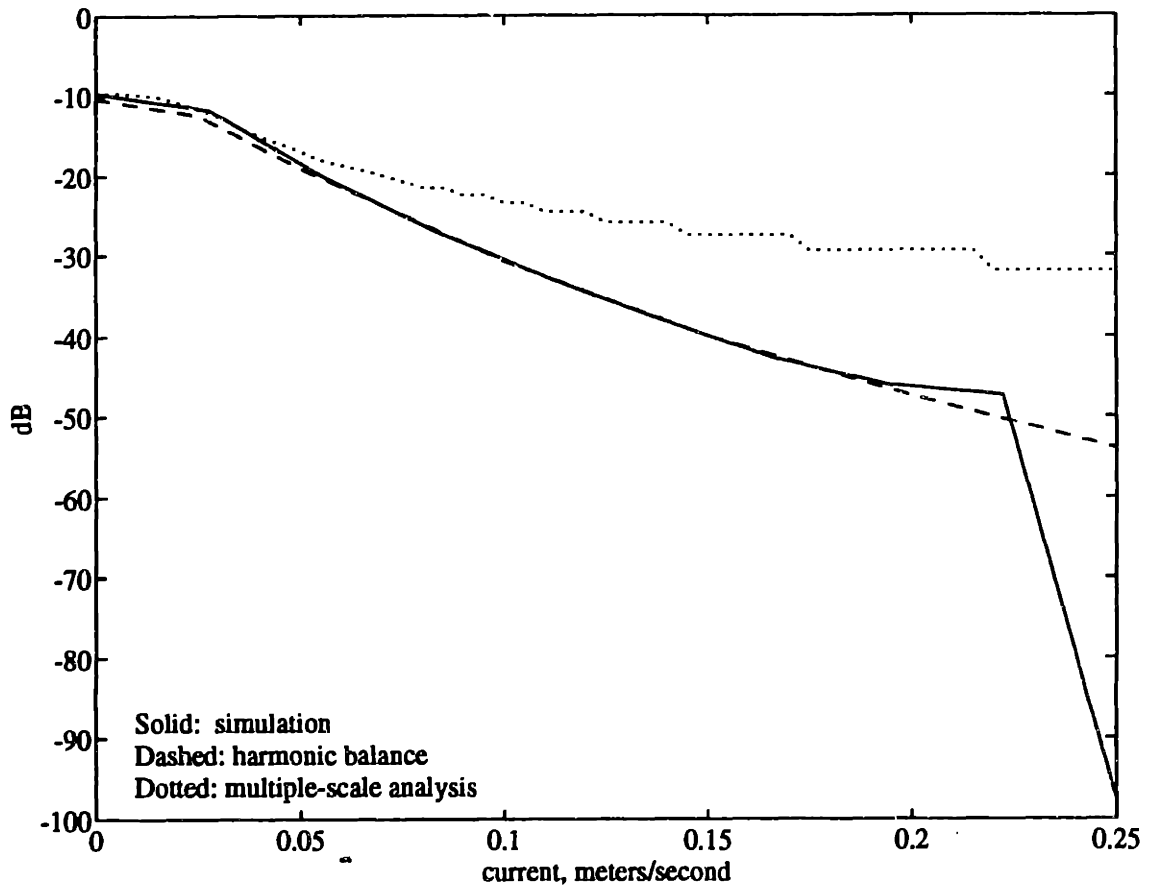
Figure 2-14: Comparison of attenuation of frequency responses in current: simulation, harmonic balance, and multiple-scale analysis.

numerical procedures for modeling this type of system may have fifty or more nodes.

There is available a large body of literature on the feedback control of linear infinite-dimensional systems (e.g., [31], [28]). The main issues are quantification of the effects of finite-dimensional control, and alternatively, the reduction of plant model order while maintaining small modeling errors [69], [85]. These techniques are largely based on frequency-domain properties, and there are by comparison very few tools available for general nonlinear problems.

For this thesis, model reduction is carried out using an ad hoc time-domain technique [55]. Essentially, the reduction process is viewed as a system identification in which the structure of the resulting model is highly constrained; in fact, it is a low-order finite-difference approximation (see Section 2.7). Data from either physical tests, or from high-order models are taken as "truth," and an iterative search in the parameter space is conducted to minimize the simulation errors of the reduced model [18]. As this approach has no guarantees, the best we can do is carry out the identification for a truth I/O data set that has the expected characteristics of the closed-loop maneuvers embedded in it. Modeling error issues are revisited in Chapters 4 and 5.

The usual manifestions of model reduction errors in feedback control are observation and control "spillover" [6]. Control spillover refers to the excitation of high-frequency plant modes by the controller, and observation spillover refers to the contamination of state measurements by these modes. Observation spillover can be reduced greatly by appropriate filtering, so closed-loop stability is not usually a problem when the plant is stable. The performance of such a feedback system may suffer, however, due to control spillover, and the situation is exacerbated when the plant is lightly damped. The next two sections suggest that the cable of interest will not suffer large, high-frequency motions.

2.6.2 Energy Dissipation in Vibratory Modes

For a long cable in water, it can be argued that the effects of high-frequency excitation are negligible, due to the very large drag terms associated with such motions. We consider a cable under constant tension with fixed ends, in a viscous fluid. The trivial eigenvalue problem gives the n-th natural frequency as follows:

$$\omega_n = \frac{n\pi}{L}\sqrt{\frac{T}{m + m_a}}.$$

57

We wish to characterize how energy is dissipated into the fluid, and one useful measure is the ratio of the energy dissipated in a quarter-cycle to the initial kinetic energy associated with the mode. With q as the amplitude of the mode shape, the kinetic energy turns out to be

$$E_K = \frac{q^2 T n^2 \pi^2}{4L}.$$
(2.62)

To get the energy lost to the fluid in one quarter cycle, we must evaluate the integral

$$E_L = \frac{1}{2}\rho C_d d v^3 \int_0^{\frac{\pi}{2\omega_n}} \int_0^L \sin^2(\frac{n\pi s}{L}) \cos^2(\omega_n t) \mid \sin(\frac{n\pi s}{L}) \cos(\omega_n t) \mid ds dt,$$

where $v = \omega_n q$. Because the modes are symmetric in space and because $\cos(\omega_n t) \geq 0, t \in [0, \pi/2]$, we have

$$E_L = \frac{1}{2}\rho C_d d v^3 n \int_0^{\frac{\pi}{2\omega_n}} \int_0^{\frac{L}{n}} \sin^3(\frac{n\pi s}{L}) \cos^3(\omega_n t) ds dt.$$
(2.63)

Separating the integrals and using standard identities, we find

$$E_L = \frac{4\rho C_d d q^3 T n^2 \pi}{9(m + m_a)L}, \text{ or}$$
(2.64)

$$\frac{E_L}{E_K} = \frac{64\rho C_d q}{9\pi^2 d(\rho + \rho_c)}.$$
(2.65)

For a typical deep-water system, this ratio is on the order of $10q$, for steel cables, and $50q$ for synthetic cables (with q expressed in meters). Inspection shows that a larger diameter and cable density leads to a smaller ratio; that is, there will likely be more residual oscillations. For modal amplitudes greater than a few centimeters, however, the initial kinetic energy is generally lost well before the quarter-cycle is completed, suggesting that no overshoot will occur in the real system.

Very small-scale motions that do allow oscillation may correspond to a very low Reynolds number, for which the assumed quadratic law law should be replaced by a linear one. This change can be incorporated for $Re < 1000$ [81]. Calculations show that when oscillatory motions are admitted by the energy argument, the linear damping ratio comes out to be approximately 0.9.

2.6.3 Limit Cycling in the Closed Loop

Another way to quantify the effects of model reduction is to analyze the limit-cycling behavior in closed-loop operation. It often happens in applications that the robustness conditions cannot be met at all points in the state space. For example, the natural damping in a towed cable may tend to zero as the operating speed is reduced, and the standard margins supplied with an LQ regulator might well be exceeded. In such a case, however, the system does not go wildly unstable; what we usually see is the state entering into a limit cycle. Intuitively, the instability mechanism is held in check by the growing drag on the cable as the motions get larger.

The describing function technique [45] has historically been the most common way to estimate analytically the size of a limit cycle. In this procedure, only linearized plants are considered, and one looks for the linearizations which cause the Nyquist plot to cross the critical point (-1). These linearizations then serve as estimates of the states associated with the stability boundary. The method is an approximate one, and offers no guarantees; one need only look at the many counterexamples to Aizermann's conjecture (see, e.g. [92], [102]).

The alternative route we pursue in this section is a perturbation study of the closed-loop system. The approach is inherently the same as the describing function technique in how it linearizes the system, and thus is subject to the same pitfalls. However, by extending our earlier perturbation technique, we can easily consider the full infinite-dimensional plant under linear feedback control and arrive at *simple algebraic equations that govern the closed-loop response*. The describing function technique, on the other hand, requires evaluation of a large number of linearized plants. As before, we expect our approximation to be good for frequencies near the natural modes of the plant, with small ϵ.

We build upon the conventions of Section 2.5.4, listing only the terms that come out differently for the current situation. The control law is of the form:

$$\bar{\eta} = -k\underline{\eta}, \qquad (2.66)$$

implying through Equation 2.52 that the compensator transfer function is $O(\epsilon^2)$.

With k consisting of a real and an imaginary part, we set $\gamma := \frac{|k|}{\epsilon^2}$. Redefining

$$\gamma_2 := \frac{\gamma \omega_n^2}{2\alpha k_1} J(\underline{z}) \left(\frac{\alpha_2}{4\alpha k_1} - \frac{k_2}{k_1} \alpha_3 \right),$$

$$\gamma_3 := \frac{\gamma \alpha_3}{2\alpha} J(\underline{z}),$$

we obtain a result similar to that in Section 2.5.4:

$$\gamma_1 i \left(\frac{dG}{d\underline{\tau}} + Gi \frac{d\xi}{d\underline{\tau}} \right) + (\gamma_2 + \gamma_3)G + \left\{ \begin{array}{l} \gamma_4 G \mid G \mid i \\ \gamma_5 Gi \\ \gamma_6 i \end{array} \right\} = 0. \tag{2.67}$$

Separating the real and imaginary parts, and looking at the steady-state solution only, one finds that the real part of Equation 2.67 does not depend on the drag term. We thus have the frequency perturbation

$$\frac{d\xi(\underline{\tau})}{d\underline{\tau}} = \frac{\gamma_{2r} + \gamma_{3r}}{\gamma_1}, \tag{2.68}$$

for all three cases, where the "r" subscript denotes the real part, and "i" denotes the imaginary part.

To find the amplitudes, the three drag cases are as follows.

1. The imaginary part of Equation 2.67 gives

$$\gamma_1 \frac{dG}{d\underline{\tau}} + (\gamma_{2i} + \gamma_{4i})G + \gamma_3 G \mid G \mid = 0. \tag{2.69}$$

From the definitions, it is easy to see that $\gamma_1 > 0$, and $\gamma_3 > 0$, so that the quadratic drag is stabilizing. The impact of the control transfer function k is in $\gamma_{2i} + \gamma_{4i}$, which can easily be negative for a range of values of k, depending on the mode. If $\gamma_{2i} + \gamma_{4i} \geq 0$, then we predict no limit cycle for the associated mode; if the converse is true, then the steady-state amplitude can be written simply as:

$$\mid G \mid = -\frac{\gamma_{2i} + \gamma_{4i}}{\gamma_3}. \tag{2.70}$$

2. In the presence of a large current which exceeds the local cable velocity at *all* points on the cable, Equation 2.68 is still valid, but the imaginary part of the equation now

60

gives

$$\gamma_1 \frac{dG}{d\underline{\tau}} + (\gamma_{2i} + \gamma_{4i} + \gamma_5)G = 0. \tag{2.71}$$

Thus, depending on the control k, we have either first-order instability or stability. Instability leads to Case 3; alternatively, if Equation 2.71 is stable, the decaying amplitude G stays in the regime of Case 2.

3. When $\nu_1 + u$ has zero crossings, matters are complicated significantly, as indicated in Section 2.4.3. The condition associated with the imaginary part is

$$\gamma_1 \frac{dG}{d\underline{\tau}} + (\gamma_{2i} + \gamma_{4i})G + \gamma_6 = 0, \tag{2.72}$$

which has no simple dependence on G, unlike Cases 1 and 2. Here it is necessary to iterate a few times to get an appropriate value for G in the steady-state.

The frequency deviation is expressed directly in terms of the real part of the compensator, while the amplitude is related to the imaginary part of the compensator. This is clearly a restriction, since a purely real compensator (proportional feedback) leads to limit-cycling behavior. However, the accuracy of the perturbation result is unclear when the compensator is complex, or even purely imaginary.

For the purposes of validation, we consider a compensator which is of the proportional-plus-integral (PI) type. This form was chosen because it is simple, proper, and easily programmed, and because the loop transfer function thus generated is of the general shape that we would like to have (see Figure 2-12). With $k = k_p + \frac{k_I}{i\omega}$, the corner frequency is given the values 0.01, 0.02, 0.05, 0.1 (first mode of the nominal system), 0.2, and 0.5 radians/second. By varying k_p and looking at these six cases, we can investigate the effects of varying control bandwidths and phase angles in the compensator.

Figure 2-15 shows the results of this analysis, with each simulation point drawn as an "x," and the approximation taken about the first mode only. Higher modes were computed, but only the odd modes had nonzero amplitudes, and those were all several orders of magnitude less than that associated with the first mode. For the nominal system, $\epsilon = .205$, and since $|k|$ is assumed to be of order ϵ^2, we would not expect good results much above $k_p = .04$.

The figure indicates that this is not the case, as we obtain good accuracy up to $k_p = .1$ for all six of the cases considered.

The response rolloff predicted by the analysis can be explained as follows: large values of k_p cause the frequency deviation to grow, through Equation 2.68 , and thus, $\frac{1}{i\omega}$ in the control law is reduced. Equation 2.70 then predicts that the amplitude will be affected; in the case of the first mode, it is reduced.

This rolloff is in sharp contrast to the simulation results, in which the amplitude of the limit cycle is quite large at $k_p = 1$. In fact, the system is unstable for $k_p > .9$ when the corner frequency is .2 radians/second, and for $k_p > .4$ when the corner frequency is .5 radians/second. These situations correspond to a "sub-first" mode, in which the cable is being drawn through the water so rapidly that it loses 180 degrees of phase below the first natural mode. This loss of phase is easily seen in Figures 2-3 and 2-7. *The sub-first mode instability is an important motivation for the nonlinear controllers we pursue in Chapter 4.*

Another observation is that the amplitudes reported by both the analysis and simulations are quite small when a reasonable controller design is used. This finding is consistent with our earlier arguments, and suggests that well-chosen feedback laws may be unstable when applied to an undamped cable system, yet can be quite acceptable in practice. Figure 2-15(d), for example, implies that even placing the corner frequency at the first resonant mode, with unity gain at that point, leads to motions of under one-meter amplitude.

A final note is that attenuation of the limit-cycle is predicted when current acts upon the cable. For example, with $U = .01$ meters per second and a corner frequency of .5 radians per second, the analysis predicts *no* limit cycle up to $k_p = .45$, and a reduced limit cycle above that point. However, because this analysis does not take into account the loss of plant phase which accompanies currents, such results are generally inaccurate.

2.7 Lumped-Mass Models

In this section, we describe our standard lumped-mass model for the lateral dynamics of the cable system. This model will be used through the rest of the thesis. Beginning with the drag-coupled first-order Equations 2.38, we discretize the cable into segments of length ds, and adopt the standard $O(ds^2)$ centered finite-difference approximations to the spatial derivatives:
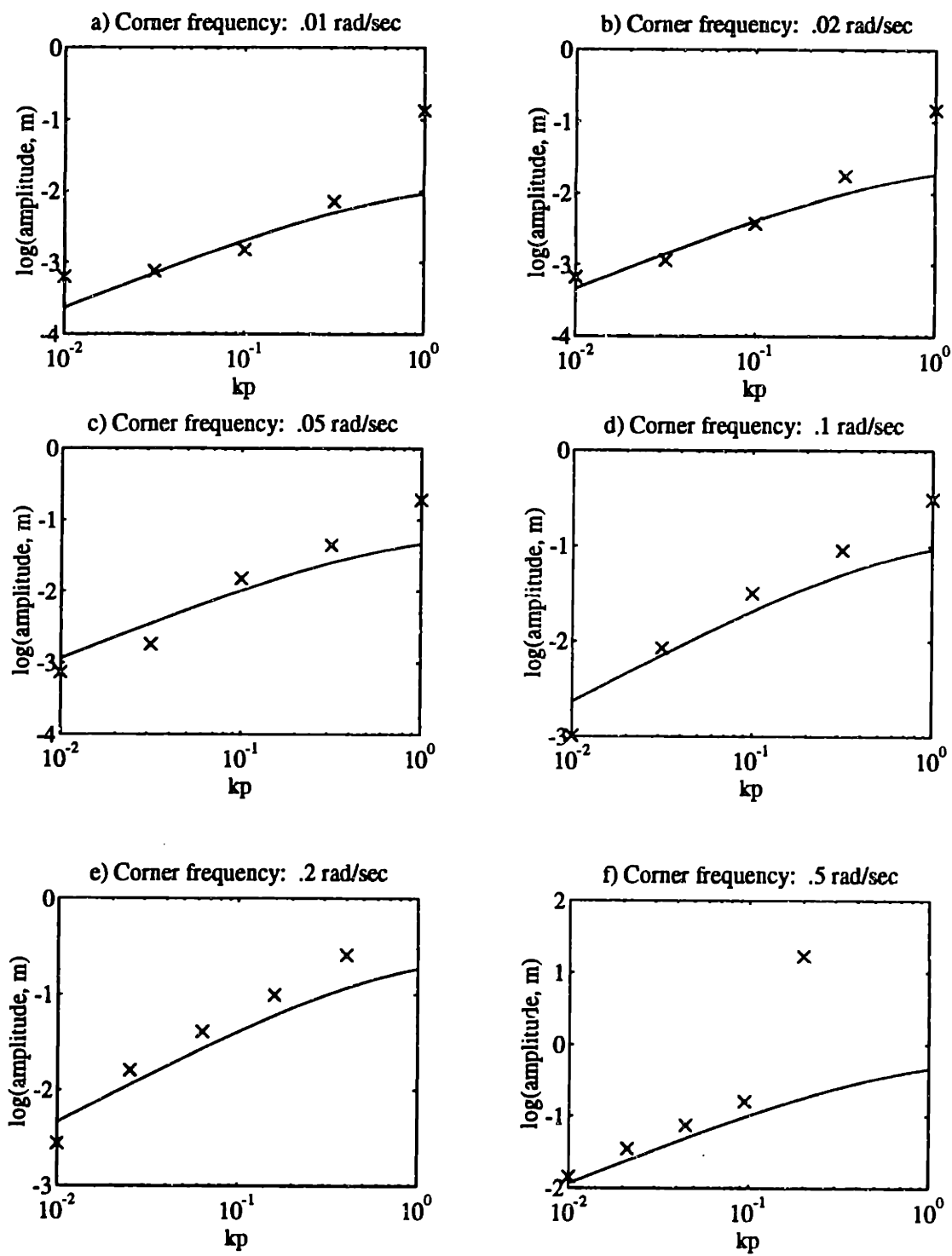
Figure 2-15: Comparison of approximated (solid lines) limit-cycle amplitudes and those obtained by simulation (x), for six corner frequencies.

$$q_{ss,i} \simeq \frac{q_{i+1} - 2q_i + q_{i-1}}{ds^2}$$

$$q_{s,i} \simeq \frac{q_{i+1} - q_{i-1}}{2ds}.$$

Making the substitutions, we have

$$q_{tt,i} \simeq \frac{w_o s_i + W}{(m+m_a)}\left(\frac{q_{i+1}-2q_i+q_{i-1}}{ds^2}\right) + \frac{w_o}{m+m_a}\left(\frac{q_{i+1}-q_{i-1}}{2ds}\right) - \frac{\rho C_d d}{2(m+m_a)}q_{t,i}\sqrt{q_{t,i}^2 + r_{t,i}^2} \quad (2.73)$$

$$r_{tt,i} \simeq \frac{w_o s_i + W}{(m+m_a)}\left(\frac{r_{i+1}-2r_i+r_{i-1}}{ds^2}\right) + \frac{w_o}{m+m_a}\left(\frac{r_{i+1}-r_{i-1}}{2ds}\right) - \frac{\rho C_d d}{2(m+m_a)}r_{t,i}\sqrt{q_{t,i}^2 + r_{t,i}^2}.$$

The top boundary condition of the cable is an imposed displacement of the endpoint. The first node in the discretization should thus be placed a length ds down from the surface, so that Equation 2.73 is valid there. At the lower boundary is a clump weight whose dynamic response is given by

$$(M + M_a P)q_{tt} = Wq_s - \tfrac{1}{2}\rho C_{d,towfish}A_P q_t\sqrt{q_t^2 + r_t^2} \quad (2.74)$$

$$(M + M_a R)r_{tt} = Wr_s - \tfrac{1}{2}\rho C_{d,towfish}A_R r_t\sqrt{q_t^2 + r_t^2}.,$$

In a model with n nodes, by definition we impose the vehicle dynamics on the first node, with the $O(ds)$ forward-differences approximation $q_s = q_{s,1} \simeq (q_2 - q_1)/ds$.

This formulation does not quite lead to a simple mass-spring system; it can be easily shown that a carelessly constructed mass-spring approximation has a fundamentally different response, even as the number of nodes goes to infinity. In addition, it is noteworthy that linearizations of this model do not have a pure delay, nor any zeros. The lack of zeroes is consistent with Figure 2-12, and for most systems, the time constant is several orders of magnitude larger than the pure delay.

The number of nodes needed for a good approximation appears to be very small [55]. In particular, models with *two* nodes might be adequate, although inputs with high bandwidth clearly necessitate a few more.

2.8 Summary

This chapter began with the complete equations of motion for a cable in water, and detailed a number of valid simplifications. These pertain to the neglect of torsional, rotational inertia, and elongation effects, and to the specific forms of the added mass and quadratic drag terms. In addition, geometric coupling was largely eliminated. Finally, since a very low order finite-difference approximation is advocated, the continuous nature of the cable is lost as well. The result is a simple model structure suitable for control system design and analysis.

The lateral frequency response of a deeply-towed cable system is strongly dependent on the amplitude of excitation, as shown by both the harmonic balance and perturbation studies of this chapter. The general rule of thumb coming out of the analysis is that the gain of the plant is inversely related to the square root of the excitation frequency. In addition, the analyses reveal a deterioration of resonant peaks with growing excitation amplitude, and an arbitrarily large loss of phase, even well below the first natural mode. These results are suggestive of the need for nonlinear control strategies.

It was then shown, however, that control spillover effects are likely to be damped out very quickly in practice, due to the large drag terms. Also, closed-loop limit-cycling brought about by application of a linear feedback law was predicted to be of quite small amplitude, even for a poorly-designed compensator. These results bode well for linear control, in a very limited sense.

Chapter 3

Open-Loop Maneuvers

3.1 Introduction

Studying maneuvers in which the vessel motions are "preshaped" is important as a first step in positioning the towed underwater system more accurately. Preshaping is an open-loop idea and quite distinct from feedback control, which is discussed in Chapter 4. Preshaping accomplishes our first objective, which is to speed up the dynamic response of the towed system, by anticipating in a constructive way how the plant will respond to excitation. Because it is an open-loop procedure, it has no instabilities, and is therefore "safe" from the point of view of the helm.

We discuss two aspects of preshaping vessel trajectories in this chapter. The first involves the so-called point-to-point maneuver: the object is to move the lower end of the cable or riser, at rest, to a new location and achieve the rest configuration again in minimum time. The second approach involves specified trajectories for the towfish, and more mathematics to invert the cable dynamics. In this chapter, we outline the techniques, and present verifying experimental data from a full-scale test.

3.2 Point-to-Point Moves

The point-to-point move is a common one for many operations, and has been considered numerically by Paul and Soler [80]. Neglecting the presence of currents for the moment, we assume that the system begins at rest; that is, the tether is hanging vertically due to the weight of the system. The goal is to move the towfish horizontally to a new location and to
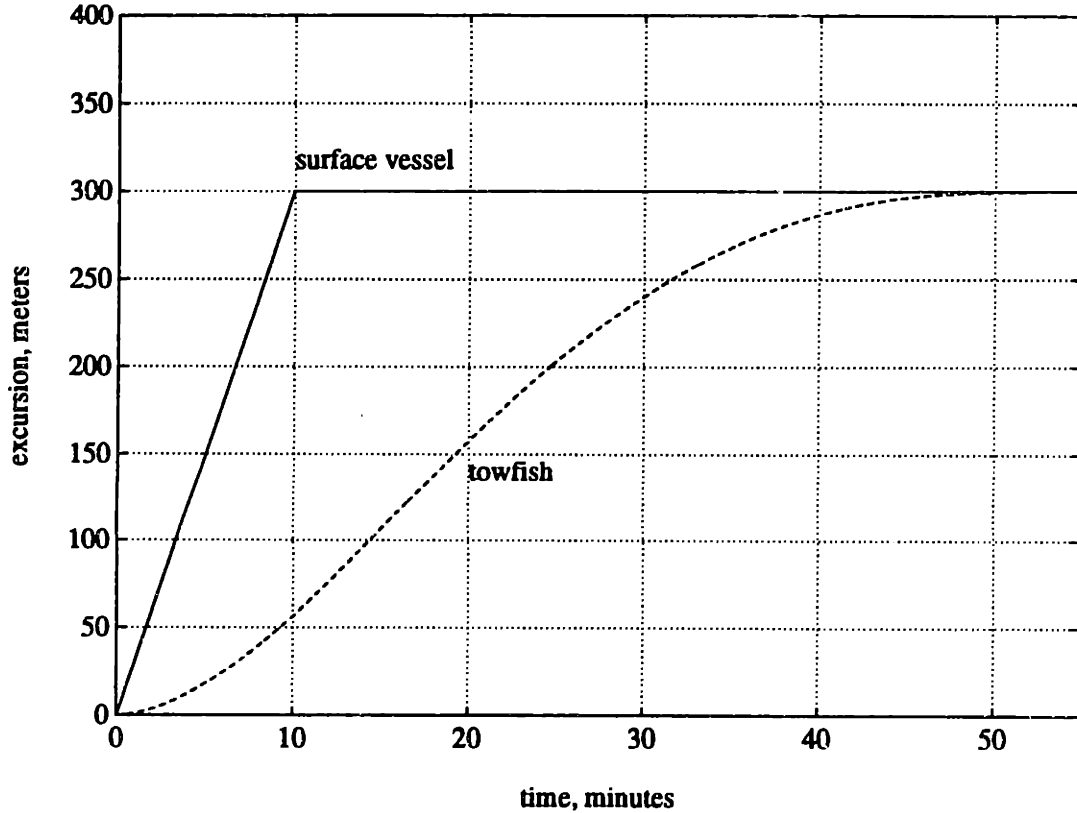
Figure 3-1: Slow towfish response to a point-to-point vessel maneuver.

bring it to rest, by moving the surface vessel appropriately. As was seen in Chapter 2, the cable usually acts like a low-pass nonlinear filter in transmitting ship motions to towfish motions. This property is illustrated in another way in Figure 3-1, which shows a simulated response for the case where the vessel is moved directly to a new location. The towfish settling time to 10 meters for this example (2000 meters of 6.4-millimeter steel wire, 740 Newtons static tension at the bottom) is approximately 40 minutes.

It is intuitively clear that to reduce the settling time of the fish, we should alter the vessel trajectory to incorporate the cable response more vigorously. There are many ways of posing this problem mathematically; we consider the task of minimizing the time integral of towfish position error. More formally, let the function g map the vessel trajectory $x_v(t)$ to the towfish trajectory $x_t(t)$. Then we want to satisfy

$$x_v(t) = arg \ min \int_{t_0}^{t_f} | \ x_{t,desired}(t) - g(x_v(t)) \ | \ dt, \qquad (3.1)$$

subject to various constraints on the vessel motions. Note that $x_{t,desired}$ is a step function for the point-to-point maneuver.

3.2.1 Approximate Solution

Given that g in Equation 3.1 is a nonlinear operator with memory, there appears to be no general closed-form solution to the optimization problem stated above. However, it can be argued that the best vessel trajectory moves the whole cable first, and the towfish indirectly. Thus, we consider an initial vessel overshoot to "stretch out" the cable over the desired location, and then a return to that location. During this return, the vehicle falls into place over the target. This is the basic approach taken by Paul and Soler, who minimized the settling time to a given radius. Since the overshoots of this thesis and of their paper have the same shape, it is clear that the two minimization problems are very similar; the settling time minimization of of Paul and Soler's paper requires an extra parameter, namely the settling radius.

Our general overshoot maneuver may be parameterized by four variables, shown in Figure 3-2:

1. a_{max}: the absolute value of the maximum acceleration of the vessel

2. v_f: the absolute value of the maximum forward speed of the vessel

3. v_r: the absolute value of the maximum reverse speed of the vessel

4. $t_{reverse}$: the time elapsed at which the vessel changes from forward to reverse movement

The acceleration and speeds are generally governed by operational considerations; e.g., how hard to work the DP system, or what cable angles are acceptable. For many operations, the maximum speeds are only several knots. The distinction between maximum forward and reverse speeds is made because the cable may be drawn close to the vessel hull when backing down. Thus, we have effectively reduced the number of unknowns in the trajectory $x_v(t)$ to one: the reversal time $t_{reverse}$. The problem is reduced to a single parameter optimization of the cost integral of Equation 3.1.

Paul and Soler showed that the settling time for the towfish is a convex function of the overshoot distance; this implies that lengthy search algorithms are not necessary to

a_{max}

X

v_f v_r

a_{max}

a_{max}
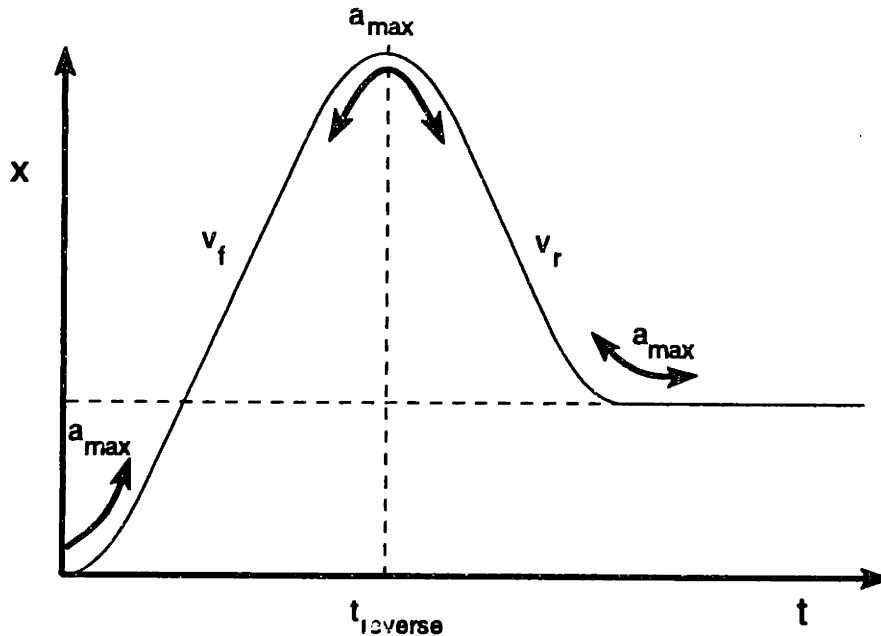
$t_{reverse}$ t

Figure 3-2: Assumed optimal vessel trajectory.

find $t_{reverse}$. Instead, we may simply start from the zero overshoot trajectory, and increase $t_{reverse}$ until the computed cost integral has reached its minimum. The compactness of our finite-difference model plays a crucial role in making this procedure computationally feasible.

3.2.2 Full-Scale Experimental Setup

The full-scale data to be presented were obtained during a cruise at the Juan de Fuca Ridge in July 1991, aboard R/V Laney Chouest. This ridge is in the Pacific Ocean, approximately 300 kilometers west of Washington state, and has been the site of numerous recent geological studies. The deployment was designed as a fairly close approximation of the ARGO/JASON system, and in fact was set up just prior to ARGO/JASON operations; it is schematized in Figure 3-3 and Table 3.1. The vessel was navigated with a dynamic positioning system, using fixes from the Global Positioning Satellite system and a long-baseline acoustic net. The acoustic frequencies were between five and fifteen kilohertz, and the net had an average side length of approximately five kilometers. An acoustic transceiver was placed at the end of 2000 meters of hydrographic wire, along with a steel clump weight, and the motions of this clump weight were tracked with the same long-baseline net. The vessel was headed into
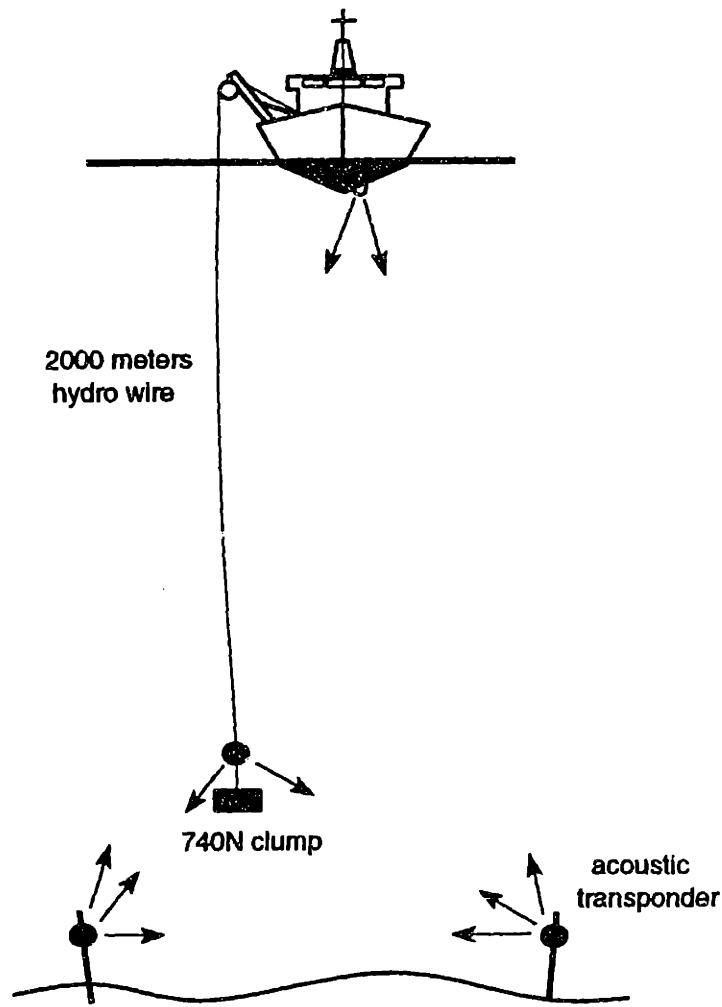
Figure 3-3: Schematic view of full-scale deployment.

the sea during each of the runs, and the weight was deployed over the side amidships. There were no significant currents in any of the experiments conducted, based on the observed offsets.

The required vessel trajectories were executed with the existing dynamic positioning system. Since this system did not have the capability to follow complex trajectories, we operated in regulation mode and had the setpoint follow the trajectories specified by our algorithms. Our model of the experimental plant was initially estimated from its physical parameters (mass, weight, cable diameter, etc.; see Section 2.7), before the cruise. This model was then updated at sea using preliminary test data, and the experiments which follow were based on the new model, which had four nodes. Finally, the data which follow

Actuator	R/V Laney Chouest (2400 tons)
Maximum towing speed	1 m/s
Vessel tracking	GPS, acoustic ($\sigma \simeq 5$ m)
Vessel DP bandwidth	.02 rad/s
Cable material	6.4 mm hydrographic wire
Cable effective mass	.181 kg/m
Cable weight/length in water	1.14 N/m
Cable C_d	1.4
Depth	2000 m
Towfish	steel plates (740 N)
Towfish effective mass	100 kg
Towfish frontal area	340 cm^2
Towfish C_d	2
Towfish tracking	acoustic ($\sigma \simeq 5$ m)
Pure delay	$\simeq 20$ s

Table 3.1: Physical parameters for full-scale experiments.

have not been post-processed in any way, except for the manual removal of several "fliers."

3.2.3   Overshoot: Full-Scale Experimental Results

As described above, the goal of the experiment was to show that point-to-point relocation of the towfish can be made more efficient by using the calculated overshoot idea. Our simulations, and those of Paul and Soler [80], show that reductions in the towfish settling time (to a specified radius) can approach twenty-five percent or more, depending on the physical system and the parameters of the move. We give two experimental illustrations of this reduction in settling time.

Figure 3-4 shows an overlay of results from two tests; one test consisted of a flat vessel move at 0.25 meters/second, and the other had an overshoot of approximately 150 meters, at 0.25 meters/second. The relocation distance was 300 meters for both runs. The settling time to 10 meters for the flat case is approximately 45 minutes, while for the overshoot, it is approximately 40 minutes (this takes into account the fact that our vessel trajectory settled at 310 meters).

The second case involved a much more vigorous overshoot for the vessel; see Figure 3-5. The relocation here was 100 meters, with maximum velocities of 0.5 meters/second. For this
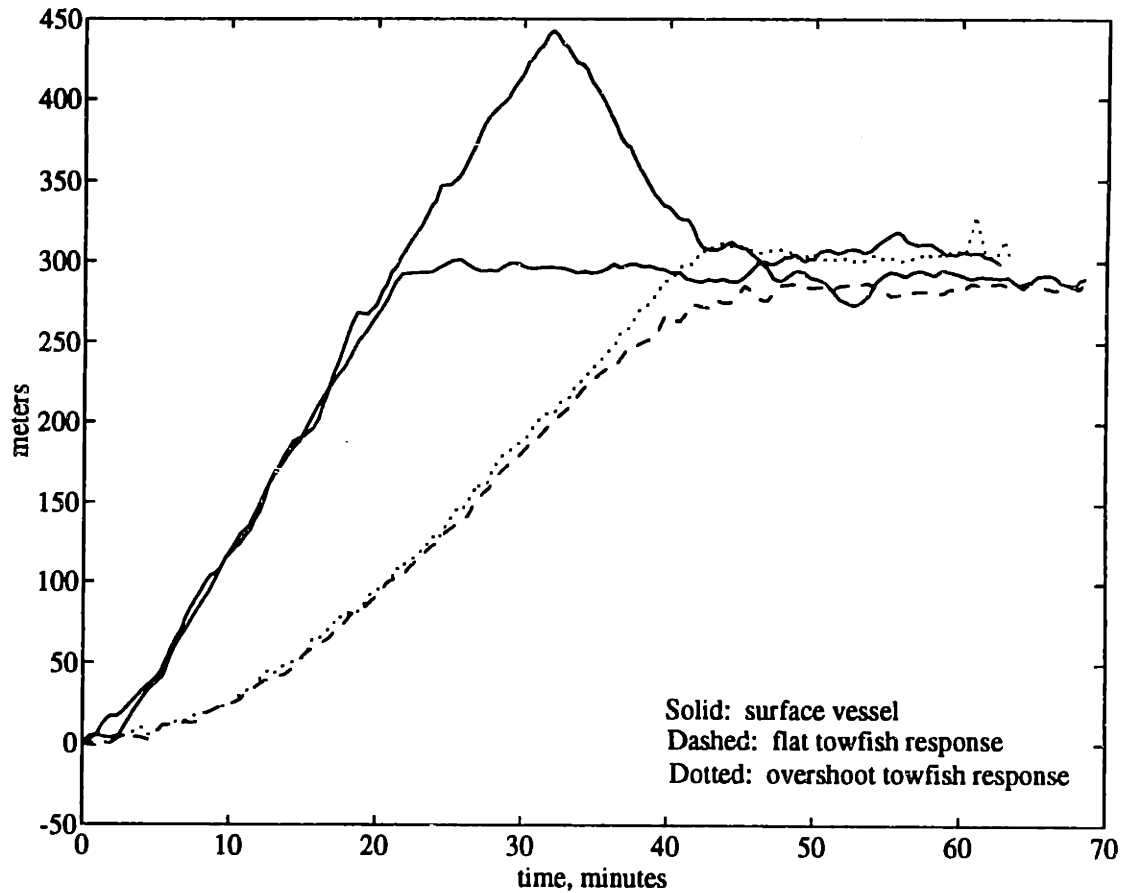
Figure 3-4: Comparison between overshoot and flat responses for first full-scale move.

run, we let the vessel stay relatively stationary for part of the "stretch" period, instead of making a single sharp reversal at $t_{reverse}$. The flat run has a 10-meter settling time of about 22 minutes, although there are apparent transients at the start and at the end of the data set. The overshoot leads to a different response, characterized by faster towfish motion as before, and a much sharper stop. Note that through modeling and vessel trajectory errors, the towfish itself has an overshoot of approximately 10 meters. The 10-meter settling time for the overshoot is approximately 17 minutes; the difference between the flat and overshoot responses is more significant for this run.

Another way to see the effects of the overshoot is to look at a side view of the towfish motion; Figure 3-6 gives such a view for the runs of Figure 3-5). We see that the towfish trajectories for the flat and overshoot cases are nearly identical early in the move, with high frequency vertical oscillations caused by heaving of the surface vessel. Later, while the flat

72
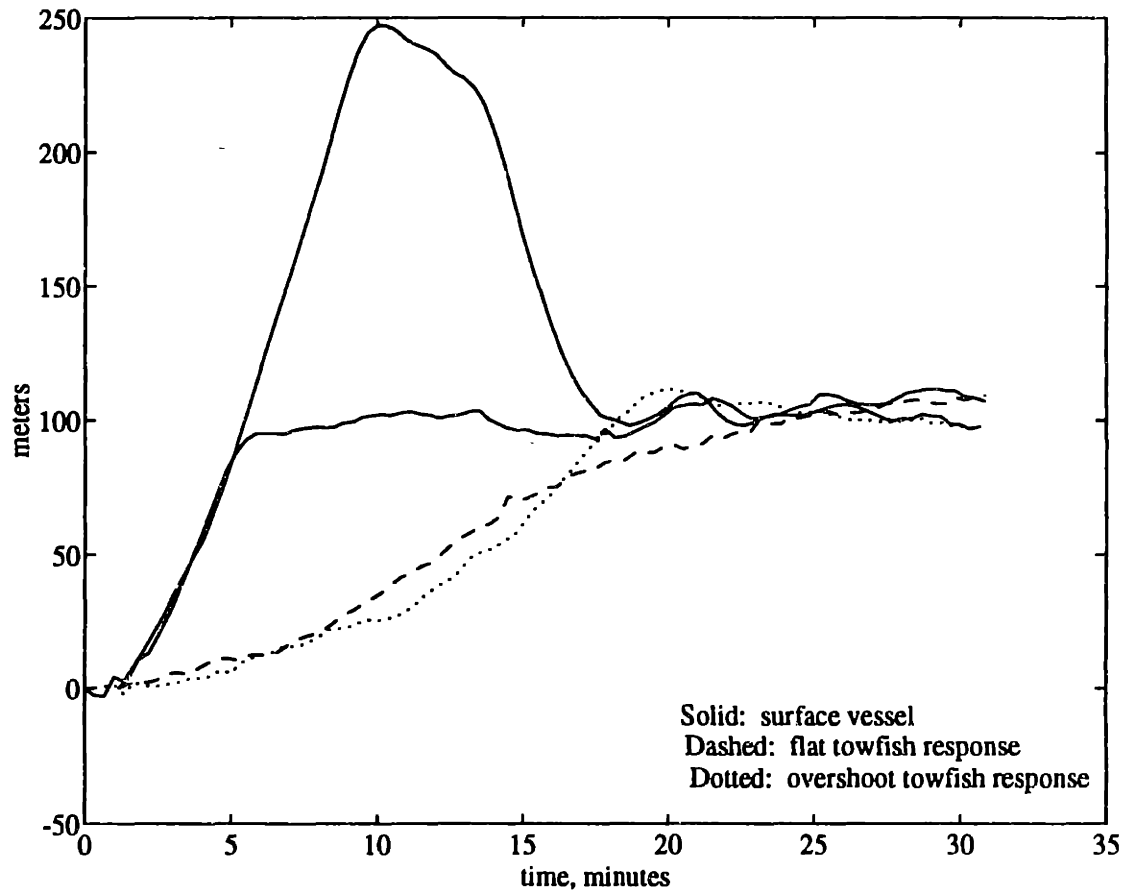
Figure 3-5: Comparison between overshoot and flat responses for second full-scale move.
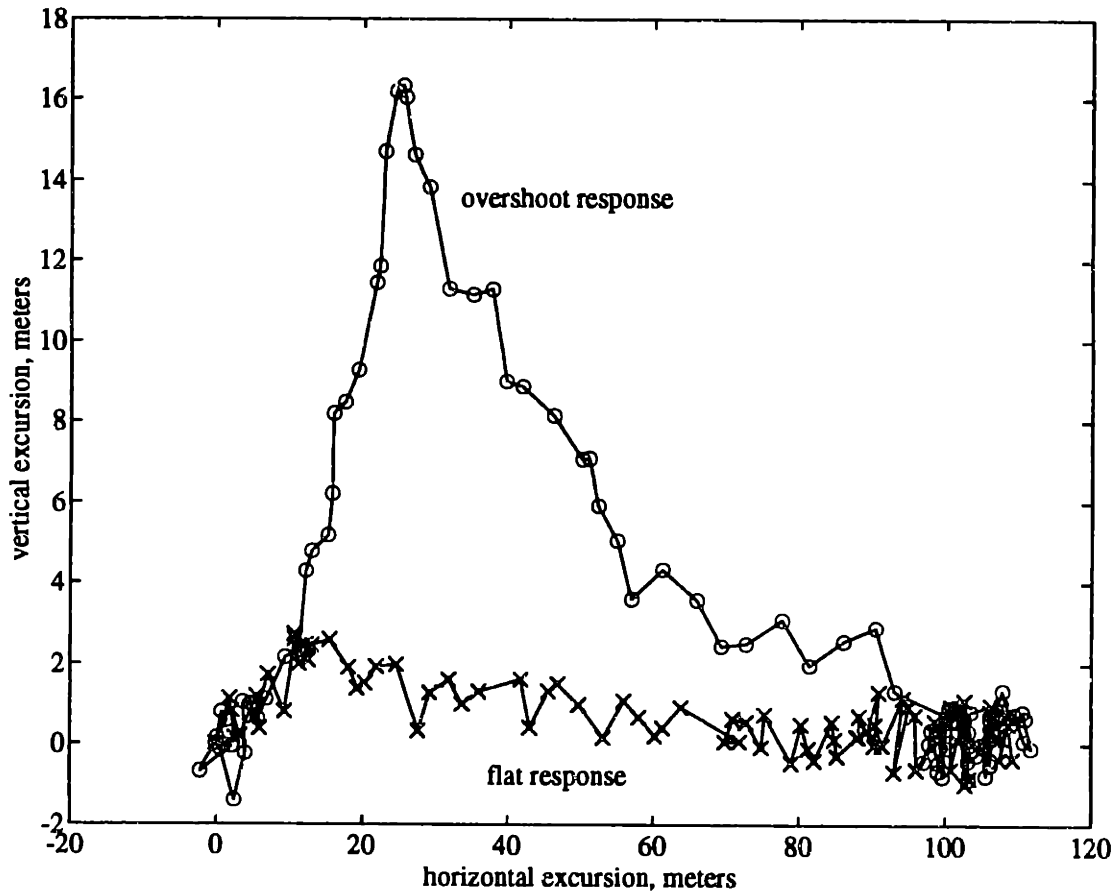
Figure 3-6: Side views of overshoot and flat towfish trajectory.

run requires some time for the towfish to drift slowly down into the new rest position, the overshoot leads to a towfish trajectory which is better described as dropping. This behavior is consistent with the notion that the overshoot move is trying to *stretch the cable out over the desired rest position, and then let it drop into place.*

As a more practical use for the overshoot concept, we now consider the construction of patterns (in the horizontal plane) using cascaded overshoot maneuvers in different directions. The primary motivation for this extension is grid searches in which the towfish, often gathering acoustic data, must move in straight lines in a grid. The traditional procedure involves a lengthy turnaround maneuver at the end of each trackline, which allows the cable to become aligned in one vertical plane before starting the next trackline. With our overshoot procedure, sharp corners in the towfish trajectory can be achieved, eliminating the necessity of the standard turnaround maneuvers. See Figure 3-7.
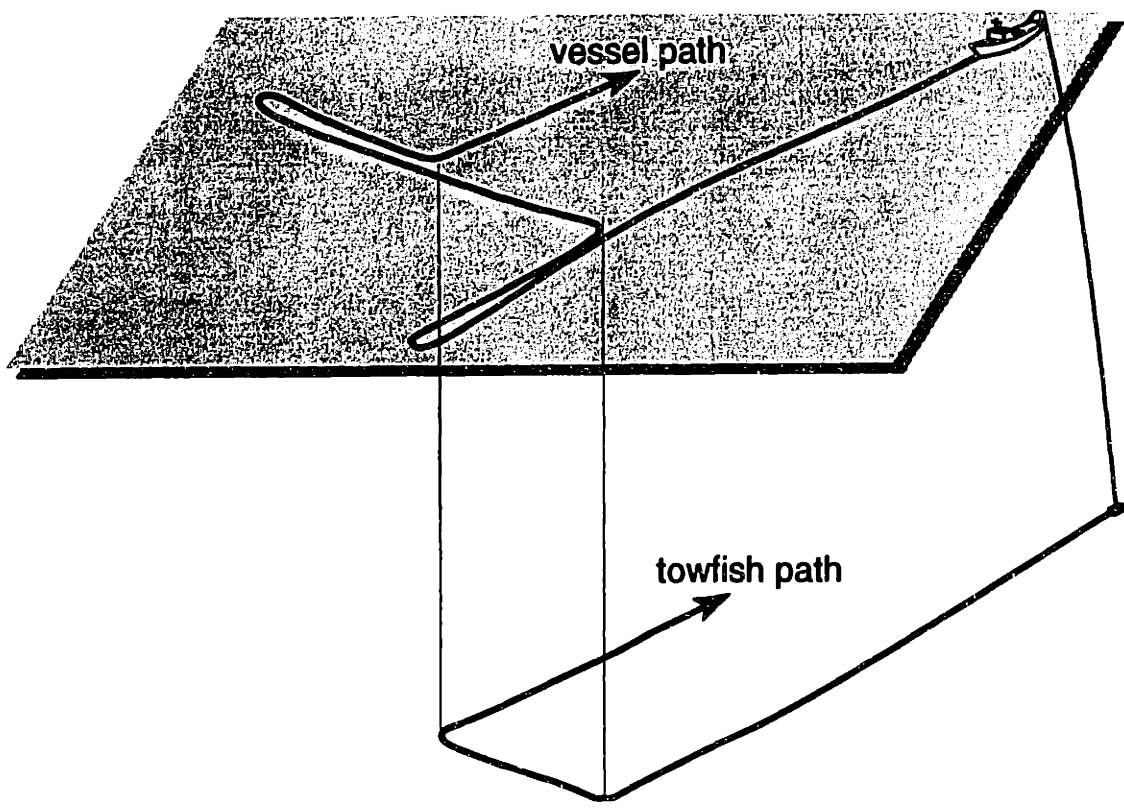
Figure 3-7: Cascaded overshoots for precision grid-following.
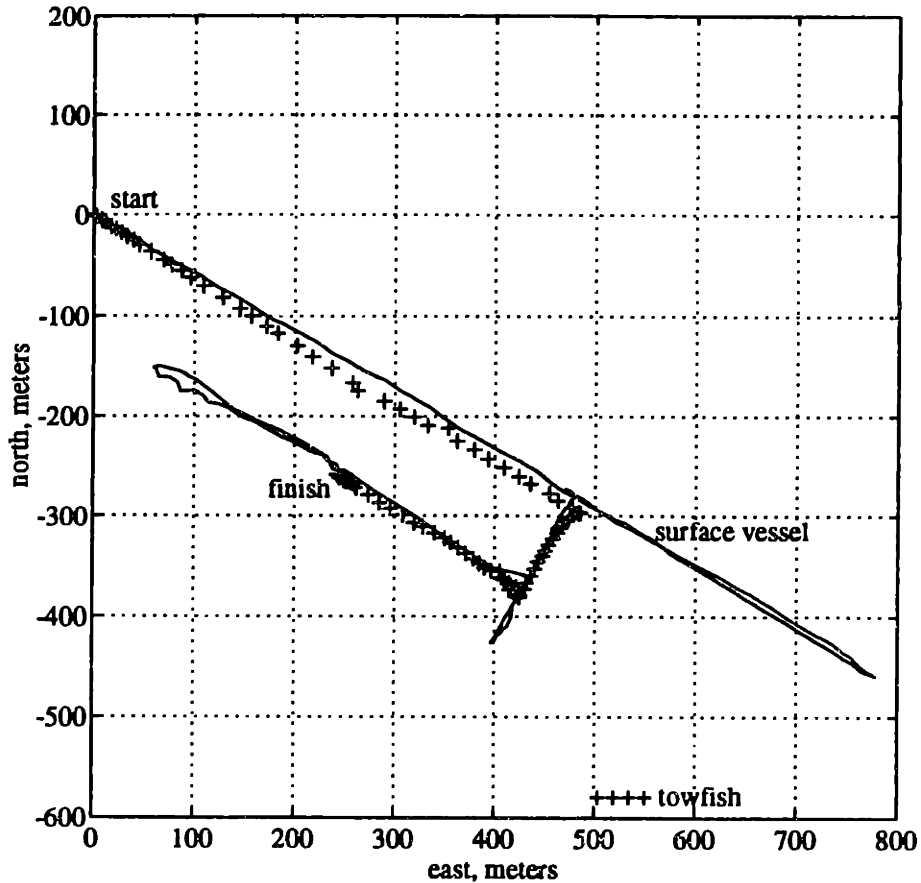
Figure 3-8: Bird's-eye view of sharp corners executed by the towfish.

Three overshoot maneuvers were pieced together in immediate succession to obtain the full-scale results of Figure 3-8, which gives a bird's-eye view of the vessel and resulting towfish trajectories. The first leg moved the towfish 550 meters (at 0.5 meters/second) to the southeast, the second leg moved it 100 meters (at 0.25 meters/second) to the southwest, and the third leg moved it 200 meters (at 0.5 meters/second) to the northwest. These projections are given in Figure 3-9. All three of the overshoots were effective, especially the two northwest-southeast moves.

3.2.4 Discussion

In the first two in-plane runs, the approximate reductions in settling time to ten meters are approximately 11% and 23% of the flat maneuver settling time; these numbers are consistent with those predicted by simulations. The overshoot maneuver appears to be most useful in

Projection on 300-degree azimuth

Solid: surface vessel
Dashed: towfish

Projection on 30-degree azimuth
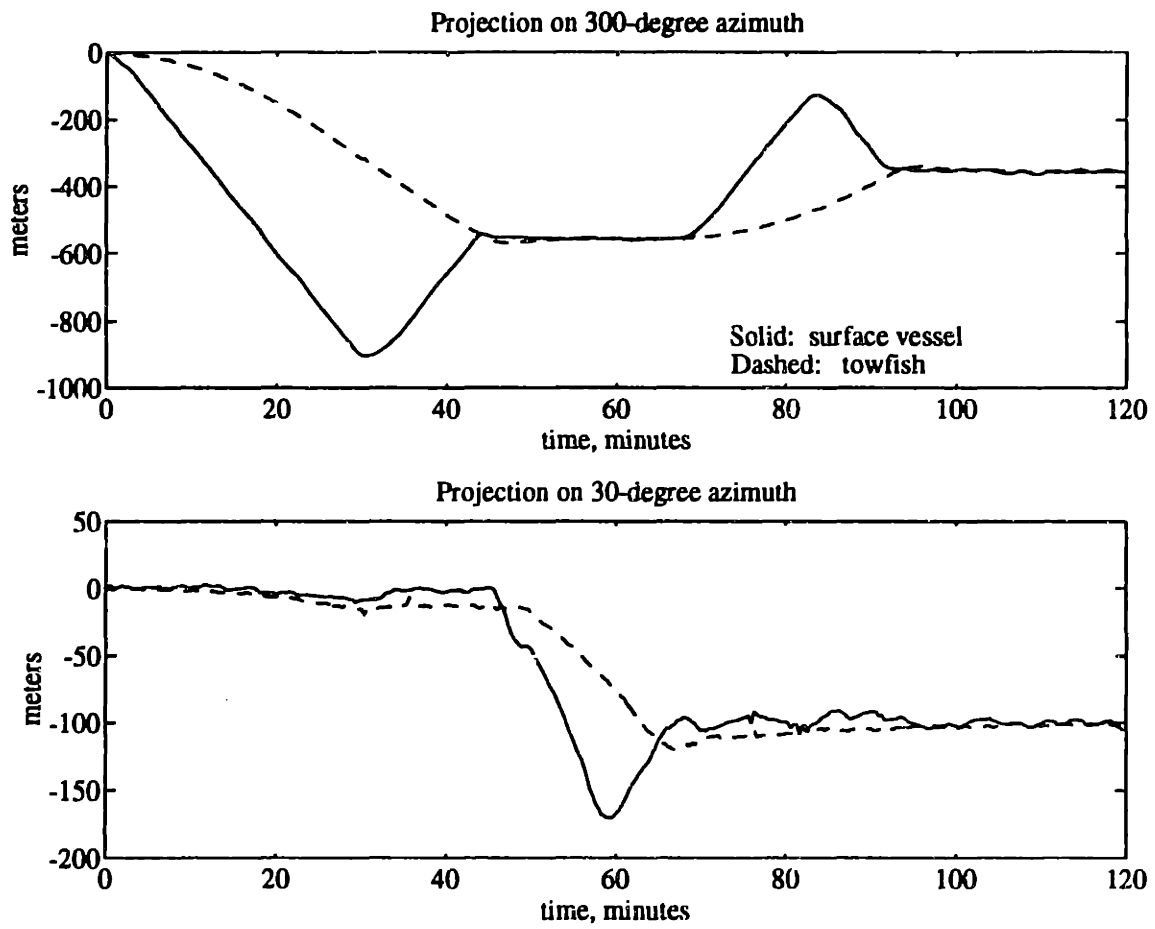
Figure 3-9: Projections along perpendicular azimuths for three overshoot moves.

moves of short net distance and high vessel speed, also consistent with previous results.

The most dramatic effects of the overshoot maneuver are found in the cascaded run of Figure 3-8, however. Since the emphasis is on turning sharp corners with the towfish, it is interesting to compare the experimental results to the response of a model without the overshoots (in lieu of experimental results with flat vessel trajectories). To this end, we used a model with coupled drag terms, and drove it with the recorded vessel trajectory for this run, but with the overshoots truncated. A zoom view of the experimental corners and the simulation corners is given in Figure 3-10. We see that the simulation with flat vessel motion is missing the sharp corners found in the experimental data, to the order of fifty meters error, and yet the time to execute the total maneuver is identical in both cases. The implication is that fol'owing a trackline with corners cannot be achieved as precisely without the overshoots, for the same time period and the same vessel speeds. Indeed, the deterioration of this northwest-southeast trackline is a good example of why the usual long turnaround has traditionally been used.

An important property of the overshoot response is that the towfish goes through substantial altitude changes; during the vessel "return" period, the rate of altitude loss may be high. For the experiments reported here, the maximum vertical velocity of the towfish was under 0.2 meters/second. Many winches can keep up with velocities in this range, and it is expected that constant altitude during these overshoot moves can be maintained, if necessary, by actively using the winch. One must be aware, however, that the vessel trajectories of this section do not involve horizontal velocities greater than 0.5 meters/second; the altitude problem will surely be ﹍acerbated in operations at higher speeds.

3.3 Open-Loop Trajectory Following

We consider now the task of input preshaping for more general trajectory following. Assuming that the operator has specified the trajectory of the towed body as a time series, the problem is to specify the required ship motions to bring about this response. The special case of a time-optimal step change in position of the lower endpoint (as above) is a subclass of the trajectory-following problem.
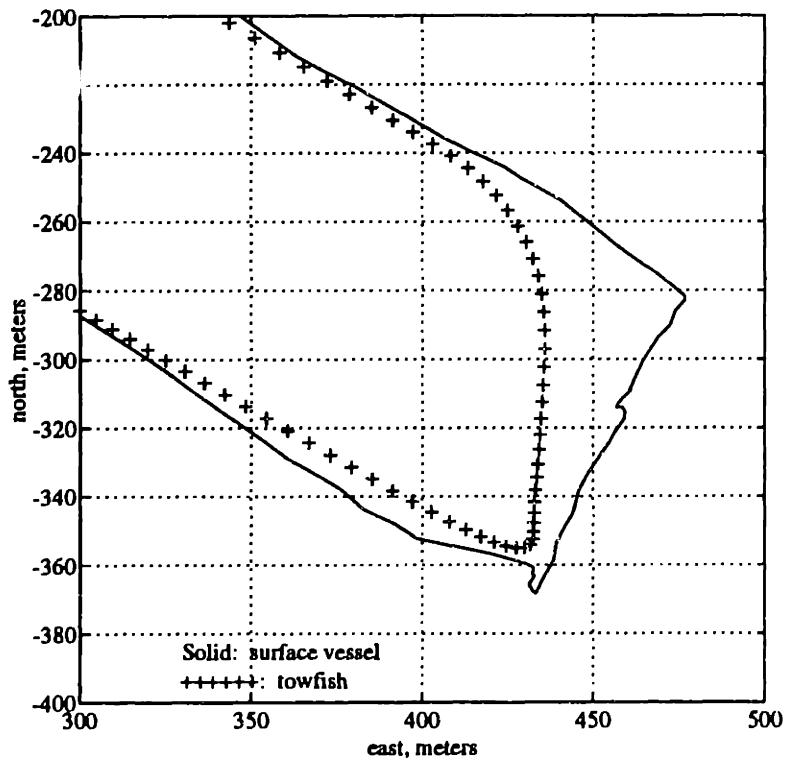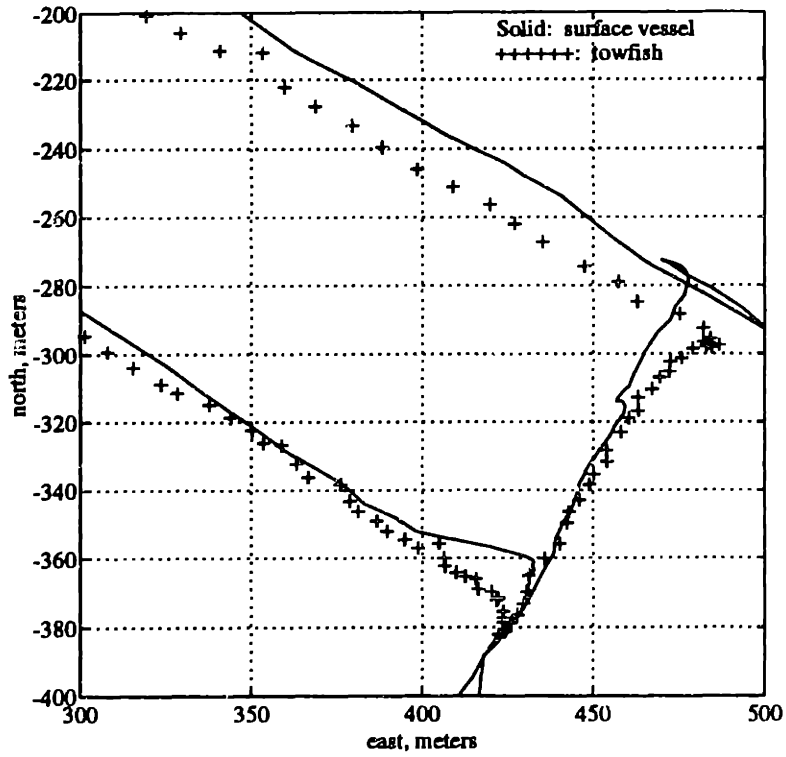
Figure 3-10: Comparison of corners achievable with (top) and without (bottom) overshoots.

3.3.1 Background

The concept of input preshaping is an intuitive one; we seek to "undo" the dynamics of the physical system, calling what is an output from the real system (towfish motion) an input to the algorithm, and vice versa. The alternative to preshaping is feedback applied to a moving reference point. This technique will be considered experimentally in Chapter 5, but it is clear that robustness considerations are likely to cause sluggish performance in comparison to a full inversion procedure.

A novel approach has recently been applied to the feedforward component of tracking control for flexible robots by Bayo et al. [9], [11], [12], [10]. In short, they use a finite-element discretization of the link, and an inversion in the frequency domain. Given the desired acceleration profile of the endpoint, and if the arm follows linear dynamics, a single computation gives the necessary hub torque profile. One notable feature of this approach is that, because the inversion occurs in the frequency domain, the hub torque command can precede the desired endpoint motions so as to account for the flexure in the arm, and the pure time delay. In the case of nonlinear terms in multilink arms (Coriolis and centrifugal torques), these researchers have implemented a simple iterative scheme which apparently converges to the correct results.

We begin with this formulation and modify it to fit our system. The towing problem differs in that pointwise nonlinearities must be allowed, since the cable follows a quadratic drag law. In addition, a finite-difference scheme is used to model the distributed system, instead of the finite-element method; these models are described in Section 2.7. The only other change is that we initially neglect bending stiffness for the simple reason that it is small for our applications.

In the two sections that follow, we outline the iterative method of inversion for the in-plane problem, and then give a proof for the convergence of the nonlinear scheme.

3.3.2 The Iterative Method

In the following, the qualifier "(t)" indicates a time-domain quantity, and "(ω)" indicates the frequency domain equivalent. ι_k is a column of zeros with a one in the k-th row, and I_{-k} is the identity matrix with a zero replacing the one in the k-th row. The sizes of ι_k and I_{-k} will be clear from context.

The generalized n-node system is modeled as in Section 2.7, but we cast it in a different form:

$$Mx''(t) + Bx'(t) + Kx(t) = Gu(t) - N(t, x(t), x'(t)), \qquad (3.2)$$

where M, B, and K are the linear mass, damping, and stiffness matrices, respectively. M and B are diagonal, and K is tridiagonal for the cable system without bending stiffness. The vector $x(t)$ is the length $n + 1$ position vector including the vessel; $x(t) :=$ $[x_v(t) \ q_n \ q_{n-1} \ \cdots \ q_1]^T$. This notation makes q_1 the position of the towfish, consistent with the discretization scheme of Chapter 2. $u(t)$ is the input (in units of force) at the vessel, so that $G = \iota_1$. $N(t, x(t), x'(t))$ is the nonlinear force vector to be specified. Without loss of generality, we can write Equation 3.2 in the frequency domain to give

$$[-\omega^2 M + i\omega B + K]x(\omega) = Gu(\omega) - \mathcal{N}(\omega). \qquad (3.3)$$

Here, $x(\omega)$ is the Fourier transform of the position vector $x(t)$. $\mathcal{N}(\omega)$ can be thought of as the Fourier transform of the time-domain nonlinear force $N(t)$. Renaming the bracketed expression $H(\omega)$ and setting $F(\omega) := H^{-1}(\omega)$, one finds that the linear solution comes from

$$
\begin{aligned}
x(\omega) &= F(\omega)Gu(\omega), \text{ or} \\
u(\omega) &= \frac{1}{F_{n+1,1}(\omega)} q_1(\omega).
\end{aligned}
\qquad (3.4)
$$

When $\omega = 0$, a diagonal matrix with small elements can be added to K to make $H(0)$ invertible. In addition, Herbert and Jones [54] noticed that when $H(\omega)$ is tridiagonal, $F_{n+1,1}(\omega)$ has a particularly simple cofactor form, which reduces the inversion of $H(\omega)$ to essentially one determinant calculation. This fact would be useful for a very high-order system.

Thus, the procedure in the linear case is to first specify $q_1(t)$ as a finite time series of length p, and convert it to the frequency domain. The above equation then has to be solved for each distinct frequency in the domain of interest for the physical system. Once the transformed input has been solved for the relevant frequency range, one inverse Fourier

81

Transform gives the required input for the physical system.[1]

In the lumped-parameter framework, we propose that the nonlinear term may be iteratively solved as follows:

1. Derive an expression for $u(\omega)$ involving the linear part found above, and the nonlinear part $\mathcal{N}(\omega)$ (initially zero). There are at least several ways to do this—the form we use is as follows:

$$u_{k+1}(\omega) = \frac{1}{F_{n+1,1}(\omega)}[q_1(\omega) + \iota_{n+1}^T F(\omega) \mathcal{N}_k(\omega)], \qquad (3.5)$$

where the k subscript denotes the iteration index. This formula is the simplest to derive, and has a nonlinear part which is additive with the original linear component.

2. Evaluate the pointwise position transforms based on this new $u(\omega)$. Note that $x_{n+1}(\omega)$ does *not* need to be reevaluated since it is just q_1. We have

$$x_{k+1}(\omega) = \iota_{n+1} q_1(\omega) + I_{-(n+1)} F(\omega)(G u_{k+1}(\omega) - \mathcal{N}_k(\omega)). \qquad (3.6)$$

3. Calculate the new value of the nonlinearity based on $\underline{x}_{k+1}(\omega)$; all time derivatives and integrals are related by multiples of the factor $i\omega$. We bundle these operations, in addition to the fundamental nonlinearity term, into the operator ϕ:

$$\mathcal{N}_{k+1}(\omega) = \phi(\omega, x_{k+1}(\omega_1), x_{k+1}(\omega_2), ..., x_{k+1}(\omega_p)). \qquad (3.7)$$

As written, the nonlinearity may involve more than one of the p frequency components. For example, a square nonlinearity makes ϕ a convolution operator in the frequency domain.

---

[1] A similar relation, which avoids the finite-difference approximation, can be derived from the linear wave equation, with appropriate boundary conditions. It takes the form of an irrational transfer function from the input u to the output q_1; to solve the inverse dynamics, one merely has to invert the transfer function. However, this approach is somewhat cumbersome with depth-varying tension and is impractical when nonlinearities are introduced.
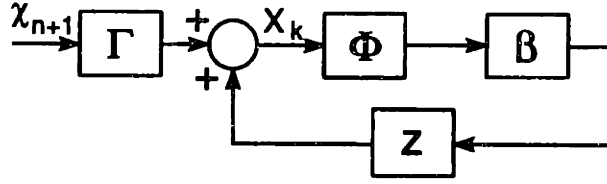
Figure 3-11: Iterative loop as a discrete-time system.

3.3.3 Stability Proof for the Iterative Scheme

The procedure of the previous section can be seen as a discrete feedback loop involving a new and very large $(n+1)p \times 1$ state vector $X := [x(\omega_1)^T \quad x(\omega_2)^T \quad \cdots \quad x(\omega_p)^T]^T$. This loop is drawn in Figure 3-11, and is described by

$$X_{k+1} = \Gamma \chi_{n+1} + \beta \Phi(X_k), \tag{3.8}$$

where $\chi_i := [x_i(\omega_1) \quad x_i(\omega_2) \quad \cdots \quad x_i(\omega_p)]^T$, Γ is an $(n+1)p \times p$ constant matrix, and β is an $(n+1)p \times (n+1)p$ constant matrix. We have also set

$$\Phi(X) := \begin{bmatrix} \phi(\omega_1, x(\omega_1), \cdots, x(\omega_p)) \\ \vdots \\ \phi(\omega_p, x(\omega_1), \cdots, x(\omega_p)) \end{bmatrix}.$$

The nonlinear operator Φ carries $\mathbf{R}^{(n+1)p}$ into itself. It is noteworthy that we have totally eliminated u from the loop; it is only $x_1 := x_v$ that is of interest.

In order to show loop stability, we consider the transition matrix β, and then its interaction with the nonlinearity Φ. To begin, β is the block-diagonal of p frequency-specific parts $\beta'(\omega_i)$:

$$\beta := \begin{bmatrix} \beta'(\omega_1) & & & 0 \\ & \beta'(\omega_2) & & \\ & & \cdots & \\ 0 & & & \beta'(\omega_p) \end{bmatrix}.$$

For this system, the matrix $\beta'(\omega_i)$ is completely defined by $H(\omega_i)$ and some trivial vectors

83

$$F = \begin{bmatrix} \bar{F}_{1,1} & & & F_{1,n} \\ \bar{F}_{1,1} & & \bar{F}_{i,j} & \\ & & \beta_{i,j} & \\ F_{n,1} & & F_{n,j} & F_{n,n} \end{bmatrix}$$
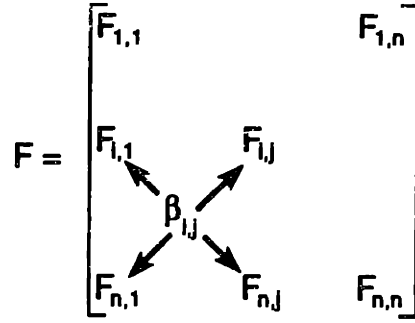
Figure 3-12: β as a matrix of two-determinants of F.

as follows:

$$\beta'(\omega_i) = I_{-(n+1)}F(\omega_i)\left(\frac{1}{F_{n+1,1}}G\iota_{n+1}^T F(\omega_i) - I_{n+1}\right), \qquad (3.9)$$

and on carrying through the multiplications, we find that $\beta'(\omega_i)$ has a first column and last row of zeros. Dropping the frequency argument for clarity, the other terms are given by:

$$\beta'_{i,j} = \frac{F_{i,1}F_{n+1,j}}{F_{n+1,1}} - F_{i,j} \text{ for } i = 1,...,n \text{ and } j = 2,...,n+1. \qquad (3.10)$$

We are particularly interested in the elements of $\beta'(\omega_i)$ in the lower triangle, these terms are multiples of specific two-determinants of $F(\omega_i)$ which are cornered in the lower left of $F(\omega_i)$. For this reason, these elements of $\beta'(\omega_i)$ will be called "corner-2-determinants". Their graphical interpretation is given in Figure 3-12.

The following proposition applies to a single $H(\omega_i)$, and hence the argument ω_i is omitted again for clarity:

Proposition: Let H be an invertible tridiagonal matrix of size $(n+1)\times(n+1)$. The corner-two-determinants described above, which involve the lower left corner element of H^{-1} and any other element which lies in the lower triangular portion of H^{-1}, are identically zero. More formally,

$$F_{i,1}F_{n+1,j} - F_{n+1,1}F_{i,j} = 0 \text{ for } i = 2,\cdots,n \text{ and } j = 2,\cdots,i. \qquad (3.11)$$

Proof: The algebraic proof proceeds in three parts: we show successively that the corner-2-determinants of the 1) first and second columns, 2) of the first and third columns, and 3) inductively of the first and j-th columns, are zero.

1. The definition of the inverse matrix is $FH = I$. This gives

$$F_{i,1}H_{1,1} + F_{i,2}H_{2,1} = 0, \ i = 2, \cdots, n+1. \tag{3.12}$$

One obtains the desired result immediately for the second column of β', by considering the i-th and the $n+1$-th rows;

$$F_{i,1}F_{n+1,2} - F_{n+1,1}F_{i,2} = 0 \text{ for } i = 2, \cdots, n. \tag{3.13}$$

2. The identity gives, for the remaining lower triangle elements of F:

$$F_{i,j-2}H_{j-2,j-1} + F_{i,j-1}H_{j-1,j-1} + F_{i,j}H_{j,j-1} = 0 \text{ for } j = 3, \cdots, n+1, \ i = j, \cdots, n+1. \tag{3.14}$$

Consider the case $j = 3$; we have

$$F_{i,1}H_{1,2} + F_{i,2}H_{2,2} + F_{i,3}H_{3,2} = 0 \text{ for } i = 3, \cdots, n, \tag{3.15}$$

$$F_{n+1,1}H_{1,2} + F_{n+1,2}H_{2,2} + F_{n+1,3}H_{3,2} = 0. \tag{3.16}$$

We substitute the value of $F_{i,2}$ from Equation 3.13 into Equation 3.15, multiply Equation 3.16 by $\frac{-F_{i,1}}{F_{n+1,1}}$, and add the results. This gives

$$F_{i,1}F_{n+1,3} - F_{i,3}F_{n+1,1} = 0 \text{ for } i = 3, \cdots, n. \tag{3.17}$$

3. Now we generalize to the case for arbitrary j, but we must start with $j = 4$, and incrementally move to $j = n + 1$ in Equation 3.14. As in Part 2), we can write a pair of equations, one for the i-th row, and one for the $n + 1$-th row:

$$F_{i,j-2}H_{j-2,j-1} + F_{i,j-1}H_{j-1,j-1} + F_{i,j}H_{j,j-1} = 0, \quad i = j, \cdots, n, \quad (3.18)$$

$$F_{n+1,j-2}H_{j-2,j-1} + F_{n+1,j-1}H_{j-1,j-1} + F_{n+1,j}H_{j,j-1} = 0. \quad (3.19)$$

In general, the computations for the previous two columns provide the "bridge" back to the first column. For example, in the case $j = 4$, one substitutes the value of $F_{i,3}$ from Equation 3.17 and $F_{i,2}$ from Equation 3.13 into Equation 3.18, multiplies Equation 3.19 by $\frac{-F_{i,1}}{F_{n+1,1}}$ as before, and adds the results. The conditions on the previous two columns are

$$F_{i,1}F_{n+1,j-1} - F_{n+1,1}F_{i,j-1} = 0 \text{ for } i = j - 1, \cdots, n, \quad (3.20)$$

$$F_{i,1}F_{n+1,j-2} - F_{n+1,1}F_{i,j-2} = 0 \text{ for } i = j - 2, \cdots, n. \quad (3.21)$$

These operations are repeated until $j = n$ is reached; in this way, the proposition is proved. □ □ □

Each $\beta'(\omega_i)$, and thus β, has eigenvalues which are zero, since the lower triangular elements are zero. As will be shown, however, β has a particularly interesting structure which protects the discrete-time system dynamics from potentially destabilizing nonlinear effects and guarantees convergence in n iterations. We need the following *assumption*: the nonlinearity Φ may span across different frequency components, but does not span from node to node in the physical system. Mathematically, this means

$$\frac{\partial \Phi_i}{\partial X_j} = 0 \text{ unless } i = j + (n+1)k, \ k \text{ some integer}. \quad (3.22)$$

This is a sufficient condition for the final thrust of the section: it specifies that the nonlinear effects depend on physical quantities which are *local*. The fluid drag nonlinearity fits this assumption neatly, but a Coriolis torque on a flexible manipulator, for example, does not.

With the above assumption and the known structure of β, it is apparent that *the discrete system of Figure 3-11 will converge in n iterations*. To show this, we make the following arguments. First, β represents an order-n deadbeat system matrix, since its only nonzero

elements are in the diagonal blocks $\beta'(\omega_i)$, which are themselves order-n deadbeat system matrices (order-n because β does not affect χ_{n+1}). Thus, if Φ were set to the identity, an additional p states in X would become invariant on each iteration, giving total convergence of X in n iterations.

In the presence of a local nonlinearity Φ, the nature of this convergence is unchanged. The reason is that each element of $\Phi(X)$ depends on only one χ_i, consistent with Equation 3.22. This dependence is so arranged that the order-n deadbeat nature of β is fully exploited.

Example: Suppose $n + 1 = 3$ and $p = 2$; then

$$
\beta = \begin{bmatrix}
0 & \beta_{1,2} & \beta_{1,3} & 0 & 0 & 0 \\
0 & 0 & \beta_{2,3} & 0 & 0 & 0 \\
0 & 0 & 0 & 0 & 0 & 0 \\
0 & 0 & 0 & 0 & \beta_{4,5} & \beta_{4,6} \\
0 & 0 & 0 & 0 & 0 & \beta_{5,6} \\
0 & 0 & 0 & 0 & 0 & 0
\end{bmatrix}.
$$

The lower endpoint motions are fixed, so also fixed are χ_3, x_3 and x_6. We have $X_1 = \Gamma \bar{\chi}_3$, and let $\bar{\chi}_i$ be the original value of χ_i and $\bar{x}_i$ be the original value of x_i. With some abuse of notation, the evolution of the state X is as follows:

$$
X_2 = \begin{bmatrix}
\beta_{1,2}\Phi_2(\bar{\chi}_2) + \beta_{1,3}\Phi_3(\bar{\chi}_3) + \bar{x}_1 \\
\beta_{2,3}\Phi_3(\bar{\chi}_3) + \bar{x}_2 \\
\bar{x}_3 \\
\beta_{4,5}\Phi_5(\bar{\chi}_2) + \beta_{4,6}\Phi_6(\bar{\chi}_3) + \bar{x}_4 \\
\beta_{5,6}\Phi_6(\bar{\chi}_3) + \bar{x}_5 \\
\bar{x}_6
\end{bmatrix},
$$

$$X_3 = \begin{bmatrix} \beta_{1,2}\Phi_2(\beta_{2,3}\Phi_3(\bar{\chi}_3) + \bar{x}_2, \beta_{5,6}\Phi_6(\bar{\chi}_3) + \bar{x}_5) + \beta_{1,3}\Phi_3(\bar{\chi}_3) + \bar{x}_1 \\ \beta_{2,3}\Phi_3(\bar{\chi}_3) + \bar{x}_2 \\ \bar{x}_3 \\ \beta_{4,5}\Phi_5(\beta_{2,3}\Phi_3(\bar{\chi}_3) + \bar{x}_2, \beta_{5,6}\Phi_6(\bar{\chi}_3) + \bar{x}_5) + \beta_{4,6}\Phi_6(\bar{\chi}_3) + \bar{x}_4 \\ \beta_{5,6}\Phi_6(\bar{\chi}_3) + \bar{x}_5 \\ \bar{x}_6 \end{bmatrix} , \text{ and}$$

$$X_4 = \begin{bmatrix} \beta_{1,2}\Phi_2(\beta_{2,3}\Phi_3(\bar{\chi}_3) + \bar{x}_2, \beta_{5,6}\Phi_6(\bar{\chi}_3) + \bar{x}_5) + \beta_{1,3}\Phi_3(\bar{\chi}_3) + \bar{x}_1 \\ \beta_{2,3}\Phi_3(\bar{\chi}_3) + \bar{x}_2 \\ \bar{x}_3 \\ \beta_{4,5}\Phi_5(\beta_{2,3}\Phi_3(\bar{\chi}_3) + \bar{x}_2, \beta_{5,6}\Phi_6(\bar{\chi}_3) + \bar{x}_5) + \beta_{4,6}\Phi_6(\bar{\chi}_3) + \bar{x}_4 \\ \beta_{5,6}\Phi_6(\bar{\chi}_3) + \bar{x}_5 \\ \bar{x}_6 \end{bmatrix} .$$

One sees that χ_3 is indeed unaffected by the loop. After the first iteration, it is clear that χ_2 is fixed, and after the second, that χ_1 is fixed.

The iteration scheme generates the complete motion of successive points along the cable, one at a time. This is precisely how one would solve this problem with backward time integration, one node at a time. However, it has been shown by Serna and Bayo [88] that straightforward backwards integration cannot work in general, due to numerical instabilities. A time-domain computation of the impulse response integral has been suggested as a panacea, although such an approach is valid only for linear systems. We do not pursue time-domain computations further here.

3.3.4 Applications

Many physical systems fit into the tridiagonal system matrix form, and lateral spring-mass-damper approximations of the wave equation are clearly suitable. The assumption 3.22 allows a very large range of nonlinearities to act upon such a system, as long as they act locally, and the analysis indicates that the rate of convergence is independent of the nature of this nonlinearity. The current section presents four examples (simulations only) of the

usefulness of this procedure.

An important note is that, for ocean applications, we require the Fourier series to be truncated. This is in contrast to Bayo's results, in which torque commands with very high bandwidth can be applied. An immediate reason to truncate is that a reduction in computation time by several orders of magnitude can be gained, since there are several inversions of $H(\omega_i)$ for each frequency retained. Another consideration is that when the full series is kept, the algorithm presented here may give discontinuities or very high velocities in x_v, even if q_1 is smoothed. At present, we have no mechanism in place that prefers smooth x_v; obviously, one could filter the resultant x_v after the algorithm is completed.

Extensive experience with the algorithm indicates that stability of the algorithm is an issue only when the number of terms in the Fourier series is inconsistent with the order of the plant. For example, it is physically impossible to obtain fast transients at the towfish if the cable model is second-order. The higher the order of the plant, the sharper are the transients we are able to achieve, using more frequency components. In addition, the algorithm appears to fail if *any part* of the cable takes on this imbalance. The typical failure scenario is as follows: a smooth towfish trajectory is specified, but the velocities are so large that sharp motions are required near the top of the cable, to overcome drag in the lower portion. When the frequency content of these motions exceeds that of the retained Fourier series, the iterative procedure may be unstable. Thus, the user should work with a model of sufficiently high order, and keep only the frequency content required for the application.

There are a few inescapable numerical flaws worth noting. The first is the way in which $\Phi(X_k)$ is computed; the operator Φ takes an X_k in the frequency domain, into a force, also in the frequency domain. To do the calculation, it is almost always necessary to take the inverse transform of X_k, get the time-domain force, and then transform back to the frequency domain. The fault of this procedure is that the two transforms are generally approximations if any of the series is missing, and spurious components in $\Phi(X)$ could be generated and amplified. Another point is that the inversion of $H(\omega_i)$ can never be exact, which leads to roundoff errors in β. Finally, Gibb's phenomenon almost always leads to poor behavior when sharp transients appear in any component of x. This response may be somewhat alleviated by filtering or windowing techniques.

The results of this section required no particular attention to the stability issue, and we give a full description of the parameters for each run to indicate the normal behavior of the

algorithm.

Drill String with Quadratic Drag

The t example is a simulation in which a full-scale drill string system[2] is subjected to quadratic drag, during an arbitrary in-plane towfish trajectory. Figure 3-13 shows this run as a time history of the endpoints, and gives a stroboscopic view of the cable shape evolution through the first 80 minutes of the run. The series truncation corresponds to a bandwidth of .0037 radians/second, and $n + 1$ is thirteen. The algorithm took nine iterations to converge to within an error norm of 10^{-6}.

The acausal nature of the algorithm is evident from the figure, as the surface vessel motion precedes the towfish motion in both of the startups at 2000 seconds and 7000 seconds. We also see Gibb's phenomena clearly in the vessel trajectory before the large reverse move. Finally, the algorithm has successfully recovered the overshoot concept of Section 3.2; the vessel trajectory beginning at 7000 seconds has a 300-meter overshoot to move the towfish back to the origin.

Inclusion of Small Bending Stiffness Terms

Clearly, when the cable or riser has significant bending stiffness, the tridiagonality of Equation 3.2 is lost. As such, convergence of the iterative scheme we have given cannot be guaranteed. Nonetheless, it seems reasonable that one might try to carry out the inversion with bending stiffness anyway, since it is small for many deep ocean systems. In fact, this turns out to work quite well, as is shown in Figure 3-14. The parameters for the run are exactly the same as in the previous case, except that we have included a bending stiffness which is ten times the actual stiffness for the pipe. The bending moments were computed using the standard finite-difference formulas for fourth derivatives. Ten iterations were required for this run.

The major feature here is that the stiffness of the pipe enables the algorithm to use the weight more effectively, requiring less overshoot. Gibb's effect is still visible, but, as before, does not cause numerical difficulties or significant deviation of the towfish.

---

[2]see Chapter 5 for its specifications
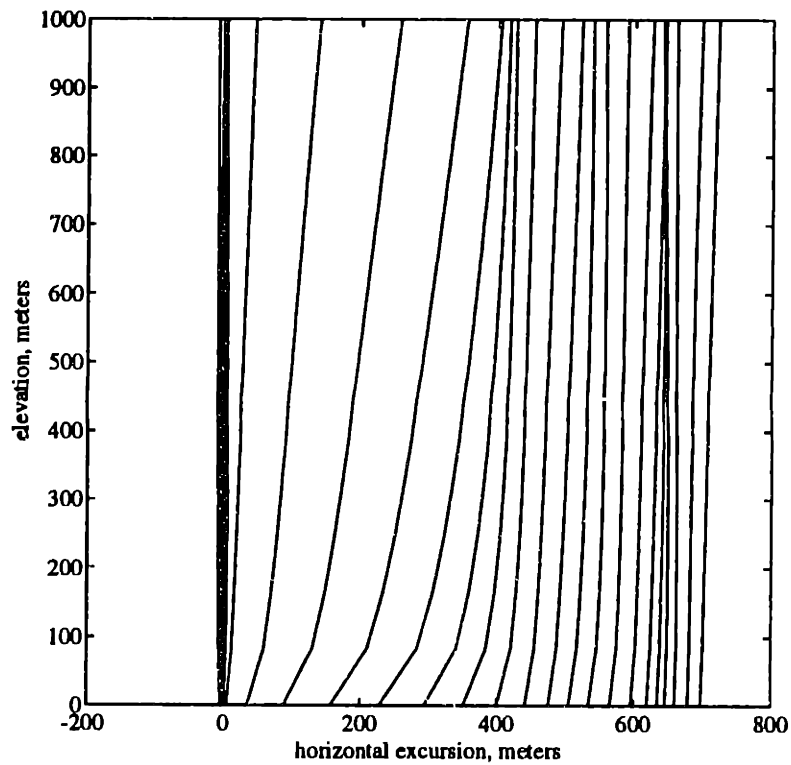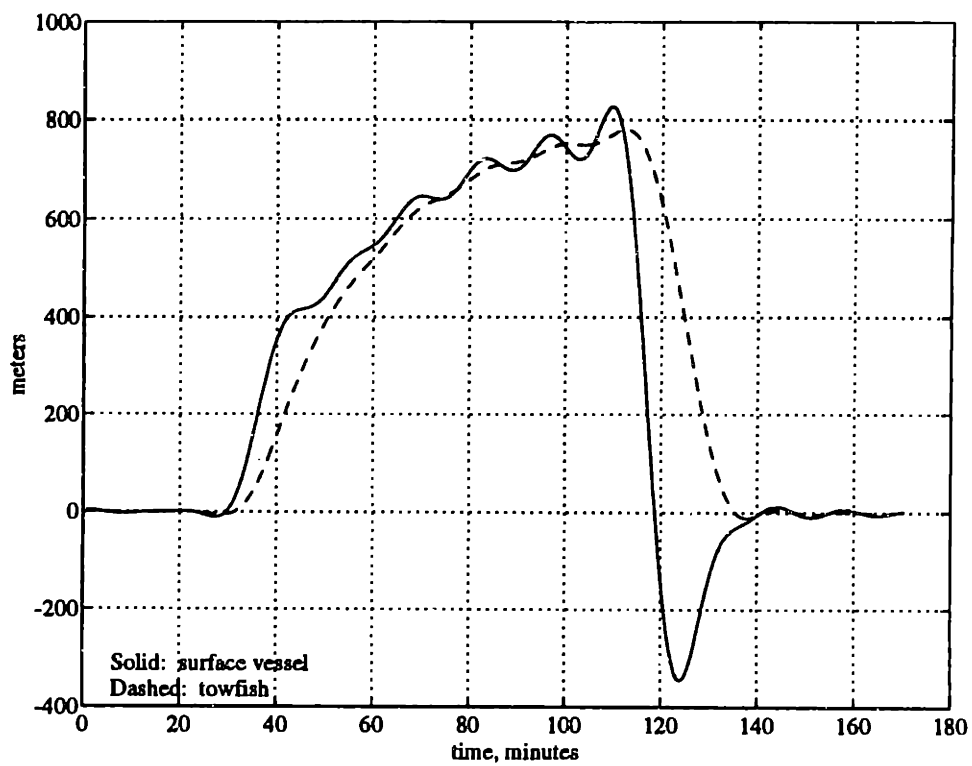
Figure 3-13: Time series (top) and 60-second strobed side view (bottom) of a flexible drill string response during preshaping run.

91
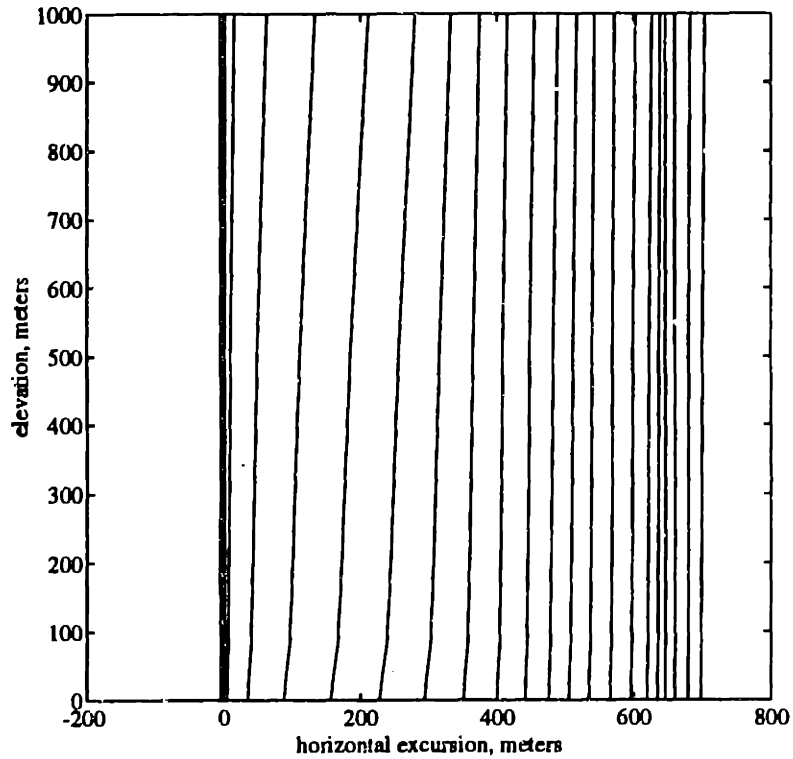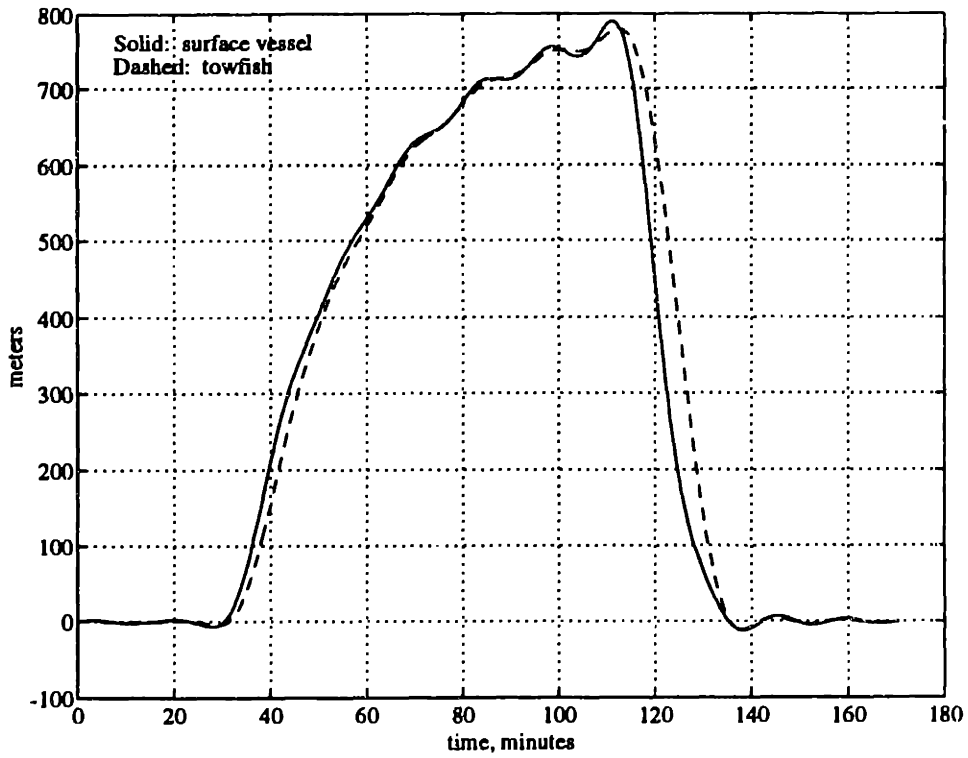
Figure 3-14: Time series (top) and 60-second strobed (bottom) side view of a stiff drill string response during preshaping run.

Coupled In-Plane and Out-of-Plane Towing

As was shown in the derivations of Section 2.5, the zeroth-order three-dimensional dynamic equations for a cable are geometrically uncoupled. In the ocean, this means that the drag term alone links in-plane motions to out-of-plane motions. The presence of a coupling nonlinearity between distinct tridiagonal physical systems can be handled quite easily with our technique. Since each iteration fixes the trajectory of one more physical point on the cable, we can solve the two parallel problems separately, point by point. The key is that the nonlinearity is a simple function of the local in-plane and out-of-plane velocities, which are known.

Figure 3-15 shows how this procedure may be used to compute a vessel trajectory that leads to a preplanned response of the lower endpoint of the cable. For this example, a nominal *ARGO/JASON* system with 3000 meters of cable[3] is to execute a 200-meter radius towfish circle at one-half knot. The surface vessel trajectory is essentially a larger radius circle, with starting and stopping transients. The fact that the ship trajectory is not round is an artifact of the series truncation, as before. Sixteen components, for a bandwidth of .0049 radians/second, were retained for the run, which involved ten iterations.

It can be verified that the vessel trajectories required for rectangular grid patterns come out to be essentially the same as those used in Section 3.2. As a final note, in the deep ocean, there are often known currents which have a significant effect on the motions of the cable. These currents can be incorporated into the scheme easily by explicitly including them in the time-domain calculation of drag forces.

The Heat Equation with Radiative Cooling

Other problems can be solved with the inversion method. This example considers a situation in which the far end of a long metal bar is to be heated by applying heat to the near end. The application might be annealing in a foundry, where very precise temperature trajectories are required, or a long rod in space. We suppose that the bar is long and thin enough that the one-dimensional heat equation is valid, and we assume linear convective cooling of the rod, as well as radiative cooling. We have, in nondimensional form [59],

---

[3]see Chapter 5 for its specifications
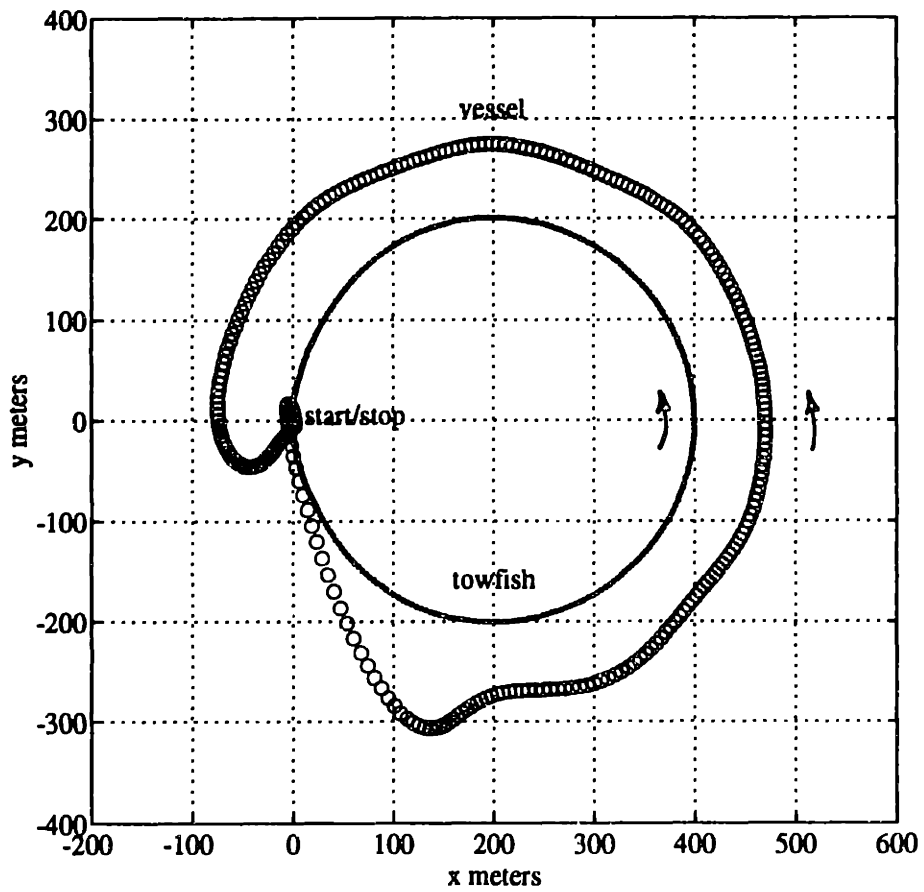
Figure 3-15: Bird's-eye view of coupled in-plane- and out-of-plane inversion of a 3000-meter *ARGO/JASON* system.

$$\frac{\partial T(x,t)}{\partial t} = \frac{\partial^2 T(x,t)}{\partial x^2} - \alpha_c(T(x,t) - T_{ambient}(x,t)) - \alpha_r T^4(x,t), \qquad (3.23)$$

where T is the nondimensional temperature in the rod, t is nondimensional time, and α_c and α_r are positive constants controlling the convective and radiative heat losses, respectively. The boundary condition is

$$\frac{\partial T(0,t)}{\partial t} = \frac{\partial Q(t)}{\partial t}, \qquad (3.24)$$

where Q is the heat going into the bar at $x = 0$. The form of the equation is familiar; it clearly can be cast in a tridiagonal finite-difference approximation, and the nonlinearity is local, as required. An example of the inversion method applied to this problem is given in Figure 3-16. The parameter α_r was taken to be unity, and α_r was set to .01. The ambient temperature was assigned a sinusoidal time dependence, and zero on the temperature scale T corresponded with two on the absolute scale, for computation of the radiation term.[4] The inversion here required seven iterations, and the number of nodes in the model was thirteen; sixteen Fourier components were kept, out of a possible 256.

The inversion scheme is able to account for the continual dissipation of heat due to radiation: the near end temperatures are higher when the far end temperature is high. It also takes care of the time-variations of the ambient temperature: fluctuations in the near end temperature are out of phase with the ambient temperature.

3.3.5 Preshaping: Full-Scale Experimental Results

During the same cruise that was described in Section 3.2, tests were conducted to verify the dynamic inversion procedure in a single plane. We made two full-scale tests: the results are shown in Figures 3-17 and 3-18. The top plot of each set gives the output of the inversion program with the towfish motions specified in advance. In the first case, the clump weight is required to accelerate from rest and travel at constant speed for thirty minutes, then decelerate to a slower speed for another thirty minutes, then reverse and follow a similar profile back to the original location. The inversion required six iterations for a five-node plant model, with twelve frequency components retained. In the second case, the clump weight is only to accelerate to a constant speed and then stop after approximately thirty

---

[4]In dimensional units, zero on our T scale would correspond to 273 kelvins.
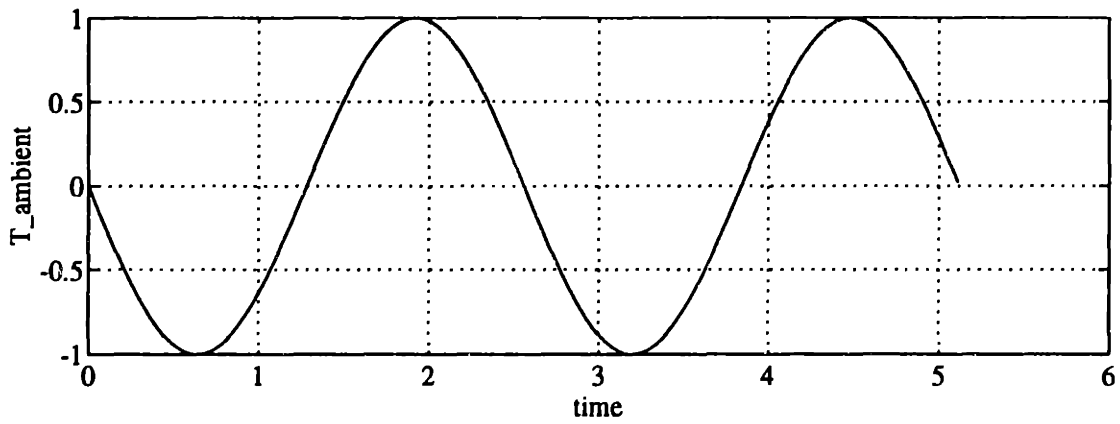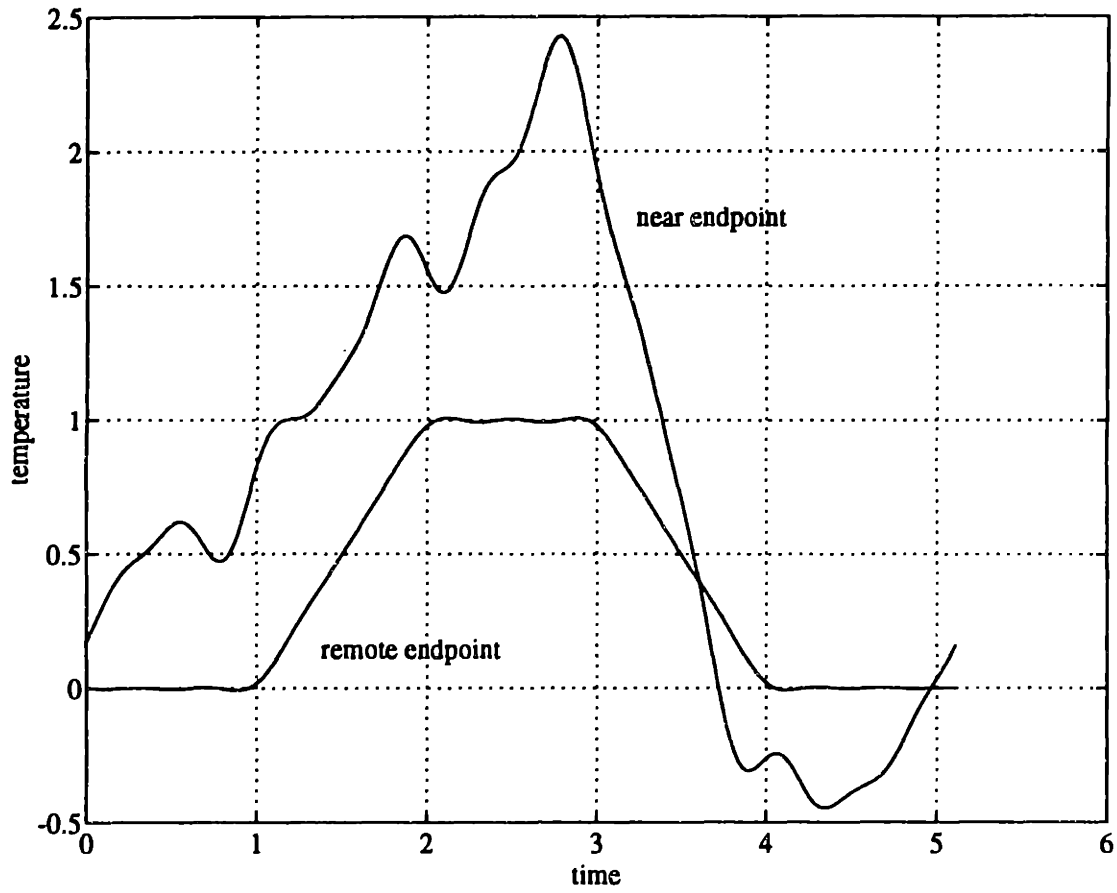
Figure 3-16: Endpoint temperature profile (top) and ambient temperature (bottom) for inversion of the nondimensional heat equation.

minutes. This run also took six iterations to converge. The time scales chosen for these two plots reflect the fact that the experimental runs were initiated at different points in the "total trajectory" specified by the inversion; that is, the second test was given a much longer lead-in time.

The experimental results are shown in the lower portions of the figures. In the first test, only one preliminary oscillation in the ship motion was included, and the clump weight moved a significant distance in response. A very clean movement from twenty to forty-two minutes elapsed followed, and the change in velocity at forty-two minutes was sharp. The lower-velocity forward motion was very smooth also. We lost GPS tracking at seventy-two minutes and were unable to regain it until one-hundred minutes time elapsed. As a result, the latter part of the run was made with a delay of approximately twenty minutes. The cable evidently assumed the proper shape again in time to achieve a very sharp stop at 142 minutes elapsed, within seven meters of the starting point.

For the second test, the lead-in oscillations were included in the vessel trajectory. As shown in Figure 3-18, this extra motion resulted in some movement of the clump weight, but qualitatively, the acceleration beginning at thirty minutes elapsed was better than in the first run. The constant-speed period was quite smooth, and the deceleration at the end of the run was sharp. The final position error of approximately forty meters can be largely attributed to the response of the clump weight to oscillations early in the run.

A side view of the motions of the towfish for the second preshaping run is given in Figure 3-19. In comparison with Figure 3-6 for the pure overshoot case, this run is more aggressive, in the sense that the vertical excursion of the towfish was twice as large. This difference is largely due to the fact that vessel velocities for the present run were near 0.7 meters per second, compared to 0.5 meters per second in the overshoot case. Nonetheless, the vertical excursions should not be a problem for most winches to keep up with, as the maximum rate of altitude change for this run is under 0.25 meters per second.

3.4 Summary

The results of this chapter indicate that the idea of input preshaping is an effective way both to improve the speed of response in simple point-to-point moves of the towfish, and to execute complex, coupled trajectories. The full-scale experimental data show that effective
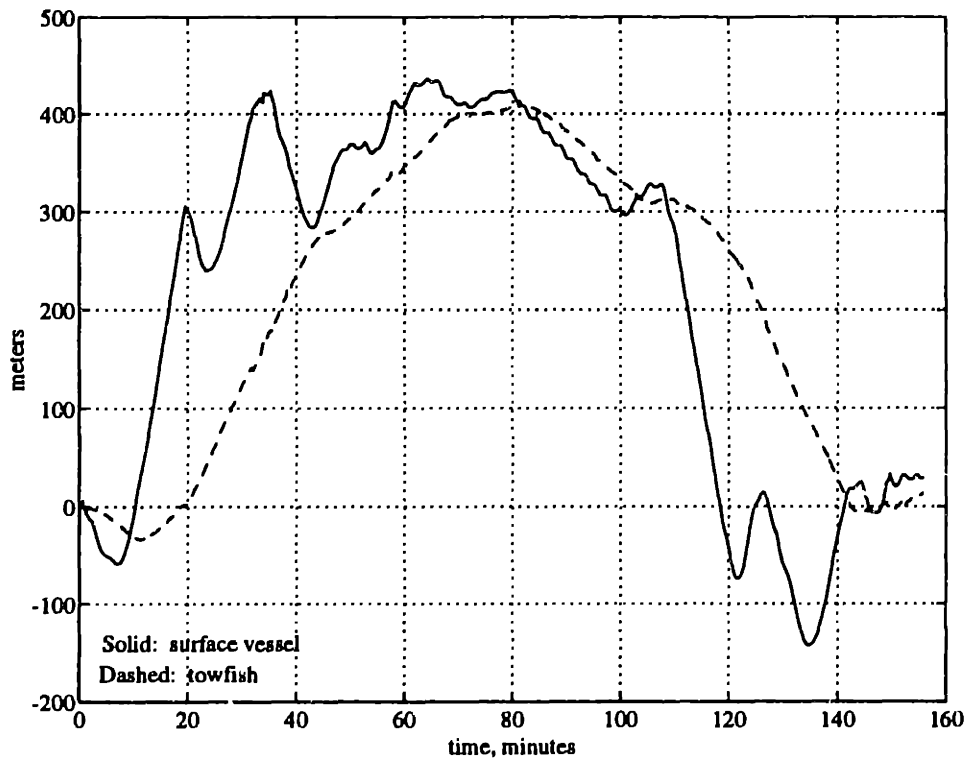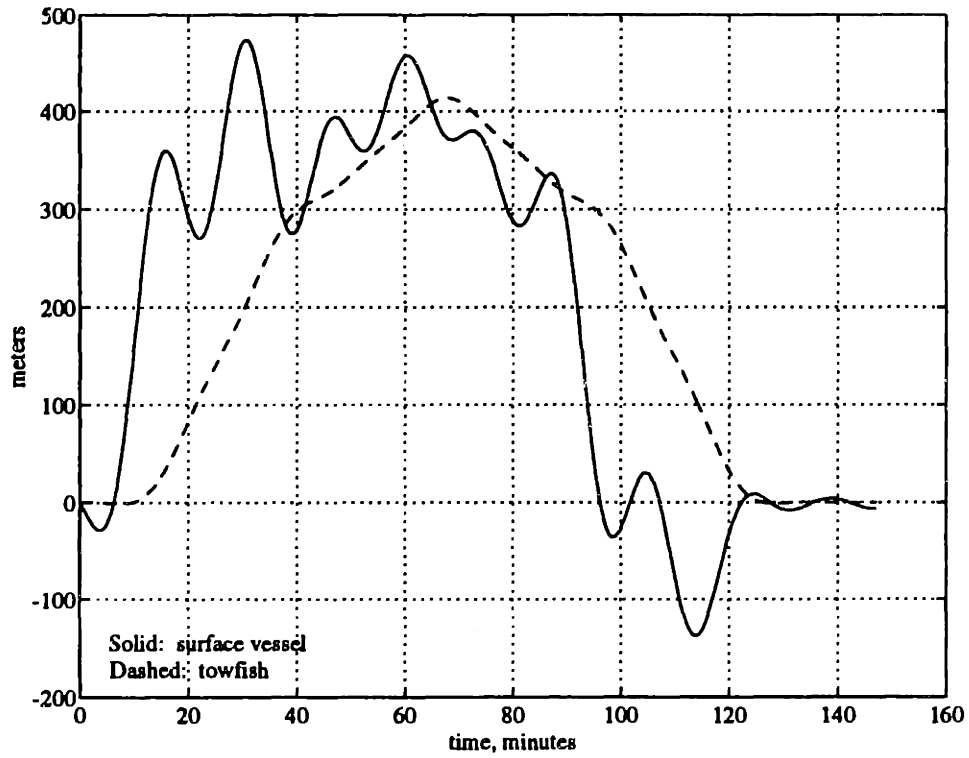
Figure 3-17: Analytical trajectory (top) and experimental results (bottom) for the first full-scale test.
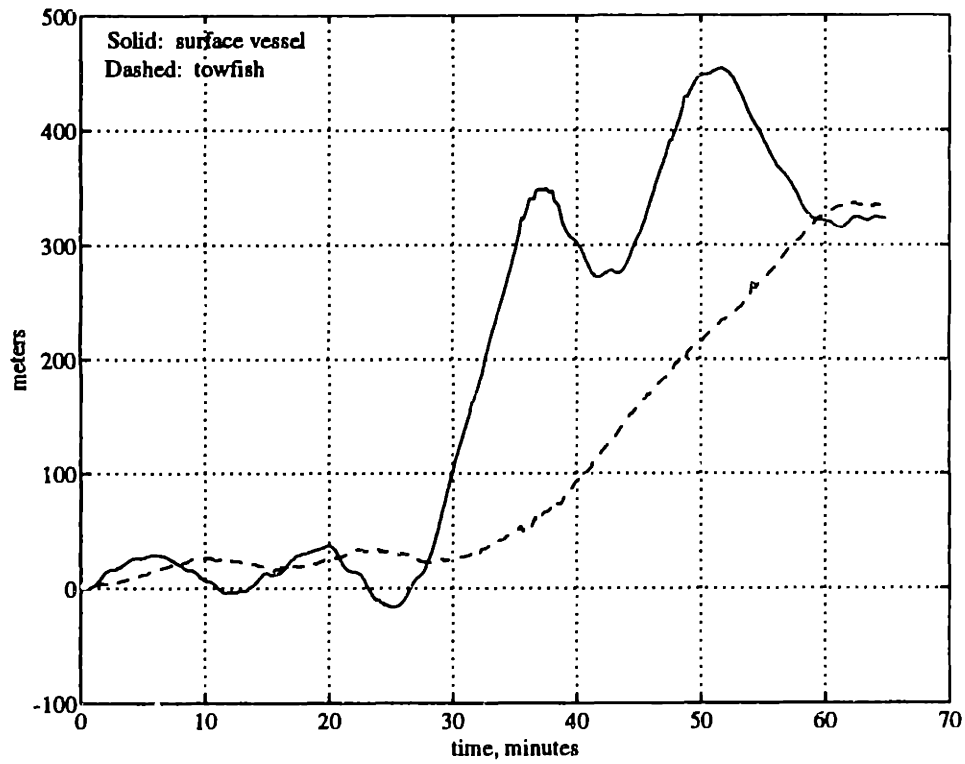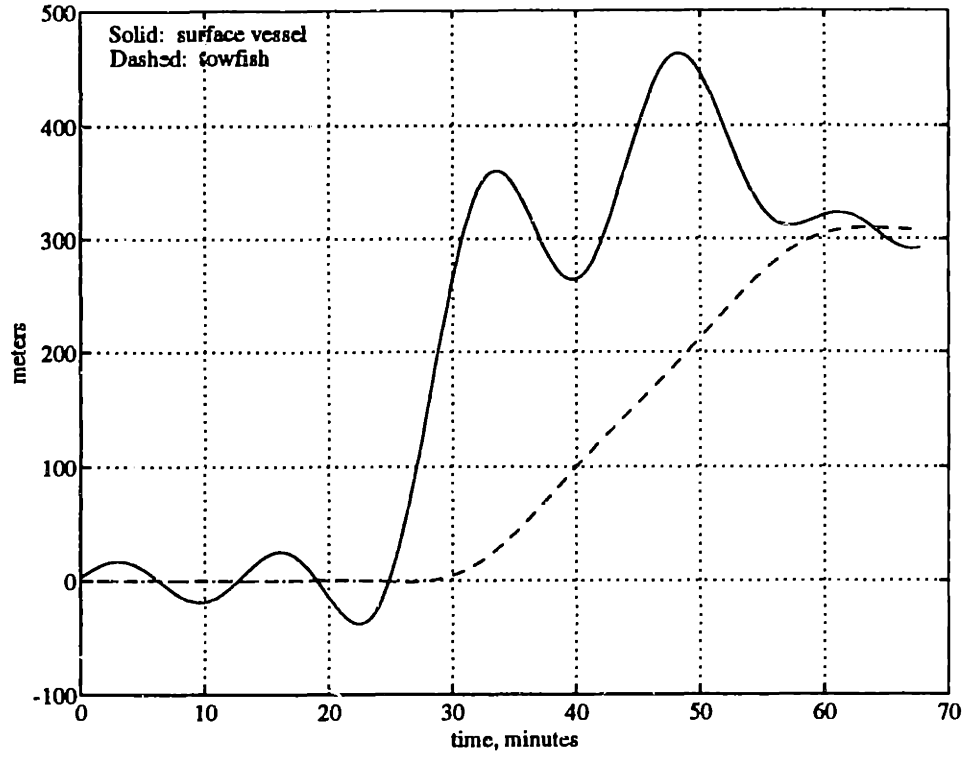
Figure 3-18: Analytical trajectory (top) and experimental results (bottom) for the second full-scale test.
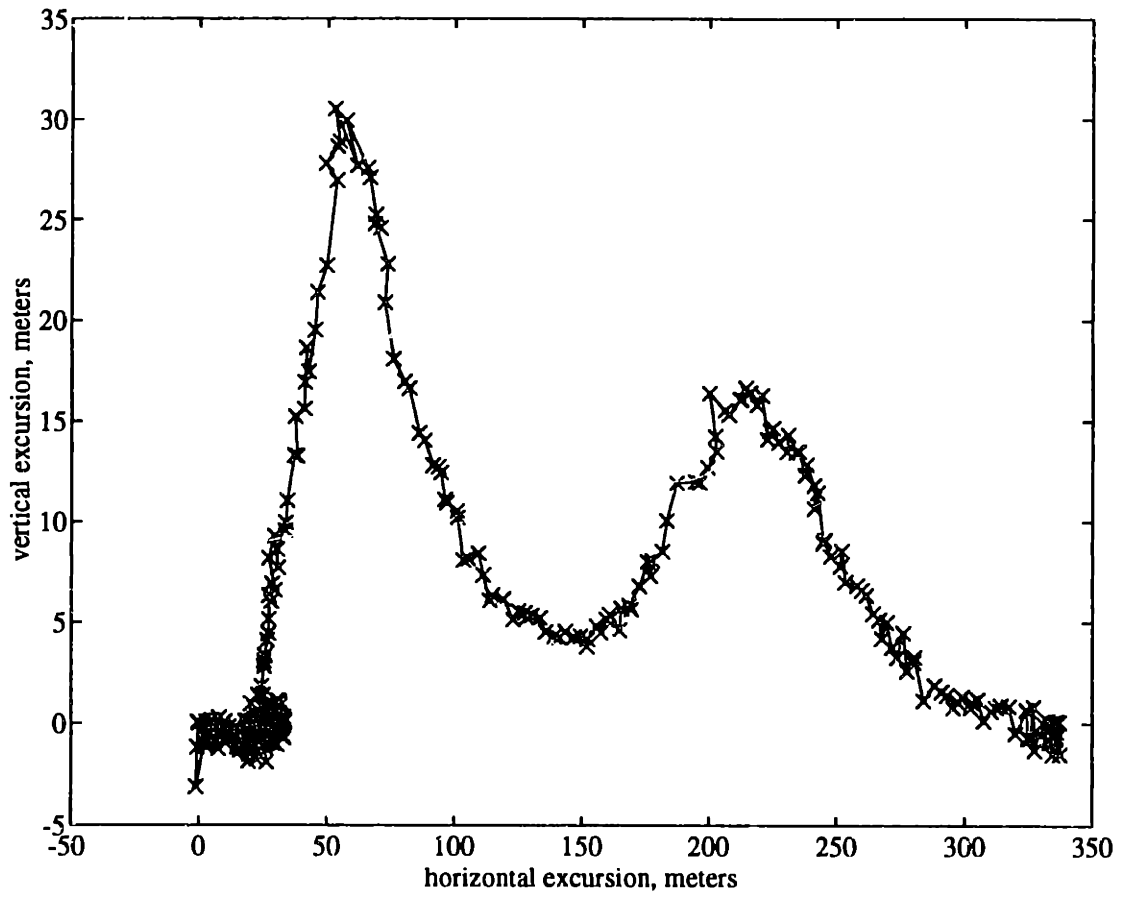
Figure 3-19: Measured heave response during the second full-scale preshaping test.

dynamic positioning of the surface vessel plays a crucial part; the runs could have been cleaner if the DP system had the capability to follow predefined trajectories, for example. At the same time, the inherent safety of this technique has been illustrated through the navigation failure in the first preshaping test. Since the procedures involve no feedback, such a failure means only that the plant will deviate from the desired track, and return smoothly to it after navigation is restored. Finally, the vertical excursions of the towfish during these tests were slow enough that typical winches should have no difficulty in maintaining constant altitude.

Chapter 4

Tools for the Cable Feedback Control Problem

4.1   Introduction

This chapter considers feedback control for positioning of a towed cable system. The problem is important because many deep ocean operations with towed vehicles require accurate positioning in the presence of unknown disturbances such as currents. Further, if the depth is large, and the drag forces are large, then the plant is clearly infinite-dimensional and nonlinear. These properties make the problem difficult, as the guarantees built into many control techniques cannot be valid. In Chapter 2, an attempt was made to justify each step of the model simplification process. Now, we investigate performance and robustness guarantees with respect to the reduced-order models. We build upon a great deal of work by other researchers, and, as such, a large part of this chapter covers known material.

4.2   Overview

Since the internal state of a cable (between the endpoints) clearly has a dominant role in the dynamic response at the endpoint, full-state feedback schemes require adequate sensors or state estimation. There are at least several conceivable ways in which state measurement could be carried out for a deep-water cable system. First, additional transceivers could be affixed to the cable; given the calculations of Section 2.6.2, perhaps only a few would be required. Alternatively, measurement of the cable angle at the surface could be used in an

102

energy-based feedback law (e.g., [92]). The idea would be to move the vessel in such a way that energy is always being extracted from the cable. Both of these approaches, however, are difficult to envision in heavy weather—the cable angle would be an extremely noisy measurement, and the attachment of transceivers on the cable would be very dangerous. For these reasons, we assume in this chapter that the only available navigation is of the towfish and of the surface vessel. With typical long-baseline acoustic navigation systems and GPS, the noise variance of both measurements is approximately five meters or less.

The use of estimators in closed-loop control has been a central issue in the literature for at least two decades. For the linear case, the counterexample of Doyle [36] showed that arbitrary coupling of Kalman filters with linear quadratic regulators (LQR) carries no firm robustness guarantees, even though the robustness properties of each part are good; such guarantees had been hypothesized by Safonov and Athans [84]. The existence of this counterexample was sufficient to motivate the Loop Transfer Recovery (LTR) procedure, which has been a widely favored version of the LQG approach for a decade.

To date, there is no accepted analogue for nonlinear systems, although Safonov gave a nonlinear separation principle, which we state here (see Appendix A for definitions):

Theorem[82]: Suppose a nonlinear feedback system is closed-loop bounded (finite-gain stable) with the feedback $u = -g(x)$, where g is a causal nonlinear dynamical operator with finite incremental gain. Let $\hat{x}$ be an estimate of x which is nondivergent (with finite gain). Then the feedback system with $\hat{x}$ replacing x in the control law, is closed-loop bounded (finite-gain stable).

The idea is that if a nondivergent estimator can be obtained for the system, then one can implement a possibly nonlinear control law based on exact state measurement and expect the closed-loop system to perform well. As with linear separation, however, there is no accommodation for uncertainty in the plant model. To get around this shortcoming, Grunberg and Athans [50],[51] applied the idea of loop transfer recovery to nonlinear systems; their methodology was termed Loop Operator Recovery (LOR). Like LTR, the LOR has dual formulations, one of which recovers the controller loop and the other the estimator loop. Unfortunately, the more useful estimator loop recovery procedure has been proven only for systems in controller and observer form (e.g., robots). Recovery of the controller loop is much easier to achieve theoretically, although it puts severe limitations on the performance

and robustness specifications.

The control techniques that are considered in this chapter include nonlinear model-based observation, and the design of nonlinear regulators, for direct use with Grunberg's control loop recovery procedure. Thus, we first outline what LOR entails, and detail some properties of various estimators (nominal nondivergence, parameterization) and control loops (robustness and performance). Then the primary contribution of the chapter is developed: a *practical*, approximately optimal nonlinear feedback law for high-order plant models.

4.3 Loop-Operator Recovery

In this section, we describe more specifically the LOR technique that is to synthesize nondivergent estimators with the LQR or the nonlinear optimal controller. Along with listing the relevant theorem, the practical shortcomings of the approach are discussed, to be revisited experimentally in Chapter 5.

4.3.1 The LQG/LTR Technique

What follows is a review of loop transfer recovery [39], [94], given because such a discussion is helpful to the uninitiated, and because the nonlinear LOR technique of the next section is in complete analogy with LTR. Our discussion is brief because one need not use LTR to solve the linear SISO problem associated with our cable system, and because LTR has been the topic of countless papers and books in the last decade. LTR takes two forms; one hinges upon the good properties of the LQR loop, and the other takes advantage of the similar properties of the Kalman filter loop. As noted previously, we will be recovering the control loop only.

The first step is to carry out the LQR design procedure for the plant $(sI - A)^{-1}B$, with $Q = C^T C$ and ρ chosen to put the crossover at an appropriate frequency.[1] This gives a feedback gain matrix G, and the control loop $G(sI - A)^{-1}B$ has a good shape for robustness against modeling errors and disturbances at the plant input. Although the command-following and output disturbance rejection properties of such a loop cannot be manipulated explicitly, these designs are usually acceptable nonetheless, at least for for minimum-phase plants [4]. The control loop transfer function ideally is very large at low

---

[1]The notation is established in Sections 4.4 and 4.5.

frequencies, passes smoothly through the crossover region, and attenuates rapidly at high frequencies.

To recover this target loop while using a state estimator, we choose $L = B$, and let μ be a free parameter in the filter design. It can be shown that $\lim_{\mu \to 0} \sqrt{\mu} H = BW$, where W is an orthonormal matrix, and eventually that as $\mu \to 0$, $K(s)P(s) \to G(sI - A)^{-1}B$. Here, H is the filter gain, $K(s)$ is the control transfer matrix, and $P(s) = C(sI - A)^{-1}B$ is the plant. Thus, we recover all of the robustness and performance properties that accompany the LQR loop.

4.3.2 Nonlinear Extension—Loop Operator Recovery

The idea of nonlinear loop-operator-recovery (LOR) is completely analogous to the LTR results above. We present here only one of three variations, since the other two (LOR at the plant output and formal loop shaping) require conditions that are overly restrictive [50].

The method calls for recovery of the controller loop. Thus, the control law itself can be designed with any technique, but the main requirement is that it yield a loop with good robustness and performance properties. If a nonlinear optimal solution is used, these properties have been found to be very good (see Section 4.5.2). As in the LTR situation, we then use a parameterized filter such that as the sensor noise intensity goes to zero, the full closed-loop system with the observer emulates the pure feedback system with perfect measurements. The crucial theorem is as follows:

Theorem[51]: Let the filter gain H_μ be parameterized by μ such that $\lim_{\mu \to 0} H_\mu \sqrt{\mu} = BW$, where W is some orthonormal matrix. If B is linear then $\lim_{\mu \to 0}(-K)(-P) = G\Phi B$, where P is the nonlinear plant operator, K is the control operator, and the nonlinear plant is ΦB.

In this theorem, the control law G may be nonlinear, time-varying, or could be a dynamical system itself. The generality of this result is very attractive, as it allows any nominally stabilizing controller to be used, and admits a wide range of observers. In all cases, nominal nondivergence of the estimator, and stability of the control law must be maintained.
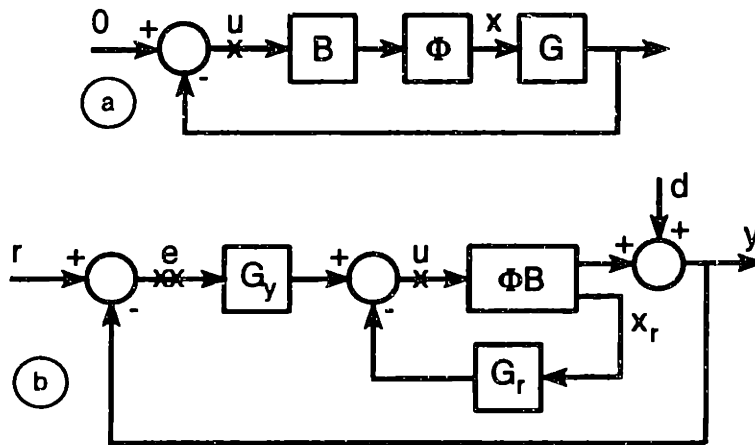
Figure 4-1: Limitations of the LQ servo.

4.3.3 Recovering the Regulator Loop

It is important to reiterate that this technique recovers not the filter loop, but the control loop. Thus, in the same way that LQR-loop recovery in the linear case is restrictive, the situation here is not ideal. Figure 4-1 gives a simple explanation of why recovering the control loop is so restrictive. Part a) gives the standard regulator loop, which, with LQR or nonlinear feedback designs, has good properties broken at the plant input (x). Part b) is an expanded version of a); we have broken the state vector into observed (y) and unobserved (x_r) parts. With the loop-breaking point (x) at the same spot in the overall loop, we see that the properties of the loop broken at the point (xx) are not the same. The latter location is important in terms of output disturbance rejection and command following. In short, we cannot get direct access to the output y, the variable upon which output disturbances, sensor noise, and reference signals act directly. Also, we must place our modeling uncertainty at the plant input, along with the disturbances.

In the absence of a better approach, we have to settle for designing the loop to meet robustness conditions at the plant input, and for taking whatever command-following and output disturbance rejection characteristics come with the loop. For minimum-phase linear systems, it has been found that the performance can be still quite good [4], and we expect a similar trend for the nonlinear case.

106

4.4 State Estimation

4.4.1 Kalman Filter

We outline the well-known linear observation problem to start, since most nonlinear observers are similar in form. The general n-state linear system is defined as

$$\frac{dx}{dt} = Ax + Bu + L\xi \qquad (4.1)$$
$$y = Cx + \theta,$$

where x is the $n \times 1$ state vector, u is the control input, and y is the observed output. A is the system matrix, B the input gain matrix, C the output gain matrix. The system is affected by process noise ξ, which acts through the gain matrix L and has intensity Ξ, and also by measurement noise θ of intensity Θ.

The Kalman Filter (KF) takes the form [44]

$$\frac{d\hat{x}}{dt} = A\hat{x} + Bu + H(y - C\hat{x}), \qquad (4.2)$$

for which the filter gain matrix H is computed off-line as $H = \Sigma C^T \Theta^{-1}$. The error covariance matrix Σ is the symmetric positive definite solution of the filter algebraic Riccati equation:

$$A\Sigma + \Sigma A^T + L\Xi L^T - \Sigma C^T \Theta^{-1} C\Sigma = 0. \qquad (4.3)$$

The solution Σ is guaranteed to exist if $[A, L]$ is stabilizable and $[A, C]$ is detectable; the standard technique today for solving algebraic Riccati equations involves a Schur vector decomposition [61].

The Kalman filter is known to be nominally nondivergent, and to be robust against uncertainties at the plant output [39]. However, it does not provide nondivergent estimation for nonlinear plants.

4.4.2 Extended Kalman Filter

Now we consider the generic nonlinear system

$$\frac{dx}{dt} = f(x) + Bu + L\xi \tag{4.4}$$

$$y = Cx + \theta,$$

where $f(\cdot)$ is a nonlinear operator, and the other variables are as described for Equation 4.1.

Solving the full optimal estimation problem [30] for nonlinear systems involves the real-time propagation of a partial differential equation, and the memory and computational requirements of such a technique are usually prohibitive, although the estimate provided is indeed nondivergent. These practical difficulties lead to suboptimal approximations, one of which is the Extended Kalman Filter (EKF). The EKF was developed as a direct extension to the Kalman Filter, and uses a nonlinear model with a time-varying filter gain matrix [44]:

$$\frac{d\hat{x}}{dt} = f(\hat{x}) + Bu + H(y - C\hat{x}), \tag{4.5}$$

$$H = \Sigma C^T \Theta^{-1}, \tag{4.6}$$

$$\frac{d\Sigma}{dt} = \nabla f(\hat{x})\Sigma + \Sigma \nabla f(\hat{x})^T + L\Xi L^T - \Sigma C^T \Theta^{-1} C\Sigma. \tag{4.7}$$

The parallels between these equations and those of the Kalman filter are obvious. For a long time, there was no theoretical justification for the EKF, although users recognized heuristically that it had very good properties. Grunberg [50] then showed that the EKF is in fact nondivergent under very broad conditions. In particular, we cite the following result:

Theorem [51]: Suppose $\mid \nabla f(x) \mid \leq B_f < \infty$ [2], and that $\Xi^{\frac{1}{2}}$ is positive definite.[3] Under these conditions, if there exists any nondivergent estimator for the nonlinear system, then the EKF is nondivergent.

Given that the EKF provides nondivergent estimates for a wide range of nominal nonlinear plants, one can investigate its other properties so that LOR can be carried out. For the current work, the asymptotic behavior of the gain matrix as the sensor noise goes to zero is

---

[2]This may be relaxed, leading to small-signal results.

[3]$\left(\Xi^{\frac{1}{2}}\right)^T \Xi^{\frac{1}{2}} = \Xi.$

most important, since we will be recovering the regulator loop, to be defined in Section 4.5. With $\theta = \mu I$, the condition we need is as follows:

$$\lim_{\mu \to 0} \sqrt{\mu} H_\mu(t) = LW(t), \tag{4.8}$$

where W is an orthonormal, time-varying matrix. The proof that this is the case for the KF and the CGEKF of the next section is well-known [60], but the EKF presents more of a difficulty, since the propagation of Σ is obviously dependent on the state estimate. To date, the asymptotic properties of the EKF are known only locally, that is, for initial Σ within a small neighborhood of the origin [106]. Nonetheless, it may be numerically verified that for many Lipschitz nonlinearities, the asymptotic behavior we need holds nonetheless for the EKF.

The EKF loop does carry some robustness properties also; they are analogous to those of the Kalman filter loop, and have been discussed by Grunberg [50]. The cost for all of the good attributes of the EKF is that it is somewhat laborious to propagate because the covariance matrix $\Sigma(t)$ has to be integrated forward in time. Although modern computers make it easier to use the EKF in real-time, there are many situations in which these demands are simply too great.

4.4.3 Constant-Gain Extended Kalman Filter

The Constant-Gain Extended Kalman Filter (CGEKF) [84], is a simplification of the EKF, as it avoids costly time integration of the covariance matrix Σ. In short, the CGEKF uses the known nonlinearities in propagating $\hat{x}$, but with a constant filter gain matrix H. H is usually chosen based on a nominal value of $\nabla f(x)$, which we call A. In a sense, the CGEKF is a hybrid between the EKF and the KF, as the filter gain is computed once according to Equation 4.3, and the state estimate propagates as in Equation 4.5.

A condition for the nondivergence of the CGEKF is the following:

Theorem[84]: If uniformly

$$(A - \nabla f(x))\Sigma + \frac{1}{2}(\Xi + \Sigma C^T \Theta^{-1} C \Sigma) > 0, \forall x \exists R^n \tag{4.9}$$

then the CGEKF is nondivergent with finite gain.

A similar condition has been provided by Tarn and Rasis [95]. Needless to say, these conditions must be checked for a range of operating points, since the robustness measures are with respect to the nominal linear design plant. If an uncertain linear element is placed at the plant output, the condition listed above yields infinite upward gain margin, 50 percent gain reduction tolerance, and at least 60 degrees of phase margin in every output channel. Thus, the CGEKF can be used in loop-operator recovery of the controller loop, but the nondivergence must be checked numerically throughout the operating range.

A critical shortcoming of the CGEKF is that there is *no robustness* to variations in the nonlinear plant. The model in Equation 4.5 must be exactly right. As a result, the dual LQR approach is pointless with the CGEKF.

4.4.4 Other Nonlinear Observers

This list of approaches (from Section 4.4.1 on) is by no means exhaustive, for there exist many other nonlinear observation techniques. The ones above are listed because they are among the simplest, and because they have some guaranteed nondivergence properties. This nondivergence with respect to a nominal nonlinear plant is crucial in the application of LOR. For some other observer ideas, the reader is referred to the survey paper by Misawa and Hedrick [68], and the references therein, as well as papers by Thau [96], Slotine et. al [91], and Bestle and Zeitz [17].

4.5 Full-State Feedback

We now consider the complementary problem to observation: feedback assuming perfect measurements. As in the LTR technique, the eventual properties of the nonlinear closed loop depend on either the estimator or the control law. Since our strategy is to recover the control loop, we pay special attention to the loop properties associated with these control laws.

4.5.1 Nonlinear State Feedback

The unperturbed nonlinear system is defined as follows:

$$\frac{dx}{dt} = f(x) + Bu. \tag{4.10}$$

110

Our problem is to find the control $u = -g(x)$ such that the cost function J is minimized:

$$J = \frac{1}{2} \int_0^T [x^T Q x + u^T R u] dt. \tag{4.11}$$

Of course, different cost functionals may be used, involving more complex combinations of x and u, and terminal constraints. We will keep the quadratic form, however, because it is a requisite for the main theorem we wish to use. Another constraint is that 4.10 is linear in the input; this point also is important for our method, and is consistent with the models in Section 2.7.

There are two parallel approaches for solving this optimization problem; dynamic programming and Pontryagin's Maximum Principle.

Dynamic Programming

The dynamic programming approach is due to Bellman [14]; in it, one defines the optimal return function as the cost associated with the optimal trajectory, beginning at some intermediate time t. For example, with the cost functional given by Equation 4.11, the optimal return is

$$V(x, t) = \min_u \frac{1}{2} \int_t^T [x^T Q x + u^T R u] dt. \tag{4.12}$$

The *Hamilton-Jacobi-Bellman* (HJB) equation provides the mechanism for minimizing $V(x, t)$ at each point along the way:

$$\frac{\partial V(x, t)}{\partial t} + \min_u \left[\frac{1}{2} x^T Q x + \frac{1}{2} u^T R u + \frac{\partial V(x, t)}{\partial x}(f(x) + Bu) \right] = 0. \tag{4.13}$$

with the terminal condition that $V(x(T), T) = 0$. The minimization is made by setting the derivative of the bracketed expression with respect to u, equal to zero. This step gives the control u as a function of $V(x, t)$, namely

$$u = -R^{-1} B^T \frac{\partial V(x, t)}{\partial x}^T,$$

which leads to another form of the HJB equation:

$$\frac{\partial V(x,t)}{\partial t} + \frac{1}{2}x^T Q x - \frac{1}{2}\frac{\partial V(x,t)}{\partial x}BR^{-1}B^T\frac{\partial V(x,t)}{\partial x}^T + \frac{\partial V(x,t)}{\partial x}f(x) = 0. \qquad (4.14)$$

Inspection shows that we have a partial differential equation to solve, and since $V(x(T), T) = 0$, it has to be solved backwards in time. In the limit as $T \to \infty$, however, the partial time derivative of $V(x,t)$ can be set to zero, as we expect it to approach some constant value toward $t = 0$. The remaining terms in this case form an algebraic matrix equation which has to be solved for $\frac{\partial V(x,t)}{\partial x}$ at all points on the optimal trajectory x_*. In practice, one could set up a grid in some region of the state space, and solve Equation 4.14 a priori for $\frac{\partial V(x,t)}{\partial x}$ at each point, storing the results. The construction of such a "look-up" table would require a way to store and access these data effectively [40].

Alternatively, Lukes [65] and Willemstein [103] developed a technique for solving the HJB equation by a power series expansion about the origin. Given analycity of f, they expanded the control u and the optimal return function $V(x,t)$, and with the HJB equation and a similar relation, showed that local convergence of the control law holds. This technique has been used effectively by many authors, including Dabbous and Ahmed [32] and Dwyer and Sena [41]. As with all perturbation techniques, sometimes an analytical solution can be achieved, but the numerical advantages are also significant in their own right.

Minimum Principle

Another way to formulate the optimal control problem involves Pontryagin's Minimum Principle. It begins with the definition of the Hamiltonian:

$$H(x, u, \lambda, t) := \frac{1}{2}x^T Q x + \frac{1}{2}u^T R u + \lambda^T(f(x) + Bu), \qquad (4.15)$$

where λ is the $n \times 1$ costate vector. The costate propagates according to

$$\frac{d\lambda}{dt} = -\frac{\partial H(x, u, \lambda, t)}{\partial x}^T, \text{ or}$$

$$\frac{d\lambda}{dt} = -\frac{\partial f(x)}{\partial x}^T \lambda - Qx, \qquad (4.16)$$

with the terminal condition that $\lambda(T) = 0$. The minimum of the Hamiltonian is found by

differentiating with respect to u, giving

$$\frac{\partial H}{\partial u} = u^T R + \lambda^T B = 0 \implies$$

$$u = -R^{-1} B^T \lambda. \tag{4.17}$$

Thus, the link between the dynamic programming approach and the minimum principle approach is that $\lambda = \frac{\partial V(x,t)}{\partial x}^T$, where λ is to be propagated backwards in time like V.

In the same spirit of the expansions of Lukes and Willemstein, Yoshida and Loparo [105] devised a perturbation technique to solve the optimal control problem in the context of the minimum principle. However, these authors were able to show not just local convergence of the power series for the control u, but global convergence. Starting from this expansion, we will describe a general framework for implementing approximately optimal nonlinear controllers in Section 4.6.

4.5.2 Properties of Optimal Nonlinear Control Loops

Optimal nonlinear control loops have nominal stability, tunable performance, and good robustness properties. First we define the operator Φ to take Bu to x as $\Phi := (s - f)^{-1}$, where s is the derivative operator. With this notation, the nonlinear system of Equation 4.5 can be written simply as $y = C\Phi Bu$.

To begin, the "return difference condition" of optimal controllers [70], [51] is that

$$\| (I + G\Phi B)^{-1} \|_{2,\tau} \leq 1. \tag{4.18}$$

where the control law is $u = -G(x)$. Simple manipulations from this point show also that

$$\| G\Phi B(I + G\Phi B)^{-1} \|_{2,\tau} \leq 2, \text{ and} \tag{4.19}$$

$$\frac{\| (I + (G\Phi B)^{-1})u \|_{2,\tau}}{\| u \|_{2,\tau}} \geq \frac{1}{2}. \tag{4.20}$$

Equation 4.18 clearly implies that the system is nominally closed-loop stable. In addition, Equation 4.20 provides stability-robustness as in the LQR case; for example, the presence
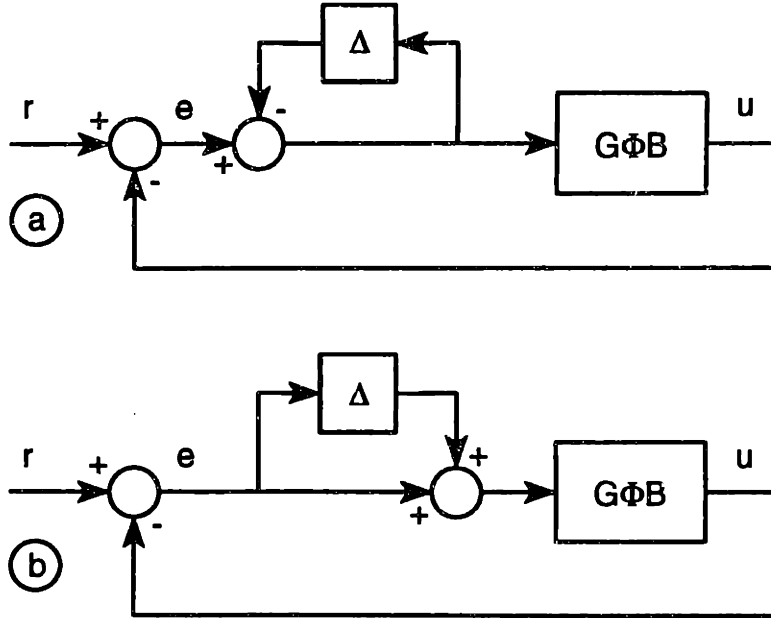
Figure 4-2: Two model uncertainty structures: a) pre-multiplicative, and b) pre-division.

of a multiplicative unstructured uncertainty Δ (see Figure 4-2) at the plant input can be tolerated so long as $\parallel \Delta \parallel_{2,r} \leq \frac{1}{2}$ [50]. Similarly, through Equation 4.18, a division error with $\parallel \Delta \parallel_{2,r} \leq 1$ can be tolerated. These margins are identical to those of LQR designs: 50 percent gain reduction tolerance, infinite upward gain margin, and 60 degrees of phase margin in all input channels [99]. However, it is noteworthy that these margins are all to be taken with respect to the nominal nonlinear plant.

Good performance is also provided by the nonlinear optimal regulator, and as in the LQR, the primary handle on performance is the control penalty ρ. A standard result is that stability with large gain implies good tracking performance:

Theorem[35]: Let **R** be a set of reference trajectories r of interest. If

$$\parallel (I + G\Phi B)^{-1}r \parallel_{2,r} << \parallel r \parallel_{2,r}, \forall r \exists \mathbf{R}, \text{ then } \parallel r - u \parallel_{2,r} << \parallel r \parallel_{2,r}, \forall r \exists \mathbf{R}.$$

In linear systems, the reference signals in **R** are generally of low frequency. For nonlinear systems, it is not so clear what is in **R**, although intuitively the signals still should be slow.

114

This theorem is consistent with the fact that integral action drives the steady-state errors to zero, even in nonlinear systems [34]. Furthermore, the optimal nonlinear control loop is insensitive to disturbances at the plant input, although the controller is obviously unable to distinguish between the disturbance and a change in the reference signal.

The optimal controller also possesses a parameterization similar to the LQR cheap control result, which makes it possible to recover the nonlinear filter loop in the dual LQR procedure [51]. Again, this thesis considers only recovery of the control loop.

4.5.3 LQR Designs

We now consider the application of a constant linear feedback law, as found through the LQR procedure. Namely, we let the feedback matrix be $G = \frac{1}{\rho} B^T K$, where K is the symmetric positive definite solution to the algebraic Riccati equation

$$0 = KA + A^T K + Q - \frac{1}{\rho} K B B^T K.$$

Safonov and Athans gave a condition for closed-loop finite-gain stability with nonlinear plants [83]; we must have uniformly

$$K(A - \nabla f(x)) + \frac{1}{2}(Q + \frac{1}{\rho} K B B^T K) > 0, \forall x \exists R^n. \tag{4.21}$$

This matrix is generally computed with respect to the nominal state linearization, $A = \nabla f(x_0)$. The condition may be massaged to reveal that the LQR control law has the 50 percent gain reduction tolerance, infinite upwards gain margin, and 60 degrees of phase margin in all input channels. In contrast to the margins of optimal nonlinear control laws, however, these apply to the nominal linear plant, so we are likely to lose this guarantee if the plant ventures far away from the nominal operating point.

4.6 Approximate Nonlinear Optimal Feedback by Perturbations

The above developments of other researchers indicate that the optimal nonlinear feedback law possesses attractive properties in terms of the recovered control loop. These include tunable performance and robustness at the plant input, with respect to a *nonlinear nominal*

plant, and so synthesis of such a control law with a nondivergent observer such as the EKF can be expected to yield good results through the LQR procedure. Thus, in the current section we present a framework for the analytical approximation of the optimal nonlinear feedback law.

A feedback controller for the cable problem of interest needs to have several specific attributes in order to be tractable. First, it is apparent that a *nondynamical* feedback law would be advantageous. Given the computational effort that is likely to be required for nonlinear observation, it makes sense not to have two dynamical systems running in software. Also, the control law should be computed in real-time, without resorting to large lookup tables. Solving the HJB equation a priori on a grid may be effective for low-ordered systems, but can be very difficult when the plant order is high, as in our cable models.

The perturbation method of Yoshida and Loparo [105] is suitable in that it leads to nondynamical, real-time control laws. The basic idea is to construct auxiliary vectors which are nonlinear functions of the state vector, and then find the appropriate matrices that take these new vectors linearly into the command signal. As will be seen in the sequel, however, these matrices are nontrivial to find; in the literature, one finds only examples of second- and third-order systems, for which these matrices can be worked out by hand. Clearly, for a nonlinear regulator to control a cable system, we must achieve the generality to construct the necessary matrices for plants of arbitrary order. This generalization of the perturbation method is presented in this section.

4.6.1   Foundations of the Perturbation Approach

Suppose $f(x)$ is analytic and can be written as

$$f(x) = Ax + \sum_{k=2}^{\infty} F_k x^{[k]}, \tag{4.22}$$

where A is the Jacobian of $f(x)$ evaluated at the origin. The vectors $x^{[k]}$ contain terms of order x^k, and are to be specified later, although it is apparent that the actual nonlinearity should be modeled as a polynomial series. We also assume that the costate λ is of the form

$$\lambda = \sum_{k=1}^{\infty} P_k x^{[k]}. \tag{4.23}$$

This formulation is completely dual to the Maximum Principle derivation of the LQR, and

gives rise to a perturbation-type technique for successively finding the matrices P_k. Yoshida and Loparo showed that this particular expansion has the following property:

Theorem [105]: Suppose that the unforced system of Equation 4.5 does not have a finite escape time. If, in addition, f is an analytic function of the state, $f(0) = 0$, and the set $[A, B, C]$ is controllable and observable, then the optimal regulator given by

$$u = -R^{-1}B^T \sum_{k=1}^{\infty} P_k x^{[k]} \qquad (4.24)$$

converges absolutely and uniformly on $[0, \infty]$, for any $x(0) \exists R^n$. This regulator also satisfies the HJB equation.

In the same paper, a necessary and sufficient condition for the optimal regulator to have a finite series expansion was derived, although it is usually difficult to verify.

We now outline the relevant expanded equations, to generate the optimal control law above. With an infinite horizon, $\frac{dP_k}{dt} = 0$, for all k. Then substituting Equations 4.22 and 4.23 into Equation 4.16 gives

$$0 = Qx + (A^T + \sum_{k=2}^{\infty} x_x^{[k]T} F_k^T) \sum_{k=1}^{\infty} P_k x^{[k]} + \sum_{k=1}^{\infty} P_k x_x^{[k]}(Ax + \sum_{k=2}^{\infty} F_k x^{[k]} - K \sum_{k=1}^{\infty} P_k x^{[k]}). \qquad (4.25)$$

where $K := BR^{-1}B^T$. The subscript "x" denotes the first partial derivative with respect to x, defined such that $f_x(x = 0) = A$. On collecting terms of like powers, we obtain the first-order equation as follows:

$$Q + A^T P_1 + P_1 A - P_1 BR^{-1}B^T P_1 = 0. \qquad (4.26)$$

The reader will notice that this is just the matrix algebraic Riccati equation. The LQR with a plant linearized at the origin can therefore be seen as an estimate of the loop shape before the nonlinear terms are added.

4.6.2 Obtaining the Higher-Order Matrices

From this point onward, we present the development specific to a plant with a symmetric cubic polynomial approximation (like quadratic drag), as a special case of the perturbation

117

expansion. Since this means that the even-powered terms disappear, and that we will not consider terms higher than third-order, some of the generality is lost at this point. Nonetheless, the derivations will indicate the nature of the calculations involved, and could serve as a basis for more general cases in which the plant order may be high.

First, it must be noted that the quadratic drag function is in fact *not* analytic, so that the convergence theorem above cannot apply formally to our underwater cable system. Although this might lead to some argument over the applicability of this approach to the cable problem, one has to remember that 1) quadratic drag itself is invalid near the origin, 2) we will not be carrying the infinity of terms required to reconstruct most analytic functions $f(x)$, and 3) we will not be carrying out full-state feedback. The point is that the nonlinearity can be approximated quite well with third-order polynomials in a given regime, obviously better than a linear drag model. Our goal in Chapter 5 will be to show results that make it worthwhile. For example, we expect that situations requiring a very large dynamic range will be served well by nonlinear feedback, as linearizations can be valid only locally.

Since we are considering odd functions, the matrix F_2 is zero and the $O(x^2)$ equation is

$$(A^T - P_1 K)P_2 x^{[2]} + P_2 x_x^{[2]}(A - KP_1)x = 0. \tag{4.27}$$

The unique solution is $P_2 = 0$; this can be verified numerically for any values of x. Following through, the $O(x^3)$ equation is found to be:

$$(A^T - P_1 K)P_3 x^{[3]} + P_3 x_x^{[3]}(A - KP_1)x + x_x^{[3]T} F_3^T P_1 x + P_1 F_3 x^{[3]} = 0. \tag{4.28}$$

The third-order equation above can be solved for all x provided that we are able to specify a matrix $T_{[3]}$ such that

$$z_x^{[3]}(A - KP_1)z = T_{[3]} z^{[3]}, \forall z \exists R^n, \tag{4.29}$$

and another matrix $X_{[3]}$ such that

$$z_x^{[3]T} F_3^T P_1 z = X_{[3]} z^{[3]}, \forall z \exists R^n. \tag{4.30}$$

118

4.6.3 Definitions and Relations in Matrix Calculus

We first need to define a few tools for matrix calculus. A good reference is Brewer [20].

I_n is an identity matrix of size $n \times n$. Let the elementary matrix $E_{ij}^{p \times q}$ be a $p \times q$ matrix with a one in the i-th row, j-th column element, and all other terms zero. Let A be a $p \times q$ matrix, and B be an $r \times l$ matrix. The *Kronecker product* [15] of A and B is the $pr \times ql$ matrix

$$
A \otimes B := \begin{bmatrix} a_{11}B & a_{12}B & \cdots & a_{1q}B \\ a_{21}B & \cdots & & \\ \cdots & & & \\ a_{p1}B & & & a_{pq}B \end{bmatrix}.
$$

Repeated Kronecker products are denoted by

$$
A^{\otimes k} := \underbrace{A \otimes A \otimes \cdots \otimes A}_{k \text{ times}}
$$

The $pq \times pq$ permutation matrix $U_{p \times q}$ is

$$
U_{p \times q} = \sum_{i=1}^{p} \sum_{j=1}^{q} E_{ij}^{p \times q} \otimes E_{ji}^{q \times p}.
$$

Example:

$$
U_{2 \times 3} = \begin{bmatrix} 1 & 0 & 0 & 0 & 0 & 0 \\ 0 & 0 & 1 & 0 & 0 & 0 \\ 0 & 0 & 0 & 0 & 1 & 0 \\ 0 & 1 & 0 & 0 & 0 & 0 \\ 0 & 0 & 0 & 1 & 0 & 0 \\ 0 & 0 & 0 & 0 & 0 & 1 \end{bmatrix}.
$$

The j-th column vector of a matrix A is denoted as $A_{*,j}$. Then the vectored representation of A [75], $vec(A)$, is given as

P.1	$B \otimes A = U_{r \times p}(A \otimes B)U_{q \times l}$
P.2	$(A \otimes B)(C \otimes D) = AC \otimes BD$
P.3	$vec(AB) = (B^T \otimes I_p)vec(A)$
P.4	$\frac{\partial'(AB)}{\partial z} = \frac{\partial' A}{\partial z}B + (I_n \otimes A)\frac{\partial' B}{\partial z}$
P.5	$\frac{\partial'(A \otimes B)}{\partial z} = \frac{\partial' A}{\partial z} \otimes B + (I_n \otimes U_{p \times r})\left(\frac{\partial' B}{\partial z} \otimes A\right)U_{l \times q}$

Table 4.1: Properties of Kronecker products and matrix calculus.

$$vec(A) := \begin{bmatrix} A_{*,1} \\ A_{*,2} \\ \vdots \\ A_{*,q} \end{bmatrix}.$$

We use the expression "$unvec(\cdot)$" to mean the unstacked form of the argument.

The formal derivative of a matrix with respect to a column vector z of length n is defined as follows:

$$\frac{\partial' A}{\partial z} := \sum_{i=1}^{n} E_i^{n \times 1} \otimes \frac{\partial A}{\partial z_i}.$$

It is important to note that this definition puts vector derivatives of vectors at variance with the normal definition, indeed with that of Equation 4.28. The two are related simply by $y_z = unvec\left(\frac{\partial' y}{\partial z}\right)$, and we shall keep this distinction in the sequel. The reason for not using equivalent forms is that manipulations with the formal derivative are clearer, as will be seen in the sequel.

Table 4.1 gives a number of properties that will be useful in our development. P.1 is due to Barnett [7], P.2 is due to Bellman [15], P.3 is due to Neudecker [75], and P.4 and P.5 are from Vetter [100].

4.6.4 Specification of $z^{[k]}$

The $O(z^k)$ vector $z^{[k]}$ in Equation 4.22 is taken to satisfy the implicit equation

$$z^{\otimes k} = \frac{1}{k!} \left[unvec \left(\frac{\partial'^k z^{[k]}}{\partial z^k} \right) \right]^T z^{[k]} = G^T z^{[k]}. \tag{4.31}$$

This may seem a rather odd definition, and in fact it is not unique. One solution that works is $z^{[k]} = z^{\otimes k}$; in this case, $G = G^T$, although it is not the identity.

Example: Let $n = 2$ and $k = 2$. Then

$$z^{[2]} = \begin{bmatrix} z_1 z_1 \\ z_1 z_2 \\ z_2 z_1 \\ z_2 z_2 \end{bmatrix}, \text{ and } G = \begin{bmatrix} 1 & 0 & 0 & 0 \\ 0 & \frac{1}{2} & \frac{1}{2} & 0 \\ 0 & \frac{1}{2} & \frac{1}{2} & 0 \\ 0 & 0 & 0 & 1 \end{bmatrix}.$$

The redundancy in $z^{[k]}$ can be eliminated by merging repeated combinations in the subscripts of the elements. We call a $z^{[k]}$ thus reduced a minimal representation of $z^{\otimes k}$. $z^{\otimes k}$ has length n^k, while $z^{[k]}$ has length $m := \begin{pmatrix} n+k-1 \\ k \end{pmatrix}$ [63].

We now show that if $z^{[k]}$ is a minimal form of $z^{\otimes k}$, then there is a unique scaling of the elements in $z^{[k]}$ such that

$$z^{\otimes k} = G^T z^{[k]} \implies z^{[k]} = G z^{\otimes k}. \tag{4.32}$$

This fact is important for our later specification of $T_{[3]}$. To show that this is true, we compute $GG^T z^{[k]}$ explicitly and then substitute. Let the operator $\partial'_{ij...}(\cdot)$ denote the repeated formal derivative of the argument with respect to z_i, then z_j, and so on. There are a total of k subscripts. We have

$$G^T z^{[k]} = \frac{1}{k!} \begin{bmatrix} \partial'_{11...}(z_1^{[k]}) & \cdots & \partial'_{11...}(z_m^{[k]}) \\ \vdots & & \vdots \\ \partial'_{nn...}(z_1^{[k]}) & \cdots & \partial'_{nn...}(z_m^{[k]}) \end{bmatrix} \begin{bmatrix} z_1^{[k]} \\ \vdots \\ z_m^{[k]} \end{bmatrix} = \frac{1}{k!} \begin{bmatrix} \sum_{j=1}^m \partial'_{11...}(z_j^{[k]}) z_j^{[k]} \\ \vdots \\ \sum_{j=1}^m \partial'_{nn...}(z_j^{[k]}) z_j^{[k]} \end{bmatrix},$$

$$\tag{4.33}$$

121

where the ordering of derivative subscripts is consistent with the definition of the formal derivative. In particular, the last subscript is changing slowly down the column in the right-hand side above. If $z^{[k]}$ contains no repeated combinations, then each summation above reduces to just one term. For simplification, let us define an operator $g(\cdot)$ which takes an integer into a k-tuple of integers defining the derivative. For example, $g(1) = \{1, 1, \cdots\}$ and $g(n^k) = \{n, n, \cdots\}$. In addition, let the sorting operator $s(\cdot)$ rearrange k-tuples of integers into ascending order. For instance, $s(1, 1, 2, 1) = \{1, 1, 1, 2\}$. Combining these observations and definitions into Equation 4.33, we find that

$$
GG^T z[k] = \frac{1}{(k!)^2}
\begin{bmatrix}
\partial'_{s(g(1))}(z_1^{[k]}) & \cdots & \partial'_{s(g(n^k))}(z_1^{[k]}) \\
\vdots & & \vdots \\
\partial'_{s(g(1))}(z_m^{[k]}) & \cdots & \partial'_{s(g(n^k))}(z_m^{[k]})
\end{bmatrix}
\begin{bmatrix}
\partial'_{s(g(1))}(z_{l_1}^{[k]}) z_{l_1}^{[k]} \\
\vdots \\
\partial'_{s(g(n^k))}(z_{l_{n^k}}^{[k]}) z_{l_{n^k}}^{[k]}
\end{bmatrix}.
\tag{4.34}
$$

We need two more indicial operators: let $f(\cdot)$ take a k-tuple of integers into an n-tuple of integers which give the multiplicity of terms in the argument. For example, if $n = 5$ and $k = 8$, then $f(1, 1, 2, 2, 1, 3, 4, 2) = \{3, 3, 1, 1, 0\}$. The number of *visually unique* permutations of a k-tuple, denoted $p(\cdot)$, is related to f as follows:

$$
p(\cdot) = \frac{k!}{\prod_{j=1}^{n} f_j(\cdot)!}.
\tag{4.35}
$$

Now we consider the i-th row of $GG^T z^{[k]}$. G_{ij} is nonzero if and only if $s(g(j)) = s(\iota(z_i^{[k]}))$ where $\iota(\cdot)$ is the index k-tuple.[4] The number of such occurrences in this row of G is precisely $p(\iota(z_i^{[k]}))$, and it is clear that these multiply with like-indexed terms in the vector $G^T z^{[k]}$. Therefore the value of the i-th row element of $GG^T z^{[k]}$ is

$$
\left[GG^T z^{[k]}\right]_i = \frac{1}{(k!)^2} p(\iota(z_i^{[k]})) \left(\partial'_{\iota(z_i^{[k]})} z_i^{[k]}\right)^2 z_i^{[k]}.
\tag{4.36}
$$

The derivatives in this equation are scalars, and if $z_i^{[k]}$ has associated with it a coefficient α_i, then

$$
\partial'_{\iota(z_i^{[k]})} z_i^{[k]} = \alpha_i \prod_{j=1}^{n} f_j(\iota(z_i^{[k]}))! .
\tag{4.37}
$$

---

[4]e.g., $\iota(z_1 z_3 z_2) = \{1, 3, 2\}$

Some cancellation then occurs in Equation 4.36, and we find that

$$\left[GG^T z^{[k]} \right]_i = \frac{\alpha_i^2}{p(\iota(z_i^{[k]}))} z_i^{[k]}.$$ (4.38)

Thus, if we set $\alpha_i = \sqrt{p(\iota(z_i^{[k]}))}$, then we have the result that

$$z^{[k]} = GG^T z^{[k]}.$$ (4.39)

Simple substitution of Equation 4.31 into this form gives the desired conclusion that

$$z^{[k]} = Gz^{\otimes k}.$$ (4.40)

To round things out, we also have

$$z^{\otimes k} = G^T Gz.$$ (4.41)

When $z^{[k]}$ is minimal and has the proper scaling, Equations 4.31, 4.39, 4.40, and 4.41 provide useful relations between $z^{\otimes k}$ and $z^{[k]}$. We see that $G^T G$ may not be the identity because $z^{\otimes k}$ has repeated terms. On the other hand, GG^T must be the identity because there are no repeated terms in $z^{[k]}$. A special case of our permissible $z^{[k]}$ is the lexicographic listing of Brockett [22], also used by Loparo and Blankenship [63] and Yoshida and Loparo [105]. As an example, for $n = 3$ and $k = 2$, the lexicographic vector is

$$z^{[2]} = [z_1^2 \quad \sqrt{2}z_1 z_2 \quad \sqrt{2}z_1 z_3 \quad z_2^2 \quad \sqrt{2}z_2 z_3 \quad z_3^2]^T.$$

From this point on, our developments incorporate this specific arrangement.

The lexicographic vector has a number of other interesting properties, including the following useful one:

Suppose $y = Ax$, where A is $n \times n$. Then the matrix equation $y^{[k]} = A^{[k]} x^{[k]}$ is satisfied by

$$A^{[k]} = GA^{\otimes k} G^T.$$ (4.42)

Showing this requires only a few operations: we have

$$
\begin{aligned}
A^{[k]}x^{[k]} &= GA^{\otimes k}G^T x^{[k]} \quad \text{by hypothesis,} \\
&= GA^{\otimes k} x^{\otimes k} \quad \text{by Equation 4.31,} \\
&= G(Ax)^{\otimes k} \quad \text{by P.2,} \\
&= Gy^{\otimes k} \quad \text{by } y = Ax, \\
&= y^{[k]} \quad \text{by Equation 4.40.}
\end{aligned}
$$

4.6.5 Solving for $T_{[k]}$

Now we finally address the problem of how to pick a matrix $T_{[k]}$ such that

$$
z_z^{[k]} Tz = T_{[k]} z^{[k]}, \tag{4.43}
$$

where $T = A - KP_1$ in the case of Equation 4.29. An important point is that

$$
\text{if } \frac{dz}{dt} = Tz, \text{ , then } \frac{dz^{[k]}}{dt} = z_z^{[k]} Tz, \tag{4.44}
$$

and following Brockett [21], one has

$$
\begin{aligned}
z(t + dt) &\simeq (I_n + dtT)z(t) \implies \\
z^{[k]}(t + dt) &\simeq (I_n + dtT)^{[k]} z^{[k]}(t) \implies \tag{4.45} \\
z^{[k]}(t + dt) - z^{[k]}(t) &\simeq \left[(I_n + dtT)^{[k]} - I_m \right] z^{[k]}(t) \implies \tag{4.46} \\
\frac{dz^{[k]}}{dt} &= \lim_{dt \to 0} \frac{1}{dt} \left[(I_n + dtT)^{[k]} - I_m \right] z^{[k]} \implies \tag{4.47} \\
T_{[k]} &:= \lim_{dt \to 0} \frac{1}{dt} \left[(I_n + dtT)^{[k]} - I_m \right]. \tag{4.48}
\end{aligned}
$$

This definition holds for arbitrary n and k. Thus, we have only to evaluate Equation 4.48 with $T = A - KP_1$ and $k = 3$ in order to get the matrix $T_{[3]}$ of Equation 4.29. With this notation, Equation 4.28 becomes:

$$
(A^T - P_1 K)P_3 x^{[3]} + x_x^{[3]T} F_3^T P_1 x + P_3 T_{[3]} x^{[3]} + P_1 F_3 x^{[3]} = 0. \tag{4.49}
$$

124

4.6.6 Specification of $X_{[3]}$

The remaining task now is to find a matrix $X_{[3]}$ such that Equation 4.30 is satisfied. The specification of $X_{[3]}$ is somewhat different than that of $T_{[3]}$, since the derivative $z_z^{[3]}$ is transposed, preventing us from using the derivative arguments above. A solution can be obtained nonetheless, and in this section we consider only the $k = 3$ case. As before, the nature of the required calculations for more general situations will be apparent.

First, we take three formal derivatives of Equation 4.30 and unstack to obtain

$$unvec\left(\frac{\partial'^3}{\partial z^3}\left[z_z^{[3]T}F_3^T P_1 z\right]\right) = 6X_{[3]}G, \tag{4.50}$$

Now the simplifying substitutions that $a := z_z^{[3]T}$, and $b := F_3^T P_1$ are invoked, and using Property P.4, we can expand out the left-hand side of Equation 4.50 as follows:

$$
\begin{aligned}
\frac{\partial'^3(abz)}{\partial z^3} =\ & \frac{\partial'^3 a}{\partial z^3}bz + \left(I_n \otimes \frac{\partial'^2 a}{\partial z^2}\right)(I_n \otimes b)\frac{\partial' z}{\partial z} + \\
& \frac{\partial'}{\partial z}\left(I_n \otimes \frac{\partial' a}{\partial z}\right)(I_n \otimes b)\frac{\partial' z}{\partial z} + \left(I_n \otimes I_n \otimes \frac{\partial' a}{\partial z}\right)(I_n \otimes I_n \otimes b)\frac{\partial'^2 z}{\partial z^2} + \\
& \frac{\partial'^2(I_n \otimes a)}{\partial z^2}(I_n \otimes b)\frac{\partial' z}{\partial z} + \left(I_n \otimes \frac{\partial'(I_n \otimes a)}{\partial z}\right)(I_n \otimes I_n \otimes b)\frac{\partial'^2 z}{\partial z} + \\
& \frac{\partial'}{\partial z}(I_n \otimes I_n \otimes a)(I_n \otimes I_n \otimes b)\frac{\partial'^2 z}{\partial z^2} + \\
& (I_n \otimes I_n \otimes I_n \otimes a)(I_n \otimes I_n \otimes I_n \otimes b)\frac{\partial'^3 z}{\partial z^3}.
\end{aligned} \tag{4.51}
$$

Since z has only the first derivative with respect to itself nonzero, and since a is $O(z^2)$, all but the second, third, and fifth terms on the right hand side above are zero. Using the properties P.1 and P.5 now to simplify Equation 4.50 further, we see more nice symmetry :

$$
\begin{aligned}
& 6X_{[3]}G = \\
& unvec\left[(U_{n \times n^3} + I_n \otimes U_{n \times n^2} + I_n \otimes I_n \otimes U_{n \times n})\left(\frac{\partial'^2 a}{\partial z^2} \otimes I_n\right)U_{m \times n}(I_n \otimes b)vec(I_n)\right].
\end{aligned} \tag{4.52}
$$

There is presumably a close relationship between $\frac{\partial'^2 a}{\partial z^2} \otimes I_n$ and G; it is a fact that with the current notation,

$$\frac{\partial'^{k-1}}{\partial z^{k-1}}(z_z^{[k]T}) = k!G^T. \tag{4.53}$$

This may be verified for arbitrary k by simply writing out the matrix expressions. Making this substitution into Equation 4.52 above, and invoking property P.3, we have (in stacked format) that

$$(U_{n \times n^3} + I_n \otimes U_{n \times n^2} + I_n \otimes I_n \otimes U_{n \times n})(G^T \otimes I_n)U_{m \times n}(I_n \otimes b)vec(I_n) \doteq (G^T \otimes I_n)vec(X_{[3]}). \tag{4.54}$$

The only remaining task is to get the two terms $(G^T \otimes I_n)$ to drop out. Since the first parenthetical expression on the left hand side of Equation 4.54 cannot be the identity, we must show instead that $(G^T \otimes I_n)$ has a left inverse. Using property P.2 and the fact that $CG^T = I_m$, it is easy to see that $(G \otimes I_n)$ does the trick:

$$(G \otimes I_n)(G^T \otimes I_n) = (GG^T) \otimes I_n = I_{mn}. \tag{4.55}$$

The final result is then that

$$vec(X_{[3]}) = (G \otimes I_n)(U_{n \times n^3} + I_n \otimes U_{n \times n^2} + I_n \otimes I_n \otimes U_{n \times n})(G^T \otimes I_n)U_{m \times n}(I_n \otimes b)vec(I_n), \tag{4.56}$$

which can be solved using straightforward matrix algebraic operations.

A direct investigation of Equation 4.30 indicates that for $k = 2, 3$ at least, we could also use

$$X_{[k]} = k \sum_{j=1,n+1,2n+1,\cdots}^{n^k - n + 1} \left[c_j^{j+n-1}(G) \right]^T b \left[c_j^{j+n-1}(G) \right]^T, \tag{4.57}$$

where $c_j^{j+n-1}(\cdot)$ means to take only the j-th through $j + n - 1$-th column of the argument. Arriving at this conclusion, however, requires a very large amount of inspection. The connection between Equation 4.57 and Equation 4.56 can be verified.

Now the solution for P_3 is at hand: Equation 4.28 reduces to

$$(A^T - P_1 K)P_3 + P_3 T_{[3]} + (X_{[3]} + P_1 F_3) = 0. \tag{4.58}$$

This is a standard equation in Sylvester form.

4.6.7 Discussion

This section has presented a technique for computing $T_{[k]}$ for arbitrary plant order and arbitrary k. In addition, we laid out the crucial machinery for finding $X_{[k]}$ under the same conditions; even though the solution was carried out for $k = 3$, Equation 4.56 is general in that when k changes, only the summation of U's changes. An important restriction of these developments is that they do *not* provide all the necessary tools for solving the $O(z^k)$ versions of Equation 4.25. An inspection of that equation shows that some other complicated terms arise even at $k = 4$; for example, one of them is $x_z^{[2]} F_2^T P_3 x^{[3]}$. Despite the inadequacy of the current methods to treat such situations, it is expected nonetheless that these problems will require only extensions of our techniques. This would be an excellent (although perhaps rather tedious) topic of further research.

This method of solution has the generality to treat plant models of arbitrary order. The user should keep in mind that although the matrix P_3 is of size $n \times m$, some of the intermediate matrices in the calculations can be extremely large. For example, Equation 4.56 requires the use of square matrices containing n^8 elements; this would be an unreasonable requirement for any n above five or so. Luckily, the heuristic form of Equation 4.57 has no such demands. The only required matrices are G, which is size $m \times n^3$, and b, of size $m \times n$. The largest remaining matrix in the algorithm is $A^{\otimes 3}$, which has n^6 elements. Depending on the hardware and memory available, the plant order can thus be relatively high, as will be demonstrated.

The matrix operations are relatively straightforward; the only nontrivial operation is solving the Sylvester equation (4.58). However, without going into the details, it has been found for the current work that the standard algorithms are completely adequate (e.g., [8]).

Another important design point is that polynomial approximations can be valid only in a neighborhood of the origin. Outside of this regime, the approximation and the true nonlinearity must diverge, which may give rise to instability or poor performance in the closed loop. More will be said about this issue in Chapter 5.

127

4.7 Design Example

The design technique outlined above is ideally suited to plants with "hardening" types of nonlinearity. A saturation nonlinearity, for example, is difficult to express as a low-order polynomial series. Our method, however, can accommodate unstable plants, and here are to be found the most dramatic differences between the nonlinear optimal control solution (referred to in the sequel as "NLQR") and the LQR. As a design example, we consider a plant based on the first-order models of Chapter 2, but incorporate a positive drag law, such that near the origin the drag forces are stabilizing, but away from it, they are destabilizing. The plant is described by:

$$
\begin{bmatrix} x_1' \\ x_2' \\ x_3' \\ x_4' \\ x_5' \\ x_6' \end{bmatrix} = \begin{bmatrix} |x_1|-1 & -2 & 0 & 1 & 0 & 0 \\ 1 & 0 & 0 & 0 & 0 & 0 \\ 0 & 1 & |x_3|-1 & -2 & 0 & 1 \\ 0 & 0 & 1 & 0 & 0 & 0 \\ 0 & 0 & 0 & 1 & |x_5|-1 & -1 \\ 0 & 0 & 0 & 0 & 1 & 0 \end{bmatrix} \begin{bmatrix} x_1 \\ x_2 \\ x_3 \\ x_4 \\ x_5 \\ x_6 \end{bmatrix} + \begin{bmatrix} 1 \\ 0 \\ 0 \\ 0 \\ 0 \\ 0 \end{bmatrix} u
$$

The polynomial approximation involves a linear plus a cubic part, and the coefficients for these terms can be found by least-squares minimization. The state penalty matrix Q is taken to be $C^T C$ with $C := [0 \ \ 0 \ \ 0 \ \ 0 \ \ 0 \ \ 1]$, $R = 1$, and the initial displacement error is one unit.

The LQR and NLQR algorithms alike are sensitive to the linearization (LQR) or domain of polynomial approximation (NLQR). For this reason, we first consider two designs with no model error, based on two speed regimes. In Figure 4-3 is shown the simulated response of the closed-loop system for speed envelopes of 0.7 (top) and 3.5 (bottom). The value of 0.7 is the maximum speed reached in the NLQR response; it is evident that when the envelope is minimized in this way, the LQR is the superior design. The cost integrals over twenty seconds are $J = 3.21$ and $J = 5.60$ for the LQR and NLQR responses, respectively. This may be regarded as a very good linearization from the point of view of the LQR, and a tenuous one for the NLQR, as any plant speeds outside the envelope access an inaccurate cubic drag in the control law.

One may extend the speed envelope to encompass all the motions that might be encountered, giving the NLQR a greater operating range. The effects of this design modification applied to the same plant are illustrated in the lower half of Figure 4-3. We observe that the NLQR response is largely the same as in the previous case ($J = 4.59$), but that the LQR suffers drastically, as linear damping cannot apply to the entire speed envelope. It is interesting, however, that rather than exhibiting instability, the LQR limits the response speeds to well within the regime of negative drag.

The issue of robustness provides another scenario for comparison of the LQR and NLQR. For example, the runs of Figure 4-3 have been repeated in Figure 4-4, with the following modeling errors incorporated in the design plant: 1) underestimation of mass by one-half, 2) overestimation of stiffness by a factor of two, and 3) underestimation of the "drag coefficient" by one-half, to be applied as $\frac{1}{2}(| z_i | -1)$. In the case of the 0.7 speed envelope, the LQR loop is unstable, while the NLQR leads to approximately the same result as before ($J = 2.77$). The NLQR performs well in the 3.5 speed envelope case as well ($J = 1.98$), and the LQR repeats the slow but stable response of Figure 4-3.

The effects of different envelope sizes, modeling uncertainties, and other topics are discussed further in Chapter 5, using experimental data. For the example of this section, it is apparent that the NLQR has a significantly larger range of operation than the LQR, and has improved robustness properties, as expected.

4.8   Proposed Synthesis Techniques

We have developed the necessary machinery for model-based, closed-loop control of finite-dimensional models of a towed cable system. The approaches are built upon the LOR technique for nonlinear control, and thus benefit from nonlinear estimators and control laws. The complete controller can be synthesized into numerous combinations; six of them are proposed for the towing problem:

1. Linear loopshaping.

2. LTR: LQR with KF

3. LOR: LQR with CGEKF.

4. LOR: LQR with EKF.
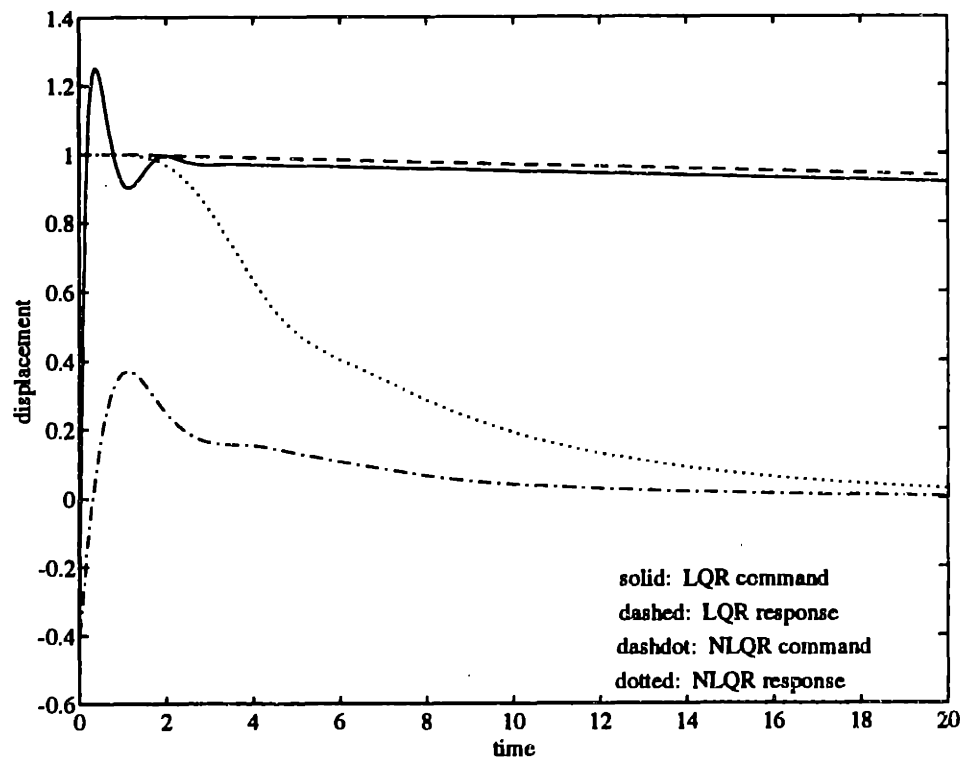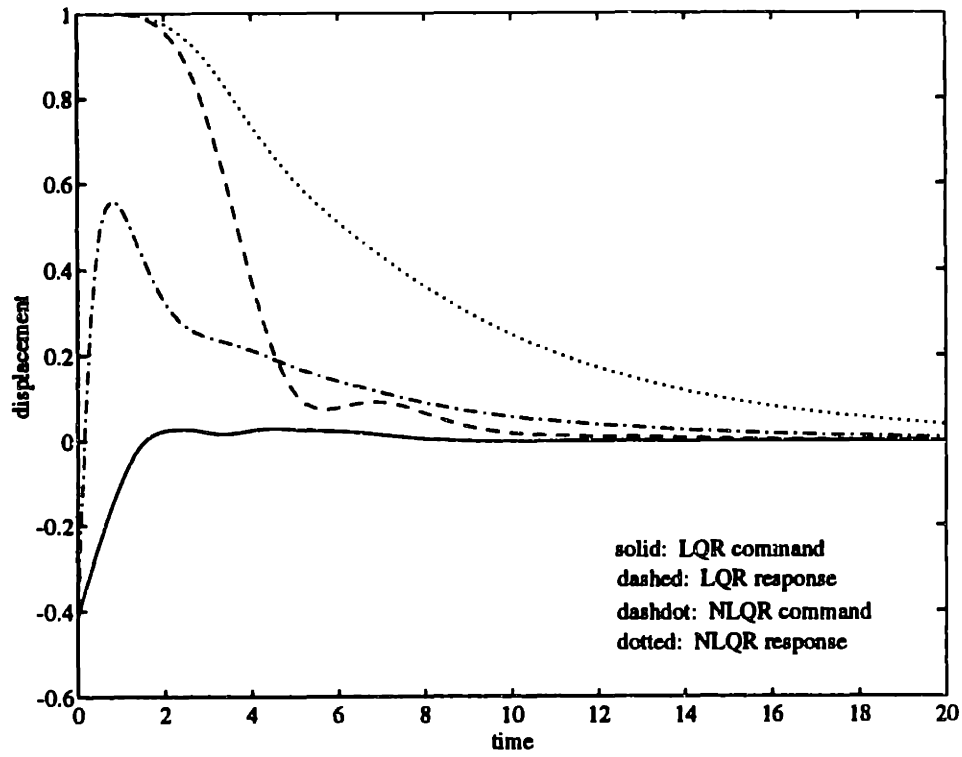
Figure 4-3: Simulations of LQR and NLQR responses for design speed envelopes of 0.7 (top) and 3.5 (bottom).
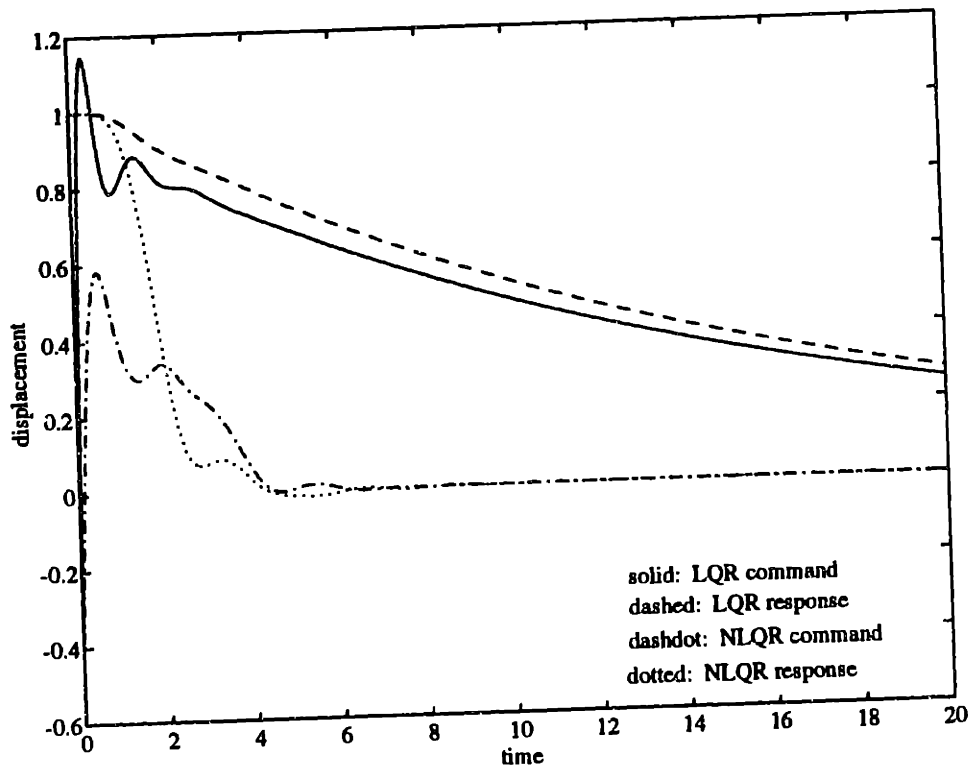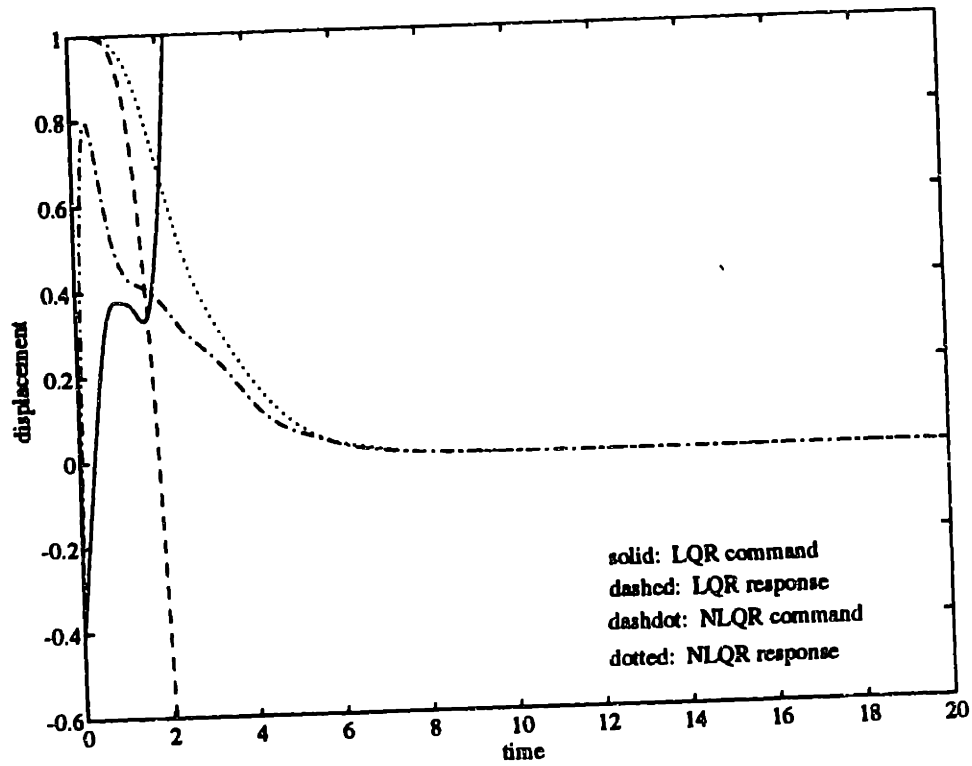
Figure 4-4: Simulations of LQR and NLQR responses for speed envelopes of 0.7 (top) and 3.5 (bottom), with modeling uncertainty.

5. LOR: Optimal nonlinear control with CGEKF.

6. LOR: Optimal nonlinear control with EKF.

Linear loopshaping (e.g. [38]) is to be considered because it is by far the easiest compensator to design for a SISO linear plant model. The LTR method can be expected to provide control nearly identical to that of loopshaping, but is computed nonetheless since its parameters are used directly in the nonlinear components which follow. The proposed nonlinear designs cover the range of possible combinations valid in LOR, and are listed in order of increasing computational requirements. As previously noted, the nonlinear optimal feedback law is denoted "NLQR" in the sequel.

Chapter 5

Closed-Loop Experiments

5.1 Introduction

In this chapter, we apply the theory of Chapters 3 and 4 in order to physically control scale models of two relevant physical systems. Since the plant is known to be naturally stable, the main emphasis is not on stability, but on the myriad of other properties to which the designs aspire. These include transient performance and long-term behavior, robustness, disturbance rejection, and many other points.

The physical systems, scaling procedure, and experimental apparatus are described first. Then some practical implementation issues are discussed, such as model identification and controller design and implementation. Experimental results in regulation and closed-loop tracking are provided for the scaled systems, and the general trends are discussed.

5.2 Experimental Setup

5.2.1 Specification of Two Nominal Full-Scale Systems

The model tests were scaled to study the behavior of two full-scale systems of interest. The first is a version of the *ARGO/JASON* system, which has a very slender cable and a significant clump weight. The second is a drilling deployment, which entails a very large, stiff pipe, and a comparatively small towfish at the lower endpoint. The physical parameters for these two nominal systems are given in Table 5.1.

	ARGO/JASON	Drill String
Vessel maximum speed	1 m/s towing	1 m/s towing
Vessel bandwidth	.02 rad/s	.02 rad/s
Cable diameter	1.73 cm	41 cm
Cable eff. mass	1.18 kg/m	378 kg/m
Cable weight in water	6.9 N/m	1118 N/m
Cable drag coefficient	1.6	1.6
Cable EI	878 $N \cdot m^2$[1]	76e6 $N \cdot m^2$
Depth	1000 m	1000 m
Towfish effective mass	900 kg	1000 kg
Towfish weight	6900 N	8000 N
Towfish area	1 $meter^2$	2 $meter^2$
Towfish drag coefficient	2	2

Table 5.1: Physical parameters for two nominal full-scale systems.

5.2.2 Laboratory Scale-Models

The nondimensionalization of the first-order lateral cable equations in Section 2.5.3 leads directly to a set of nondimensional par [PrinterError: out of paper]   ameters that must be maintain also [79]). They are repeated here:

$$k_1 = \frac{w_o}{(m + m_a)g},$$

$$k_2 = \frac{W}{L(m + m_a)g},$$

$$k_4 = \frac{W}{(M + M_a)g},$$

$$\epsilon = \frac{\rho C_d d^2}{2(m + m_a)}, \text{ and}$$

$$\varepsilon := \frac{\rho C_{dt} A_t d}{2(M + M_a)}.$$

It is noteworthy that the variable ε, which was not included in Chapter 2, is the ratio of nonlinear vehicle drag forces to vehicle inertial forces. In addition to these five parameters, the Reynolds number should be maintained through scaling, and the amplitude-to-diameter ratio should be kept large. These steps ensure that we are not working with two drastically different flow regimes. In addition, the bending stiffness parameter of Section 2.2.3 should

134

be small for both the full-size and the scaled systems.

A test rig was built at the Coastal Research Laboratory of the Woods Hole Oceanographic Institution to carry out the scale-model tests. The physical arrangement is shown in Figure 5-1. An I-beam across the surface of the 3.3-meter-deep test tank was fitted with a rolling carriage, which served as the upper endpoint for the cable in the water, and was positioned through a chain drive and motor, controlled from a personal computer. The carriage position was tracked using the resolver in the motor, and the lower endpoint of the cable was fitted with a small acoustic transducer. This transducer communicated with a short-baseline acoustic net in the 300 kHz range, mounted in the test tank.

The first experimental setup was designed to approximate the *ARGO/JASON* full-scale system. For the cable, the coaxial link from the transducer to the surface was adequate, and the transducer alone gave a good approximation of the *ARGO/JASON* towfish. Table 5.2 shows how well the scaling held. As required, the bending stiffness was kept small, the Reynolds number was in the same flow regime as the full-scale system, and the amplitude-to-diameter ratio was high.

The second experimental setup was a scaled version of the full-scale drill-string system. In this case, the much larger diameter and weight required the use of half-inch Tygon tubing, with two 3.2-millimeter wire ropes and the coaxial cable inside for mass and weight. In order to eliminate the significant in-water weight of the transceiver at the bottom (0.57 Newtons), foam flotation was added at the bottom of the cable. This foam introduced significant frontal area and added mass to the transducer, but made the overall scaling in the cable itself much better. In other words, we could achieve good scaling in the cable *or* at the endpoint, but not both; the former was chosen for this work. In Table 5.2, we see that the parameters k_4 and ε are in significant error.

Another important note is that flow around a full-scale drill string may be supercritical at one meter per second, while in the test tank, we were unable to match this regime because of velocity constraints. In supercritical flow, such a pipe could have a substantially reduced drag coefficient, especially if its surface is smooth [81]. This scaling disparity may or may not be significant from a practical control systems point of view, and it was decided to use the scale model as described above, given the difficulty of matching all the nondimensional parameters. In the experiments which follow, however, we do consider the case where the modeled drag terms are overestimated by a factor of three.
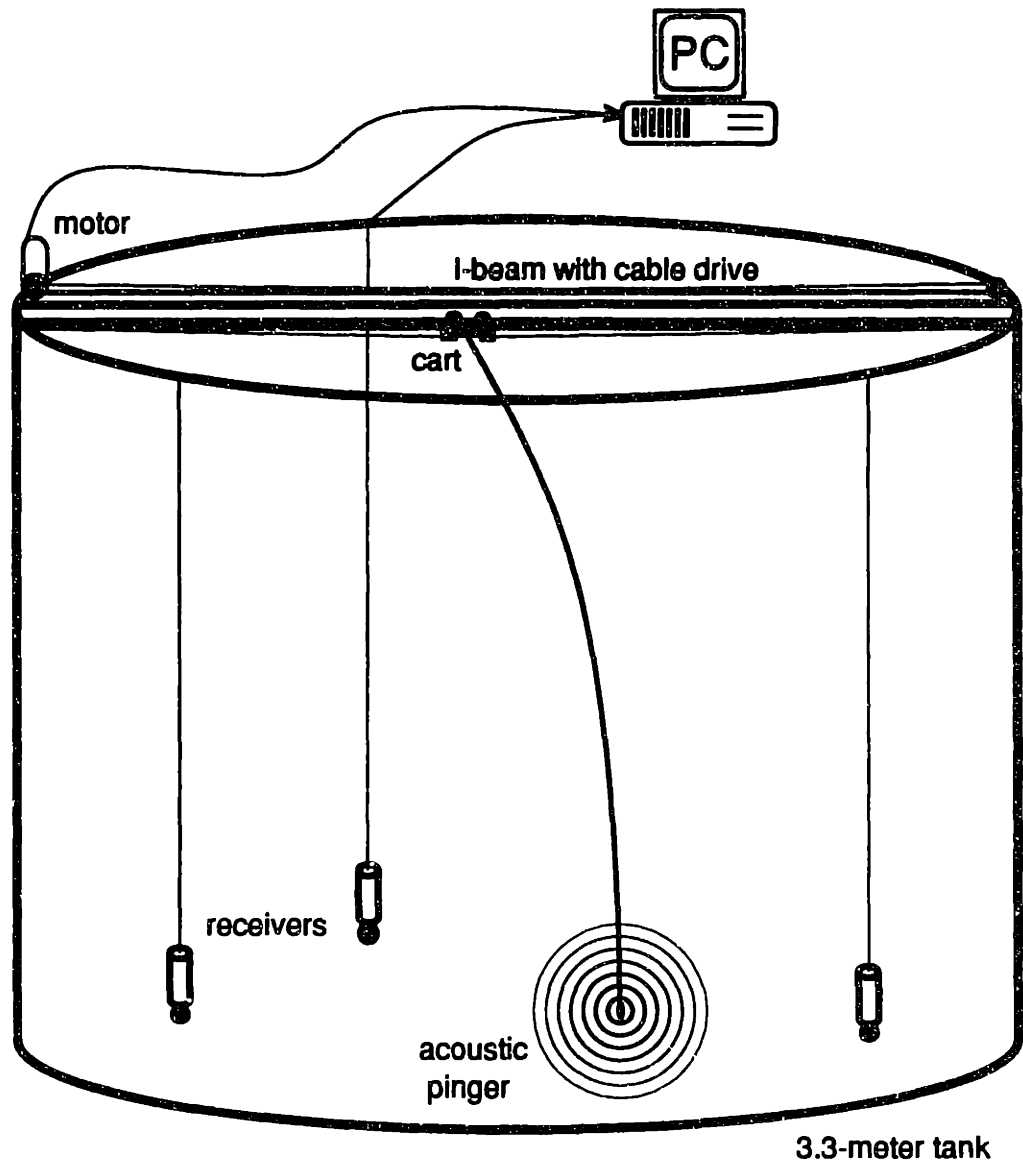
Figure 5-1: Schematic view of the WHOI test tank.

	ARGO/JASON	Scale A/J	Drill String	Scale DS	J. de Fuca
k_1	.59	.59	.30	.27	.64
k_2	.60	.79	.0022	.0017	.21
k_4	.78	.73	.82	.014	.75
ϵ	.21	.21	.36	.37	.16
ε	.020	.027	.83	.22	.0022
$\frac{EI}{(w_oL+W)L^3}$	7.5e-9	4.0e-5	2.1e-5	2.2e-4	1.1e-10
Re	1.3e4	1.8e3	3.1e5	9.8e3	4.9e3
A/d	5.8e3	4.2e2	2.5e2	7.9e1	1.6e4

Table 5.2: Scaling for model tests.

With regard to the lateral motions themselves, since the ratio of excitation to diameter was small for both the full-scale and model systems, the important nondimensional variable became the angle θ. As $\frac{L}{d}$ was at least an order of magnitude smaller in the test tank than in the full-scale systems, preserving θ meant that the angle ϕ had to be that much larger in the test tank. Thus, a one-meter excursion in the test tank corresponds to approximately thirty-three meters for the full-scale drill string, and just seven for the *ARGO/JASON* system. In addition, the full-scale frequencies correspond with model frequencies approximately twenty times as fast. Thus, a vessel with a DP bandwidth of 0.05 radians per second implies an upper frequency limit of one radian per second in the test-tank.

Vertical excursions of the towfish were not scaled accurately in our test tank, since we only scaled the first-order cable equations, which entail no vertical coupling.

The full listing of physical parameters for the scale experiments of this thesis is given in Table 5.3.

5.2.3 Dividing the Systems

Table 5.2 indicates a significant physical difference between an *ARGO/JASON*-type deployment and a drill string deployment. In particular, the fraction $\frac{k_2}{k_1}$, which is the the ratio of towfish weight to the weight of the cable, differs by two orders of magnitude. In practical terms, this means that the cable shape for a towed ROV system is dominated by the weight of the towfish, and the cable is generally concave downwards. For a drill string, the lower portions of the pipe have decreasing resistance to drag forces because of the small tension; the end of the pipe is comparatively free to "whip." As a result, the shape of a towed drill

	Scale A/J	Scale DS
Maximum towing speed	1 m/s	$\Longleftarrow$
Maximum excursion	3.5 m	$\Longleftarrow$
Cart tracking	motor resolver	$(\sigma \simeq .1 \text{ mm})$
Actuation bandwidth	3 rad/s	$\Longleftarrow$
Cable material	2.4 mm coax	12.7 mm Tygon with steel wire
Cable effective mass	.022 kg/m	.353
Cable weight/length in water	.13 N/m	.92
Nominal cable C_d	1.6	1.6
Depth	2.74 m	$\Longleftarrow$
Towfish	transceiver .57 N weight	transceiver and foam, .05 N
Towfish effective mass	.080 kg	.15
Towfish area	9 cm^2	25
Nominal towfish C_d	2	2
Towfish tracking	acoustic	$(\sigma \simeq 1 \text{ mm})$
Sample rate (no computations)	0.22 seconds	$\Longleftarrow$
Sample rate (computations)	0.275 seconds	$\Longleftarrow$
Pure delay	$\simeq 0.5$ seconds	$\simeq 1.6$

Table 5.3: Physical parameters for WHOI test tank experiments.

string is usually concave upwards.

These two systems differ not only in their physical structure, but also in their usual operation. A towfish which is part of an ROV system often has a tether of length fifty or more meters connecting it to the ROV, so high accuracy positioning is not crucial. As a sensor platform, however, the towfish may be required to follow predetermined tracklines. The drill string presents a different operational need: there is usually no requirement for trajectory-following, but regulation of the endpoint position is crucial.

The fact that these two full-scale plants are so different in terms of their physical response suggested experimental tests with two scaled systems. For example, it was unclear what the effects of endpoint whipping would be on closed-loop stability. At the same time, the *operational* differences pointed to a natural division between the types of experiments to be conducted. In the data of this chapter, we therefore present regulation runs for the scaled drill string system, and trajectory-following runs for the scaled ROV system. This division limits the results for each system, although it has been verified that the drill string motions can be successfully preshaped, and that regulation with the ROV system can be very good also.

5.3 Practical Issues

5.3.1 Drag Coupling and Polynomial Approximation

The restriction of cable motions to a single plane is unrealistic because physical disturbances act in all directions, and because we may want to follow reference trajectories with turns or curves. The first-order three-dimensional equations are coupled only through drag, and the drag force coupling of Equation 2.38 indicates that motions in one plane tend to increase the effective drag seen in the other plane. For this reason, one would not expect dramatic changes in performance if the in-plane and out-of-plane control problems were addressed separately using the techniques discussed so far. Indeed, if linear techniques are used, then one sees this procedure immediately, since a linear drag law has no coupling. Technically, this makes the problem multi-input/multi-output, although it is clear that the two subsystems are completely separate, and SISO loopshaping can be used.

Incorporation of the drag coupling is not difficult in the context of our nonlinear approaches. In Safonov's theorems for nominal nondivergence of the CGEKF (Equation 4.9)

and stability of the LQR (4.21), the drag coupling leads to slightly different tolerances, but the bounds are roughly the same as in the single-plane case. The EKF maintains its robustness properties as well, so long as the estimator model contains the coupled forces.

The drag coupling may be easily included in the nonlinear optimal approximation of Section 4.6. The key is to modify the formulation for F_3 so that the appropriate coupling is achieved; the rest follows easily within the framework of the chapter. Toward this end, perhaps the easiest way to generate the coefficients is to carry out a least squares fit for grid points on a subset of the $x - y$-plane. For example, for points over a disc of unit radius, one obtains:

$$x\sqrt{x^2 + y^2} \simeq 0.3413x + 0.6896x^3 + 0.6865xy^2,$$

leading to a maximum difference between the functions of 0.033, with an RMS error of 0.012. In the best-fit linear approximation, an x-coefficient of 0.7963 gives a maximum error of 0.19 and an RMS error of 0.081. For the in-plane case, we have

$$x \mid x \mid \simeq 0.3040x + 0.7493x^3,$$

with a maximum error of 0.029 (0.018 RMS). The coefficient in the linear case is 0.7308; the maximum error is 0.21, with an RMS value of 0.11. In general, it is apparent that the higher-order approximation improves the overall accuracy by a factor of six, roughly.

5.3.2   System Identification

The two scaled systems were modeled by minimizing the open-loop simulation error [55], as discussed in Section 2.6. The input data set used to create the I/O data was generated through the following technique:

1. A random series with a Gaussian probability density, zero mean, and unity variance was padded with zeros at the start and the end.

2. The series was filtered using a second-order digital Butterworth filter, with a cutoff frequency at three radians per second. This frequency scales to 0.15 radians per second, and was well within the bandwidth of the apparatus.

3. An absolute multiplier was applied to the series so that the full dimensions of the tank were utilized.

4. The maximum velocity was checked so as to not exceed the capabilities of the apparatus. This speed, about one meter per second, corresponds to approximately 1.65 meters per second for the full-scale drill string system, and 0.35 meters per second for the full-scale ROV system.

The weight terms were calculated beforehand, leaving the cable and endpoint drag, and the cable and endpoint effective mass as unknowns to be identified; then system identification was carried out as described in Chapter 2. The performance of two- and four-node models for the scaled drill string system are shown in Figure 5-2; the four-node model is clearly superior.

5.3.3   Quantification of Modeling Errors

The models generated by the above method come with no quantitative measures of goodness that are useful for control. Since the robustness properties for optimal controller loops are known (see Section 4.5.2), we now consider the problem of quantifying the uncertainty operator Δ. In particular, the fundamental measure of the uncertainty is the L_2-gain of Δ.

The gain of a nonlinear operator usually must be found from actual response (simulation or physically obtained) data, although clearly no amount of experimenting can guarantee that the maximum value has been found. This is in contrast to a linear operator $\hat{G}(\omega)$, for which the L_2-norm of the output is related to the L_2-norm of the input by

$\| \hat{G}(\omega) \|_\infty \| u(t) \|_2$ [38]. It has been typical in the literature to estimate the gain of nonlinear operators by forcing them with swept-sine inputs of various amplitudes. While this approach obviously does not yield much information about the gain during transients, like the describing function technique with harmonic excitation it aspires to cover all of the regimes through which an unstable, oscillatory trajectory could pass. For this reason, we consider only swept-sine wave signals as inputs in this section.

Another difficulty is that the operator we are interested in is located at the plant input, consistent with our recovery of the controller loop. As a result, we cannot compare the output of our model with the output of the actual plant for a given input and get useful numbers. We require a completely new computational approach. Inspection shows that the
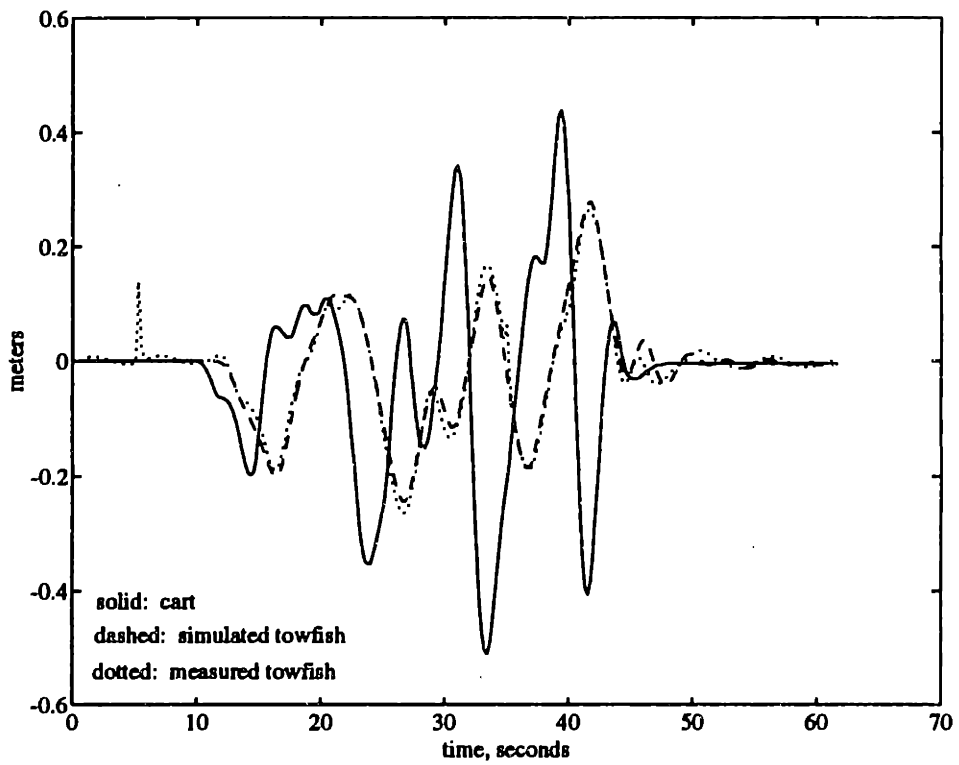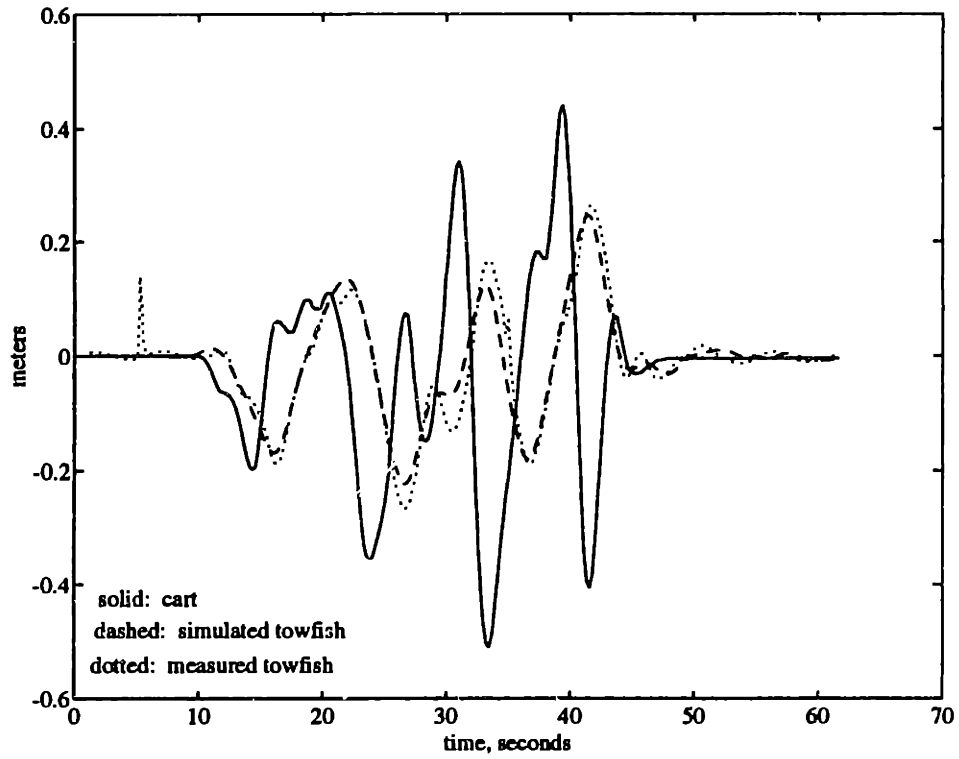
Figure 5-2: Identification of two-node (top) and four-node (bottom) models for the scale drill string system.

142

uncertainty operator Δ (see Figure 4-2) can be expressed in terms of the actual plant G_a, and the nominal plant G_n, for pre-multiplicative and pre-division uncertainty structures, as follows:

$$\Delta = G_n^{-1} G_a - I : \text{pre-multiplicative} \qquad (5.1)$$

$$\Delta = G_a^{-1} G_n - I : \text{pre-division}. \qquad (5.2)$$

It is apparent that G_n^{-1} can be calculated using our dynamic inversion scheme of Chapter 3, and G_a can be found by high-order simulation or actual experiments. This immediately gives us a way to quantify $\| \Delta \|_{2,\tau}$ *explicitly*, for a pre-multiplicative structure. A procedure for calculating it is outlined as follows.

1. It was shown in Section 2.5.4 that the plant gain increases monotonically as the excitation amplitude decreases, and might become quite large for small excitations. $\| \Delta \|_{2,\tau}$ also might be quite large in this regime, so a lower limit of excitation amplitude should be picked, below which the plant response is inconsequential.

2. Generate an input signal u that satisfies the lower bound and covers the relevant frequency range. A swept-sine signal with sections at different amplitudes would be an effective choice.

3. Drive the plant or a high-order model (G_a) with this u. The output is $y := G_a u$.

4. Solve the inverse dynamics for y, yielding $\hat{u} := G_n^{-1} G_a u$. Thus $\hat{u} - u = \Delta u$.

5. Define a "notching" operator $n_\omega(u)$ whose support is confined to a single period of oscillation, the frequency being ω. Thus, $u_t := n_\omega(u)$ is a truncated version of u, whose tails outside a single period are set to zero. Similarly, let $\hat{u}_t$ be a version of $\hat{u}$ with the same tails set to zero. Then we have the estimate $\hat{u}_t - u_t \simeq \Delta u_t$, and

$$\| \Delta \|_{2,\tau} \simeq \max_\omega \frac{\| \hat{u}_t - u_t \|_{2,\tau}}{\| u_t \|_{2,\tau}}. \qquad (5.3)$$

Clearly, the above calculation is accurate only if the rate of change of frequency in the swept sinusoid is slow enough to accommodate nearly steady-state plant responses.
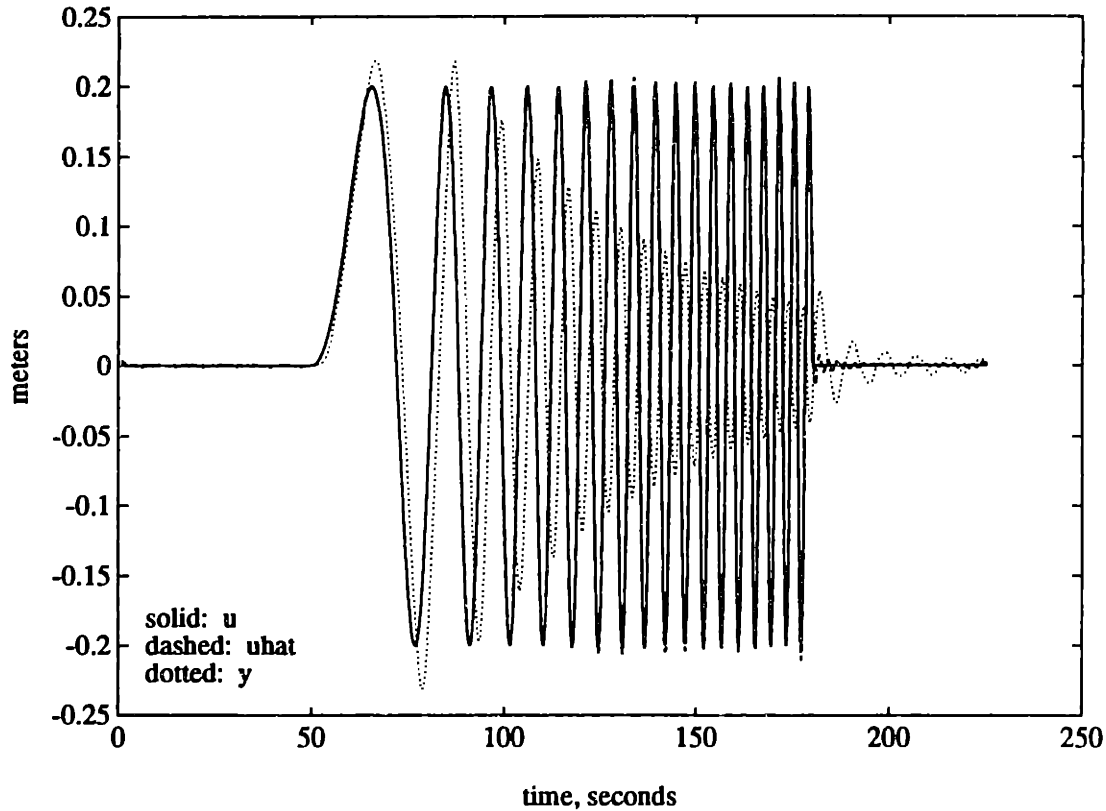
Figure 5-3: Verification of dynamic inversion scheme for calculation of Δ.

The notching operator is useful because the gains are computed for complete periods of oscillation.

First, we give an illustration that the inversion scheme is up to the task by letting $G_n = G_a$ for the scaled drill-string system. As outlined above, the swept-sine input u was run through G_a, then y through G_n^{-1} . Figure 5-3 shows u, $\hat{u}$, and y; the plant has clearly been inverted properly, as the difference between u and $\hat{u}$ is almost imperceptible.

Swept-sine inputs and experimental responses for the scaled drill string system are given for full-scale amplitudes of one, two, five, and ten meters, for full-scale frequency ranges between .01 and .1 radians per second, in Figure 5-4. An example inversion for the third graph of Figure 5-4 is shown in Figure 5-5, demonstrating the usual deterioration of model accuracy as the frequency increases. It is intuitive that small variations in the experimental towfish response can lead to large variations in $\hat{u}$; since the forward system is a low-pass filter, we expect the inverse system to amplify high-frequency inputs to some degree.

144

Excitation: .031m (1m)

Excitation: .063m (2m)

Excitation: .156m (5m)

Excitation: .313m (10m)
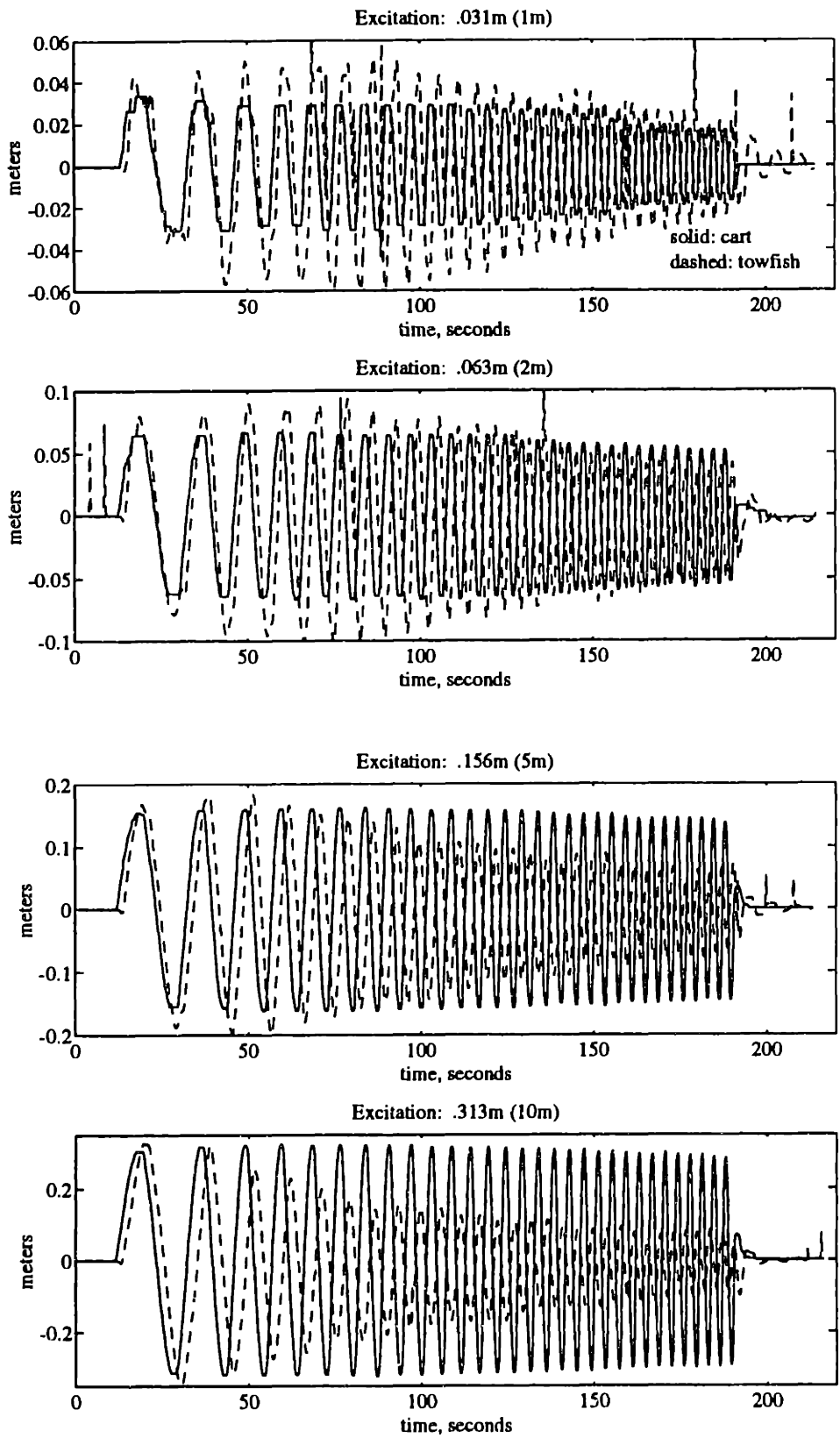
Figure 5-4: Swept sinusoid experiments with the scaled drill string system.
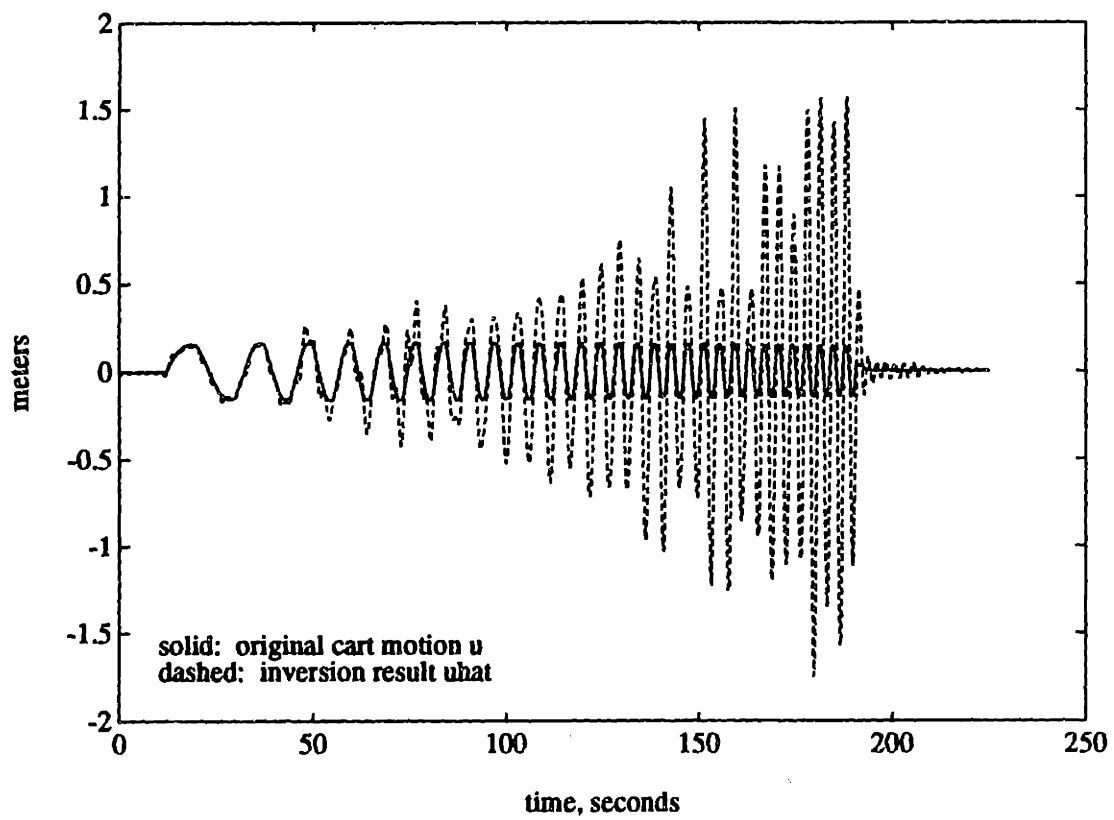
Figure 5-5: Example of u and $\hat{u}$ for experimental G_a.
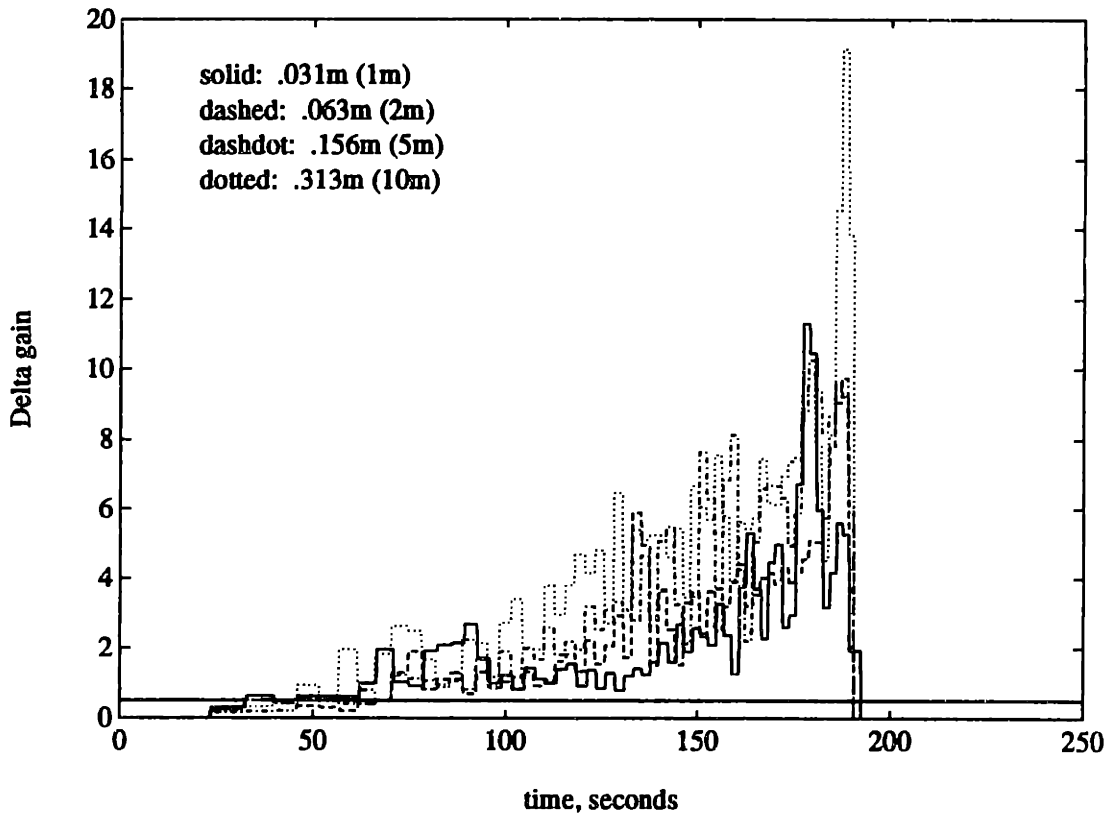
Figure 5-6: Gains of uncertainty operator as a function of frequency.

Once the inversions are completed for the range of amplitudes, the L_2 gain of Δ may be computed according to Equation 5.3, for the various frequency regimes. These frequency-dependent gains are plotted for the scale drill string system, in Figure 5-6. Since by Section 4.5.2, closed-loop stability of the nonlinear optimal control loop is guaranteed when $\| \Delta \|_2 \leq \frac{1}{2}$, we see that the modeling errors are acceptable below an excitation frequency of approximately 0.5 radians per second.

5.3.4   Controller Design

The crossover frequency for the nominal linear design should be selected in a manner consistent with the actuation limits, and so that the basic guidelines of loopshaping and LTR are followed. Typically, these pertain to a smooth loop transfer function with reasonable phase loss in the crossover region, and a stable compensator. For the scale drill string system, the maximum crossover is approximately 0.2 radians per second, which compares well with

the modeling error analysis above, and the first natural mode of the scaled plant located at about 0.8 radians per second.

For a given plant model, and speed envelope, an entire family of compensators can be constructed as follows. The loopshaping and LTR controllers are first designed to the same specifications, and the nonlinear designs are obtained through straightforward extensions:

1. The gain matrix H from the KF is used in the CGEKF.

2. The process noise gain matrix L for the EKF is set to B, and the sensor noise μ is the same as that used in the LTR design.

3. The nonlinear optimal controller utilizes the same value of ρ as in the LTR design, and has $Q = C^T C$.

Thus, the LTR forms the link between the basic characteristics of the loopshaping design, and the parameters for the nonlinear components in the more complex controllers. An example LTR design loop transfer function is shown in Figure 5-7; the linearization speed for this case is 0.2 meters per second.

5.3.5 Formal Properties of the CGEKF and LQR

In Chapter 4, it was noted that the CGEKF and LQR can be applied to some nonlinear systems with guaranteed results [82]. In general, we must satisfy a bound on the size of the discrepancy between A for the linearized system, and ∇f for the nonlinear system. The conditions are to be checked through the operating regime. Figure 5-8 gives an indication of how these hold for the scaled drill string system for the plant model and controller design of Figure 5-7, in the presence of quadratic drag, with a linearization speed of 0.1 meters per second. For each speed value on the abscissa, actual nodal speeds are taken as uniformly random numbers between fifty percent and one-hundred-fifty percent of the speed on the axis. Overall, we see that the conditions are generally met above the linearization speed, but not below it. Hence, *the only way to obtain guaranteed properties from the CGEKF and LQR with respect to the drag nonlinearity is to set the linearization speed extremely low.* This requirement usually has the effect of slowing down the transient response of the closed-loop system, as will be verified.
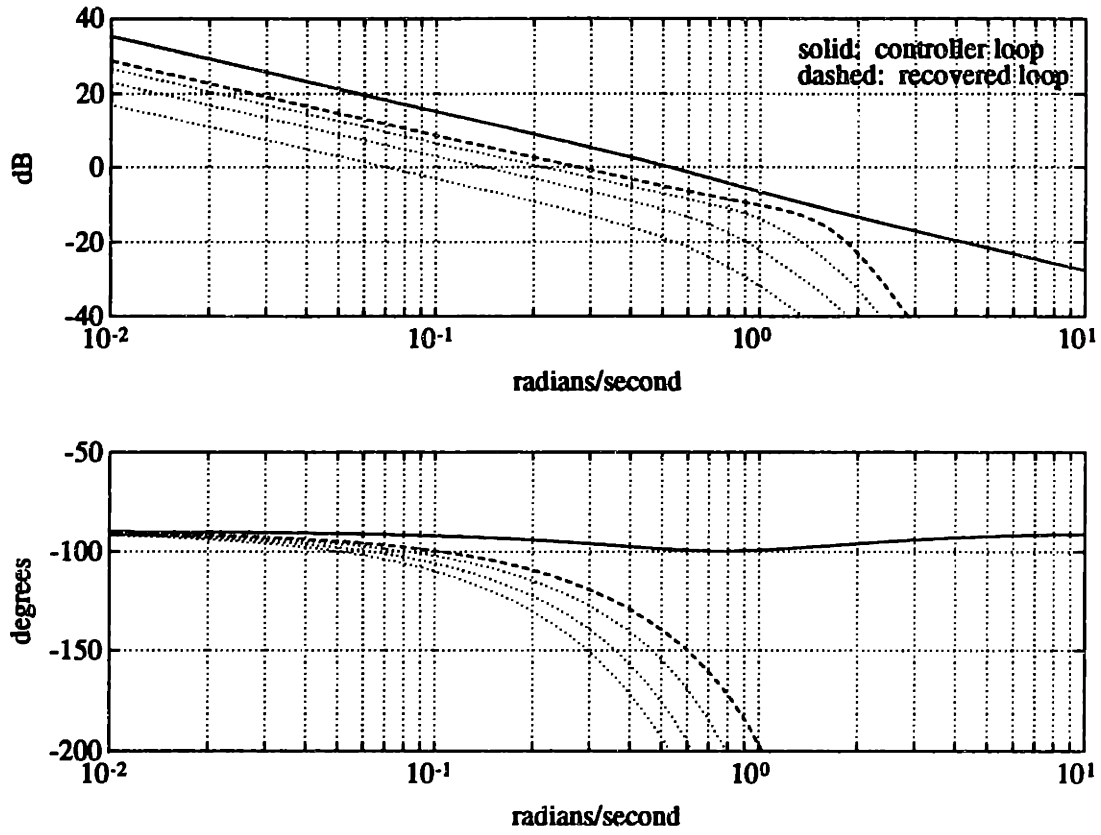
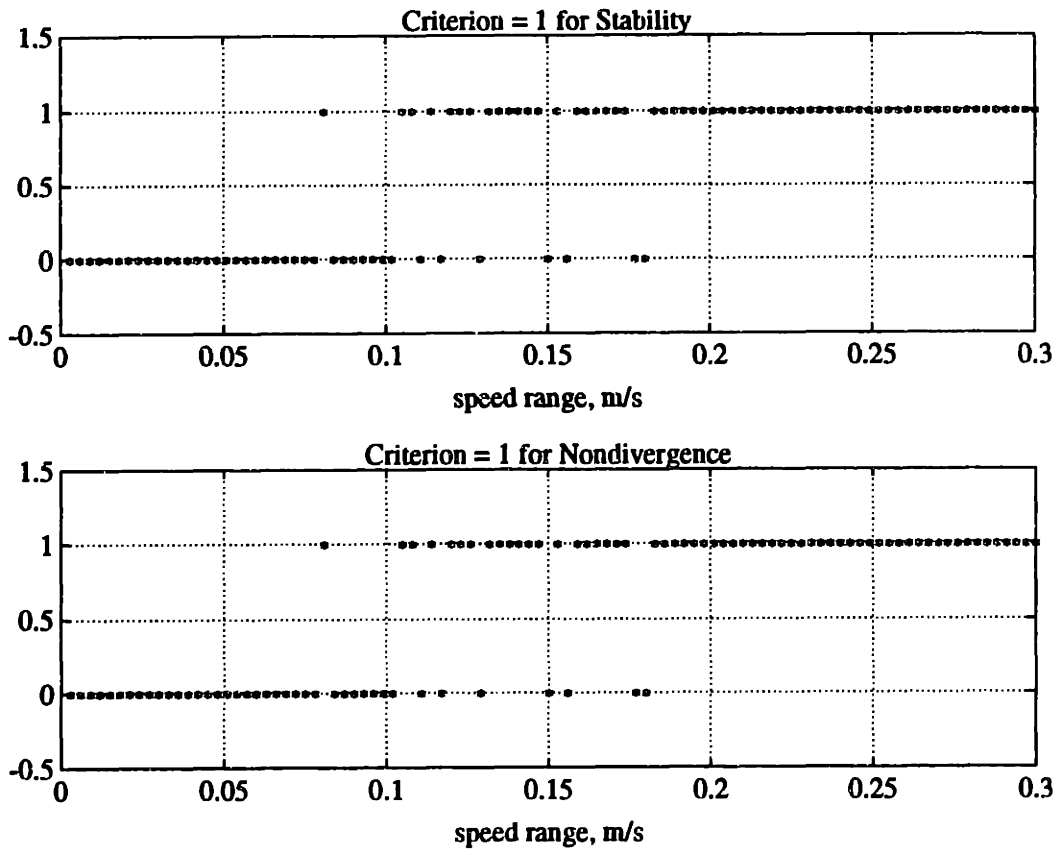Figure 5-7: Nominal LTR design loops for a scaled drill string system.

Figure 5-8: Formal guarantees for LQR (top) and CGEKF (bottom) for a design linearization of 0.1 meters per second.

	0.1 m/s ramp	0.2 m/s ramp	0.4 m/s ramp
0.1 m/s envelope	Figure 5-9	Figure 5-10	Figure 5-11
0.2 m/s envelope	Figure 5-12	Figure 5-13	Figure 5-14
0.4 m/s envelope	Figure 5-15	Figure 5-16	Figure 5-17

Table 5.4: Combinations of ramp speed and design envelope for experimental step responses.

5.4 Step Responses

In this section, the ramped setpoint change is viewed as a generic operation for the drill string system, verifying the stability of the closed-loop system, and revealing the transient response and long-term behavior (i.e., limit cycling). We consider changes in the setpoint of 2.0 meters, corresponding to 66-meter moves for the full-scale drill string system. All of the designs have a crossover frequency of 0.2 radians per second, and are based on the two-node model. In order to establish the basic tradeoffs for the different design approaches, nine combinations of speed envelope and ramp speed for the setpoint are considered; these are listed in Table 5.4.

The responses in each figure are arranged in order of increasing complexity and computational load for the control and estimation algorithms. Each experiment initiates with a ten-second dead time, to allow settling of the physical system, and a ten-second period in which the controller is enabled but the setpoint is still at the origin. The duration of the runs is chosen to be long enough that the limit cycling, if any, is completely developed. Finally, as stated earlier, the controllers all have integral action, so no steady-state offsets are expected. However, as the controllers are only of Type 1 (a single integrator), tracking errors during steady towing are not corrected.

There are a number of general observations which can be made about the designs, based on these data. The most striking point is that the EKF in every case leads to reduced limit-cycling behavior. In contrast, it is known that the linear Kalman filter has no nondivergence properties when applied to nonlinear systems, and that the CGEKF is valid only for operating speeds above the linearization. These facts are corroborated by the data, and suggest that all other results aside, the EKF is a crucial part of the best controller designs, with LOR.

It is apparent that since the physical plant is very stable, one can achieve asymptotically

Figure 5-9: Step responses with 0.1 m/s envelope, 0.1 m/s ramp speed.
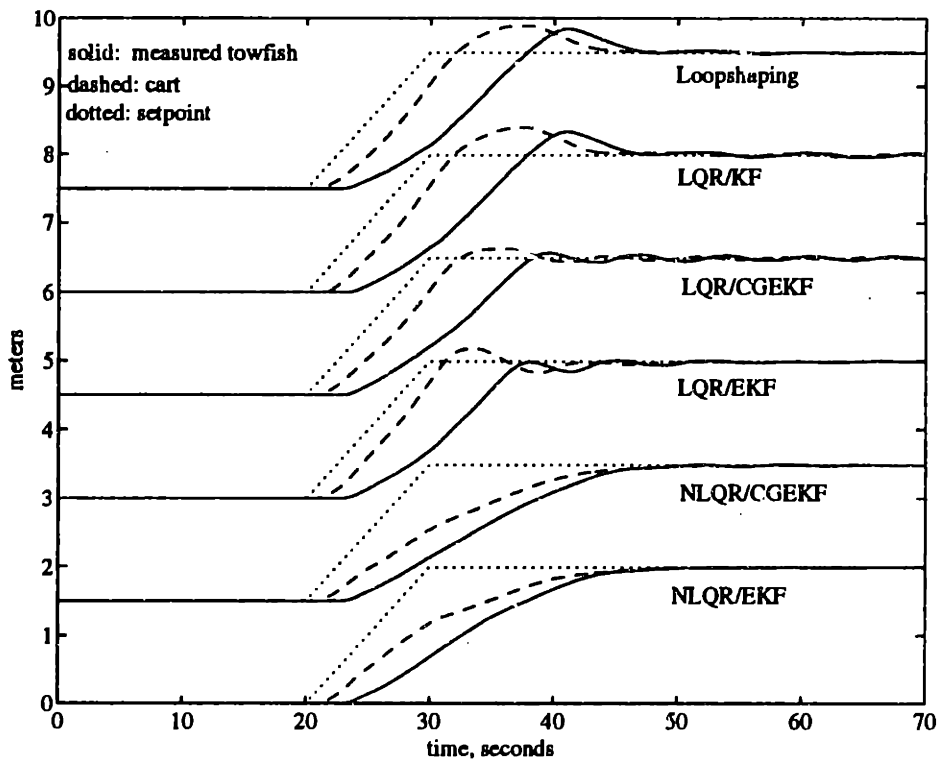
Figure 5-10: Step responses with 0.1 m/s envelope, 0.2 m/s ramp speed.

152
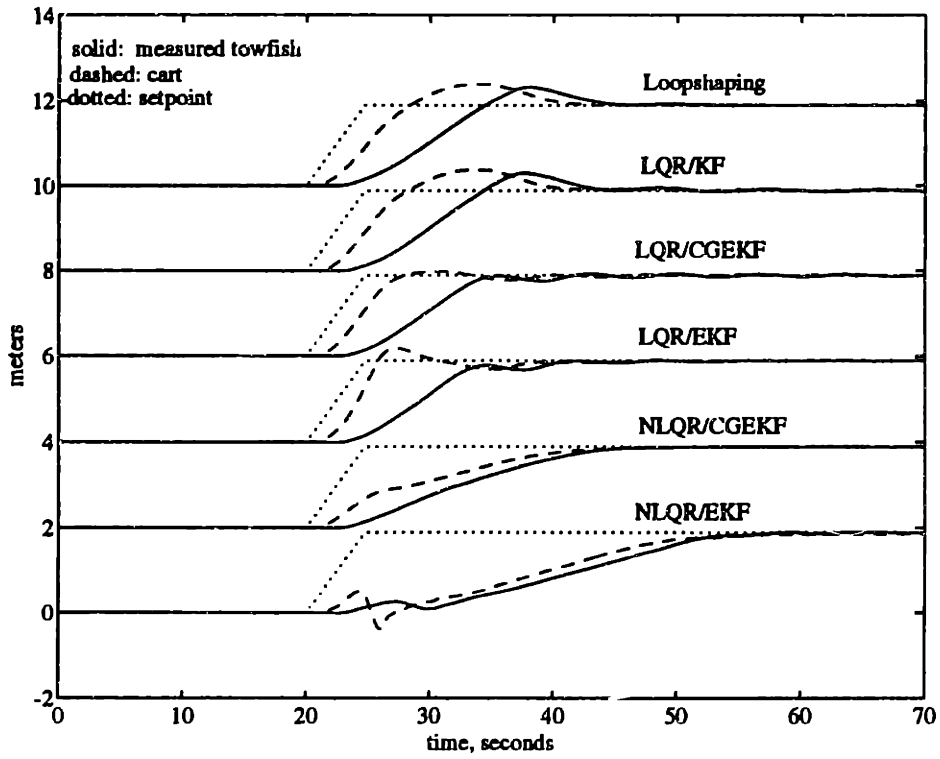
Figure 5-11: Step responses with 0.1 m/s envelope, 0.4 m/s ramp speed.
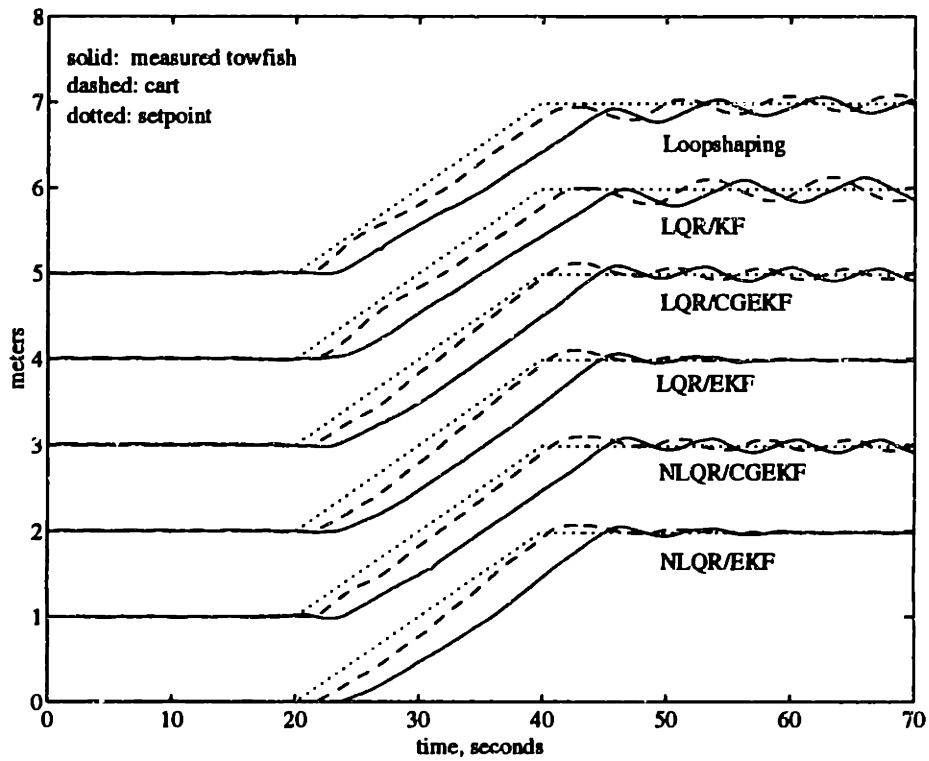
Figure 5-12: Step responses with 0.2 m/s envelope, 0.1 m/s ramp speed.

153
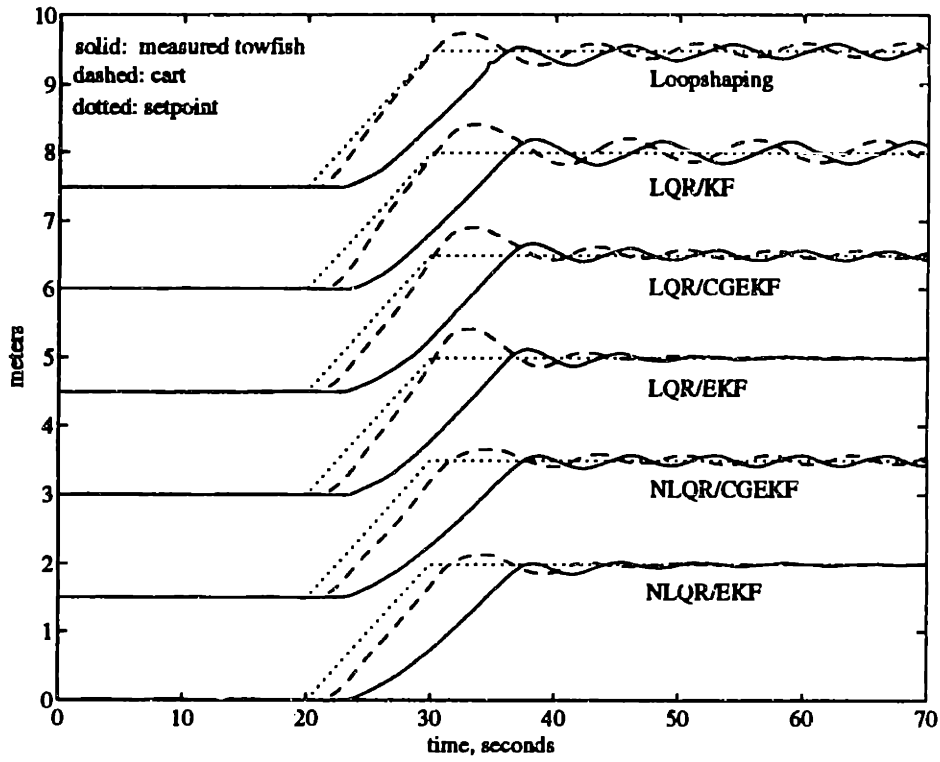
Figure 5-13: Step responses with 0.2 m/s envelope, 0.2 m/s ramp speed.

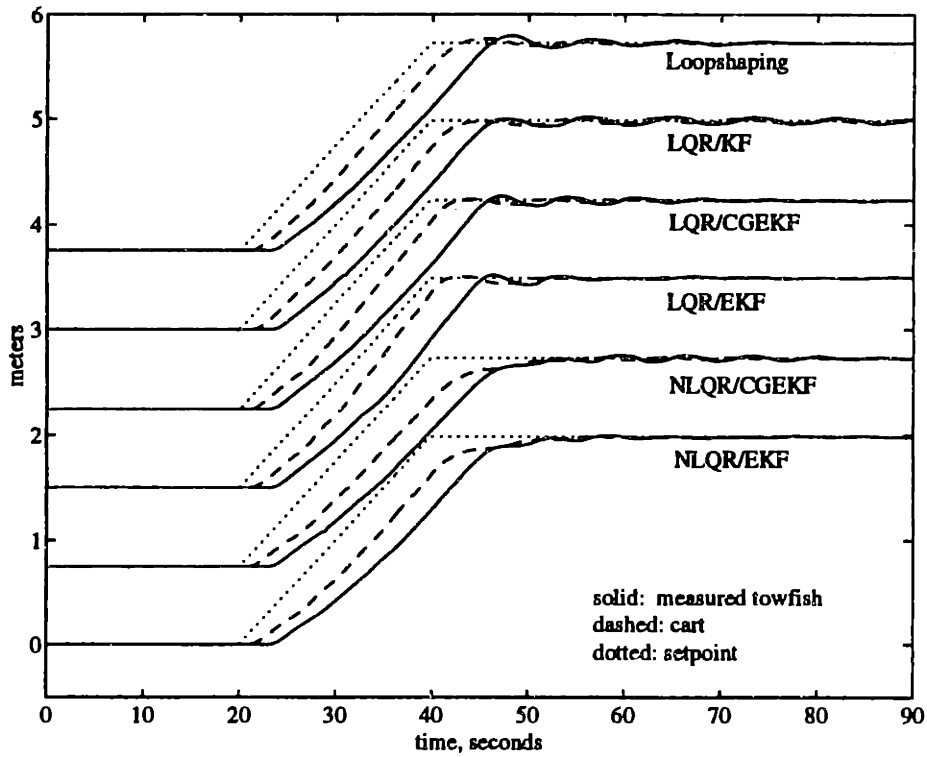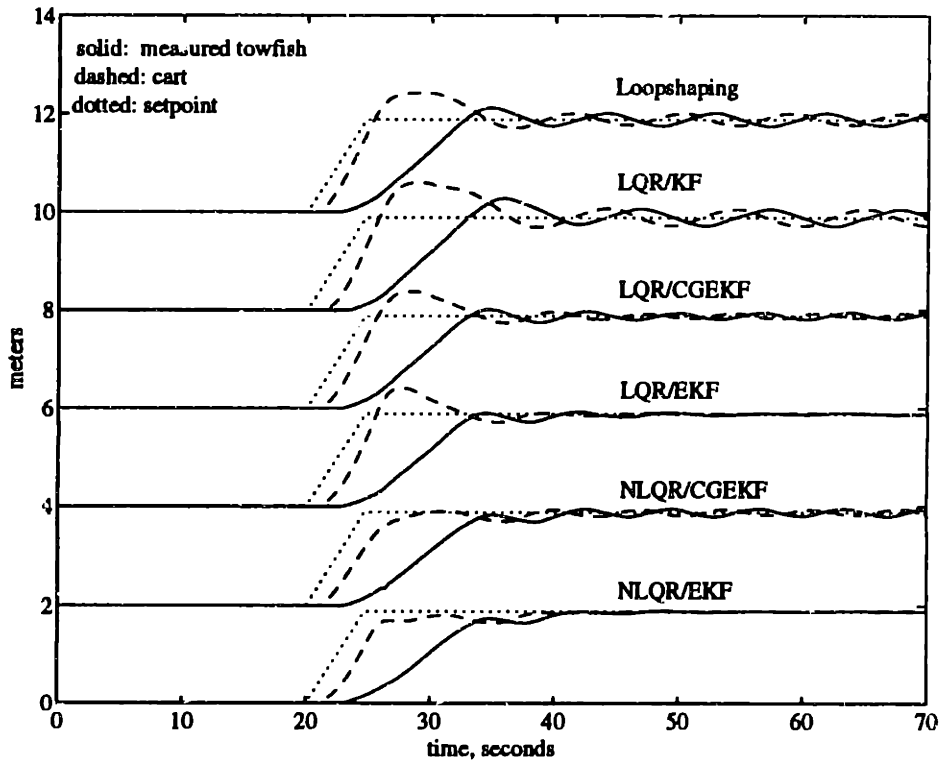Figure 5-14: Step responses with 0.2 m/s envelope, 0.4 m/s ramp speed.
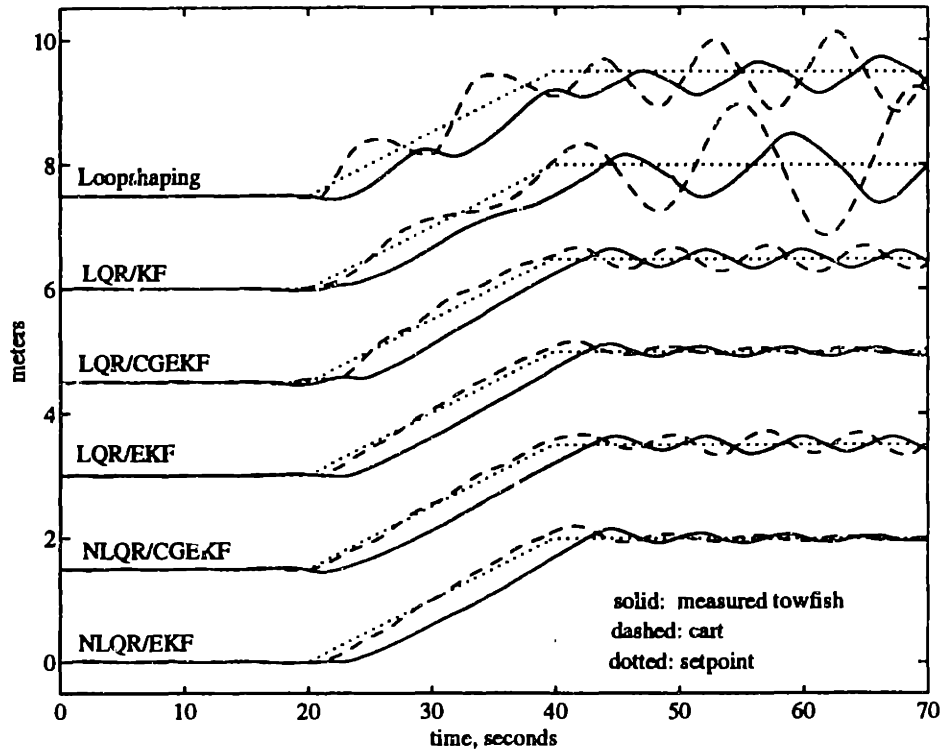
Figure 5-15: Step responses with 0.4 m/s envelope, 0.1 m/s ramp speed.
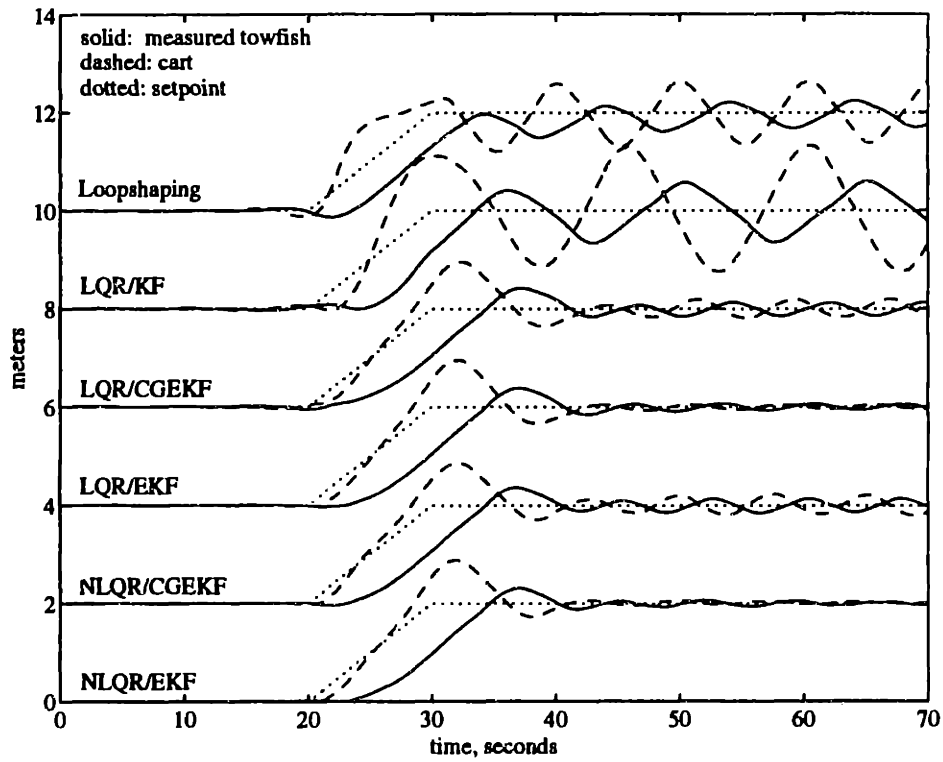
Figure 5-16: Step responses with 0.4 m/s envelope, 0.2 m/s ramp speed.
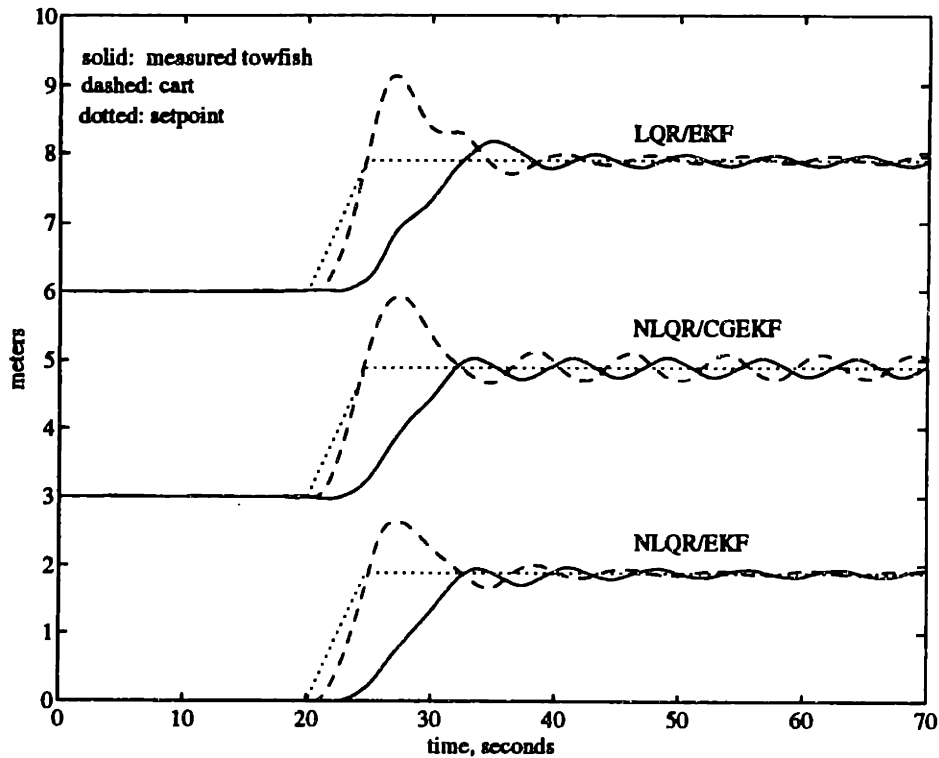
Figure 5-17: Step responses with 0.4 m/s envelope, 0.4 m/s ramp speed.

stable results from any linear design technique by making the design envelope very small (e.g., Figure 5-9). We recall that Safonov's conditions validate both the LQR and the CGEKF in this situation, and it seems that the Kalman filter works well also. As a general approach, however, the specification of a small envelope implies poor performance far away; that is, at high speeds. This trend may be seen in Figure 5-11, where the loopshaping and LTR responses contain a substantial overshoot.

The NLQR presents a special problem because when its design envelope is exceeded, the cubic term in the design plant model rapidly overtakes the actual drag in the plant. Thus, the plant has substantially less drag than the control law expects. This fact is in contrast to the LQR, in which the plant has more drag than the control law expects outside the envelope. Unlike the general deterioration of LQR performance, the failure of the NLQR in this situation is catastrophic, leading to extremely high bandwidth commands and raising the likelihood of numerical instabilities. As an example, Figure 5-11 contains a NLQR/EKF design on the verge of instability. As such, one has no choice but to increase the design envelope to encompass all expected and tolerable velocities reported by the filter. Toward

156

this end, the limiting of ramp velocity during maneuvers becomes not just a good rule of thumb; for the NLQR, it becomes imperative.

Because the NLQR is by definition accurate over a larger operating regime than the LQR, the disadvantages of a large envelope are less serious for the NLQR. The primary difficulty with the LQR is that performance must always be traded with limit-cycling. In Figure 5-15, for example, the loopshaping response limit cycle corresponds to fifteen-meter peak to peak oscillations for the full-scale system. The designs with nonlinear filtering and the NLQR are seen to have less limit cycling, especially with the EKF. In fact, direct comparisons of Figure 5-15 with Figure 5-9, and of Figure 5-16 with Figure 5-10 show that the nonlinear designs with an envelope of 0.4 meters per second, are superior overall to the linear designs with an envelope of 0.1 meters per second.

Aside from the limit cycling present in large-envelope linear designs, the linear approaches prove entirely inappropriate when the ramp speed is increased. For instance, Figure 5-17 gives only the responses of the LQR/EKF, NLQR/CGEKF, and NLQR/EKF controllers because the other designs led to commands that were beyond the capabilities of the apparatus. Several times, the cart hit the side of the tank, and in all cases, cart speeds of greater than one meter per second were demanded by the controller. Had the apparatus been able to support these motions, the response may well have been found to be stable. Nonetheless, the ramp speed is reasonable at 0.4 meters per second, so the linear designs are too aggressive at best. In contrast, the motions in Figure 5-17 indicate that the controllers are able to execute effective overshoots, reminiscent of our results in Chapter 3.

To summarize, the use of purely linear designs may be unsatisfactory because eliminating limit-cycling sacrifices performance, and improving transient performance causes limit cycling. The various nonlinear design techniques are attractive in that a higher design envelope can be used to ensure good transient performance, but with reduced oscillations because no linearizations are made. Among these techniques, the LQR/EKF appears to be the best, as the design for a 0.4 meters per second envelope worked well for all the runs. The NLQR/EKF designs were equally effective, but apparently offer no significant improvements over the LQR/EKF, based on these data. Computationally, the NLQR requires the construction of the auxiliary state vector $x^{[3]}$ at each time step, which is relatively insignificant compared to propagation of the EKF.

-2

-2.1

-2.2

depth, meters

-2.3

Loopshaping

NLQR/EKF

-2.4

-2.5

-2.6

0   0.5   1   1.5   2   2.5

horizontal excursion, meters
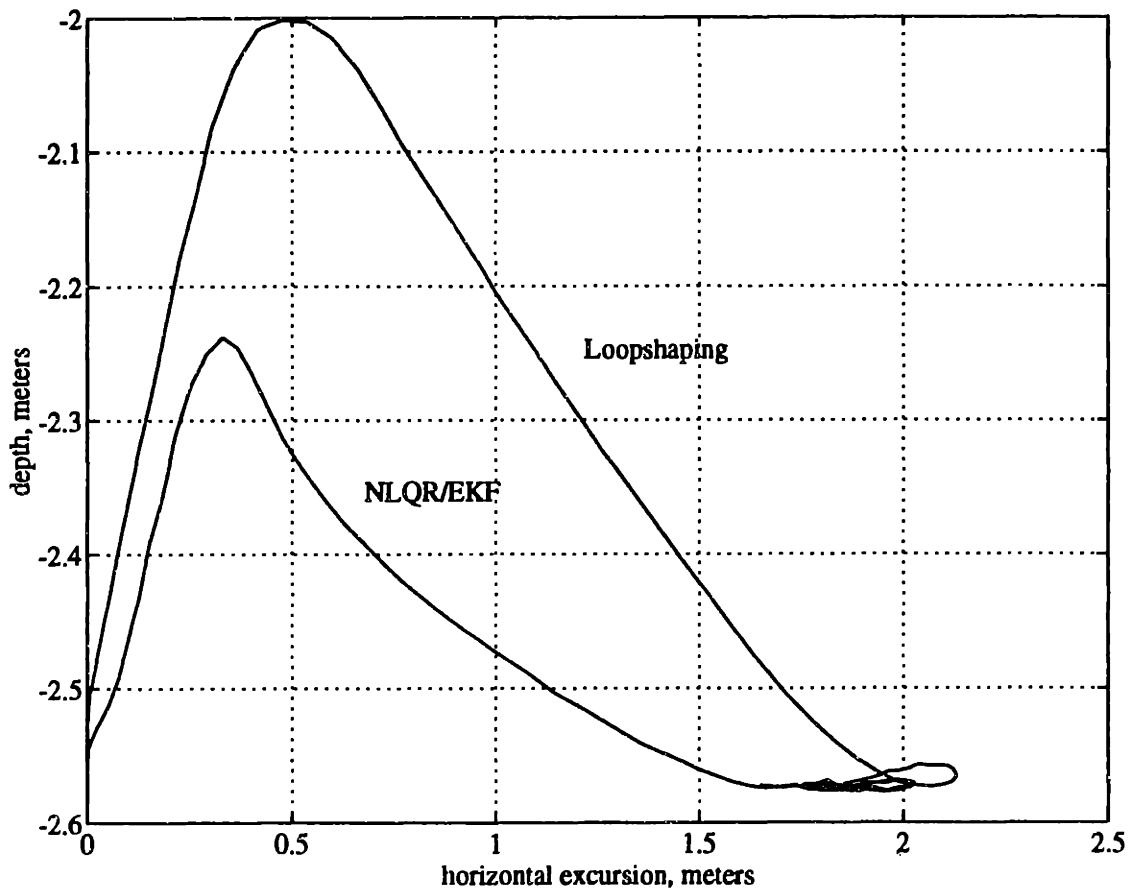
Figure 5-18: Side view of typical step responses.

5.4.1 Heave Response

The heave response of the plant during these runs is not large, as is evident in Figure 5-18. The data here are from the runs of Figure 5-14. Vigorous motions at the top of the cable again lead to strong vertical excursions at the towfish. In this particular case, the linear feedback leads to vertical excursions that are three times as large as for the nonlinear controllers. As stated earlier, these excursions should not be taken as a direct scaling of the vertical response of a full-scale system; the plot is intended only as an general indication of the system's vertical response.

5.4.2 Effects of Ambient Currents on Oscillatory Behavior

The developments of Chapter 2 indicate that the lateral frequency response of a cable in water is strongly attenuated in the presence of ambient currents. Furthermore, we expect closed-loop limit cycling to be reduced in currents, based on the (less conclusive) perturbation results of that chapter. Here, experimental verification of this hypothesis is considered, by executing feedback during a very slow setpoint trajectory. The design of Figure 5-13 was incorporated into two-meter moves with a ramp speed of 0.05 meters per second, and the data are presented in Figure 5-19, for the loopshaping and NLQR/EKF designs. In these runs, the feedback control was enabled for thirty seconds before the setpoint move, in order to allow any limit cycles to develop fully.

Clearly, the ramp speed is slow enough that the cable in both cases reaches a steady towing configuration. For the loopshaping design, the nominal limit cycle of 0.25 meters (peak-to-peak) is entirely eliminated during the transit, but then reemerges when the artificial current is "turned off." The NLQR/EKF response shows no limit cycling tendencies during any portion of the run, as expected.

An important note is that this ramp speed is very small on an ocean scale, since the full-scale speed of eight centimeters per second is common in many large gyres and circulation systems. As a result, many full-scale deployments automatically have this stabilizing element, which qualifies the linear designs to some extent.

5.4.3 Incorporation of Actuator Dynamics

In a very deep deployment, the actuation bandwidth is usually very much higher than that of the cable in the water. In the present case, stiction in the cart drive mechanism led to an approximate pure delay of 540 milliseconds, which corresponds to about eleven seconds in the full-scale system. These actuation dynamics are not troublesome, but it may make sense to account for them in situations where the delay is longer, or the cable response is faster. Toward this end, one could append the plant model with one or two states to model the actuator, although the addition of these states might make the NLQR computationally difficult. For example, the fifth-order nonlinear control design of Chapter 4 requires the storage of a 15,625-element matrix, while the seventh-order design involves a 117,659-element matrix.
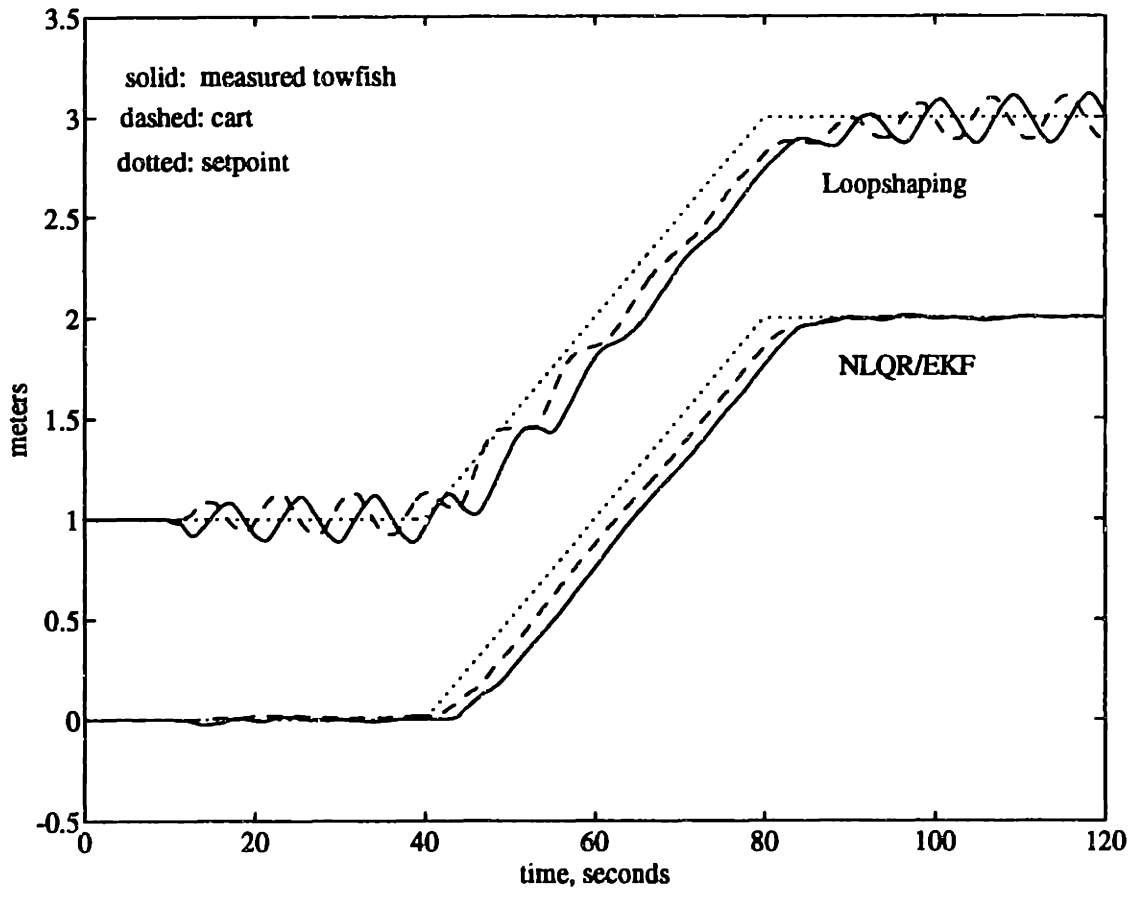
Figure 5-19: Experimental verification of limit cycle attenuation in ambient current.
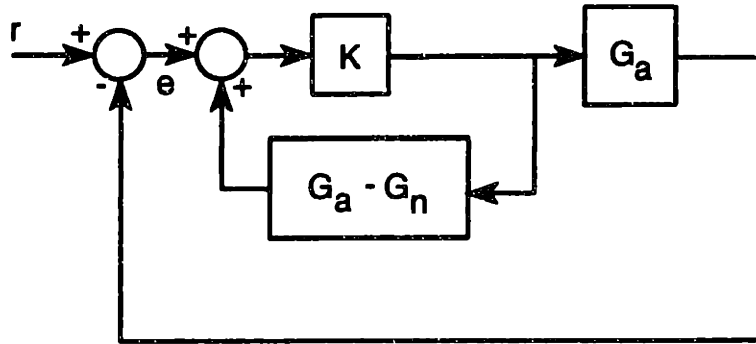
Figure 5-20: Generalized Smith feedback block diagram.

Another approach that could be used is delayed *Smith feedback* around the compensator [93]. The Smith predictor has been used extensively in linear systems, and may be derived for the nonlinear case by using the Loop Transformation Theorem [33]. A schematic view of generic Smith feedback is given in Figure 5-20. The basic idea is first to construct the compensator K to stabilize the nominal plant G_n, and then feed back around the compensator the difference between the outputs of the nominal plant and the actual plant model G_a. In the case where G_a is simply G_n with a pure delay, we feed back a delayed and nondelayed version of the plant output. As such, from a computational point of view, the predictor may be simply added onto an existing compensator, but does require its own state estimation. The estimates inherent in the CGEKF and EKF cannot be used because they are continually being corrected.

The present experiments incorporate the delayed Smith scheme, largely because the motor servo looks more like a pure delay (stiction driven by the integrator in the motor servo) than a first- or second-order lag. In addition, the acoustic fixes arrive one time step late, so setting the delay at 820 milliseconds accounts for both delays. An illustration of the effects of delayed Smith feedback is given in Figure 5-21, for the controllers of Figure 5-13. The transient responses appear to be improved only slightly for these runs, while the limit cycle is practically unchanged. The actuation with Smith feedback is somewhat less vigorous, however, and a larger delay would presumably enhance the stabilizing properties of this scheme.

The remainder of tests in the thesis are made using delayed Smith feedback, *including*
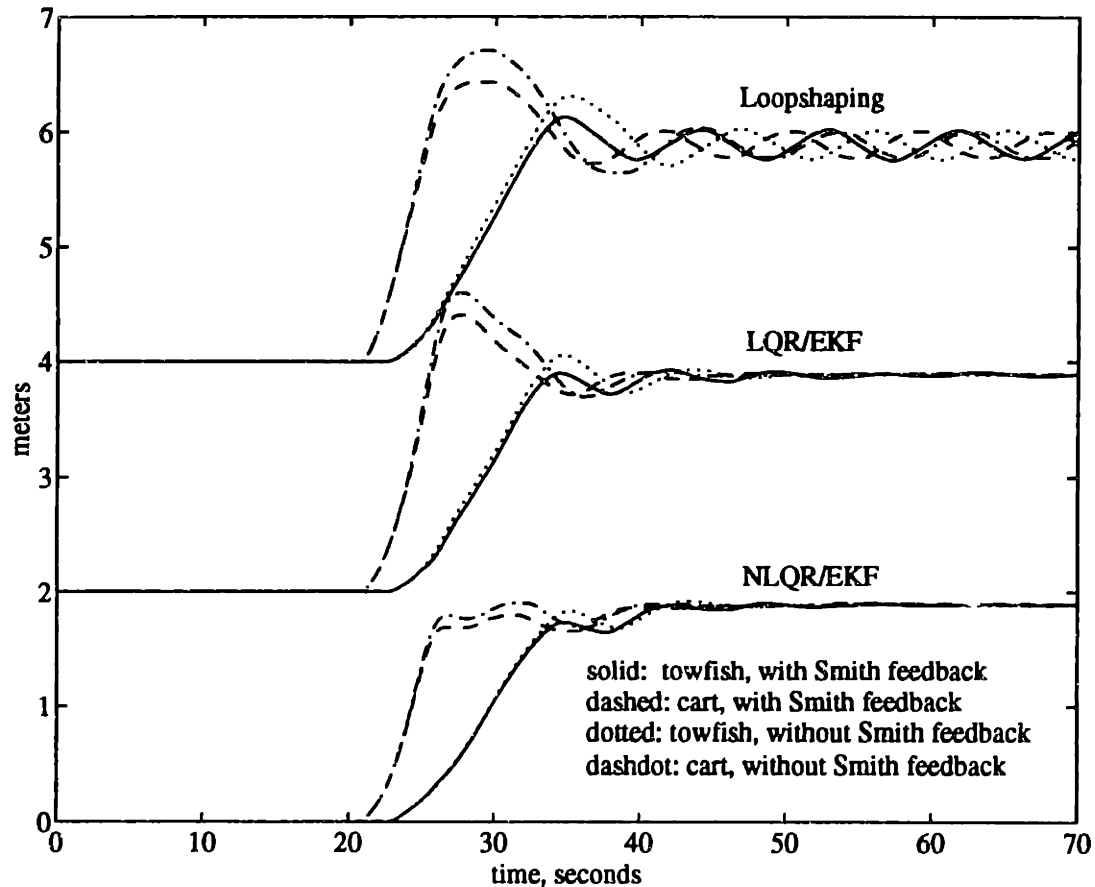
Figure 5-21: Effects of delayed Smith feedback (0.82 seconds) around the compensator.

those of Figures 5-9 to 5-17 above. An important note is that for linear controllers, the Smith feedback uses a linear model. In addition, when errors are purposely inserted in the nominal plant model, these errors also are incorporated in the Smith feedback.

5.4.4 Full Smith Feedback

Another situation in which the concept of Smith feedback is useful is in the NLQR designs with a large envelope. As seen in Section 5.3.1, the cubic approximation of quadratic drag is linear near the origin; on the unit line, the slope at the origin is approximately 0.3. As a result, when the envelope is large, the NLQR may induce limit cycling for the same reasons that the linear designs do. Smith's scheme can be used effectively in this case also, by letting G_a be a quadratic model with delay, and letting G_n be a model with the cubic

162
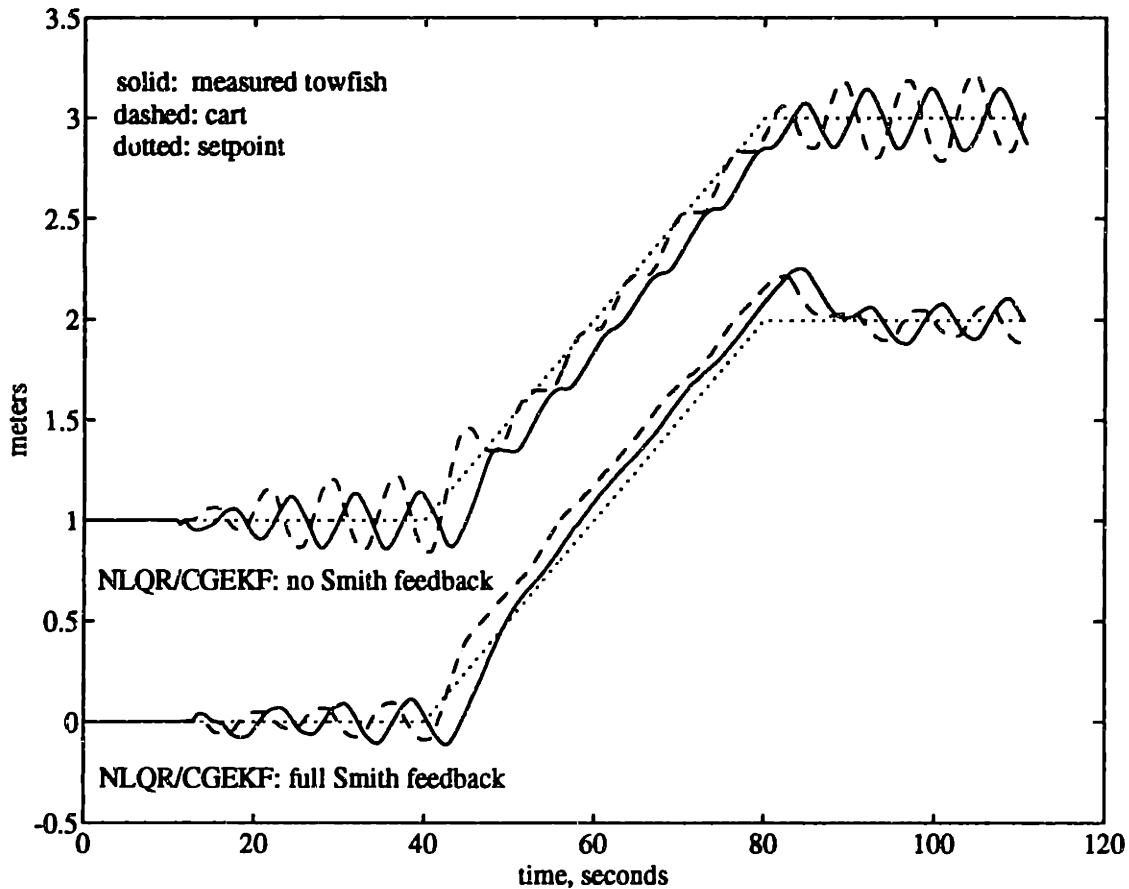
Figure 5-22: Effects of full Smith feedback on limit-cycling behavior of the NLQR/CGEKF.

approximation and no delay.

This technique has very little theoretical justification, since the model with quadratic drag is, of course, in error. Nonetheless, it is presumably closer than the cubic model. An heuristic attempt was made to reduce the oscillations of the NLQR/CGEKF design in Figure 5-15, which has an envelope of 0.4 meters per second, and oscillations of thirty centimeters peak-to-peak (ten meters in the full-scale system). Results without and with the full Smith feedback are given in Figure 5-22. While holding station, the limit cycle has been reduced to eighteen centimeters (six meters in the full-scale system) peak-to-peak. Furthermore, we see that the oscillations during the transit are eliminated under the full Smith feedback. Finally, an artifact of this strategy has the towfish *leading* the setpoint, contrary to all of the other runs made in this chapter.

163

5.4.5 Disturbance Rejection

The rejection of slow disturbances by the closed-loop system is important because of currents that may act along the cable. Simulating this situation in the test tank proved to be problematic, since the small diameter of the tank made it impossible to reach steady-state at any realistic velocity. A simple alternative scheme was devised, involving a nonlinear spring attached to the cable midpoint: see Figure 5-23. The spring consisted of a weight and a string, attached to the tank and to the cable, so that moving away from the walls caused a large offset in the cable position. Figure 5-24 shows that the controllers handle the disturbance as expected. The design was the same as in Figure 5-13.

Other disturbances which are likely to be encountered in ocean operations are those of wave forces on the surface vessel, and limit cycling of the vessel due to its own closed-loop dynamics. Clearly, the wave-induced motions are much faster than the limit cycle, and they are both much faster than the cable. In order to assess the possible impacts on stability and performance of such motions, a sinusoidal cart motion was imposed upon the step responses of Figure 5-13. This motion corresponds to a ten-meter peak-to-peak surge at .15 radians per second; physical constraints prevented the scale implementation of larger or faster motions. Two results are given in Figure 5-25; clearly there is no loss of performance or stability associated with these high-frequency motions. In fact, for the loopshaping design, the high-frequency motions *eliminated* the limit cycling almost entirely, and they reduced the oscillations in the NLQR/EKF application. This trend is indicative of increased system damping due to high velocities in the upper portion of the cable. For both controllers, the motion which reached the bottom of the cable corresponds to approximately 1.5 meters peak-to-peak in the full-scale system. Transmitted motions are attenuated further when the amplitudes are smaller, or when the frequency is higher.

5.4.6 Higher-Order Controller Designs

The four-node model of Figure 5-2 is more accurate than the two-node model, for the scaled drill string system. More generally, one would expect that higher-order models have even better performance for very long cables, in which higher modes may be excited and sustained. Thus, it makes sense to compare the performance of controllers based on the four-node model with those of the two-node model.

164
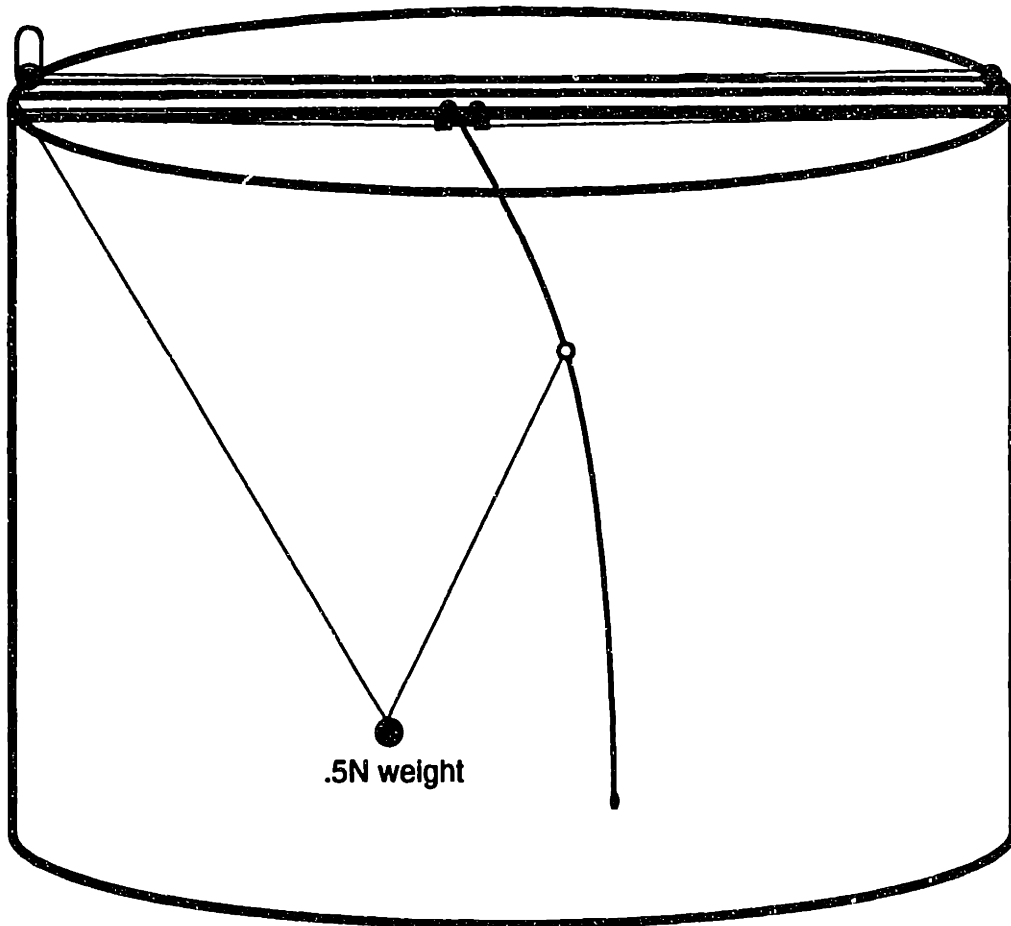
Figure 5-23: Physical application of an unmodeled spring force to the cable.
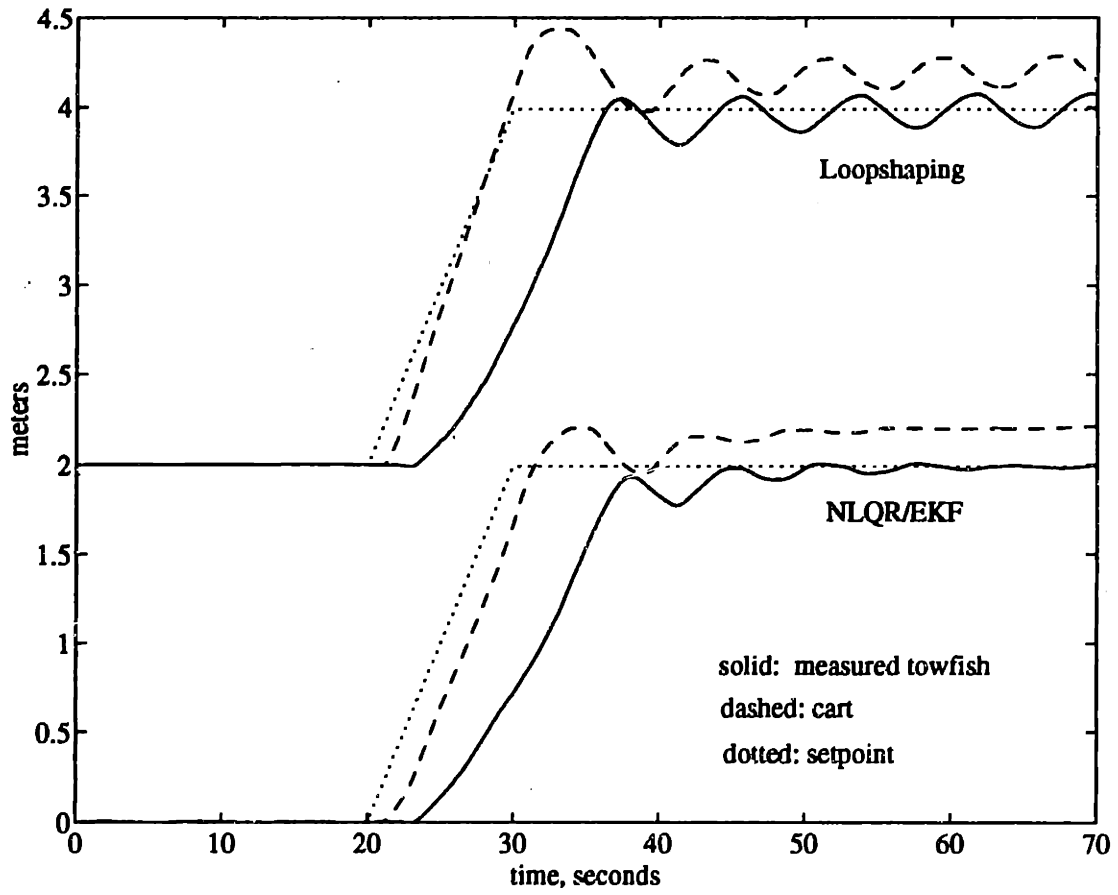
.5N weight

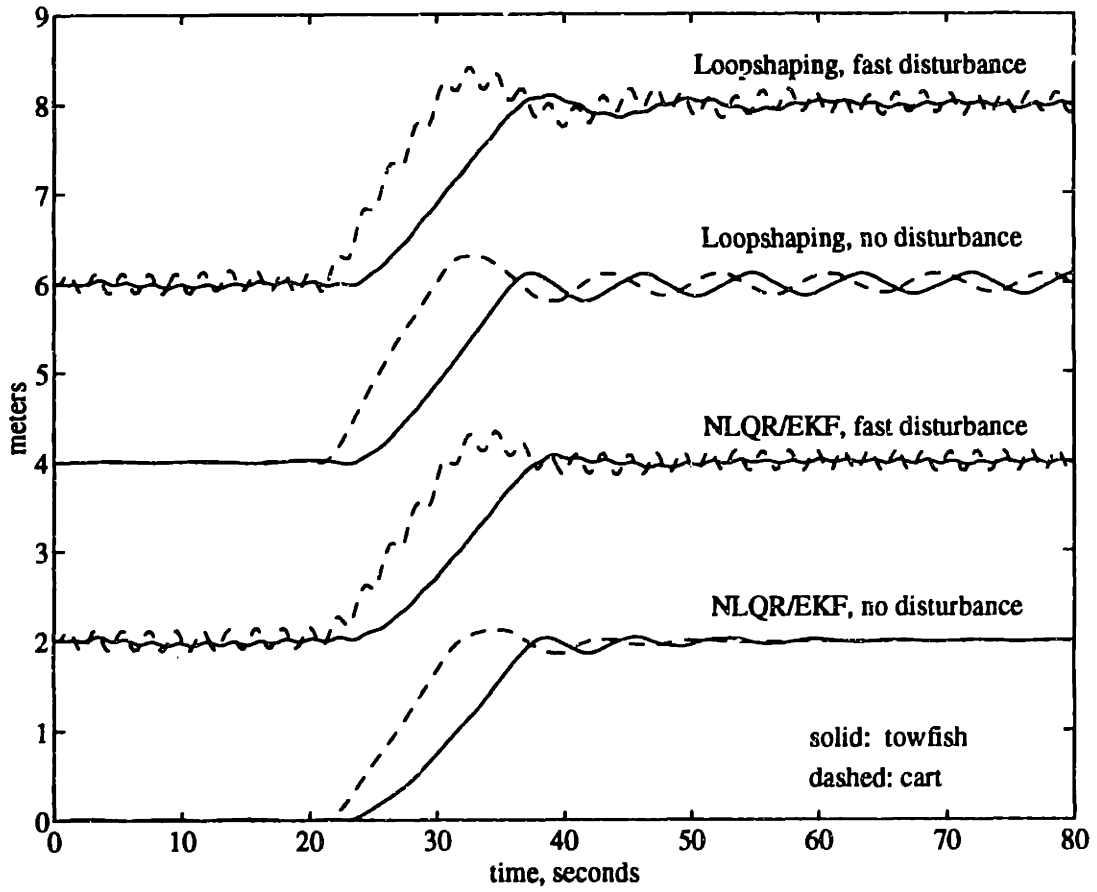**Figure 5-24: Illustration of slow disturbance rejection.**

Figure 5-25: Closed-loop responses in the presence of fast cart surge motions.

The design programs are written to be transparent to model order, so the only difficulty is the construction of the NLQR, which entails a model order of length nine (including one integrator), a lexicographic state vector of length 165, and a triple Kronecker product with 531,441 elements. With double precision arithmetic, this large matrix temporarily occupies approximately 4.25 megabytes of memory. In the execution of the program, we simultaneously propagated a ninth-order EKF, a ninth-order Smith feedback estimator, and applied a 9×165 feedback matrix. The necessary integrations were made with a second-order Adams-Bashforth scheme at ten cycles per acoustic fix, and the discrete-continuous forms of the CGEKF and EKF were utilized throughout. In the experiment, the control loop rate was kept at 0.275 seconds. These runs represent the computational extremes for this chapter.

The runs for the controllers based on a four-node model are given in Figure 5-26; the designs were based on the same envelope (0.2 meters per second) and ramp speed (0.2 meters per second) as in Figure 5-13. The effects of model order are clearer in Figures 5-27 and 5-28, in which the tracking error of the towfish is plotted for the the two-node and four-node design runs, respectively. The integral square error for each response is given in the plots as well. We see that the four-node loopshaping result is very poor, while the LQR/KF results are virtually identical in all respects. The transient responses of the nonlinear designs in general are slightly slower for the four-node designs, but have fewer residual oscillations, and greatly reduced limit cycle amplitudes. The reduction of oscillatory behavior in the four-node design results is consistent with the notion that higher-order controller designs can account for more structural modes. In the present case, our familiar limit cycle is eliminated by the increased resolution of the four-node controllers.

5.4.7 Robustness

In this section, we experimentally investigate the robustness properties of the various controller design techniques. There are many sources of model uncertainty in a towed cable system which make robustness of the closed-loop system crucial. To begin, the effective drag coefficient along the cable may vary a great deal, due to complex hydrodynamic processes. For example, the onset of vortex-induced vibration can cause the cable to vibrate in the out-of-plane direction enough to double the effective drag coefficient. These vibrations may be steady or temporary, and may be localized or widespread, or even travel along the cable

solid: measured towfish
dashed: cart
dotted: setpoint

Loopshaping

LQR/KF

LQR/CGEKF

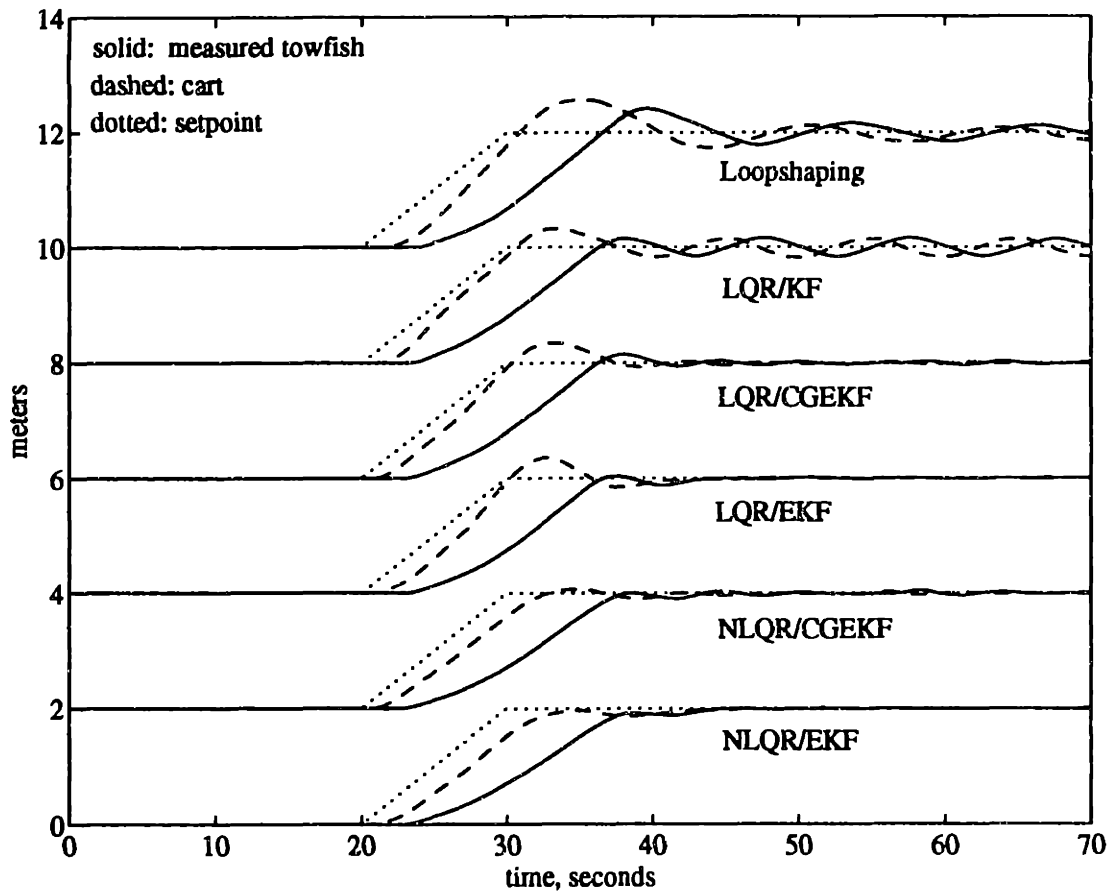LQR/EKF

NLQR/CGEKF

NLQR/EKF

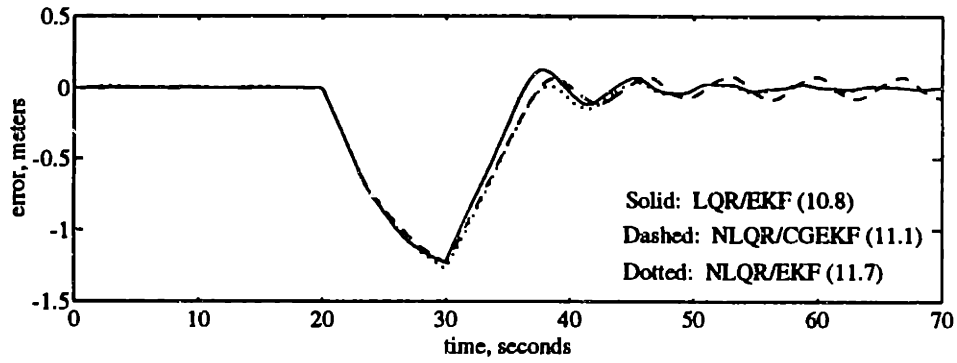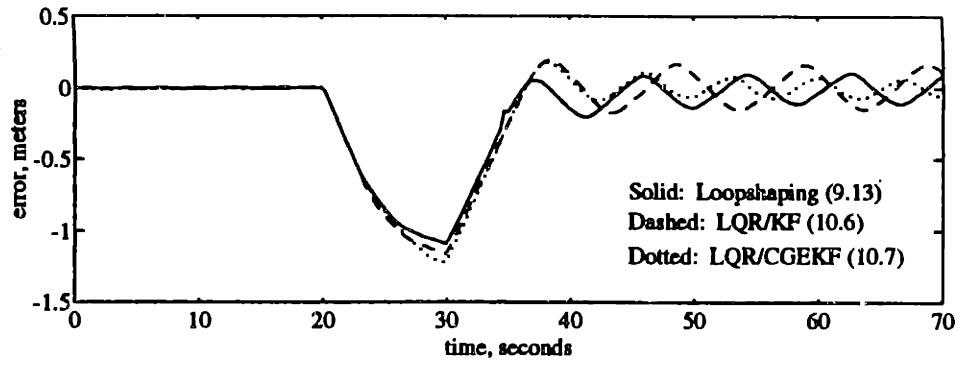Figure 5-26: Step responses for controllers based on a four-node plant model.

169

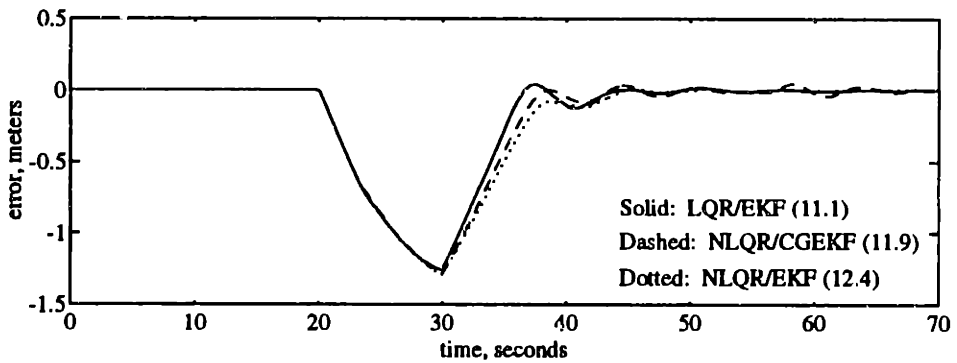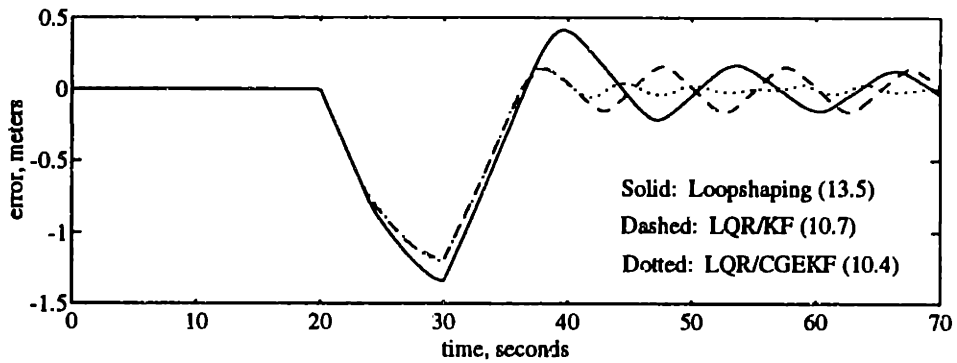Figure 5-27: Tracking errors for controllers based on a two-node plant model.

Figure 5-28: Tracking errors for controllers based on a four-node plant model.

170

[49]. At the other extreme, above $Re \simeq 10^5$ one may encounter supercritical flow, which leads to reduction of the drag coefficient by up to seventy percent [81].

Other sources of modeling error could include possible changes in the unit mass of a riser, depending on what materials are inside (e.g., mud, water, slurry). The tensions in such a riser can be affected if bottom contact is made, or if the payload is altered. The tensions are also changed if the length of the towed system is modified; ideally, we want a controller to work for a range of depths near the design depth.

Linearisation and the Nature of Quadratic Drag

The nonlinear optimal controller of Chapter 4 is to provide a control law based on nonlinear drag, and therefore is nominally better than the linear control law for a range of the state space. A velocity envelope is selected for the NLQR, over which the polynomial approximation is to be good, and the linearization for linear designs is selected to be good over the same domain.[2] See, for example, Figure 5-29.

We first consider the case in which the quadratic drag coefficient is estimated too low; the cubic approximation is superior to the linearization near the origin and at high velocities both inside and beyond the envelope. See Figure 5-29. Figure 5-30 shows a case where the modeled drag coefficient has been made three times too small. The design parameters for this run are the same as in Figure 5-13; the bandwidth is 0.20 radians per second, with an envelope of 0.2 meters per second. This type of model error leads to very stable responses all around, as the low product of linearization speed and modeled drag eliminates limit cycling in the linear designs. It is apparent that the transient performance of all the designs is deteriorated by the modeling error, although less for the nonlinear designs than for the linear ones.

In the event that the drag coefficient is overestimated, the properties of the cubic and linear approximations are quite different. In particular, the linearization becomes better than the cubic approximation for velocities in the higher portion of the domain, and for all velocities beyond the domain. Thus, in this case, *the linear controller designs may be superior because the nominal linearization is closer to the perturbed quadratic drag than is the nominal cubic approximation.* This fact clearly does not detract from the

---

[2]Changing the linearization speed and modifying the modeled drag coefficient are identical from the point of view of the linear designs, but quite distinct for the nonlinear designs.
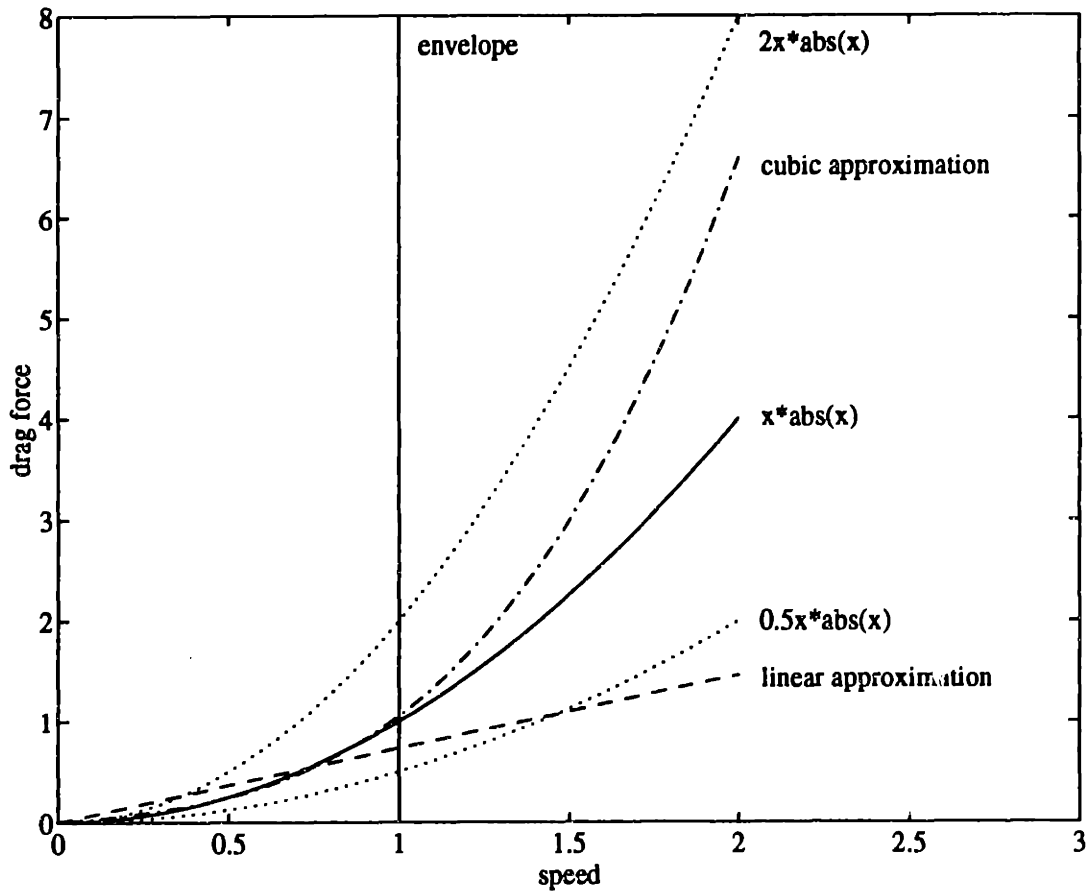
Figure 5-29: Approximation of quadratic drag by linearization and a cubic polynomial.
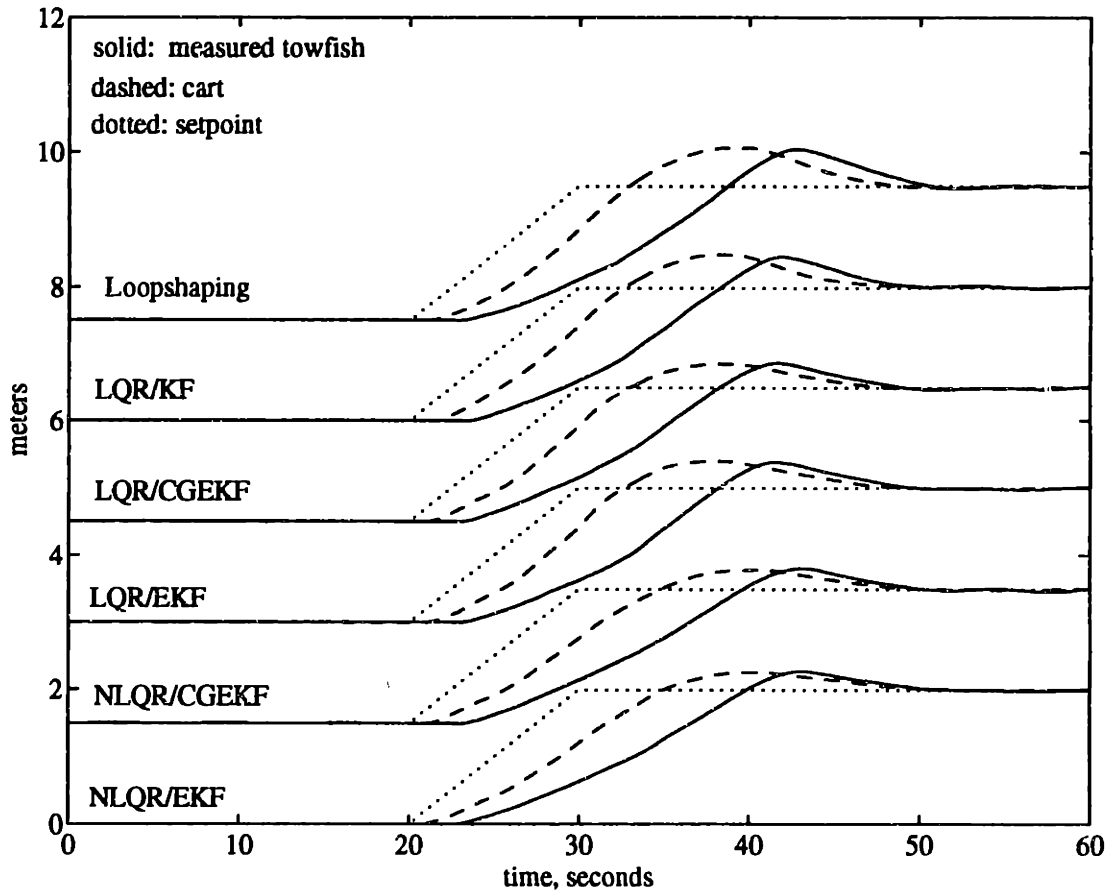
Figure 5-30: Effects of underestimation of drag coefficient.
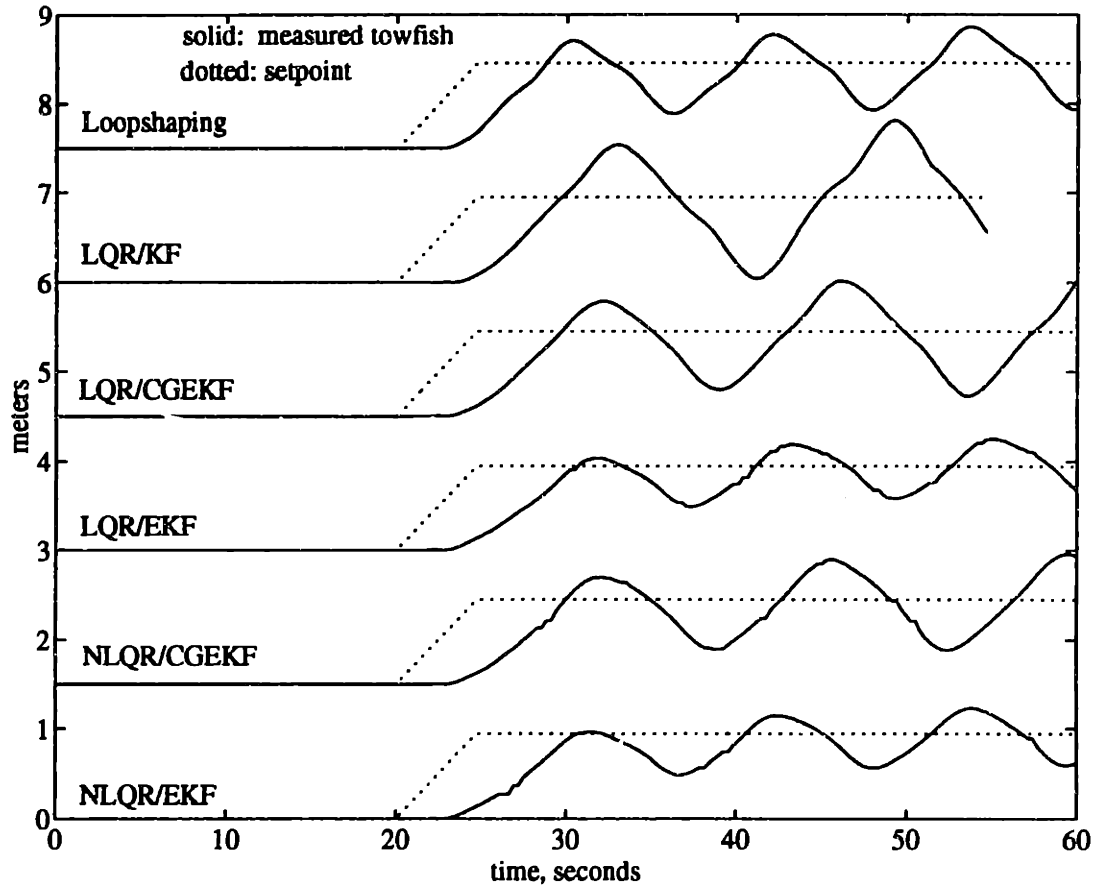
Figure 5-31: Effects of threefold overestimation of drag coefficient.

fundamental robustness properties of the nonlinear optimal regulator, but instead enhances the robustness properties of the linear designs. Safonov's criteria suggest no guarantees for the LQR or the CGEKF when the linearizations are too high.

In the experiments, we indeed find that the NLQR cannot provide better robustness to this type of drag error than the linear designs; see Figure 5-31. Here, the drag coefficient was overestimated by a factor of three in the design plant model, the envelope was 0.2 meters per second, and the crossover frequency was 0.15 radians per second. None of these designs have acceptable performance, as the responses are dominated by very large limit cycling. The corresponding cart motions occupied the entire tank, and the cart hit the wall fifty-five seconds into the LQR/KF run.

In the face of these disappointing responses, there are several redeeming points that are noteworthy. First, the controller design would rarely use such a poor model; if identification

runs are to be made, these would ideally incorporate a regime of supercritical flow. In addition, the dramatic changes in drag coefficient occur during *fully-developed* supercritical flow. As such, these changes are unlikely to be seen in transient motions or in limit-cycling, although an exception could arise during operations in extremely fast, steady currents (greater than one meter per second).

Another point is that the onset of supercritical flow is strongly influenced by the roughness of the cylinder. For example, when the characteristic roughness ratio (grain size divided by diameter) is 0.005, the reduction in drag coefficient is only about forty percent [81]. Similarly, the presence of kill- and choke-lines on a marine riser could be advantageous. Finally, we reiterate that as the natural plant is very stable, one can always find a stabilizing control law by reducing the bandwidth or speed envelope in the design.

Robustness to Tension and Mass Variations

We now investigate the robustness of the various designs with specific regard to tension and mass variations. For the first example, the weight in water of the towfish was doubled, as was the weight of the cable, in the design plant model. As before, designs with a speed envelope of 0.2 meters per second were considered, having a bandwidth of 0.20 radians per second. The results are shown in Figure 5-32. The fact that all of the responses seem quite stable is not surprising, as the actual plant has a significantly higher natural frequency than the control law expects. In comparison with Figure 5-14, we see that the limit cycling is almost completely eliminated, and that all the designs suffer some loss of transient performance. The tracking errors are plotted for the two cases in Figure 5-33 and 5-34, for the the correct and incorrect designs respectively.

Modeling the plant as too light was expected to have a detrimental effect on the closed-loop responses, as in this case the controller is paired with a plant whose natural frequencies are reduced. To investigate this hypothesis, the design of Figure 5-13 was incorporated, but the foam flotation on the cable was removed, and a 2.0-Newton (in water) weight was affixed approximately 35 centimeters up from the transceiver. Thus, the static tensions were increased by 2.52 Newtons uniformly. The results are shown in Figure 5-35, which may be compared to Figure 5-13, generated with the correct model. Overall, this modeling error induces a limit cycle in the responses of the nonlinear designs, but does not affect the linear responses nearly as much. The amplitude of the limit cycle in the NLQR/EKF run,

175
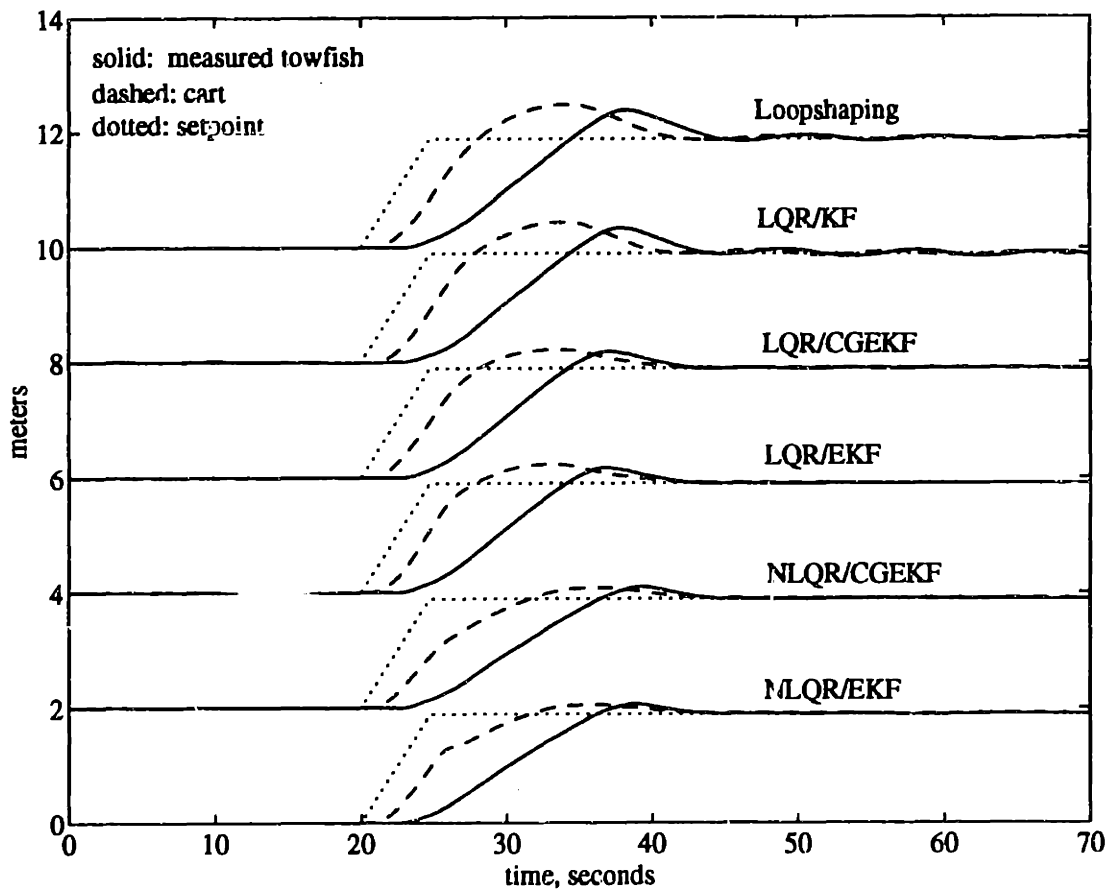
Figure 5-32: Effects of designing with a heavy design plant model.
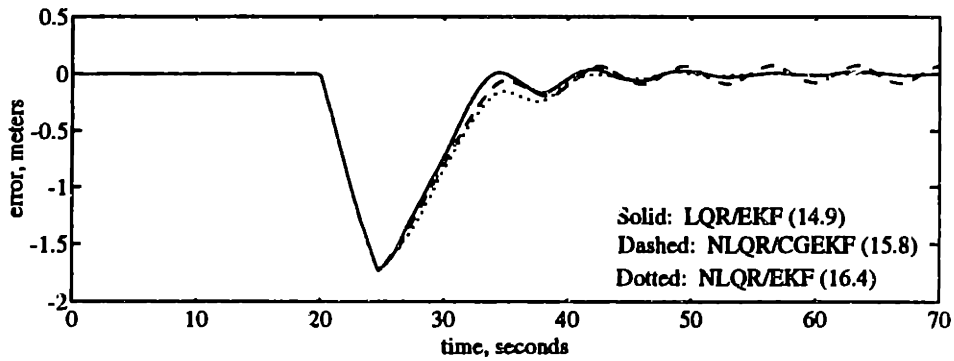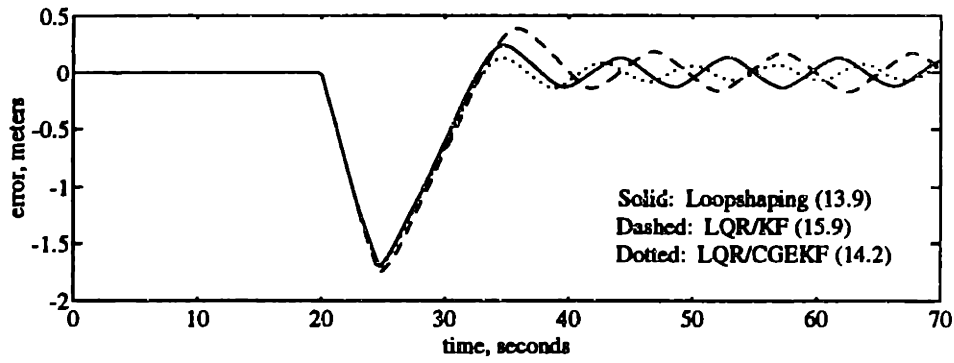
Figure 5-33: Tracking errors with correct design plant model.
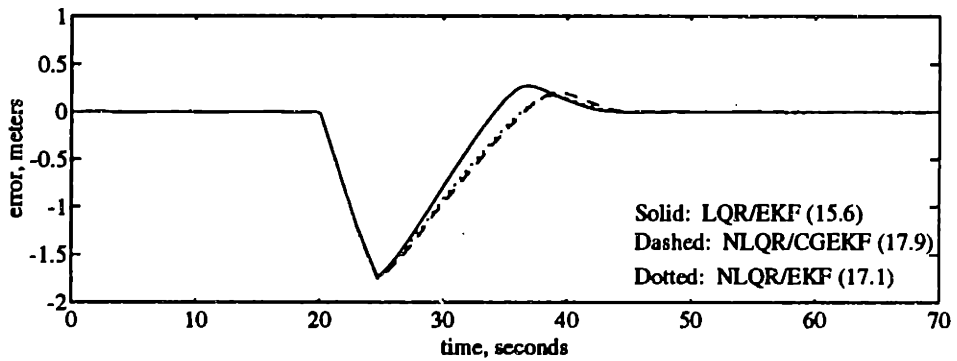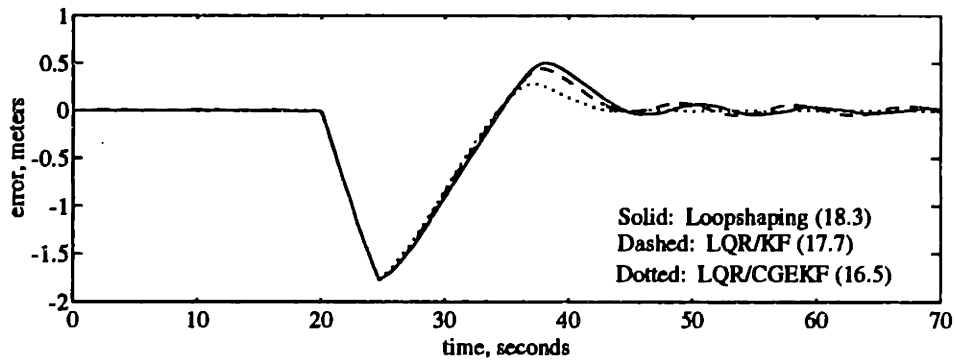
Figure 5-34: Tracking errors with heavy design plant model.

177
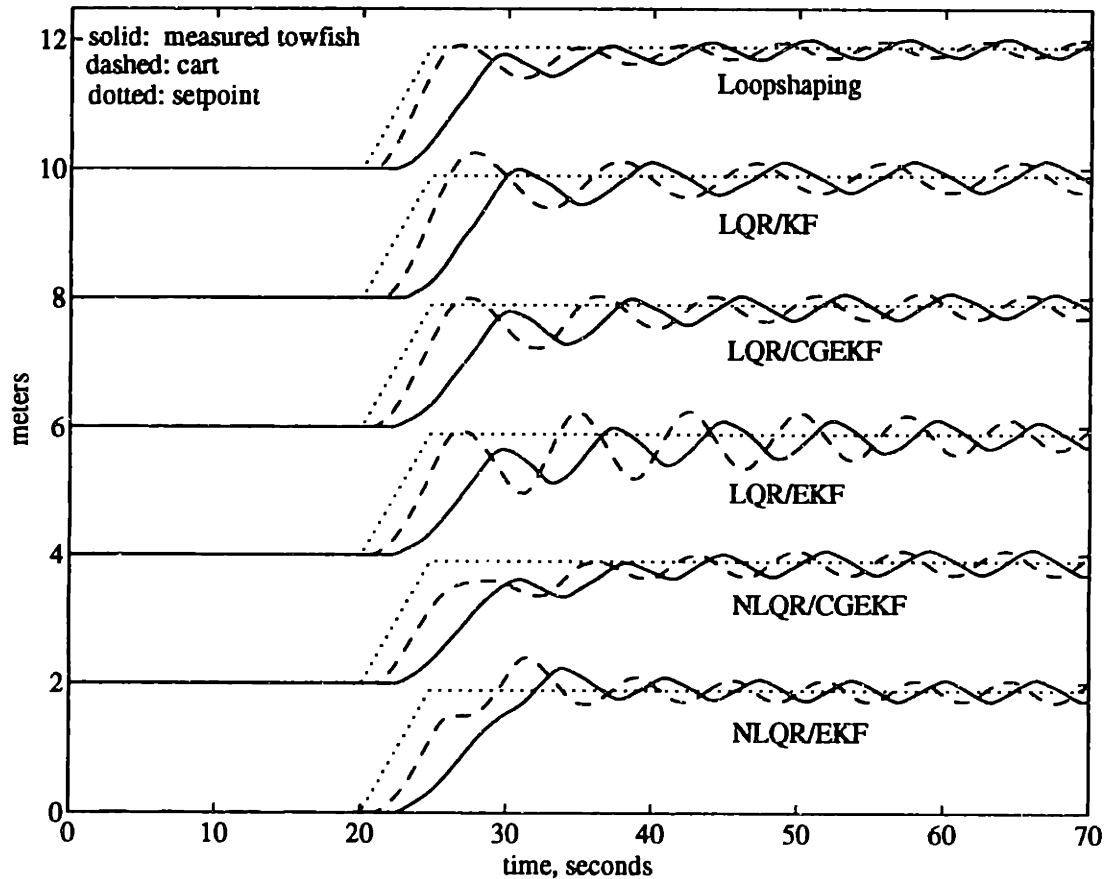
Figure 5-35: Effects of adding weight to the bottom of the cable.

for example, is thirty-six centimeters peak-to-peak, corresponding to approximately twelve meters for the full-scale system. There is no associated limit cycle in 5-13.

As all the designs appear susceptible to this behavior, our only consolation is that these data were obtained for a case in which the unmodeled weight was *equal* to the weight of the entire modeled system. Obviously, this is a very severe error.

5.5 Setpoint-Following

The good results of the previous section, and those of Chapter 3, suggest the design of a controller with the necessary capability of regulation and the benefits of preshaping. More specifically, we assume that a vessel trajectory has been found through our inversion technique, and now we would like to apply feedback to correct for modeling errors and

disturbances. It is apparent that *a regulator can be applied to the plant in a reference system which moves along the preshaped path.* In other words, the position error used by the regulator is the distance between the measured towfish and the *moving* setpoint. At the same time, the control action coming out of the regulator is added to the *moving* reference trajectory, which is the result of the inversion.

Our first example is given for the scale *ARGO/JASON* system, with a linearization speed of 0.1 meters per second, a crossover frequency of 0.5 radians per second. The best two-node model available was used, and the Smith feedback scheme above was fully utilized. For the preshaping, a towfish trajectory was defined which involved very large transients, as well as periods of zero and low velocity. Figure 5-36 gives the results for five different approaches to the problem. The top plot shows the actual motions of the system, while the bottom plot indicates the tracking errors. The top curves in the upper plot show the pure feedforward solution, with no feedback. In the two middle sets of curves, we have attempted to follow the setpoint using the loopshaping and NLQR/EKF regulators. Finally, in the bottom pair of curves, the linear and nonlinear regulators have been layered on top of the preshaped trajectories.

In general, we see that the dynamic inversion for this run is very successful. In fact, it is so good that the application of feedback makes the response slightly *worse.* As expected, the pure regulation results are quite poor due to the conservativeness in the designs. The basic conclusion can be stated as follows: *when the inversion is known to be good, as in the cases when the model is very good or there are no disturbances, one cannot obtain better performance than by application of the preshaped input alone.* This conclusion is not surprising, since the control of completely known plants obviously does not require feedback.

We now consider the same trajectory, and the same regulators in runs where the nonlinear spring of Section 5.4.5 is employed. The data are shown in Figure 5-37. In the application of the preshaped input alone, the towfish trajectory first shows the effects of the spring (rather suddenly) at approximately eighteen seconds elapsed. For the middle portion of the run, it then assumes a somewhat constant offset from the setpoint, crossing over it to take a bias in the other direction when the setpoint goes negative. The pure regulation results are as slow as in the unperturbed case, but the advantage of the integrator in the control is evident as the tracking error is small in the flat middle portion of the run.

179

Figure 5-36: Tracking performance in the absence of disturbances; trajectories (top) and tracking errors (bottom).

180

The good properties of both the preshaping and regulation techniques are culminated in the final two curves, where the control is layered as before. The feedback becomes active only after a tracking error is detected, allowing the high frequency move with overshoot to be completed successfully. Then, the offset due to the disturbance is eliminated by feedback on a slower time scale. The layering of preshaping trajectories and feedback laws is thus seen to be an effective means for achieving the high-bandwidth trajectories allowed by preshaping, and the important corrective action of feedback.

5.6 Summary

The arguments for nonlinear control in this application revolve around the choice of design envelope, and the resulting dynamic range. The data show that the linear designs can be quite stable with a low design speed, and can have good performance with a high design speed. However, it seems difficult to attain both properties with a single design, for any reasonable range of operating conditions. The nonlinear designs, in contrast, have an improved dynamic range which makes large-envelope designs successful for a wide operating regime. This improved dynamic range is especially crucial to the NLQR, which *must* have a large envelope anyway to ensure that the polynomial approximation is valid. Overall, the LQR/LKF emerges as the most useful among the four nonlinear approaches that were considered, despite the predicted failures of the LQR at low operating speeds.

From a design point of view, the parameters for the nonlinear approaches are based wholly on those of linear designs, so one can effectively shape the nonlinear controller by manipulating quantities in a linear framework. Also, the auxiliary scheme of delayed Smith feedback provides a useful means for accommodating pure delays in the control loop, while keeping the design problem tractable.
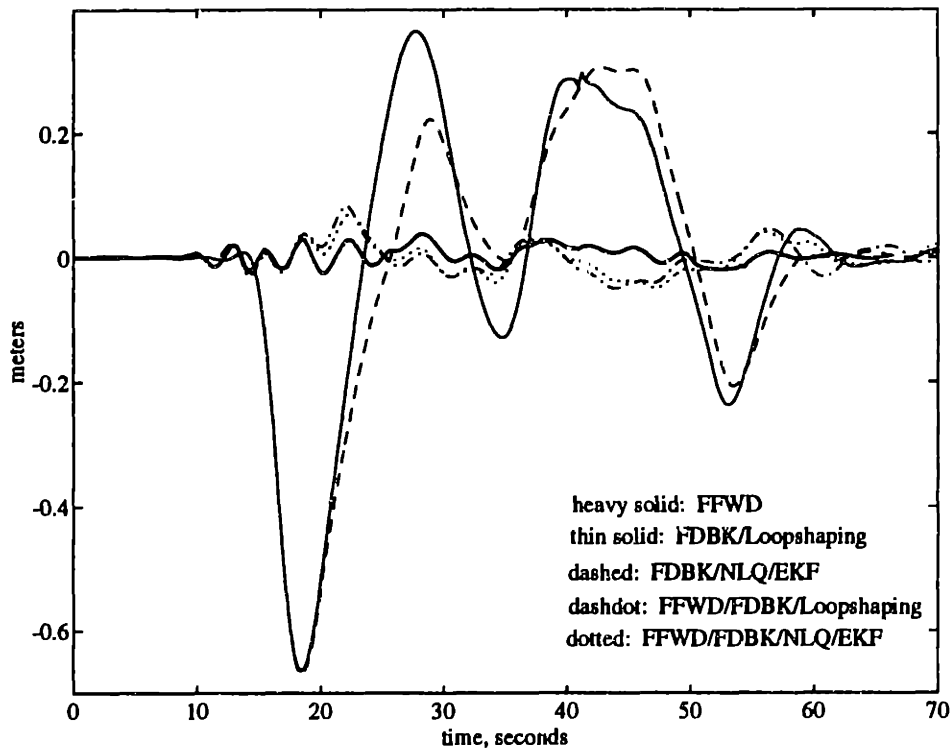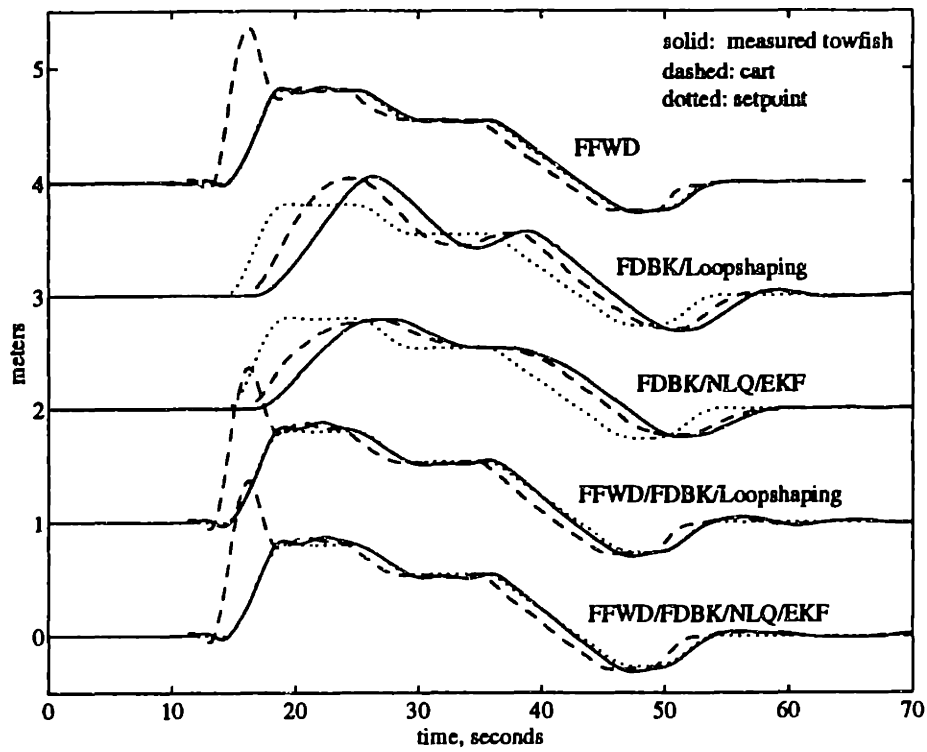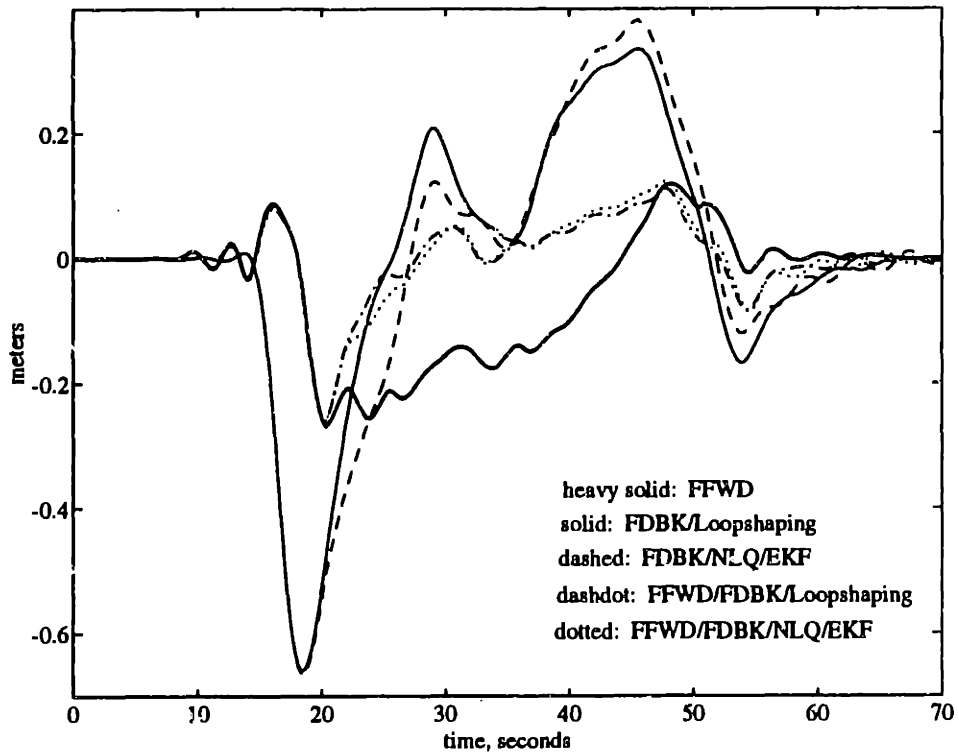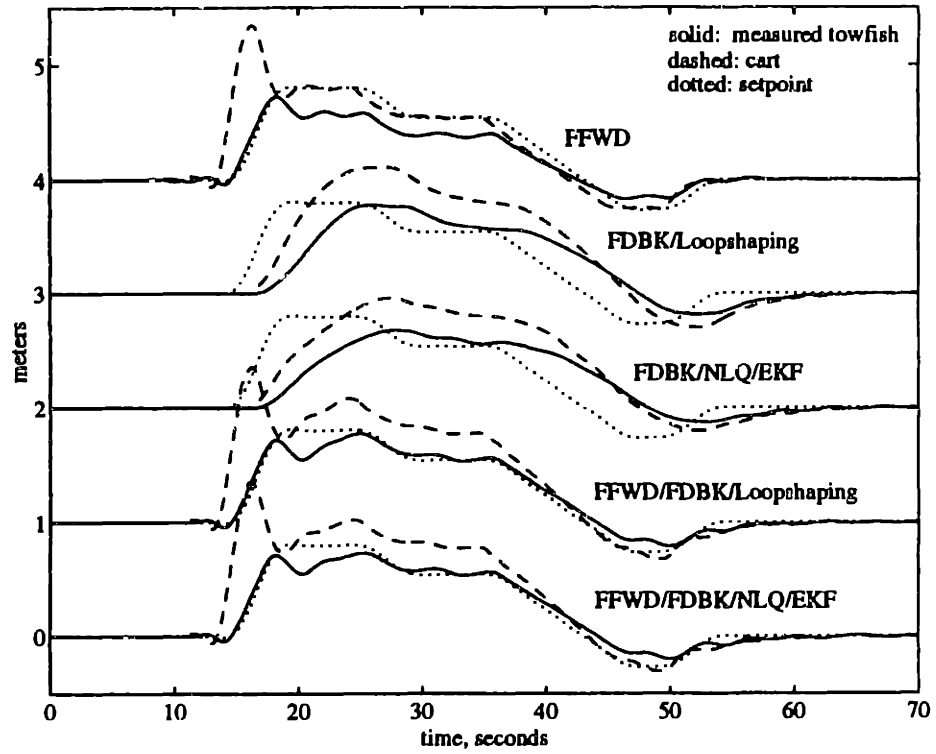
Figure 5-37: Tracking performance in the presence of disturbances; trajectories (top) and tracking errors (bottom).

Chapter 6

Conclusions and

Recommendations

6.1 Summary of Chapter 2

The purpose of Chapter 2 was to develop a model for towed cable systems, suitable for simulation and controller design, and to examine the lateral frequency response of such a cable. Toward this end, the relevant equations describing the motions of underwater cables were described, and two methods of approximate analysis were presented. The harmonic balance approach gave estimates of the lateral frequency response which compared well with both simulations and later experimental data. This response is typified by a strong amplitude dependence, and the potential loss of phase at arbitrarily low frequencies. A multiple-scale perturbation analysis was also conducted, verifying the amplitude dependence of the the frequency response, and providing an algebraic relationship between the excitation amplitude and frequency, and the amplitude of the towfish motion. This compact formula is only marginally useful away from the natural modes. The extension of this perturbation approach to include linear feedback was successful but limited, and both the harmonic balance and perturbation methods correctly predicted the attenuation of frequency and closed-loop responses in the presence of currents in the water.

6.2 Summary of Chapter 3

The ad hoc method of overshooting a desired towfish location with the surface vessel was successfully demonstrated in full-scale tests, with a potential reduction in towfish travel time of around twenty percent, over the pure step responses. A cascade of out-of-plane overshoots was executed, and the results suggest that such a strategy would be useful for precision grid-following operations.

The idea of preshaping vessel trajectories for arbitrarily complex motions of the towfish was developed, and demonstrated in simulations for drill strings with bending stiffness, out-of-plane towing maneuvers, and the heating of a long metal bar incorporating nonlinear dynamics. These examples indicate the generality of the method, and illustrate the stability guidelines for the technique. The method was successfully demonstrated in full-scale tests as well, which punctuated the need for good dynamic positioning of the vessel. These tests also showed also that since there is no feedback involved in the procedure, navigation failures cause only deterioration of the towfish trajectory. This makes it an inherently safe procedure, which is very attractive from an operations point of view.

6.3 Summary of Chapter 4

The loop operator recovery procedure was pursued as a means for carrying out robust nonlinear model-based control. As this procedure benefits from nonlinear observation and nonlinear feedback laws, a number of estimators were outlined, and then the primary contribution of the chapter was presented: a *practical* approximate solution to the nonlinear optimal control problem. This solution is valid for plant models having analytic nonlinearities that can be approximated by cubic polynomials, and for plants having *arbitrary order*. Furthermore, the plant may be multi-input/multi-output, a fact which should make the technique useful for a great many nonlinear control problems beyond this thesis. A design example for a sixth-order, unstable nonlinear plant illustrated the superior performance and robustness properties of the nonlinear regulator, compared to the linear quadratic regulator.

6.4 Summary of Chapter 5

Chapter 5 began with the specification of two full-scale and two scale-model systems, and detailed the experimental apparatus at the test tank at the Woods Hole Oceanographic Institution. One setup resembled a deep-water ROV system, while the other was a scaled drill string system. Some of the practical issues addressed include polynomial approximation of the drag nonlinearity, quantification of modeling errors *at the plant input*, and calculation of the guaranteed properties of the Constant Gain Extended Kalman Filter and the linear quadratic regulator.

The closed-loop response to a ramped step change in the setpoint was adopted as the standard test, and numerous experiments with the scaled drill string system indicated that the nonlinear approaches have significant advantages over linear controllers. In particular, the linear approaches appear to trade limit-cycling for poor performance, depending on the linearization chosen. In contrast, the nonlinear approaches have a much larger dynamic range, so that one can achieve good performance and long-term stability simultaneously. This dynamic range is fortunate, as it was illustrated that the envelope for the nonlinear optimal control law *must* encompass the allowed operating conditions, or else catastrophic instability can occur.

A number of variations were investigated, including the application of delayed Smith feedback, the use of high-order models in controller design, and the rejection of fast and slow disturbances acting on the system. The robustness properties of the designs were considered as well, and the linear designs were found to be remarkably capable in this regard. More specifically, when stabilizing errors were made in the tension and drag terms of the design plant model, there were found only moderate improvements in transient performance by using the nonlinear approaches. However, when destabilizing errors were made, the failures of *all* the designs looked very similar. This trend is in contradistinction to that of the design example in Chapter 4, where the linear quadratic regulator performed very poorly. The main difference between that example and the later cable tests is that in the latter case, drag is naturally stabilizing, which always benefits the linear designs.

Finally, the layering of regulation designs onto a preshaped reference frame, for the scaled ROV system, was verified. This layered control approach takes advantage of the preshaping during high-bandwidth motions, and of the feedback during slow motions. Therefore, the

usual rule that robustness and performance cannot be achieved simultaneously appears to be validated. Our approach provides a smooth way to transition between regimes of performance-oriented operation, and robustness-oriented operation.

6.5   The Big Picture and Recommendations

This thesis has presented techniques that are useful for a range of typical deep-ocean operations employing long vertical cables. Along the way, more general procedures for dynamic inversion and for nonlinear optimal regulator design were developed. The inversion scheme, as it stands, has direct utility for many towing problems, and it has been verified repeatedly in full-scale and model tests, and in simulations for various other nonlinear systems. The approach should be useful for a range of tridiagonal plants with distributed states and local nonlinearities. The nonlinear optimal regulator solution that has been presented, however, has a number of limitations. To begin, as was stated previously, the "hardening" type of nonlinearity is likely to be most appropriate for the method, as the core of the procedure entails making polynomial approximations of the nonlinearities. Furthermore, it was found that the expansions become very difficult as the polynomial order exceeds three. Common saturation- or deadband-type nonlinearities cannot be handled easily with this approach; perhaps future work will enable the use of different basis functions. More work is also needed in the area of model-based nonlinear control, as the LOR technique is theoretically valid only when the controller loop is recovered. At the same time, the experimental results of the thesis are very encouraging for nonlinear control of this type.

Finally, the range of control problems associated with towed underwater cables is much larger than that covered in this thesis. Tests need to be run in the presence of large currents which could affect the closed-loop properties of our designs. The test tank was inadequate for these purposes, although experiments in a towing tank could be conducted. In addition, complications can arise in cables with large layback, due to geometric coupling between in-plane and out-of-plane, as well as vertical, motions. These situations will require models of increased complexity, and multi-input, multi-output control schemes of commensurate ability.

Appendix A

Mathematical Preliminaries

In nonlinear control, the I/O viewpoint is often useful, in which operators map signals from an input space to an output space. A standard reference for this section is Desoer and Vidyasagar [33]. The signals are entire trajectories and not just points in R^n, and their size is usually described with norms; we define the *p-norm* of a signal x to be

$$\| x \|_p = \left[\int_0^\infty | x |^p \, dt \right]^{\frac{1}{p}} . \tag{A.1}$$

In the case that $p = \infty$, we have $\| x \|_\infty = \sup_t | x(t) |$. Let L_p be the set of all signals for which $\| x \|_p$ is finite, i.e.,

$$L_p = \{ x \mid \| x \|_p < \infty \} . \tag{A.2}$$

The *truncation operator* P_τ is given by

$$(P_\tau x) = \begin{cases} x(t), \ t \le \tau \\ 0, \ t > \tau \end{cases} , \tag{A.3}$$

and the *extended space* L_p^e consists of all signals with truncations in L_p, i.e.,

$$L_p^e = \{ x \mid P_\tau x \ni L_p, \forall \tau > 0 \} . \tag{A.4}$$

Thus, L_p^e includes signals which are growing without bound, as well as those which are infinite over a set of zero measure. Finally, the truncated norm of a signal is given by

$$\| x \|_{p,\tau} = \| P_\tau x \|_p = \left[\int_0^\tau | x(t) |^p \, dt \right]^{\frac{1}{p}}. \tag{A.5}$$

The L_p-norm, or *gain*, of an operator g is defined as

$$\| g \|_p = \sup_{u,\tau} \frac{\| gu \|_{p,\tau}}{\| u \|_{p,\tau}}. \tag{A.6}$$

The L_p *incremental gain* of g is

$$\| g \|_{p,\delta} = \sup_{u_1,u_2,\tau} \frac{\| gu_1 - gu_2 \|_{p,\tau}}{\| u_1 - u_2 \|_{p,\tau}}. \tag{A.7}$$

We say that an operator is L_p-*stable* if it has finite gain; this property is often referred to as *finite-gain stability*. Similarly, if inputs of bounded norm induce outputs of bounded norm, a system is said to be *bounded*.

A nonlinear estimator generates an estimate $\hat{x}$, so that the observation error $e := \hat{x} - x$ can be viewed as the output of an operator $E_u(\xi, \theta)$ which takes as its inputs the process and measurement noises and depends on u. The estimator is said to be *nondivergent* [82] if there exists a continuous increasing function $\rho : R \mapsto R$ such that

$$\sup_{u,\tau} \| e \|_{p,\tau} \le \rho(\| \xi, \theta \|_{p,\tau}). \tag{A.8}$$

More informally, a nondivergent estimator takes norm-bounded disturbances ξ and θ into norm-bounded errors in the estimate. Note that nondivergence has to be specified with respect to a given norm. The estimate is *nondivergent with finite gain* if the norm-bound of the error is proportional to the magnitude of the disturbances.

Bibliography

[1] M.A. Abkowitz. *Stability and Motion Control of Ocean Vehicles.* MIT Press, Cambridge, Massachusetts, 1969.

[2] C.M. Ablow and S. Schecter. Numerical simulation of undersea cable dynamics. *Ocean Eng.*, 19:443–457, 1983.

[3] K.D. Amman. The Red Sea Pilot Project: lessons for future ocean mining. *J. Marine Mining*, 8:1–22, 1989.

[4] M. Athans. Class notes: Course 6.232. Massachusetts Institute of Technology, 1991.

[5] M. Athans and P.L. Falb. *Optimal Control.* McGraw-Hill, New York, 1966.

[6] M.J. Balas. Modal control of certain flexible dynamic systems. *SIAM J. Cont. and Opt.*, 16:450–462, 1978.

[7] S. Barnett. Matrix differential equations and Kronecker products. *SIAM J. Appl. Math.*, 24:1–5, 1973.

[8] R.H. Bartles and G.W. Stewart. Solution of the matrix equation AX + XB = C. *Comm. ACM*, 15:820–826, 1972.

[9] E. Bayo. A finite-element approach to control the end-point motion of a single-link flexible robot. *J. Robotic Syst.*, 4:63–75, 1987.

[10] E. Bayo and H. Moulin. An efficient computation of the inverse dynamics of flexible manipulators in the time domain. In *Proc. IEEE Int. Conf. Rob. Auto.*, Scottsdale, Arizona, 1989.

[11] E. Bayo, R. Movaghar, and M. Medus. Inverse dynamics of a single-link flexible robot. analytical and experimental results. *Int. J. Rob. and Auto.*, 3:150–157, 1988.

189

[12] E. Bayo, P. Papadopoulos, J. Stubbe, and M.A. Serna. Inverse dynamics and kinematics of multi-link elastic robots: an iterative frequency-domain approach. *Int. J. Rob. Res.*, 8:49–62, 1989.

[13] J.J. Beaman. Nonlinear quadratic gaussian control. *Int. J. Control*, 39:343–361, 1984.

[14] R. Bellman. *Dynamic Programming.* Princeton University Press, Princeton, New Jersey, 1957.

[15] R. Bellman. *Introduction to Matrix Analysis.* McGraw-Hill, New York, 1960.

[16] C.M. Bender and S.A. Orszag. *Advanced Mathematical Methods for Scientists and Engineers.* McGraw-Hill, New York, 1978.

[17] D. Bestle and M. Zeitz. Canonical form observer design for nonlinear time-variable systems. *Int. J. Control*, 38:343–361, 1983.

[18] E. Blandhol and J.G. Balchen. Determination of system dynamics by use of adjustable models. In *Proc. IFAC Cong.*, Basle, Switzerland, 1963.

[19] A. Bliek. *Dynamic Analysis of Single Span Cables.* PhD thesis, Massachusetts Institute of Technology, 1984.

[20] J.W. Brewer. Kronecker products and matrix calculus in system theory. *IEEE Trans. Circuits Syst.*, 25:772–781, 1978.

[21] R.W. Brockett. Lie algebras and Lie groups in control theory. In D.Q. Mayne and R.W. Brockett, editors, *Geometric Methods in System Theory.* D. Reidel, Boston, 1973.

[22] R.W. Brockett. Volterra series and geometric control theory. *Automatica*, 12:167–176, 1976.

[23] J.J. Burgess. *Natural Modes and Impulsive Motions of a Horizontal Shallow Sag Cable.* PhD thesis, Massachusetts Institute of Technology, 1985.

[24] J.J. Burgess and M.S. Triantafyllou. Time domain simulation of the dynamics of ocean towing lines. In *Proc. Int. Symp. Practical Design of Ships and Mobile Units*, Trondheim, Norway, 1987.

[25] R.H. Cannon, Jr. and E. Schmitz. Initial experiments on the endpoint control of a flexible one-link robot. *Int. J. Rob. Res.*, 3:62–75, 1984.

[26] S. Cetinkunt and S. Wu. Output predictive adaptive control of a single-link flexible arm. *Int. J. Control*, 53:311–333, 1991.

[27] D.A. Chapman. Towed cable behavior during ship turning manoeuvres. *Ocean Eng.*, 11:327–361, 1984.

[28] M.J. Chen and C.A. Desoer. Necessary and sufficient condition for robust stability of linear distributed feedback systems. *Int. J. Control*, 35:255–267, 1982.

[29] C.-C. Cheng. *Predictor Displays: Theory Development and Application to Towed Submersibles*. PhD thesis, Massachusetts Institute of Technology, 1991.

[30] H. Cox. Estimation of state variables via dynamic programming. In *Proc. Joint Auto. Cont. Conf.*, Stanford, CA, 1964.

[31] R.F. Curtain and K. Glover. Controller design for distributed systems based on Hankel-norm approximations. *IEEE Trans. Auto. Cont.*, 31:173–176, 1986.

[32] T.E. Dabbous and N.U. Ahmed. Nonlinear optimal feedback regulation of satellite angular momenta. *IEEE Trans. Aero. and Elect. Syst.*, 18:2–9, 1982.

[33] C.A. Desoer and M. Vidyasagar. *Feedback Systems: Input-Output Properties*. Academic, New York, 1975.

[34] C.A. Desoer and Y.-T. Wang. The robust nonlinear servomechanism problem. *Int. J. Control*, 29:803–828, 1979.

[35] C.A. Desoer and Y.-T. Wang. Foundations of feedback theory for nonlinear dynamical systems. *IEEE Trans. Circuits and Systems*, 27:104–123, 1980.

[36] J.C. Doyle. Guaranteed margins for LQG regulators. *IEEE Trans. Auto. Cont.*, 23:756–757, 1978.

[37] J.C. Doyle. Structured uncertainty in control system design. In *Proc. IEEE Conf. Dec. Cont.*, Fort Lauderdale, Florida, 1985.

[38] J.C. Doyle, B.A. Francis, and A.R. Tannenbaum. *Feedback Control Theory*. Macmillan, New York, 1992.

[39] J.C. Doyle and G. Stein. Multivariable feedback design: concepts for a classical/modern synthesis. *IEEE Trans. Auto. Cont.*, 26:4–16, 1981.

[40] T.A.W. Dwyer, 3rd. Approximation and interpolation of optimal nonlinear regulators. In *Proc. IEEE Conf. Dec. Cont.*, Las Vegas, Nevada, 1984.

[41] T.A.W. Dwyer, 3rd. and R.P. Sena. Control of spacecraft slewing maneuvers. In *Proc. IEEE Conf. Dec. Cont.*, Orlando, Florida, 1982.

[42] J. Feldman. DTNSRDC revised standard submarine equations of motion. Technical report, David W. Taylor Naval Ship Research and Development Center, 1979.

[43] B.A. Francis. *A Course in H_∞ Control Theory*. Springer-Verlag, Berlin, 1987.

[44] A. Gelb. *Applied Optimal Estimation*. MIT Press, Cambridge, Massachusetts, 1974.

[45] A. Gelb and W.E. VanderVelde. *Multiple-Input Describing Functions and Nonlinear System Design*. McGraw-Hill, New York, 1968.

[46] S.T. Glad. On the gain margin of nonlinear and optimal regulators. In *Proc. IEEE Conf. Dec. Cont.*, Orlando, Florida, 1982.

[47] K. Glover and J.C. Doyle. State-space formulae for all stabilizing controllers that satisfy an H_∞-norm bound and relations to risk sensitivity. *Syst. Cont. Let.*, 11:167–172, 1988.

[48] M.A. Grosenbaugh and M.S. Triantafyllou. A fast numerical method for dynamic analysis of buoy-cable interactions. unpublished report, 1992.

[49] M.A. Grosenbaugh, D.R. Yoerger, F.S. Hover, and M.S. Triantafyllou. Drag forces and flow-induced vibrations of a long vertical tow cable—Part 2: unsteady towing conditions. *J. Offshore Mech. and Arctic Eng.*, 113:199–204, 1991.

[50] D.B. Grunberg. *A Methodology for Designing Robust Multivariable Nonlinear Control Systems*. PhD thesis, Massachusetts Institute of Technology, 1986.

[51] D.B. Grunberg and M. Athans. A methodology for designing robust multivariable nonlinear feedback control systems. In *Proc. American Cont. Conf.*, Boston, 1985.

[52] E.L. Guerch. The deep towing of underwater fish behaviour during half-turn manoeuvres. *Ocean Eng.*, 14:145–162, 1987.

[53] P. Hagedorn. *Active vibration damping in large flexible structures.* Elsevier, New York, 1989.

[54] D.C. Herbert and R. Jones. Localized states in disordered systems. *J. Phys. C: Solid State Physics*, 4:1145–1161, 1971.

[55] F.S. Hover and D.R. Yoerger. Identification of low-order dynamic models for deeply-towed underwater vehicle systems. *Int. J. Offshore and Polar Eng.*, 2:38–45, 1992.

[56] C.T. Howell. *Investigation of the Dynamics of Low-Tension Cables.* PhD thesis, Massuchusetts Institute of Technology, 1992.

[57] W.D. Ivers and J.D. Mudie. Towing a long cable at slow speeds: a three-dimensional dynamic model. *Mar. Tech. Soc. J.*, 7:23–31, 1973.

[58] J.-N. Juang and L.G. Horta. Effects of atmosphere on slewing control of a flexible structure. *J. Guidance*, 10:387–392, 1987.

[59] F. Kreith and M.S. Bohn. *Principles of Heat Transfer.* Harper and Row, New York, 1986.

[60] H. Kwakernaak and R. Sivan. The maximally achievable accuracy of linear optimal regulators and linear optimal filters. *IEEE Trans. Auto. Cont.*, 17:79–86, 1972.

[61] A.J. Laub. A Schur method for solving algebraic Riccati equations. Technical Report LIDS-R-859, Massachusetts Institute of Technology, 1978.

[62] K.-S. Liu, F.L. Huang, and G. Chen. Exponential stability analysis of a long chain of coupled vibrating strings with dissipative linkage. *SIAM J. App. Math.*, 49:1694–1707, 1989.

[63] K.A. Loparo and G.L. Blankenship. Algebraic features of some computational problems in nonlinear stability theory. In *Proc. IEEE Conf. Dec. Cont.*, New Orleans, Louisiana, 1977.

[64] H.J. Lugt. *Vortex Flow in Nature and Technology*. Wiley, New York, 1983.

[65] D.L. Lukes. Optimal regulation of nonlinear dynamical systems. *SIAM J. Control and Optimization*, 7:75–100, 1969.

[66] R. Luus. Application of dynamic programming to high-dimensional optimal control problems. *Int. J. Control*, 52:239–250, 1990.

[67] R. Luus. Optimal control by dynamic programming using systematic reduction in grid size. *Int. J. Control*, 51:995–1013, 1990.

[68] E.A. Misawa and J.K. Hedrick. Nonlinear observers—a state-of-the-art survey. *J. Dyn. Syst. Meas. Cont.*, 111:344–352, 1989.

[69] B.C. Moore. Principal component analysis in linear systems: controllability, observability, and model reduction. *IEEE Trans. Auto. Cont.*, 26:17–32, 1981.

[70] P.J. Moylan and B.D.O. Anderson. Nonlinear regulator theory and an inverse optimal control problem. *IEEE Trans. Auto. Cont.*, 18:460–465, 1973.

[71] J.D. Mudie and W.D. Ivers. Simulation studies of the response of a deeply towed vehicle to various towing ship maneuvers. *Ocean Eng.*, 3:37–46, 1975.

[72] J.D. Mudie and K.A. Kastens. Computer aided piloting of a deeply-towed vehicle. *Ocean Eng.*, 7:743–754, 1980.

[73] M.L. Nagurka and V. Yen. Fourier-based optimal control of nonlinear dynamic systems. *J. Dyn. Syst. Meas. Cont.*, 112:17–26, 1990.

[74] A.H. Nayfeh and D.T. Mook. *Nonlinear Oscillations*. Wiley, New York, 1979.

[75] H. Neudecker. Some theorems on matrix differentiation with special reference to Kronecker matrix products. *J. Amer. Stat. Assoc.*, 64:953–963, 1969.

[76] Y. Okano. Limits of LQG control in ocean engineering. In *Proc. Int. Off. and Polar Eng. Conf.*, San Francisco, California, 1992.

[77] J.A. O'Sullivan and M.K. Sain. Nonlinear optimal control with tensors: Some computational issues. In *Proc. Amer. Cont. Conf.*, Boston, Massachusetts, 1985.

[78] B. Paden, B. Riedle, and E. Bayo. Exponentially stable tracking control for multi-joint flexible-link manipulators. In *Proc. Amer. Cont. Conf.*, San Diego, California, 1990.

[79] V.J. Papazoglou, S.A. Mavrakos, and M.S. Triantafyllou. Nonlinear cable response and model testing in water. *J. Sound Vib.*, 140:103–115, 1990.

[80] B. Paul and A.I. Soler. Cable dynamics and optimum towing strategies for submersibles. *MTS Journal*, 6:34–42, 1972.

[81] J.A. Roberson and C.T. Crowe. *Engineering Fluid Mechanics*. Houghton Mifflin, Boston, Massachusetts, 1985.

[82] M.G. Safonov. *Stability and Robustness of Multivariable Feedback Systems*. MIT Press, Cambridge, Massachusetts, 1980.

[83] M.G. Safonov and M. Athans. Gain and phase margin for multiloop LQG regulators. *IEEE Trans. Auto. Cont.*, 22:173–179, 1977.

[84] M.G. Safonov and M. Athans. Robustness and computational aspects of nonlinear stochastic estimators and regulators. *IEEE Trans. Auto. Cont.*, 23:717–725, 1978.

[85] M.G. Safonov and R.Y. Chiang. Model reduction for robust control: a Schur relative-error method. In *Proc. Amer. Cont. Conf.*, Atlanta, GA, 1988.

[86] Y. Sakawa, F. Matsuno, and S. Fukushima. Modeling and feedback control of a flexible arm. *J. Rob. Syst.*, 2:453–472, 1985.

[87] J.V. Sanders. A three-dimensional dynamic analysis of a towed system. *Ocean Eng.*, 9:483–499, 1982.

[88] M.A. Serna and E. Bayo. Trajectory planning for flexible manipulators. In *Proc. IEEE Int. Conf. Rob. Auto.*, Cincinnati, Ohio, 1990.

[89] N.C. Singer and W.P. Seering. Using acausal shaping techniques to reduce robot vibration. In *Proc. IEEE Conf. Rob. Auto.*, Philadelphia, Pennsylvania, 1988.

[90] W.E. Singhose, W.P. Seering, and N.C. Singer. Shaping inputs to reduce vibration: a vector diagram approach. In *Proc. IEEE Int. Conf. Rob. Auto.*, Cincinnati, Ohio, 1990.

[91] J.-J.E. Slotine, J.K. Hedrick, and E.A. Misawa. Sliding observers for nonlinear systems. *J. Dyn. Syst. Meas. Cont.*, 109:245–252, 1987.

[92] J.-J.E. Slotine and W. Li. *Applied Nonlinear Control.* Prentice-Hall, Englewood Cliffs, New Jersey, 1991.

[93] O.J.M. Smith. *Feedback Control Systems.* McGraw-Hill, New York, 1958.

[94] G. Stein and M. Athans. The LQG/LTR procedure for multivariable feedback control design. *IEEE Trans. Auto. Cont.*, 32:105–114, 1987.

[95] T.-J. Tarn and Y. Rasis. Observers for nonlinear stochastic systems. *IEEE Trans. Auto. Cont.*, 21:441–448, 1976.

[96] F.E. Thau. Observing the state of nonlinear dynamic systems. *Int. J. Cont.*, 17:471–479, 1973.

[97] M.S. Triantafyllou. Preliminary design of mooring systems. *J. Ship Res.*, 26:25–35, 1982.

[98] M.S. Triantafyllou and M.A. Grosenbaugh. Robust control for underwater vehicle systems with time delays. *IEEE J. Oceanic Eng.*, 16:146–151, 1991.

[99] J.N. Tsitsiklis and M. Athans. Guaranteed robustness properties of multivariable nonlinear stochastic optimal regulators. *IEEE Trans. Auto. Cont.*, 29:690–696, 1984.

[100] W.J. Vetter. Matrix calculus operations and Taylor expansions. *SIAM Rev.*, 15:352–369, 1973.

[101] T.L. Vincent, S.P. Joshi, and Y.C. Lin. Positioning and active damping of spring-mass systems. *J. Dyn. Syst. Meas. Cont.*, 111:592–599, 1989.

[102] J.C. Willems. *Analysis of Feedback Systems.* MIT Press, 1971.

[103] A.P. Willemstein. Optimal regulation of nonlinear dynamical systems on a finite interval. *SIAM J. Cont. and Opt.*, 15:1050–1069, 1977.

[104] K.S. Yeung and Y.P. Chen. Regulation of a one-link flexible robot arm using sliding-mode technique. *Int. J. Control*, 49:1965–1978, 1989.

[105] T. Yoshida and K.A. Loparo. Quadratic regulatory theory for analytic nonlinear systems with additive controls. *Automatica*, 25:531–544, 1989.

[106] O. Zeitouni and A. Dembo. On the maximal achievable accuracy in nonlinear filtering problems. *IEEE Trans. Auto. Control*, 33:965–967, 1988.